Abstract

"Oxide Ion Conductors for Energy Applications: Structure, Dynamics and Properties"

PhD Thesis Joseph R. Peet 2018

The work reported in this thesis investigates the relationships between the structural features of oxide ion conductors and the resulting oxide ion conduction mechanisms. This is achieved using a combination of attempted syntheses of new materials with novel structural features, direct observation of oxide ion dynamics *via* neutron scattering and simulation of oxide diffusion pathways using *ab initio* molecular dynamics.

The results of a variable temperature solid state ^{23}Na NMR investigation into nominal $Sr_{0.6}Na_{0.4}SiO_{2.8}$ are reported, showing conclusively that the charge carriers in the material are Na^+ ions rather than O^{2-}. The preparation, characterisation and conductivity properties of the $Sr_{1-x}La_xSiO_{3+0.5x}$ and $Sr_{1-x}La_xGeO_{3+0.5x}$ series as well as Y^{3+} and Ce^{3+} doped $BaZrSi_3O_9$ are also reported.

Quasieleastic and inelastic neutron scattering studies have been carried out, investigating diffusion processes in $La_2Mo_2O_9$, $Bi_{0.913}V_{0.087}O_{1.587}$ and $La_{10-x}Bi_xGe_6O_{27}$. These studies extend the body of work reporting the use of neutron scattering techniques on oxide ion conductors significantly. Phonon density of states derived from inelastic neutron scattering provide corroboration of the results gained from *ab initio* molecular dynamics calculations. The quasielastic neutron scattering results allow direct observation of long range oxide ion dynamics on timescales of nanoseconds, the longest timescales observed in oxide ion conductors reported to date.

The findings from in depth *ab initio* molecular dynamics (AIMD) investigations into $La_2Mo_2O_9$ and $Bi_{0.913}V_{0.087}O_{1.587}$, with a larger simulation boxes and significantly longer simulation times than those previously reported, are also presented. These calculations have allowed the individual conduction mechanisms in these materials to be examined in much greater detail than in previous work. AIMD simulations have also been carried out to probe the dynamics in $La_{10-x}Bi_xGe_6O_{27}$ and explore the effects that Bi^{3+} doping has on individual oxide conduction mechanisms and overall conductivity. The AIMD simulations are supported by the first explicit electronic calculations of the lone pair locations and orientations in apatite materials, calculated *via* the use of the electron localisation function (ELF).[1]

Oxide Ion Conductors for Energy Applications: Structure, Dynamics and Properties

Joseph R. Peet

Supervisors: Dr. Ivana R. Evans, Dr. Mark Johnson and Dr. Andrea Piovano

A thesis submitted in partial fulfilment of the requirements for the degree of Doctor of Philosophy.

Department of Chemistry
Durham University
2018

Table of Contents

List of Abbreviations

AIMD	*Ab Initio* Molecular Dynamics
BFGS	Broyden–Fletcher–Goldfarb–Shanno
C-E	Chudley-Elliott
DFT	Density Functional Theory
DOS	Density of States
EDX	Energy Dispersive X-ray
ELF	Electron Localisation Function
ESB	Erbia-Stabilised Bismuth oxide
FWHM	Full Width Half Maximum
GDC	Gadolinium-Doped Ceria
GGA	Generalised Gradient Approximation
HWHM	Half Width Half Maximum
ILL	Institut Laue-Langevin
INS	Inelastic Neutron Scattering
IT	Intermediate Temperature
KMC	Kinetic Monte Carlo
LAMP	Large Array Manipulation Program
LDA	Local Density Approximation
MAS	Magic Angle Spinning
MD	Molecular Dynamics
MDANSE	Molecular Dynamics Analysis for Neutron Scattering Experiments
MSD	Mean Square Displacement

NEB	Nudged Elastic Band
NMR	Nuclear Magnetic Resonance
NPD	Neutron Powder Diffraction
PAW	Projector Augmented Wave
PBE	Perdew-Burke-Ernzerhof
PG	Pyrolytic Graphite-
PST	Phase Space Transformation
QENS	QuasiElastic Neutron Scattering
SEM	Scanning Electron Microscopy
SIMS	Secondary Ion Mass Spectrometry
SOFC	Solid Oxide Fuel Cell
SS	Solid State
TCHZ	Thompson-Cox-Hastings
TOF	Time-of-Flight
VASP	Vienna *Ab initio* Simulation Package
VTF	Vogel-Tamman-Fulcher
XRD	X-Ray Diffraction
YSZ	Yttria-Stabilised Zirconia

Declaration

The work submitted in this thesis is entirely my own, except where I have acknowledged help from, or collaboration with, a named person, or given reference to a published source or thesis.

The research presented was performed in the Department of Chemistry, Durham University, and at the Institut Laue Langevin, between October 2014 and December 2017, the results of which have not been submitted for a degree in this or any other university.

Statement of Copyright

Chapter 1. Introduction and Literature Review

1.1. Introduction to Oxide Ion Conductors

Oxide ion conductors are crystalline materials that contain oxide ions which, rather than being fixed, can move through the crystal lattice by jumping between sites. Provided temperatures are high enough to activate this process, this property allows oxide ion conductors to transport current *via* oxide ions.[1] These materials are of considerable research interest due to their range of environmental and energy-related applications including oxygen sensors and pumps;[2] separation membranes;[3, 4] and solid oxide fuel cells (SOFCs).[1, 5, 6] Understanding the structural characteristics and resulting conduction pathways in these materials is a key requirement in improving their properties through smart design. This project is focussed on investigating these relationships with a variety of techniques.

1.1.1. Solid Oxide Fuel Cells

Solid oxide fuels cells are a particular application of oxide ion conductors that invite a lot of research interest. SOFCs are a method of electricity production that provide many advantages over conventional power generation, such as reduced NO_x, SO_x, and CO_2 emission[7] (zero if H_2 is used as the fuel) and higher efficiency.[8] With concerns about the environmental impact of technologies growing, and interest in the search for sustainable power generation increasing, the development of a viable, inexpensive SOFC would be of great importance. Additional advantages of SOFCs beyond environmental concerns include their lack of moving parts, which increases the reliability of the fuel cells while decreasing noise pollution, and their flexibility in terms of size and fuel, which makes them potentially useful in a wide variety of situations and environments.[6, 9]

1.1.1.1. Solid Oxide Fuel Cell Construction

Solid oxide fuel cells are composed of three main components, an anode, a cathode and an electrolyte, that lies between them, which takes the form of an oxide ion conductor. The components of a SOFC as well as a basic representation of its operation can be seen in Figure 1.1. Oxygen, (pure or simply as a part of air), enters the system at the cathode, where it is reduced to form oxide ions. The ions are transported from the cathode to the anode *via* the oxide ion conductor electrolyte and then react with the fuel, (depicted as H_2 in figure 1.1 but hydrocarbons can also be used[10-12]). This produces water as the waste product and liberates electrons, which flow through an external circuit back to the cathode thereby generating power.

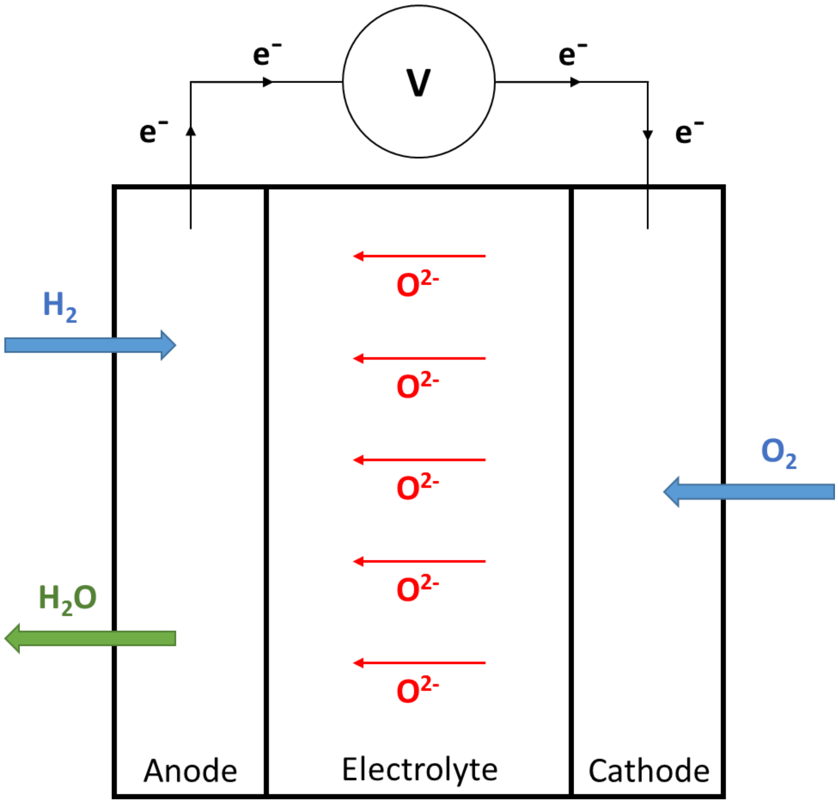

Figure 1.1: Diagram of a solid oxide fuel cell. The fuel in this case is assumed to be H_2.

Finding a suitable oxide ion conductor for use as the electrolyte in a SOFC is obviously a key factor in ensuring the future of the technology. Ideally the electrolyte would be made from readily available and cheap materials, but it must meet several other criteria in order to be useful in this application.

Firstly, and most importantly, the electrolyte should exceed the community accepted threshold conductivity of 10^{-2} S cm^{-1} at the operating temperature.[13] Secondly, the material must have high oxide ion conductivity while also being an electrical insulator.[14] This is required because if the material was also an electrical conductor, then the electrons produced at the anode would flow back through the electrolyte rather than the external circuit, therefore producing no usable electrical power. There are several methods with which it can be shown that the dominant charge carriers in a material are oxide ions rather than electrons. The oxide ionic transference number, the fraction of total current in a material that is carried by O^{2-} ions, can be determined by using a concentration cell, in which the cathode is exposed to high O_2 partial pressure and the anode low. The electromotive force across the cell can then be used to find the ionic transference number.[15] A second method is the use of tracer ions. The material is exposed for a length of time to a gas containing a high concentration of ^{18}O which diffuses into it. The concentration of ^{18}O can then be measured as a function of distance penetrated using time-of-flight secondary ion mass spectrometry. This can be used to confirm the diffusion of oxide ions in the material.[16] A final method is to measure conductivity as a function of oxygen partial pressure. If the conductivity remains unchanged over a wide range of partial pressures then the material can be said to be a purely ionic conductor rather than electronic. That these ions are O^{2-} can then be confirmed using one of the previously described methods if necessary.[17]

A third criterion that electrolytes must fulfil is that they must be chemically and mechanically stable under heating with a low coefficient of thermal expansion. Finally, electrolytes must be chemically compatible with the other parts of the SOFC system, especially the anode and cathode.

Materials making up the anode and cathode of the SOFC require somewhat different properties. In contrast to the electrolyte they must be electronic conductors with oxide ion conductivity a desirable but not strictly necessary factor. Porosity is another desirable factor, allowing the fuel at the anode and O_2 at the cathode to directly interact with the electrolyte.[18] Anodes for SOFCs have typically been made of composite materials such as Ni/yttria-stabilised zirconia (YSZ)[19] or Ni/Gd-doped ceria,[20] however the search for lower operating temperatures and the vulnerability to sulphur poisoning[21] means that studies are ongoing into mixed ionic-electronic conductor materials such as amorphous $La_2Mo_2O_{7-\delta}$[22, 23] and $PrBaMn_2O_{5+\delta}$.[10] Cathodes made of composites of doped lanthanum manganates and YSZ have been most frequently used[24, 25] although research into alternatives is being carried out.[26, 27]

1.1.1.2. Current Status of Solid Oxide Fuel Cell Technology

A major concern with SOFCs are the high operating temperatures, with the currently widely used oxide ion conductor, yttria-stabilised zirconia (YSZ), requiring a temperature of 700 °C to achieve the 10^{-2} S cm^{-1} threshold.[28] This leads to problems as cells must then be constructed to withstand such high temperatures. The construction of an intermediate temperature solid oxide fuel cell (IT-SOFC) with operating temperatures between 500 and 700 °C would lead to great improvements in terms of cost, safety, long term reliability and cell durability. Because of this much research is focused on developing an oxide ion conductor that will allow such IT-SOFC to be manufactured.

Current state-of-the-art IT-SOFCs include “The Steel Cell” developed by Ceres Power.[29] The cell operates using natural gas as a fuel with a gadolinium-doped cerium oxide electrolyte, and has reported operating temperatures of 500-600 ˚C. Another potential commercial fuel cell, “The Cube”, is developed by Redox Power Systems.[30] Although details about the materials used are minimal, it appears that this is based on bismuth oxide in a bilayer with gadolinium-doped ceria, and has operating temperatures of 650 ˚C.[31]

1.1.2. Fluorite Structure Oxide Ion Conductors

A widely studied family of oxide ion conductors are those with a fluorite structure. These include materials based on ZrO_2, δ-Bi_2O_3, and CeO_2, which as described in section 1.1.1 make up a large proportion of oxide ion conductors used in current applications.

The conductive fluorite phases in these materials have a cubic unit cell with space group $Fm\bar{3}m$. The metal cations form a face centred cubic array, and are each bonded to 8 oxygen atoms that occupy the tetrahedral holes, each bonded to four cations. This structure can be seen in figure 1.2. In order to create oxygen vacancies and increase conductivity these materials are often doped with lower valence metal cations.

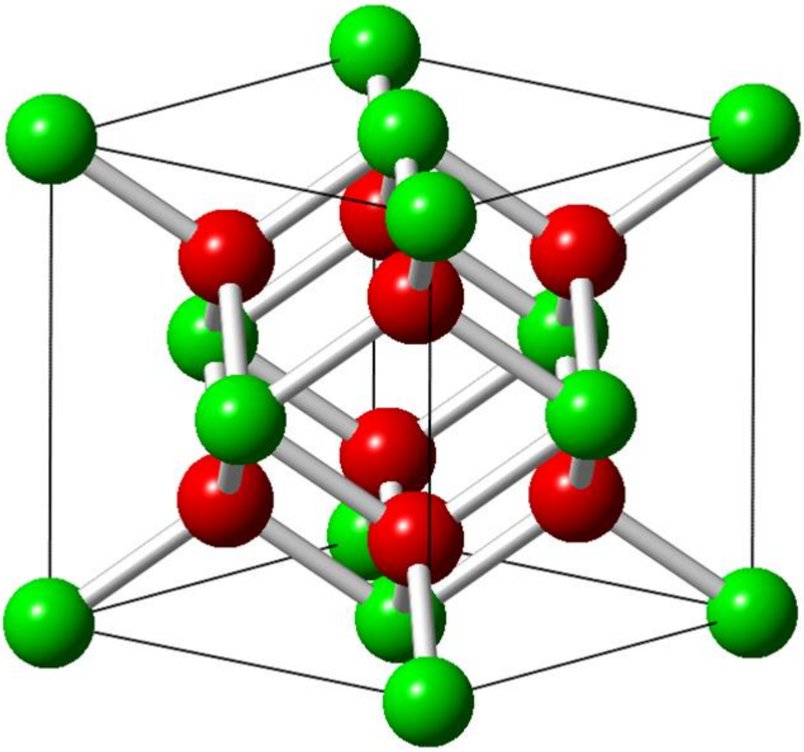

Figure 1.2: Structure of fluorite, space group $Fm\bar{3}m$. Green atoms represent the metal cations, red atoms represent oxygen atoms. The structure can be doped with M^{3+} cations causing O sites to become vacant to preserve charge balance. In the case of δ-Bi_2O_3, 25% of the O sites are vacant in the parent material.

1.1.2.1. Stabilised Cubic Zirconia

Zirconia has been the focus of a large amount of research into oxide ion conduction applications and currently finds use commercially.[32] ZrO_2 exists in several phases depending on the temperature; at room temperature it exists in a monoclinic ($P2_1/c$) phase,[33] at 1170 °C[34] it undergoes a transition to a tetragonal ($P4_2/nmc$)[35] phase, and finally at 1270 °C it transitions to a fluorite ($Fm\bar{3}m$) cubic phase. The addition of trivalent cation dopants creates oxygen vacancies in the material giving rise to oxide ion conductivity. This doping has the duel effect of stabilising the high temperature fluorite phase at lower temperatures, useful as this is the doped phase that is found to have the highest conductivity.[36]

A popular dopant for use in zirconia is yttrium. Yttria-stabilised zirconia (YSZ) is currently the most widely used oxide ion conductor commercially, with 8% doped YSZ showing oxide ion conductivity of 3×10^{-2} S cm^{-1} at 800 °C.[37] Other dopants have been used such as ytterbium[38] and scandium[39] which have been reported to have conductivities of 6.3×10^{-2} Scm^{-1} and 13×10^{-2} Scm^{-1} at 800 °C respectively. Despite the higher values for Sc and Yb dopants, YSZ remains the most widely used oxide ion conductor due to the lower costs of yttrium containing reagents. While the conductivity of YSZ is high, the approximately 700 °C temperature required to reach the 10^{-2} S cm^{-1} limit[28] is too high to make the material suitable for IT-SOFCs.

1.1.2.2. Cerium Oxide

In contrast with zirconia, CeO_2 adopts the fluorite structure at all temperatures up to 1500 °C.[40] However, as the tetrahedral oxygen sites are fully occupied, the material must be doped to introduce oxygen vacancies. Gd^{3+} is a common dopant, with gadolinium-doped ceria (GDC) reaching conductivities of around 1.8×10^{-2} Scm^{-1} at 600 °C,[41, 42] and being used in application as both an electrolyte[29] and as part of composite anodes in SOFCs.[19] Other common dopants for ceria are Sm,[43] Dy,[44] and Nd.[45]

A difficulty in working with doped ceria based oxide ion conductors is that at low partial pressures of oxygen (such as at the anode of a SOFC, where the oxygen partial pressure can reach as low as $\approx 10^{-18}$ atm)[18] Ce^{4+} reduces to Ce^{3+} causing the material to become a mixed ionic and electronic conductor.[46] Because of this, doped ceria based SOFCs are often constructed from a bilayer of two electrolytes. To prevent reduction a layer of YSZ can be used to separate the ceria electrolyte from the anode, with a YSZ thickness of 3 µm being found effective for this purpose in a GDC/YSZ bilayer.[47] A disadvantage of such systems is that the conductivity of such a bilayer is lower than that of the two constituent materials due to the formation of a low conductivity phase at the interface between them.[48-50] For example, a GDC/YSZ bilayer electrolyte has a conductivity nearly two orders of magnitude below that of YSZ and GDC at all temperatures.[48] However, recently it has been shown that by introducing a Fe_2O_3 additive to both materials the sintering temperature to form the bilayer is lowered from 1400 to 1300 °C, reducing the thickness of the interface layer and improving the conductivity at 500 °C from 5.00×10^{-5} S cm^{-1} to 6.44×10^{-4} S cm^{-1}.[51]

An alternative bilayer material for use with doped ceria is δ-Bi_2O_3 (discussed below); however, as Bi^{3+} is reduced to Bi metal at low oxygen partial pressures (≈ 10^{-13} atm),[52] the ceria material is placed at the anode to protect the δ-Bi_2O_3 layer.[53-55] The δ-Bi_2O_3 layer acts to block the flow of electrons caused by the reduction of the ceria, preventing their transport through the electrolyte from the anode to the cathode.[56] In the case of an Er-stabilised bismuth oxide (ESB)/Sm-doped ceria bilayer, Park *et al*. found that the conductivity was slightly higher in the 600-800 °C temperature range than a pure Sm-doped ceria electrolyte, indicating that unlike for YSZ/doped ceria bilayers no low conductivity interface layer is formed.[57] A SOFC constructed from an electrolyte bilayer with 10 µm thickness of GDC and 4 µm of ESB with a NiO/GDC anode and a $Bi_2Ru_2O_7$/ESB cathode showed a very high maximum power density of 1.95 W cm^{-2} at 650 °C,[58] almost double that of an identically constructed cell without the ESB layer.[59] These results indicate that these doped ceria/δ-Bi_2O_3 bilayers offer substantial improvements over the single doped ceria layer electrolytes in the intermediate temperature range. A bilayer of this type appears to be utilised by Redox power systems for their IT-SOFCs.[31]

1.1.2.3. δ-Bismuth Oxide

Another material that exhibits high oxide ion conductivity is δ-Bi_2O_3, the high temperature (>730 °C) phase of bismuth oxide.[60] δ-Bi_2O_3 adopts the fluorite structure shown in figure 1.2, with Bi atoms forming a face centred cubic array and O atoms occupying the tetrahedral holes. However, unlike in zirconia and ceria the δ-Bi_2O_3 structure contains intrinsic oxide vacancies,[61] with three O atoms distributed over the four possible tetrahedral holes. These vacancies give rise to high values for oxide ion conductivity with 1.0 S cm^{-1} being reported at 730 °C.[62]

Despite these high values of conductivity, δ-Bi_2O_3 is unsuitable for use as the oxide ion conductor in a solid oxide fuel cell for two main reasons. The first is the reducibility of Bi^{3+} to Bi metal at low oxygen partial pressures[52] which causes a δ-Bi_2O_3 electrolyte to decompose if used on the anode side of the fuel cell. As described above a bilayer electrolyte can be created to alleviate these problems with the δ-Bi_2O_3 material at the cathode and a doped ceria oxide ion conductor at the anode. Additionally, pairing δ-Bi_2O_3 with a YSZ layer at the anode also shows improved properties.[63, 64] For example, in 2017, a SOFC constructed from an electrolyte bilayer of 7 µm YSZ and 5 µm erbium-stabilised Bi_2O_3 with Ni/YSZ anode and $La_{0.8}Sr_{0.2}MnO_{3-\delta}$/ESB cathode showed the highest maximum power density (2.08 W cm^{-2} at 700 °C) reported for any SOFC with a YSZ based electrolyte to date.[65]

The second reason for the unsuitability of δ-Bi_2O_3 in applications based on oxide ion conductivity is that it forms at 730 °C and melts at 824 °C.[62] This narrow temperature range and the volume change caused by the 730 °C phase transition makes using the material in applications unfeasible. Because of this attempts have been made to stabilise the cubic phase at lower temperatures by doping with other cations. As vacancies are already present in the structure the range of potential dopants is large as isovalent and aliovalent cations can be used. Many possible dopants have been studied including Ca,[66] Sr, La,[67] Mo,[68] Re, [69] Y, Ce,[70] Nb[71] and V.[72, 73] $Bi_{0.913}V_{0.087}O_{1.587}$, reported in 2012,[73] has an oxide ion conductivity at 500 °C of 3.9×10^{-2} Scm^{-1} which remains the highest reported for a bulk material.

In addition to these fluorite materials, other newer types of oxide ion conductors have been developed. As well as investigations into $Bi_{0.913}V_{0.087}O_{1.587}$ (Chapter 5) this thesis reports the results of investigations into some of these newer materials: $La_2Mo_2O_9$ (Chapter 4)[74] and Bi-doped $La_{10}Ge_6O_{27}$ apatite (Chapter 6).[75, 76] In addition to this, potential oxide ion conductor candidates in the form of materials containing isolated Si_3O_9 groups, including doped $SrSiO_3$[77] and doped $BaZrSi_3O_9$,[78] are discussed in the introduction to Chapter 3. Previous literature work on all of these materials is discussed in the introduction sections of the respective chapters.

1.2. Mechanisms of Oxide Ion Conduction

1.2.1. Random Walk Model

A simple way of modelling the mechanism of conduction in an oxide ion conductor is the random walk model. In this model it is assumed that all charge carriers act as independent entities that react to a uniform electric field E by jumping from site to vacant site. When the electric field is applied, jumps in the same direction as the field are more energetically favourable than those in the opposite direction. This gives an overall net movement with mean velocity v in the direction of the electric field.[13] Conductivity (σ) is given by equation 1.1:

$$\sigma = cq\mu \qquad \text{Equation 1.1}$$

Where c is the concentration of charge carriers, $\mu = v/E$ is the electrical mobility of the carrier, and q is their charge, in the case of oxide ions $q = 2$. The Nernst-Einstein relationship for the diffusion of charged particles is given in equation 1.2:[79]

$$D = \frac{\mu k_\mathrm{b} T}{q} \qquad \text{Equation 1.2}$$

Where D is the diffusion coefficient, k_b is the Boltzmann constant and T is the temperature. D can also be expressed as shown in equation 1.3:

$$D = D_0 \mathrm{e}^{\frac{-(\Delta H - T\Delta S)}{k_\mathrm{b} T}} \qquad \text{Equation 1.3}$$

Where ΔH is the enthalpy of motion, ΔS is the entropy of motion, and D_0 is a constant that accounts for the probability of hopping and the frequency of attempts. D_0 is given by the expression below:

$$D_0 = \frac{zg(1 - n_c)l^2 f}{6} \qquad \text{Equation 1.4}$$

The ions have a probability to hop to a neighbouring site that depends on the number of these sites z, the probability that the target site is already occupied n_c, the distance between sites l, and the geometrical environment represented by g. The frequency of attempts is given by the vibration mode frequency of the ion in its site f.

Substituting equations 1.2 and 1.3 into equation 1.1 leads to equation 1.5 which shows an Arrhenius relationship between conductivity and temperature where $E_a = \Delta H$ is the activation energy and σ_0 contains D_0, ΔS, c and other constants.[80]

$$\sigma = \frac{\sigma_0}{T} \mathrm{e}^{-\frac{E_a}{k_\mathrm{b} T}} \qquad \text{Equation 1.5}$$

Although the Arrhenius relationship is valid for the vast majority of solid oxide ion conductors, some such as doped $La_2Mo_2O_9$,[81, 82] have shown different behaviour called the Vogel-Tamman-Fulcher (VTF) Law given by equation 1.6.[80]

$$\sigma = \frac{\sigma_0}{\sqrt{T}} \mathrm{e}^{\frac{-B}{k_\mathrm{b}(T - T_0)}} \qquad \text{Equation 1.6}$$

Where B is the VTF activation energy and T_0 is a transition temperature. Below T_0, Arrhenius behaviour is again observed. This behaviour is most often observed in glass forming ionic liquids[83] or salt polymer complexes[84] above the glass transition temperature, but has also been observed in solid Li^+ conductors.[85] The reason for this behaviour is the temperature dependence of the volume around a mobile ion. Above T_0, this volume fluctuates around a mean value with no enthalpy cost, and this mean value continues to rise with temperature.[86] The probability that the instantaneous volume is greater than that required for mobility therefore also increases with temperature and this leads to a new conduction pathways giving rise to VTF behaviour.

1.2.2. Defect Chemistry

Oxide ion conductivity is a process driven by the presence of defects in the crystal lattice of the oxide material. In the study of oxide ion conductors these defects have been found to be either be O^{2-} vacancies or interstitial O^{2-} atoms and these will remain the focus of this discussion; however, in other materials singly charged oxygen vacancies have been shown to form,[87-89] potentially indicating that in some systems oxygen transport through O^- could be possible. The O^{2-} vacancy and interstitial atom defects give rise to three different widely applicable mechanisms for conductivity; vacancy, interstitial and interstitialcy; although recent work has revealed more complex mechanisms that will be the focus of chapters 5 and 6 of this thesis.

The vacancy mechanism occurs *via* the movement of oxide ions from their lattice position into a neighbouring vacancy site. This leaves a new vacancy behind into which another O^{2-} can move. Provided the number of vacancies is small relative to the number of filled sites this diffusion can be modelled as if the vacancy is the charge carrier moving in the opposite direction. The interstitial mechanism involves the movement of an O^{2-} ion from an interstitial site to an adjacent interstitial site in the lattice. The final method, the interstitialcy mechanism, occurs when an oxide ion migrates to a vacant interstitial site, this then allows an interstitial ion to migrate to the displaced ions position.[90]

All three mechanisms rely on the presence of defects in the oxide ion conductor’s lattice and up to a point the larger the amount of defects in the material the higher the conductivity. Some materials have intrinsic defects such as the intrinsic vacancies in high temperature β-$La_2Mo_2O_9$[91] and δ-Bi_2O_3[60] but for most materials extrinsic defects must be introduced. Because of this many oxide ion conductors are synthesised by doping a parent material in order to produce these extrinsic defects. In general the parent material consists of O^{2-} anions and fixed oxidation state metal cations. Doping the cation site *via* aliovalent substitution leads to the necessity to maintain charge balance in the lattice which, for an oxide ion conductor, must be done *via* a change in the amount of O^{2-} in the structure. In the case where the dopant has a lower oxidation state than the parent cation this balance can be maintained *via* the formation of O^{2-} vacancies whereas if the dopant has a higher oxidation state then interstitial O^{2-} are required.

While initially a higher number of defects leads to higher conductivity, eventually the conductivity will reach a peak and then decrease again. This is due to defect clustering. Defect clustering can occur because it is energetically favourable for a dopant cation and a charge balancing defect to be located close to one another, ensuring local charge balance as well as charge balance of the overall lattice. As the dopant level increases then it becomes favourable for a group of dopant cations and defects to exist in a cluster rather than be statistically distributed throughout the crystal.[92, 93] In some systems, such as YSZ, it is found to be cation size rather than charge that dominates the formation of defect clustering.[94] This clustering leads to two problems. Firstly, a defect cannot move if all the sites surrounding it are occupied by other defects (high n_c in equation 1.4). Secondly, it increases the activation energy, E_a, of the diffusion as moving a defect away from the cluster becomes more energetically unfavourable. This causes the conductivity to decrease with increasing doping level after a maximum has been reached.

1.3. Computational Insight into Oxide Ion Conductors

Computational simulations offer a way to probe the mechanisms of oxide ion conductors, which may otherwise be unknown, in great detail. In the following sections several common methods of investigating oxide ion conduction are discussed. A detailed discussion of how simulations have provided knowledge of conduction mechanisms in $La_2Mo_2O_9$, δ-Bi_2O_3 based materials and apatites will be given in the background sections of chapters 4, 5 and 6 respectively. Due to this, discussion of the techniques in the sections below is focused on examples of their application to other oxide ion conducting materials.

All the methods discussed in this section can be carried out using either classical or *ab initio* calculations. Classical calculations involve modelling each atom as a charged particle bonded to other atoms through spring-like oscillators described by empirically derived force fields. *Ab initio* calculations involve using quantum mechanics to calculate the forces and have the advantage of higher precision calculations while requiring more computational power.[95] In all examples described here the *ab initio* calculations employ density functional theory (DFT), a system of approximations that simplifies solving a many-body wavefunction into a system wholly described by the electron density.[96] More detailed explanations of these methods are given in Chapter 2, section 2.6.

1.3.1. Static Lattice Calculations and Geometry Optimisation

The simplest of calculations that can be performed on a system is the determination of its ground state energy. Before these calculations a geometry optimisation is carried out to make sure that the forces on the atoms in the simulation box are at a minimum, giving the most stable geometry for that system. By comparing the energy values for several similar systems it is possible to get an estimate of their relative stabilities. This has been used in the study of ZrO_2 by Khan *et al.*[97] who showed that Ca^{2+}, Mn^{2+}, Y^{3+}, Gd^{3+} and Sc^{3+} are all favourable dopants into zirconia, stabilising the cubic phase and creating oxygen vacancies. They also found that co-doping with Y^{3+} increases the solubility of Nb^{5+} into ZrO_2, with potential to create a mixed ionic and electronic conductor for anode applications. In the study of doped CeO_2,[98] it has been shown that co-doping with pairs of Y^{3+}, Gd^{3+}, and Sm^{3+} restricts the growth of defect clusters and suppresses the ordering of oxide vacancies, potentially leading to improved conductivity in these co-doped phases. Additionally, Li *et al.*[92] found that the oxide vacancies in singly-doped CeO_2 favour nearest neighbour sites in the case of smaller cations (< 1.12 Å) and next nearest neighbours in the case of larger cations (> 1.12 Å), with the site preference minimised with Nd^{3+}. Therefore, doping with Nd^{3+} should suppress vacancy ordering and so should be most desirable for oxide ion conductivity purposes. Static lattice and geometry optimisation calculations have also been used to find the most stable oxide interstitial and vacancy sites from amongst several potential candidates in several materials including apatites (Chapter 6, section 6.2),[99, 100] $La_{2-x}Sr_xCoO_{4\pm\delta}$[101] and $La_{1.54}Sr_{0.46}Ga_3O_{7.27}$.[102]

1.3.2. Molecular Dynamics

To get a thorough picture of the mechanisms of oxide diffusion that occur in an oxide ion conductor, molecular dynamics (MD) can be used. In this method the positions and velocities of the atoms in the simulation box are calculated based on the forces acting on them and updated after a certain time step. Repeating this process over many steps allows the evolution of the system to be simulated. This allows a trajectory of all the atomic coordinates over the course of a simulation to be produced enabling the locations visited by atoms of interest over the course of the simulation to be visualised. Additionally, using these trajectories, calculations of mean square displacements, diffusion coefficients and activation energies can all be performed. MD simulations have the advantages of acting on all atoms in the system at once and having possible diffusion pathways appear as a result of the simulation rather having to be input by the investigator as is the case for the kinetic Monte Carlo method (section 1.3.4). This comes with the disadvantage of higher computing power being required.

Classical molecular dynamics simulations have been carried out on oxide ion conductors for a long time with studies on YSZ, occurring as early 1992, showing a mechanism involving diffusion of oxide ions in the <100> direction between tetrahedral sites *via* an octahedral one.[103] Subsequent simulations on the same material[104-106] have shown that neighbouring Y atoms can trap vacancies within clusters explaining the experimentally observed maximum in the conductivity versus Y dopant proportion. In classical molecular dynamics modelling bond breaking is difficult as the bonds are explicitly defined as spring-like oscillators in the starting structure. This means that when performing classical MD, insight into mechanisms of conduction is usually gained by plotting displacement clouds showing the locations visited by oxygen atoms as they move within their sites over the course of the simulation. The likely conduction mechanisms can then be inferred by the overlap of these clouds.[100-102, 107, 108] For example, in the case of $La_{2-x}Sr_xCoO_{4\pm\delta}$, MD simulations performed by Tealdi *et al.*[101] showed no overlap of oxygen displacement clouds for $LaSrCoO_4$, indicating no oxide ion conduction occurs for this composition as would be expected from the lack of oxide vacancies present. However, for the composition $La_{0.8}Sr_{1.2}CoO_{3.9}$, overlap of displacements clouds indicates that a conduction pathway along the edges of CoO_6 octahedra occurs in the *ab* plane. For $La_{1.54}Sr_{0.46}Ga_3O_{7.27}$,[102] a material formed of layers of GaO_4 tetrahedra between layers of La^{3+}/Sr^{2+} cations, no overlap between oxide ion displacement clouds was observed for layers containing no oxide interstitial atoms. For layers that did contain the interstitial atoms overlap was observed between the displacement clouds for the interstitial oxygens and other oxygens, indicating that interstitial oxygen atoms within a layer are required for conduction to occur.

While classical MD can give insight into potential conduction mechanisms, actual diffusion events (i.e. an oxygen atom moving between sites) cannot be observed due to the difficulty modelling bond breaking and formation. This makes quantification of a mechanisms contribution to the overall conductivity difficult. For *ab initio* molecular dynamics (AIMD) where bonds are not explicitly defined, the diffusion events can be observed with oxygen trajectories giving a clear picture of each individual oxygen atom’s pathway over the course of the simulation. This allows for detailed observations of the diffusion mechanisms as has been shown in many materials including $Sr_2Fe_2O_5$, for which at 600 °C and above oxide diffusion along chains of FeO_4 was observed with movement between these tetrahedra and layers of octahedral FeO_6 groups also seen at 1175 °C;[109] Nd_2NiO_4, for which an oxide ion diffusion mechanism that involved oxide ion jumps between the interstitial sites and the axial oxygen sites of the NiO_6 tetrahedra was observed;[110] as well as $La_2Mo_9O_9$,[111]several doped δ-Bi_2O_3 materials,[68, 69, 71, 72] and apatites[112] discussed in the background sections of Chapters 4, 5 and 6 respectively.

However, the problem of computing power is intensified by the use of *ab initio* over classical MD. Although offering the advantage of precision over classical methods the calculation times for *ab initio* methods are much longer meaning that while classical MD simulations have been performed on systems with millions of atoms for milliseconds of simulation time[113], AIMD requires much smaller cell sizes and much fewer time steps can be performed. As a direct comparison for oxide ion conductor MD simulations, a 2012 study reporting classical MD on YSZ performed the simulations on a 6 × 6 × 6 supercell for 1 ns;[114] whereas 2013 and 2015 AIMD studies were performed only on 3 × 3 × 2 supercell for 7 and 10 ps respectively.[115, 116] These restrictions on cell sizes and simulations must be taken into account when judging how representative the simulations are.

1.3.3. Nudged Elastic Band Method

While MD gives a more representative insight into conduction mechanisms, acting on an entire simulation box containing many atoms, the computational power required is high and calculation times are long. Because of this much research is done using alternative methods of investigating conduction mechanisms that take less time.

One of these methods is known as the nudged elastic band method (NEB).[117] This method requires two structures, one representing the simulation cell before an oxygen jump and one after the jump has occurred. The oxygen atom is then moved by a certain distance between the points and the position optimised to find the lowest energy, this can be done using classical or *ab initio* methods. From the new position the process is repeated keeping the step distance constant. This continues until the end position is reached. This allows a minimum energy path to be determined, and by looking at the energy difference between the initial position and the maximum energy on the path an activation energy can be calculated.

One example of the successful use of the NEB method in literature is in the study of doped CeO_2.[118-120] Nakayama *et al.* showed that vacancy hopping between nearest neighbour oxygen sites in the <100> direction had an activation barrier of ≈ 0.5 eV showing excellent agreement with experimental values.[118] It was also shown that vacancy hopping in the <110> and <111> directions had energy barriers 5 and 6 times higher respectively, effectively ruling these pathways out from the overall conduction mechanism. Another example of the use of this technique is that of $La_4(Ti_2O_8)O_2$, studied by Kendrick *et al.*,[121] in which an energy barrier of 1.51 eV was determined for a mechanism involving the TiO_5 chains in the material. These chains are linked by bridging oxygens which become vacant when doping the Ti sites with trivalent cations such as Ga^{3+}. The mechanism involves cooperative motion of a bridging oxygen to a terminal oxygen site while the oxygen atom previously occupying that site moves to a vacant bridging site further along the chain. The calculated energy barrier matches well with the ≈ 1.6 eV activation energy determined experimentally for $La_4(Ti_{2-x}Ga_xO_{8-0.5x})O_2$. NEB calculations were also performed for a theoretical mechanism involving interstitial oxygen atoms (as part of TiO_6 groups) and showed an even lower activation energy of 0.49 eV showing potential for increasing oxide ion mobility *via* suitable doping with higher valance cations. In the study of apatite oxide ion conductors[122-124] the NEB method has provided insight into which of multiple possible conduction pathways is most favourable (see Chapter 6, section 6.2.2). The activation energies calculated using this method can also be used in further simulations such as kinetic Monte Carlo (see section 1.3.4) as used by Imaizumi *et al.* in their work on apatite oxide ion conductors[123, 124] and Kushima *et al.* in their investigations into YSZ.[125]

While this method has been shown to be useful and has the advantage of shorter calculation times than MD, it also has some disadvantages. The primary disadvantage is the fact that an endpoint is required before the calculation begins, whereas in MD the endpoint is reached purely as a result of the calculation. This means that the outcome will be biased by the experimenter's initial prediction of the pathway which may cause the actual minimum energy pathway to be missed if it is not obvious. The second disadvantage is that the nudged elastic band method only moves one atom with the rest of the structure being static, this means that activation energies may be inaccurate if, for example, the cation framework is flexible or a mechanism involves cooperative motion of more than a single oxygen atom. With MD all atoms can move which may allow these mechanisms to be seen.

1.3.4. Kinetic Monte Carlo

The kinetic Monte Carlo (KMC) method[126] is a way of evaluating the time evolution of a system without the need to simulate all atomic motions. KMC can be primarily thought of as a way to model transitions between states, in the case of oxide ion diffusion these transitions will be oxide ion jumps. Each transition or set of transitions will have certain rate (*r*) based on an Arrhenius relationship with its activation energy and the simulation temperature, normalised so the sum of the rates of all transitions is 1. The new state is chosen by selecting a random number (*k*) between 0 and 1 and choosing the final state whose transition rate sum is closest to *k* without exceeding it. Note that this means that multiple transitions, i.e. oxide jumps, can occur in one KMC step. In this way transitions with a faster rate are more likely to be chosen. The process then repeats for another time step using the new state.

The advantage of this method is that the calculations are much less computationally intensive allowing similar properties as MD, such as mean square displacements and diffusion coefficients evolution with temperature, to be calculated over much longer simulation times using larger cells. For example, Pornprasertsuk *et al.* simulated 5 × 5 × 5 supercells of yttria-stabilised zirconia until a total of 2 million jumps had occurred in order to show that the KMC technique can accurately predict the Y^{3+} doping levels at which conductivity is maxed.[127] Due to the lower computational time it was also possible to do a larger number of simulations, with simulations in this study performed at 7 temperatures for 10 different Y^{3+} doping levels with 12 different starting configurations for each. It was found that the diffusion coefficient reached a maximum at 7-8 % Y^{3+} doping matching well with literature values and demonstrating that this technique could be useful for predicting optimum doping levels for new materials. Kushima *et al.* also used KMC in their study into the effects of strain on oxide ion conductivity in YSZ.[125] Simulations were carried out on 15 × 15 × 15 supercells of 8 % YSZ with 10 different starting configurations for 5 strain values at 4 temperatures each. The maximum in diffusion coefficient was found to be at 4 % strain for every temperature with an increase by 3 orders of magnitude observed at 400 K, leading the authors to suggest that direct control of strain may be desirable to increase the conductivity of YSZ for use in applications. KMC has also been used by Imaizumi *et al.* to quantify the occurrence of a number of mechanisms at different temperatures for both lanthanum germanate[124] and lanthanum silicate[123] apatites (see Chapter 6, section 6.2.2).

The main disadvantage of this method is that a database of possible transitions with their activation energies must be produced. In the studies by Imaizumi *et al.*[123, 124] and Kushima *et al.*[125] this database was produced using the NEB method described above. Pornprasertsuk *et al.* chose likely locations of saddle points then optimised the structure while constraining the oxide ion to be equidistant between the two sites;[127] however, this method is likely to be much less precise than NEB. Production of this database is subject to the same biases as described for the NEB method as making sure that all possible transitions are accounted for would be difficult in a complex system and missing some could give misleading results.

1.4. Neutron Scattering Insight into Oxide Ion Conductors

Neutron scattering refers to a range of techniques in which the structure and dynamics of a material are probed using their interaction with a neutron beam. A discussion of the theory and techniques behind neutron scattering experiments can be found in Chapter 2, section 2.3. In the study of oxide ion conduction mechanisms, the most useful technique and the one that is the focus of this section is quasielastic neutron scattering (QENS) that allows direct observation of the diffusion dynamics.

However, other techniques also can be useful for some aspects of the study of oxide ion conductors. Inelastic neutron scattering can allow the calculation of the phonon DOS as described in Chapter 2, section 2.3.4.1, the utility of which has been demonstrated in the study of $Nd_2NiO_{4+\delta}$ (δ = 0, 0.1, 0.25), which shows stoichiometry dependent oxide ion mobility at ambient temperature. This was investigated using a time of flight neutron scattering experiment with picosecond resolution,[110] measuring a phonon density of states that was compared with phonon modes identified using *ab initio* calculations. As δ increased the resulting DOS showed a decrease in intensity of modes involving displacement along the [100] direction and an increase in intensity of modes with displacements along [110]. This was attributed to oxygen interstitials distorting neighbouring NiO_6 octahedra and causing them to tilt in the [110] direction rather than [100], thereby increasing and decreasing the intensity of the corresponding tilting modes. Using AIMD an oxide ion diffusion mechanism was identified in which an oxide ion jumps between the interstitial sites and the axial oxygen sites of the NiO_6 tetrahedra. This movement occurs in the [110] direction and so would be enhanced by the increase in intensity of [110] tilt modes. In this way the neutron scattering data provides direct evidence to corroborate the mechanism identified using AIMD.

1.4.1. Quasielastic Neutron Scattering in Ionic Conductors

Quasielastic neutron scattering (QENS) is a very useful technique in the study of diffusion in solids.[128] A detailed explanation of the technique is given in Chapter 2, section 2.3.1.2. QENS enables the determination of the overall diffusion coefficient and activation energy of motion as well as residence times and geometry of individual atomic jump processes. The use of this technique to investigate diffusion in solids in general is extensive with studies carried out on the diffusion of hydrogen in metals,[129] in intercalation compounds,[130] and in solid state proton,[131-136] lithium,[137, 138] sodium,[139, 140] and copper ionic conductors.[141, 142]

Despite the ability of QENS to directly observe microscopic oxygen diffusion dynamics, investigations into oxide ion conduction using this technique has so far only been reported in a few studies.[68, 109, 143, 144] This is due to difficulties in performing QENS on oxide ion conductors, namely that the dynamics are very slow requiring very high resolution instruments to be used to measure them. For $Bi_{26}Mo_{10}O_{69}$[68] dynamics were measured on a picosecond timescale with a QENS signal observed that had an intensity with a strongly localised dependence on the momentum transfer between the neutron and the sample (Q). This dependence resembled that found for rotation of C_{60}[145] and Zn tetrahedra in Zn_6Sc,[146] and so this signal was attributed to localised motions of oxide ions within MoO_x polyhedra rather than long range diffusional motion. A neutron scattering study on $Sr_2Fe_2O_5$,[109] where dynamics also were measured on a picosecond timescale, reported a QENS signal at 750 °C. As the QENS linewidth was observed to be almost Q independent the signal was also ascribed to localised motions. The picosecond timescales matched well with a process observed using AIMD simulations at 600 °C and above between layers of octahedral FeO_6 groups and layers of FeO_4 tetrahedra. These motions contribute to the overall diffusion mechanism but are distinct from those within the tetrahedra layers that are believed to be the cause of long range conduction and occur on longer timescales. Long range dynamics in oxide ion conductors have only been seen in very recent studies on δ-Bi_2O_3 requiring instruments with resolutions that allow probing of timescales as slow as tens[143] and hundreds of picoseconds.[144] Both of these studies successfully allowed the variation of the QENS signal linewidth with Q to be modelled to produce values of oxide ion jump distances. The methods of modelling QENS data, and their utilisation in these two studies, are discussed below.

1.4.2. Modelling Ionic Diffusion

Quasielastic neutron scattering allows both information about dynamic timescales and geometry to be directly observed. In order to derive this information a fit of the QENS data must be carried out. The relationship of interest is that between the Lorentzian linewidth of the QENS peak, $\mathit{\Gamma}$, which represents the timescale of dynamics and the momentum transfer Q. The simplest model is that of random Brownian motion given in equation 1.7:

$$\mathit{\Gamma} = DQ^2 \qquad \text{Equation 1.7}$$

Where D is the diffusion coefficient. However, this model relies on the assumption that diffusion is unrestricted and continuous and so is not suitable for solid state ionic conductors in which local mechanisms are important.[131] A far more commonly used model is the Chudley-Elliott (C-E) model[147] which takes into account the jump length *l*.

$$\Gamma = \frac{6D}{L^2}\left(1 - \frac{\sin(Ql)}{(Ql)}\right) = \frac{1}{\tau}\left(1 - \frac{\sin(Ql)}{(Ql)}\right) \qquad \text{Equation 1.8}$$

Where τ is the residence time. This model has been successfully applied to a wide range of solid state ionic conductors in the past. These include studies into proton conductors,[134-136] Li conductors,[138] Na conductors[140] and Cu conductors.[141, 142] Fitting with this model can reveal information about jump distances and site residence times of the diffusing atoms, this can be combined with knowledge of the structure to identify likely conduction mechanisms. The values found from fits such as these can then be used to corroborate mechanisms found in AIMD by comparing jump distances found in each. For example, in the case of proton diffusion in spark plasma sintered $BaCe_{0.8}Y_{0.2}O_{3-\delta}$, [136] QENS data was collected on picosecond timescales for a temperature range of 350 to 600 °C. Fitting these data with the Chudley-Elliott model resulted in a jump length of 5 Å. This was found to coincide with a pathway identified using AIMD in which protons jump between CeO_6 octahedra, a distance of 5.0-5.2 Å.

In the case of oxide ion conductors the Chudley-Elliott model has only been applied to QENS measurements on a single material, δ-Bi_2O_3, thus far.[143, 144] The first study on δ-Bi_2O_3 was carried out by Mamontov probing timescales of 100s of picoseconds.[144] Fitting their QENS data, where $0.5 < Q < 1.7$ Å^{-1}, with the C-E model gave jump distances of 2.64-2.84 Å for various temperatures showing excellent agreement with the 2.83 Å distance between nearest neighbour oxide ion sites in the <100> direction in δ-Bi_2O_3, therefore matching the believed conductivity pathway.[13, 148] They did however, discount their collected data with *Q* values above 1.7 Å^{-1}, the inclusion of which gave a higher value of 3.19-3.24 Å for the jump distances, claimed to be due to the appearance of Bragg peaks above 1.9 Å^{-1} negatively affecting the data.

A second QENS study of δ-Bi_2O_3 was reported by Wind *et al.* and probed timescales of 10s of picoseconds.[143] However, the authors pointed out that strictly speaking the Chudley-Elliott model is valid for incoherent scattering nuclei only and, as oxygen is an almost purely coherent scatterer, this model may not be applicable for oxygen diffusion studies. Because of this a coherent scattering Chudley-Elliott model for use in oxygen diffusion studies was created which takes into account the structure factor *S*(*Q*):

$$\Gamma = \frac{1}{\tau S(Q)}\left(1 - \frac{\sin(Ql)}{(Ql)}\right) \qquad \text{Equation 1.9}$$

This model gave a much better fit to their data than the standard C-E model, with a value of 3.33 Å found for the jump distance. However, this value is larger than the 2.83 Å distance between nearest neighbour oxygen sites in δ-Bi_2O_3. To explain this Wind *et al.* proposed that jumps could occur between several other oxygen sites separated by longer distances. The 3.33 Å distance found represents the weighted average over all these possible jumps. While this gives a better fit to the data using their modified C-E model, no direct evidence of these longer distance jumps was provided and disagrees with the mechanism established in literature for δ-Bi_2O_3.[13, 148]

While this modified coherent model gave a good fit of the δ-Bi_2O_3 QENS data collected by Wind *et al.*, there are several problems with applying it to further materials. Firstly, and most importantly, the model requires knowledge of the absolute value of $S(Q)$ in the Q range of the experiment. Wind *et al.* assumed that $S(Q)$ reached 1 at the highest Q value of their measurements, as in liquids $S(Q)$ is known to reach a value of 1 at high Q, and while this assumption appeared to work in their case the general validity is not clear. Secondly, δ-Bi_2O_3 has no Bragg peaks up to a relatively large Q range (Q = 1.9 Å). For other materials the presence of Bragg peaks over the Q range of the measurements may make determination of $S(Q)$ even more difficult. Additionally, Mamontov[144] managed to get jump distance values closer to those expected based on the established mechanism using only the standard C-E model. This may mean that taking into account the coherent scattering nature of O is not necessary, possibly due to the effects being small enough to not be noticeable.

1.5. Scope of the Project

The work reported in this thesis investigates the relationships between the structural features of oxide ion conductors and the resulting oxide ion conduction mechanisms. This is achieved using a combination of attempted syntheses of new materials with novel structural features, direct observation of oxide ion dynamics *via* neutron scattering and simulation of oxide diffusion pathways using *ab initio* molecular dynamics.

A good silicate oxide ion conductor is desirable due to the low cost, sustainable and environmentally friendly nature of silicates. Attempted synthesis and property investigation of oxide ion conductor candidates La-doped $SrSiO_3$ and $SrGeO_3$ and Y- and Ce-doped $BaZrSi_3O_9$ that have novel structural features based on T_3O_9 clusters (T = Si/Ge) will be detailed. Solid state NMR work undertaken to identify the charge carriers in nominally Na-doped $SrSiO_3$ will also be reported.

As described in section 1.4, the investigation of oxide ion conductors using neutron scattering techniques has only been reported in a small number of studies. The range of oxide ion conducting materials investigated by neutron scattering techniques is extended by work in this thesis to include $La_2Mo_2O_9$, $Bi_{0.913}V_{0.087}O_{1.587}$ and Bi-doped $La_{10}Ge_6O_{27}$. For each of these materials neutron scattering measurements are carried out on the picosecond timescale to attempt to see localised motions as reported for $Bi_{26}Mo_{10}O_{69}$[68] and $Sr_2Fe_2O_5$.[109] Additional measurements carried out on the nanosecond timescale will be reported, the longest timescales reported in the study of oxide ion dynamics so far.

$La_2Mo_2O_9$ and $Bi_{0.913}V_{0.087}O_{1.587}$ contain cations able to support variable coordination number in the form of Mo^{6+} and V^{5+} respectively. This fact is believed to be a key factor in the high conductivities reported in these materials.[73, 149] To investigate this a*b initio* molecular dynamics simulations were carried out at a range of temperatures for both materials for much longer simulation times than those previously reported.[73, 111] The conduction mechanisms identified revealed in these simulations are reported and analysed quantitatively to elucidate the effects that the variable coordination cations have on the oxygen ion dynamics.

Bi-doping in $La_{10}Ge_6O_{27}$ has been shown to increase the oxide ion conductivity.[76] However, the apatite structure of this material is complex with several oxide ion conduction mechanisms reported in the literature (see Chapter 6, section 6.2) making the effects of the Bi^{3+} lone pairs on the conduction mechanisms unclear. Electron localisation function calculations were carried out to identify the locations of these lone pairs in the material and compared with an extensive *ab initio* molecular dynamics investigation to determine the effects of Bi^{3+} on the individual mechanisms and therefore overall conductivity.

1.6. References

1. S. J. Skinner and J. A. Kilner, *Materials Today*, 2003, **6**, 30-37.
2. D. Yuan and F. A. Kröger, *Journal of The Electrochemical Society*, 1969, **116**, 594-600.
3. J. Sunarso, S. Baumann, J. M. Serra, W. A. Meulenberg, S. Liu, Y. S. Lin and J. C. Diniz da Costa, *Journal of Membrane Science*, 2008, **320**, 13-41.
4. P. Dyer, *Solid State Ionics*, 2000, **134**, 21-33.
5. E. D. Wachsman and K. L. Duncan, *Ceria/bismuth oxide bilayered electrolytes for low temperature solid oxide fuel cells*, Electrochemical Society Inc, Pennington, 1999.

6. D. J. Brett, A. Atkinson, N. P. Brandon and S. J. Skinner, *Chem Soc Rev*, 2008, **37**, 1568-1578.
7. A. B. Stambouli and E. Traversa, *Renewable and Sustainable Energy Reviews*, 2002, **6**, 433-455.
8. T. S. Lee, J. N. Chung and Y.-C. Chen, *Energy Conversion and Management*, 2011, **52**, 3214-3226.
9. R. M. Ormerod, *Chem Soc Rev*, 2003, **32**, 17-28.
10. S. Sengodan, S. Choi, A. Jun, T. H. Shin, Y. W. Ju, H. Y. Jeong, J. Shin, J. T. Irvine and G. Kim, *Nature Materials*, 2015, **14**, 205-209.
11. D. Papurello, A. Lanzini, L. Tognana, S. Silvestri and M. Santarelli, *Energy*, 2015, **85**, 145-158.
12. D. Papurello, R. Borchiellini, P. Bareschino, V. Chiodo, S. Freni, A. Lanzini, F. Pepe, G. A. Ortigoza and M. Santarelli, *Applied Energy*, 2014, **125**, 254-263.
13. J. B. Goodenough, *Annual Review of Materials Research*, 2003, **33**, 91-128.
14. J. B. Goodenough, A. Manthiram, M. Paranthaman and Y. S. Zhen, *Materials Science and Engineering: B*, 1992, **12**, 357-364.
15. N.Q. Minh and T. Takahashi, *Science and Technology of Ceramic Fuel Cells*, Elsevier, Amsterdam, 1995.
16. R. Hancke, S. Fearn, J. A. Kilner and R. Haugsrud, *Phys Chem Chem Phys*, 2012, **14**, 13971-13978.
17. Subhash C. Singhal and K. Kendall, *High Temperature Solid Oxide Fuel Cells: Fundamentals, Design, and Applications*, Elsevier, Oxford, 2003.
18. W. Z. Zhu and S. C. Deevi, *Materials Science and Engineering: A*, 2003, **362**, 228-239.
19. A. Atkinson, S. Barnett, R. J. Gorte, J. T. Irvine, A. J. McEvoy, M. Mogensen, S. C. Singhal and J. Vohs, *Nature Materials*, 2004, **3**, 17-27.
20. J. B. Goodenough and Y.-H. Huang, *Journal of Power Sources*, 2007, **173**, 1-10.
21. M. Gong, X. Liu, J. Trembly and C. Johnson, *Journal of Power Sources*, 2007, **168**, 289-298.
22. G. Buvat, E. Quarez and O. Joubert, *Journal of Power Sources*, 2016, **302**, 107-113.
23. G. Buvat, H. Sellemi, U. K. Ravella, M. Barre, S. Coste, G. Corbel and P. Lacorre, *Inorganic chemistry*, 2016, **55**, 2522-2533.
24. C. Xia and M. Liu, *Advanced Materials*, 2002, **14**, 521-523.
25. N. Mahato, A. Banerjee, A. Gupta, S. Omar and K. Balani, *Progress in Materials Science*, 2015, **72**, 141-337.
26. S. Yoo, A. Jun, Y. W. Ju, D. Odkhuu, J. Hyodo, H. Y. Jeong, N. Park, J. Shin, T. Ishihara and G. Kim, *Angew Chem Int Ed Engl*, 2014, **53**, 13064-13067.
27. M. A. Laguna-Bercero, A. R. Hanifi, H. Monzón, J. Cunningham, T. H. Etsell and P. Sarkar, *Journal of Materials Chemistry A*, 2014, **2**, 9764-9770.
28. B. C. Steele and A. Heinzel, *Nature*, 2001, **414**, 345-352.
29. R. Leah, N. P. Brandon, A. Duckett, K. E. Koury and M. Schmidt, US Pat., US20130260269 A1, 2013.
30. L. Redox Power Systems, Redox Power Systems, LLC, http://www.redoxpowersystems.com/, (accessed 6th October 2017).
31. H. S. Yoon, B. M. Blackburn and E. Wachsman, presented in part at the 2014 ECS and SMEQ Joint International Meeting, Cancun, Mexico, October, 2014.
32. T. Armstrong, E. E. Batawi, M. Janousek and M. Pillai, US Pat., US9413024 B2, 2013.
33. D. K. Smith and W. Newkirk, *Acta Crystallographica*, 1965, **18**, 983-991.
34. H. A. Abbas, F. F. Hamad, A. K. Mohamad, Z. M. Hanafi and M. Kilo, *Diffusion Fundamentals*, 2007, **8**, 7.1-7.8.
35. X. Zhao and D. Vanderbilt, *Physical Review B*, 2002, **65**, 075105.
36. J. W. Fergus, *Journal of Power Sources*, 2006, **162**, 30-40.
37. K. Nomura, *Solid State Ionics*, 2000, **132**, 235-239.

38. O. Yamamoto, *Solid State Ionics*, 1995, **79**, 137-142.
39. S. Badwal, *Solid State Ionics*, 2000, **136-137**, 91-99.
40. M. Yashima, S. Kobayashi and T. Yasui, *Solid State Ionics*, 2006, **177**, 211-215.
41. R. Fuentes and R. Baker, *International Journal of Hydrogen Energy*, 2008, **33**, 3480-3484.
42. D. J. Seo, K. O. Ryu, S. B. Park, K. Y. Kim and R.-H. Song, *Materials Research Bulletin*, 2006, **41**, 359-366.
43. Y. Ma, X. Wang, S. Li, M. S. Toprak, B. Zhu and M. Muhammed, *Advanced Materials*, 2010, **22**, 1640-1644.
44. T. Mori and J. Drennan, *Journal of Electroceramics*, 2006, **17**, 749-757.
45. K. Amarsingh Bhabu, J. Theerthagiri, J. Madhavan, T. Balu and T. R. Rajasekaran, *The Journal of Physical Chemistry C*, 2016, **120**, 18452-18461.
46. B. Zhu, I. Albinsson and B. E. Mellander, *Ionics*, 1998, **4**, 261-266.
47. T. Mukai, S. Tsukui, K. Yoshida, S. Yamaguchi, R. Hatayama, M. Adachi, H. Ishibashi, Y. Kakehi, K. Satoh, T. Kusaka and K. C. Goretta, *Journal of Fuel Cell Science and Technology*, 2013, **10**, 0610061-0610066.
48. A. Tsoga, A. Gupta, A. Naoumidis, D. Skarmoutsos and P. Nikolopoulos, *Ionics*, 1998, **4**, 234-240.
49. A. Tsoga, *Solid State Ionics*, 2000, **135**, 403-409.
50. X. Zhang, M. Robertson, C. Decès-Petit, Y. Xie, R. Hui, W. Qu, O. Kesler, R. Maric and D. Ghosh, *Journal of Power Sources*, 2008, **175**, 800-805.
51. A. S. Mehranjani, D. J. Cumming, D. C. Sinclair and R. H. Rothman, *Journal of the European Ceramic Society*, 2017, **37**, 3981-3993.
52. T. Takahashi, T. Esaka and H. Iwahara, *J Appl Electrochem*, 1977, **7**, 303-308.
53. E. Wachsman, *Solid State Ionics*, 2002, **152-153**, 657-662.
54. Y. J. Leng and S. H. Chan, *Electrochemical and Solid-State Letters*, 2006, **9**, A56-A59.
55. E. D. Wachsman, *Journal of The Electrochemical Society*, 1997, **144**, 233-236.
56. J. Y. Park and E. D. Wachsman, *Ionics*, 2006, **12**, 15-20.
57. J.-Y. Park, H. Yoon and E. D. Wachsman, *Journal of the American Ceramic Society*, 2005, **88**, 2402-2408.
58. J. S. Ahn, D. Pergolesi, M. A. Camaratta, H. Yoon, B. W. Lee, K. T. Lee, D. W. Jung, E. Traversa and E. D. Wachsman, *Electrochemistry Communications*, 2009, **11**, 1504-1507.
59. K. T. Lee and E. D. Wachsman, *Science*, 2011, **334**, 935-939.
60. P. D. Battle, C. R. A. Catlow, J. Drennan and A. D. Murray, *Journal of Physics C: Solid State Physics*, 1983, **16**, L561-L566.
61. N. M. Sammes, G. A. Tompsett, H. Näfe and F. Aldinger, *Journal of the European Ceramic Society*, 1999, **19**, 1801-1826.
62. J. C. Boivin and G. Mairesse, *Chemistry of Materials*, 1998, **10**, 2870-2888.
63. S. Chan, *Solid State Ionics*, 2003, **158**, 29-43.
64. E. Wachsman, G. Ball, N. Jiang and D. Stevenson, *Solid State Ionics*, 1992, **52**, 213-218.
65. D. W. Joh, J. H. Park, D. Kim, E. D. Wachsman and K. T. Lee, *ACS Appl Mater Interfaces*, 2017, **9**, 8443-8449.
66. P. Conflant, J.-C. Boivin and D. Thomas, *Journal of Solid State Chemistry*, 1976, **18**, 133-140.
67. T. Takahashi, H. Iwahara and Y. Nagai, *J Appl Electrochem*, 1972, **2**, 97-104.
68. C. D. Ling, W. Miiller, M. R. Johnson, D. Richard, S. Rols, J. Madge and I. R. Evans, *Chemistry of Materials*, 2012, **24**, 4607-4614.
69. J. L. Payne, J. D. Farrell, A. M. Linsell, M. R. Johnson and I. R. Evans, *Solid State Ionics*, 2013, **244**, 35-39.
70. K. Huang, *Solid State Ionics*, 1996, **89**, 17-24.

71. M. L. Tate, J. Hack, X. Kuang, G. J. McIntyre, R. L. Withers, M. R. Johnson and I. R. Evans, *Journal of Solid State Chemistry*, 2015, **225**, 383-390.
72. X. Kuang, J. L. Payne, J. D. Farrell, M. R. Johnson and I. R. Evans, *Chemistry of Materials*, 2012, **24**, 2162-2167.
73. X. Kuang, J. L. Payne, M. R. Johnson and I. R. Evans, *Angew Chem Int Ed Engl*, 2012, **51**, 690-694.
74. P. Lacorre, F. Goutenoire, O. Bohnke, R. Retoux and Y. Laligant, *Nature*, 2000, **404**, 856-858.
75. M. L. Tate, D. A. Blom, M. Avdeev, H. E. A. Brand, G. J. McIntyre, T. Vogt and I. R. Evans, *Advanced Functional Materials*, 2017, **27**, 1605625.
76. M. L. Tate, C. A. Fuller, M. Avdeev, H. E. A. Brand, G. J. McIntyre and I. R. Evans, *Dalton Trans*, 2017, **46**, 12494-12499.
77. P. Singh and J. B. Goodenough, *Energy & Environmental Science*, 2012, **5**, 9626-9631.
78. B. R. Young, *Mineral Mag*, 1978, **42**, 35-40.
79. H. Mehrer, *Diffusion in solids: fundamentals, methods, materials, diffusion-controlled processes*, Springer Science & Business Media, 2007.
80. P. G. Bruce, *Solid state electrochemistry*, Cambridge University Press, 1997.
81. S. Georges, F. Goutenoire, O. Bohnke, M. Steil, S. Skinner, H. Wiemhofer and P. Lacorre, *Journal of New Materials for Electrochemical Systems*, 2004, **7**, 51-58.
82. S. Georges, *Solid State Ionics*, 2003, **161**, 231-241.
83. J. Vila, P. Ginés, J. M. Pico, C. Franjo, E. Jiménez, L. M. Varela and O. Cabeza, *Fluid Phase Equilibria*, 2006, **242**, 141-146.
84. N. Karan, D. Pradhan, R. Thomas, B. Natesan and R. Katiyar, *Solid State Ionics*, 2008, **179**, 689-696.
85. O. Bohnke, *Solid State Ionics*, 1996, **91**, 21-31.
86. M. H. Cohen and D. Turnbull, *The Journal of Chemical Physics*, 1959, **31**, 1164-1169.
87. S. Shi, D. Gao, Q. Xu, Z. Yang and D. Xue, *RSC Advances*, 2014, **4**, 45467-45472.
88. G. Yanqin, J. Jiaping, W. Yuxi and T. Gang, *Physica Scripta*, 2016, **91**, 045801.
89. M. Sterrer, E. Fischbach, T. Risse and H.-J. Freund, *Physical Review Letters*, 2005, **94**, 186101.
90. A. Chroneos, R. V. Vovk and I. L. Goulatis, *Monatshefte für Chemie - Chemical Monthly*, 2011, **143**, 345-353.
91. F. Goutenoire, O. Isnard and R. Retoux, *Chemistry of Materials*, 2000, **12**, 2575-2580.
92. Z. P. Li, T. Mori, J. Zou and J. Drennan, *Phys Chem Chem Phys*, 2012, **14**, 8369-8375.
93. Z.-P. Li, T. Mori, F. Ye, D. R. Ou, J. Zou and J. Drennan, *Physical Review B*, 2011, **84**, 180201.
94. S. T. Norberg, S. Hull, I. Ahmed, S. G. Eriksson, D. Marrocchelli, P. A. Madden, P. Li and J. T. S. Irvine, *Chemistry of Materials*, 2011, **23**, 1356-1364.
95. G. H. Grant and W. G. Richards, *Computational chemistry*, Oxford University Press, 1995.
96. T. D. Kühne, *Wiley Interdisciplinary Reviews: Computational Molecular Science*, 2014, **4**, 391-406.
97. M. S. Khan, M. S. Islam and D. R. Bates, *Journal of Materials Chemistry*, 1998, **8**, 2299-2307.
98. D. R. Ou, F. Ye and T. Mori, *Phys Chem Chem Phys*, 2011, **13**, 9554-9560.
99. A. Jones, P. R. Slater and M. S. Islam, *Chemistry of Materials*, 2008, **20**, 5055-5060.
100. E. Kendrick, M. S. Islam and P. R. Slater, *Chemical Communications*, 2008, DOI: 10.1039/b716814d, 715-717.
101. C. Tealdi, C. Ferrara, P. Mustarelli and M. S. Islam, *Journal of Materials Chemistry*, 2012, **22**, 8969-8975.
102. C. Tealdi, P. Mustarelli and M. S. Islam, *Advanced Functional Materials*, 2010, **20**, 3874-3880.

103. F. Shimojo and H. Okazaki, *Journal of the Physical Society of Japan*, 1992, **61**, 4106-4118.

104. Y. Yamamura, S. Kawasaki and H. Sakai, *Solid State Ionics*, 1999, **126**, 181-189.

105. X. Li and B. Hafskjold, *Journal of Physics: Condensed Matter*, 1995, **7**, 1255-1271.

106. R. Devanathan, W. Weber, S. Singhal and J. Gale, *Solid State Ionics*, 2006, **177**, 1251-1258.

107. E. Kendrick, J. Kendrick, K. S. Knight, M. S. Islam and P. R. Slater, *Nature Materials*, 2007, **6**, 871-875.

108. P. M. Panchmatia, A. Orera, G. J. Rees, M. E. Smith, J. V. Hanna, P. R. Slater and M. S. Islam, *Angew Chem Int Ed Engl*, 2011, **50**, 9328-9333.

109. J. E. Auckett, A. J. Studer, E. Pellegrini, J. Ollivier, M. R. Johnson, H. Schober, W. Miiller and C. D. Ling, *Chemistry of Materials*, 2013, **25**, 3080-3087.

110. A. Perrichon, A. Piovano, M. Boehm, M. Zbiri, M. Johnson, H. Schober, M. Ceretti and W. Paulus, *The Journal of Physical Chemistry C*, 2015, **119**, 1557-1564.

111. C. J. Hou, Y. D. Li, P. J. Wang, C. S. Liu, X. P. Wang, Q. F. Fang and D. Y. Sun, *Physical Review B*, 2007, **76**, 014104.

112. K. Imaizumi, K. Toyoura, A. Nakamura and K. Matsunaga, *Solid State Ionics*, 2014, **262**, 512-516.

113. M. Vendruscolo and C. M. Dobson, *Curr Biol*, 2011, **21**, R68-70.

114. G. Dezanneau, J. Hermet and B. Dupé, *International Journal of Hydrogen Energy*, 2012, **37**, 8081-8086.

115. F. Li, R. Lu, H. Wu, E. Kan, C. Xiao, K. Deng and D. E. Ellis, *Phys Chem Chem Phys*, 2013, **15**, 2692-2697.

116. M. Oka, H. Kamisaka, T. Fukumura and T. Hasegawa, *Phys Chem Chem Phys*, 2015, **17**, 29057-29063.

117. H. Jonsson, G. Mills and K. W. Jacobsen, in *Classical and Quantum Dynamics in Condensed Phase Simulations*, World Scientific, 1998, DOI: doi:10.1142/9789812839664_0016

10.1142/9789812839664_0016, pp. 385-404.

118. M. Nakayama and M. Martin, *Phys Chem Chem Phys*, 2009, **11**, 3241-3249.

119. M. Nakayama, H. Ohshima, M. Nogami and M. Martin, *Phys Chem Chem Phys*, 2012, **14**, 6079-6084.

120. Z. Fu, Q. Sun, D. Ma, N. Zhang, Y. An and Z. Yang, *Applied Physics Letters*, 2017, **111**, 023903.

121. E. Kendrick, M. Russ and P. R. Slater, *Solid State Ionics*, 2008, **179**, 819-822.

122. K. Matsunaga and K. Toyoura, *Journal of Materials Chemistry*, 2012, **22**, 7265-7273.

123. K. Imaizumi, K. Toyoura, A. Nakamura and K. Matsunaga, *Journal of Physics: Condensed Matter*, 2015, **27**, 365601.

124. K. Imaizumi, K. Toyoura, A. Nakamura and K. Matsunaga, *Journal of the Ceramic Society of Japan*, 2017, **125**, 105-111.

125. A. Kushima and B. Yildiz, *Journal of Materials Chemistry*, 2010, **20**, 4809-4819.

126. C. C. Battaile, *Computer Methods in Applied Mechanics and Engineering*, 2008, **197**, 3386-3398.

127. R. Pornprasertsuk, P. Ramanarayanan, C. B. Musgrave and F. B. Prinz, *Journal of Applied Physics*, 2005, **98**, 103513.

128. R. Hempelmann, *Quasielastic neutron scattering and solid state diffusion*, Oxford University Press, New York, 2000.

129. R. Hempelmann, *Journal of the Less Common Metals*, 1984, **101**, 69-96.

130. H. J. Kim, A. Magerl, J. E. Fischer, D. Vaknin, P. Heitjans and A. Schirmer, in *Chemical Physics of Intercalation II*, eds. P. Bernier, J. E. Fischer, S. Roth and S. A. Solin, Springer

US, Boston, MA, 1993, DOI: 10.1007/978-1-4615-2850-0_38, ch. Chapter 38, pp. 355-359.

131. M. Karlsson, *Phys Chem Chem Phys*, 2015, **17**, 26-38.
132. C. R. A. Catlow, *Journal of the Chemical Society, Faraday Transactions*, 1990, **86**, 1167-1176.
133. S. Pili, S. P. Argent, C. G. Morris, P. Rought, V. Garcia-Sakai, I. P. Silverwood, T. L. Easun, M. Li, M. R. Warren, C. A. Murray, C. C. Tang, S. Yang and M. Schroder, *Journal of the American Chemistry Society*, 2016, **138**, 6352-6355.
134. R. Hempelmann, *Physica B: Condensed Matter*, 1996, **226**, 72-77.
135. T. Matzke, U. Stimming, C. Karmonik, M. Soetratmo, R. Hempelmann and F. Güthoff, *Solid State Ionics*, 1996, **86-88**, 621-628.
136. Q. Chen, J. Banyte, X. Zhang, J. P. Embs and A. Braun, *Solid State Ionics*, 2013, **252**, 2-6.
137. M. Wagemaker, G. J. Kearley, A. A. Van Well, H. Mutka and F. M. Mulder, *Journal of the American Chemistry Society*, 2003, **125**, 840-848.
138. J. S. G. Myrdal, D. Blanchard, D. Sveinbjörnsson and T. Vegge, *The Journal of Physical Chemistry C*, 2013, **117**, 9084-9091.
139. S. Jahn, J. Ollivier and F. Demmel, *Solid State Ionics*, 2008, **179**, 1957-1961.
140. F. Demmel, T. Seydel and S. Jahn, *Solid State Ionics*, 2009, **180**, 1257-1260.
141. S. A. Danilkin, M. Avdeev, T. Sakuma, R. Macquart and C. D. Ling, *Journal of Alloys and Compounds*, 2011, **509**, 5460-5465.
142. S. A. Danilkin, M. Avdeev, M. Sale and T. Sakuma, *Solid State Ionics*, 2012, **225**, 190-193.
143. J. Wind, R. A. Mole, D. Yu and C. D. Ling, *Chemistry of Materials*, 2017, **29**, 7408-7415.
144. E. Mamontov, *Solid State Ionics*, 2016, **296**, 158-162.
145. D. A. Neumann, J. R. Copley, R. L. Cappelletti, W. A. Kamitakahara, R. M. Lindstrom, K. M. Creegan, D. M. Cox, W. J. Romanow, N. Coustel, J. P. McCauley, Jr., N. C. Maliszewskyj, J. E. Fischer and A. B. Smith, 3rd, *Phys Rev Lett*, 1991, **67**, 3808-3811.
146. B. Holger Euchner and Tsunetomo Yamada and Helmut Schober and Stephane Rols and Marek Mihalkovič and Ryuji Tamura and Tsutomu Ishimasa and Marc de, *Journal of Physics: Condensed Matter*, 2012, **24**, 415403.
147. C. T. Chudley and R. J. Elliott, *Proceedings of the Physical Society*, 1961, **77**, 353-361.
148. S. Boyapati, *Solid State Ionics*, 2001, **138**, 293-304.
149. I. R. Evans, J. A. K. Howard and J. S. O. Evans, *Chemistry of Materials*, 2005, **17**, 4074-4077.

Chapter 2. Experimental and Computational Methods

2.1. Solid state synthesis

Reactions between two solids only take place at the interface between the reactants.[1-3] Once this surface layer has reacted, the reaction may only continue if the reactants can then diffuse from within the bulk to the surface. It is this diffusion that usually represents the rate limiting step in solid state reactions.[3] The conventional solid state synthesis method, used in this work, attempts to increase the reaction rates in two ways. Firstly, the reactants are thoroughly mixed and ground together into a fine precursor powder. The smaller particle sizes give larger surface area to volume ratios of the reactants, and so as long as the precursor is suitably homogenous, the area of contact between the reactants will be high and diffusion distances relatively low. Secondly, the reactions are carried out at very high temperatures (typically between 500 and 2000 °C)[3] in order to increase the rate of diffusion. Even using these conditions, solid state reactions take many hours to complete and may require repeated cooling, grinding, and refiring to go to completion. These high temperatures and long reaction times lead to the formation of thermodynamically stable products; however for some systems it is possible to access kinetically favourable phases by using lower temperatures. The final product phase is also influenced by cooling rate. A slower cooling rate will allow more time for atoms within the structure to arrange themselves so as to have the highest binding energy, giving the most thermodynamically stable product, whereas faster cooling rates may mean that phase transitions to these phases are kinetically inaccessible. The extreme of this, where the temperature of the sample is lowered very rapidly by e.g. submerging in water, is known as quenching. This can “trap” the system in a metastable phase.

The solid state syntheses described in this report all used hand grinding using an agate mortar and pestle. The firing temperatures and times are given in the experimental sections of the individual results chapters. The masses given are all accurate to ±0.0001 g.

2.2. X-Ray Diffraction

2.2.1. Theory

Diffraction at its simplest describes the phenomenon that occurs when a wave encounters a gap in some obstacle. The propagation of waves can be described according to the

Huygens-Fresnel principle,[4] in which each point in space that the wave reaches acts as a new point source of spherical waves. The interference between these spherical waves describes the future evolution of the wave. When the wave encounters a gap in an obstacle that is equal to or smaller than its wavelength, the wave behaves as though the slit is a single point source giving the impression that the wave is spreading out from the slit. If more than one slit is present, the waves propagating from them will undergo constructive interference if they are in phase; and destructive interference if they are out of phase. These diffraction concepts are illustrated in figure 2.1.

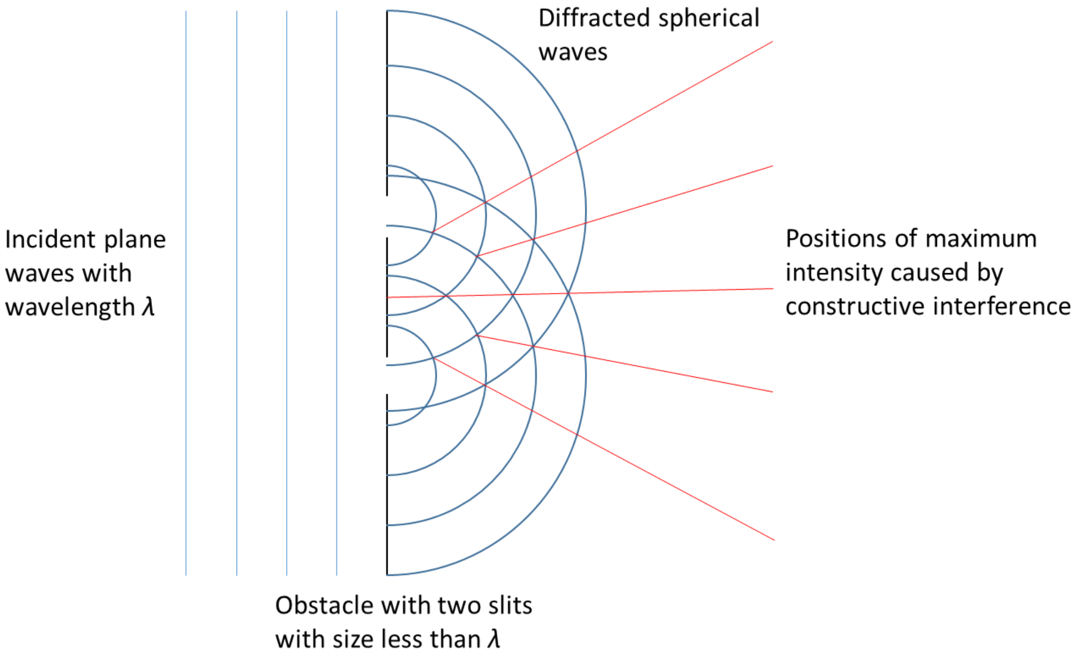

Figure 2.1: Diffraction of a wave by an obstacle with two slits.

The periodic arrangement of atoms allows a crystal to be considered a 3-dimensional diffraction grating for waves with wavelengths that closely match the interatomic distances (0.5 – 2.5 Å). X-rays are electromagnetic waves with wavelengths ranging between 0.1 and 100 Å which means that they have the potential to be diffracted by crystals.[1-3]

Incident X-rays on an atom will cause its electron cloud to oscillate; provided this interaction is elastic, this oscillation causes a spherical wave to be emitted from the atom with the same frequency as the incident wave. This occurs for all atoms in the substance and the interference between these spherical waves produces the final diffraction pattern. Due to the 3D periodic nature of a crystalline system the pattern will contain regions of high intensity where constructive interference has occurred, which take the form of spots for a single crystal sample and cones for powder samples.

In order to determine the conditions required for constructive interference, it is useful to consider a simpler model in which X-rays are reflected off parallel planes of atoms (figure 2.2). Each set of lattice planes is referred to by its Miller Indices *hkl* and the planes are separated by a constant distance d_{hkl}.

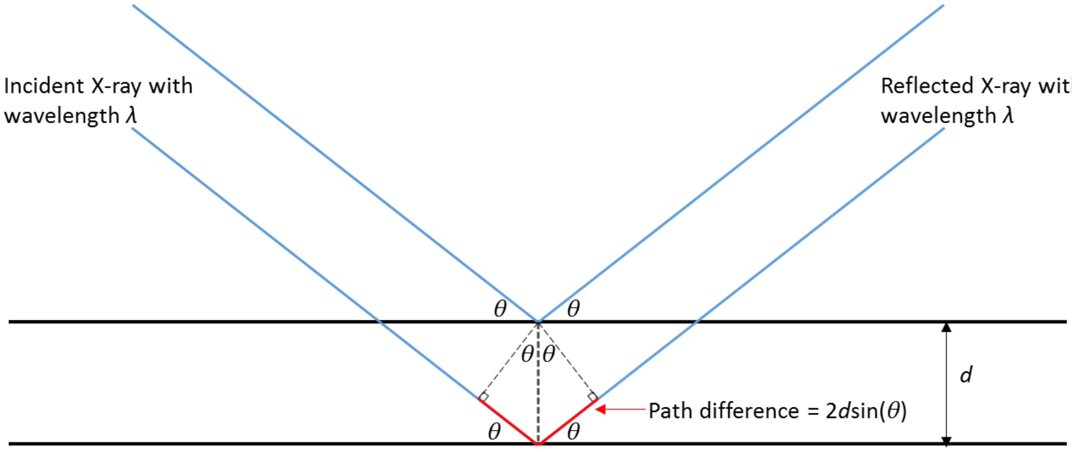

Figure 2.2: Reflection of X-rays off a set of lattice planes.

The *d* spacing for a particular lattice plane *hkl* depends only the cell parameters of the crystal lattice; lengths *a*, *b*, and *c* and angles *α*, *β*, and *γ*. In the general case the d_{hlk} values are given by equation 2.1:

$$\frac{1}{{d_{hkl}}^2} = \frac{\left(\frac{h}{a}\sin\alpha\right)^2 + \frac{2kl}{bc}(\cos\beta\cos\gamma - \cos\alpha)}{1 - \cos^2\alpha - \cos^2\beta - \cos^2\gamma + 2\cos\alpha\cos\beta\cos\gamma} + \frac{\left(\frac{k}{b}\sin\beta\right)^2 + \frac{2lh}{ca}(\cos\gamma\cos\alpha - \cos\beta)}{1 - \cos^2\alpha - \cos^2\beta - \cos^2\gamma + 2\cos\alpha\cos\beta\cos\gamma} + \frac{\left(\frac{l}{c}\sin\gamma\right)^2 + \frac{2hk}{ab}(\cos\alpha\cos\beta - \cos\gamma)}{1 - \cos^2\alpha - \cos^2\beta - \cos^2\gamma + 2\cos\alpha\cos\beta\cos\gamma} \qquad \text{Equation 2.1}$$

When incident X-rays of wavelength λ are reflected off a set of planes constructive interference will occur when the path difference between the waves reflected from different planes is equal to an integer number, *n*, of wavelengths. This relation leads to the Bragg's Law (equation 2.2):

$$2d_{hkl}\sin\theta = n\lambda \qquad \text{Equation 2.2}$$

Where θ is the angle between the incident X-ray and the plane. In practice only $n = 1$ needs to be considered as higher order reflections ($n > 1$) are indistinguishable from the first order reflections from planes with Miller Indices *nh nk nl*.[3] It should be noted that due to the reflection of the X-ray beam off the planes the constructive interference peaks are observed at angle 2θ relative to the incident beam. It is this quantity that is reported in XRD experiments.

As the interference peaks are observed at angles which can be directly related to d_{hkl} through equation 2.2, then it follows from equation 2.1 that by matching the observed peaks (known as Bragg peaks) to specific *hkl* values the unit cell parameters and angles a, b, c, α, β and γ can be determined. This is known as indexing the diffraction pattern.

The intensity of individual Bragg peaks is proportional to the square of the structure factor $\boldsymbol{F}_{hkl}$ which is defined in equation 2.3:[5]

$$\boldsymbol{F}_{hkl} = \sum_{1}^{j} f_j \mathrm{e}^{2\pi i(hx_j + ky_j + lz_j)} \qquad \text{Equation 2.3}$$

Where x_j, y_j and z_j are the fractional coordinates of each atom j in the unit cell and f_j, the atomic scattering factor, is the scattering power of the individual atoms, j. The atomic scattering factor is defined below in equation 2.4:

$$f_j = \int_0^{\infty} \rho(\boldsymbol{r}) \frac{\sin(\boldsymbol{r}.\boldsymbol{Q})}{\boldsymbol{r}.\boldsymbol{Q}} \mathrm{d}\boldsymbol{r} \qquad \text{Equation 2.4}$$

Where $\rho(\boldsymbol{r})$ is the radial distribution function of electrons around the atom, r is the distance from the nucleus and $Q = (4\pi\sin\theta)/\lambda$. Due to X-rays interacting with the electron clouds of atoms, f_j increases systematically with atomic number and so the intensities of the Bragg peaks contain information about the identities and positions of atoms in the unit cell. However, as seen by the dependence on $1/Q$ the intensity decreases with increasing 2θ. This is because X-rays scattered from different parts of an atoms electron cloud will have increasing differences in path length as 2θ increases and so will destructively interfere in increasing amounts.

Another factor affecting peak intensities is the Debye-Waller factor in which thermal vibrations of the atoms in the crystal cause the X-rays to no longer scatter elastically. This causes intensity to be lost from the Bragg peaks into the background. As well as increasing in effect with temperature due to the increasing vibrations of the atoms, the Debye-Waller factor also increases with 2θ which must be taken into account when identifying atoms from peak intensity. This can be accounted for by applying a correction to the individual atomic structure factors as shown in equation 2.5. Note that this particular correction assumes that each atom vibrates isotopically.

$$f_{\mathrm{DW}} = f_j \mathrm{e}^{-B\left(\frac{\sin\theta}{\lambda}\right)^2} \qquad \text{Equation 2.5}$$

Where *B*, the isotropic temperature factor, = $8\pi^2\langle u^2\rangle$ and $\langle u^2\rangle$ is the mean square displacement of the atom from its ideal position.

2.2.1.1. Powder X-Ray Diffraction

In powder X-ray diffraction (XRD) the sample used contains a very large number of crystallites that are ideally randomly oriented relative to the incident X-ray beam. Each individual crystallite will scatter the incident beam in the same way as a single crystal; however, due to the large number and random orientation of the crystallites the scattered X-rays will form cones with semi-apex angle 2θ. This leads to an image made up of concentric circles rather than spots. A powder XRD pattern is collected from a 1-dimensional slice of this image recording the intensity of scattered X-rays at each 2θ.

This method of data collection causes additional difficulties with identifying the Bragg peaks in the resultant pattern. This is because several different (*hkl*) reflections can have the same *d*-spacing, and so scatter at the same angle. This means that each of these reflections will overlap significantly on the 1-dimensional powder XRD pattern. Some of these are caused by symmetry equivalent reflections, the number of which is known as the multiplicity and varies depending on the space group (for example in triclinic systems only (*hkl*) and (*-h-k-l*) reflections are symmetry equivalent giving a multiplicity of 2). These have the same $\boldsymbol{F}_{hkl}$ and so the resulting intensity is the product of the intensity of one of them and the multiplicity. For other reflections, such as the (211) and (300) reflections in the cubic system, the structure factors are different despite the *d*-spacing being the same. This makes *ab initio* structure solution from powder XRD more difficult than when using single crystal XRD as the intensity from each observed peak must be correctly divided between each of the individual (*hkl*) reflections that make it up.

2.2.2. Instrumentation

The X-ray diffraction patterns included in this report for phase identification and purity confirmation were collected using a Bruker D8 Advance diffractometer operating at 40 kV and 40 mA. The X-rays used are generated in a copper X-ray tube; the CuKβ X-rays are then removed using a nickel filter leaving the CuKα_1 (λ = 1.5406 Å) and CuKα_2 (λ = 1.5444 Å) to interact with the sample. A variable divergence slit was used to ensure that at all angles the cross section of the X-ray beam falls entirely on the sample and that the same volume of the sample is probed throughout the experiment. The scattered X-rays are detected by a Lynx-eye semiconductor strip detector.

2.2.3. Sample Preparation

In preparation for powder XRD pattern collection the samples were thoroughly ground using a mortar and pestle, before being sieved onto silicon slides that were prepared with a layer of Vaseline to act as an adhesive. The slides are made from a single crystal of silicon that is cut parallel to the 511 plane, this gives a very low background as the plane does not align with the incident X-ray beam in the correct way to produce a Bragg peak at the detector. The samples were then loaded into a sample changer on the diffractometer.

2.2.4. Analysis

While solving a structure *ab initio* using powder XRD data is difficult, this is usually unnecessary as a model can instead be created from the known structures of similar materials that is then used to simulate an XRD pattern. This model is then refined by adjusting its parameters until a good fit to the experimentally collected pattern is made. All XRD refinements in this project were performed using TOPAS Academic version 5.[6] In these refinements a background function based on Chebyshev polynomials of the first kind was used. The form of this background function for n+1 terms is given in equation 2.6:

$$f_{\mathrm{Bg}}(x) = \sum_{i=0}^{n} c_i T_i(x) \qquad \text{Equation 2.6}$$

Where n is the order of the polynomial and c_i are the coefficients of terms with order i which are refinable parameters during fitting. The $T_i(x)$ are the Chebyshev polynomials of the first kind that are defined as shown in equation 2.7:

$$\begin{aligned} T_0(x) &= 1, \\ T_1(x) &= x, \\ T_n(x) &= 2xT_{n-1}(x) - T_{n-2}(x) \end{aligned} \qquad \text{Equation 2.7}$$

For refining peak shapes a Thompson-Cox-Hastings pseudo-Voigt function $TCHZ(x)$ (consisting of a linear combination of a Gaussian $G(x)$ and a Lorentzian $L(x)$) was used during refinement.[7] The form of this function is given in equation 2.8:

$$TCHZ(x) = \eta L(x) + (1-\eta)G(x) \qquad \text{Equation 2.8}$$

Where η is a mixing factor which varies depending on the full width half maxima of the Lorentzian and Gaussian functions. It is these full width half maxima values (based on 6 refinable parameters) that are fitted during refinement.

2.2.4.1. Pawley Refinement

A Pawley refinement[8] uses a structure-less model containing only the space group, refinable unit cell parameters, and instrumental parameters defining peak shape, background, and zero-point. The 2θ values are then calculated for allowed (*hkl*) reflections. During refinement the cell parameters are adjusted until these calculated peaks match up with the observed peaks. As no information about atom positions, occupancies, or temperature factors is given in the model for a Pawley fit, the peak intensities cannot be calculated and instead are given a value to best match the observed pattern.

2.2.4.2. Rietveld Refinement

In contrast a Rietveld refinement's[9] starting model contains information on the crystal structure of the material, including atomic fractional coordinates, occupancies and atomic displacement parameters, as well as the cell parameters and space group. Other sample related properties such as crystallite size, shape and preferred orientation can also be modelled. From these data, as well as the instrumental information about peak shape, background and the zero-point, a pattern is calculated then adjusted using a nonlinear least squares method to find the best match for the observed pattern. All of the above parameters may be refined except for the space group.

The least squares method of data fitting for XRD patterns attempts to minimise the sum (S) of the squared differences between the calculated (y_c) and observed (y_o) intensities at all 2θ values in the pattern. Equation 2.9 shows how this value is calculated:

$$S = \sum_i w_i (y_{oi} - y_{ci})^2 \qquad \text{Equation 2.9}$$

Where w is a weighting factor to account for the variance in the y values. As the y values are in fact a total of y_{oi} individual counts that are assumed to follow Poisson statistics, the variance is equal to y_{oi} and so w_i is taken to be equal to $1/y_{oi}$. The parameters are then adjusted and a new value calculated. This cycle continues until a minimum value of S is achieved.

In order to measure the quality of a fit the value of S cannot be used directly as it does not correct for the absolute values of intensity in the pattern. This means that higher intensities will return higher values of S making comparisons between different instruments and samples impossible. Because of this the weighted profile residual, R_{wp}, is used, which gives a quantitative measure of the quality of the fit by normalising by total measured intensity. This is calculated as shown in equation 2.10:

$$R_{wp} = \left(\frac{S}{\sum_i w_i {y_{oi}}^2}\right)^{0.5} \times 100\ \% \qquad \text{Equation 2.10}$$

If the experimental pattern has a background that represents a significant portion of the total intensity then R_{wp} can be artificially small giving the impression of a better fit than is actually present. Because of this, although the R_{wp} values can be a useful indicator, visualisation of the observed, calculated and difference patterns is still required in order to determine fit quality.[10]

2.3. Neutron Scattering

2.3.1. Theory

Neutron scattering is the name given to a variety of experimental techniques that use neutrons to probe the structure and dynamics of a target material. Neutrons are produced in either a reactor or spallation source and are then moderated to lower their energies and allow them to interact with matter on atomic length scales. The production and moderation of neutrons is discussed in section 2.3.2. Because neutrons have no charge they interact with the nuclei of the atoms in the target material rather than the electrons. The interaction strength between a neutron and a nucleus is called the scattering length, b. This can either be positive in the case where the neutron experiences a repulsive nuclear potential or negative in the case of an attractive potential. Unlike with X-rays, which interact with electron clouds and so have atomic scattering factors that vary regularly with atomic number (equation 2.4), the value of b for a nucleus is not dependent on atomic number or nuclear mass and can vary significantly between isotopes of the same element. This makes neutrons ideal for probing lighter atoms such as hydrogen, carbon and oxygen in the presence of heavier metal atoms. Additionally, due to the point like nature of the nucleus compared to the wavelengths of the incident neutrons, b is independent of the scattering angle θ, making neutrons better suited for studying scattering at large angles than X-rays.

2.3.1.1. Neutron Interaction with Matter

A diagram of a neutron scattering event can be seen in figure 2.3. An incident beam of neutrons with initial energy E_i and momentum $\boldsymbol{k}_i$ interacts with the sample and the neutrons are scattered at an angle θ with a final energy E_f and momentum $\boldsymbol{k}_j$. This gives an energy transfer to the sample $\omega = E_f - E_i$ and a momentum transfer to the sample $\boldsymbol{Q} = \boldsymbol{k}_i - \boldsymbol{k}_f$. The total number of neutrons scattered per second divided by the incident neutron flux (number of incident neutrons per unit area) is given by the total scattering cross section σ_{tot}.

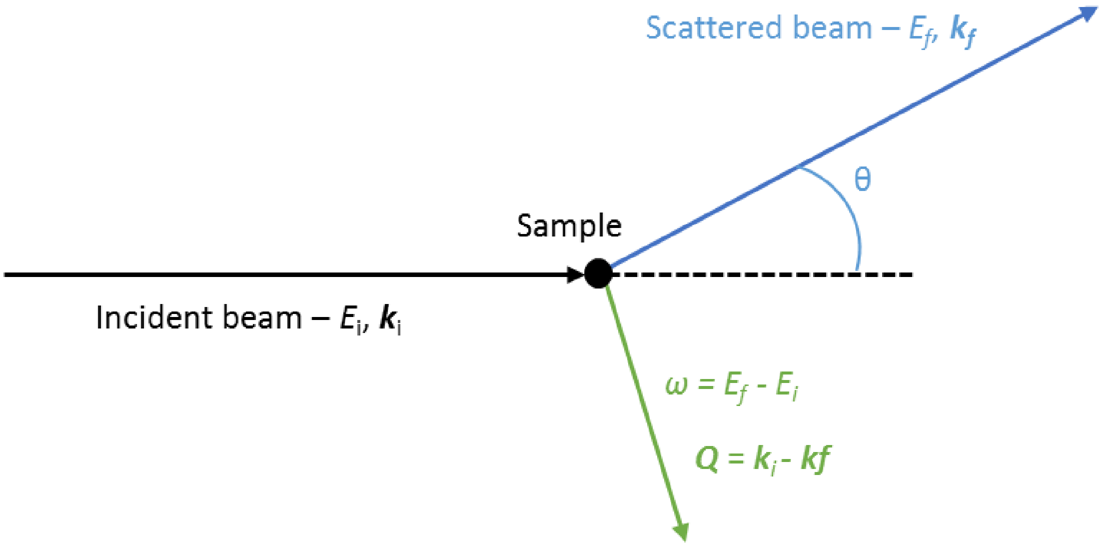

Figure 2.3: Diagram of a neutron scattering event in real space. This represents a simplified two dimensional case with $\Omega \rightarrow \theta$

In the case of elastic scattering ($\omega = 0$), as measured in neutron diffraction experiments, the number of neutrons scattered into solid angle dΩ is counted. This is given by the differential cross section:[11]

$$\frac{d\sigma}{d\Omega} = \sum_{i,j}^{N} b_i b_j \mathrm{e}^{-\mathrm{i}\boldsymbol{Q}(\boldsymbol{r}_j - \boldsymbol{r}_i)} \qquad \text{Equation 2.11}$$

Where b_i, b_j are the scattering lengths of nuclei i and j that are at positions $\boldsymbol{r}_i$ and $\boldsymbol{r}_j$. N is the total number of nuclei is the system. This expression can also be written in terms of the average scattering length in the system $\langle b \rangle$. In the case of the average over all nuclei: $\langle b_i b_j \rangle = \langle b \rangle^2$. However, in the special case when $i = j$: $\langle b_i b_j \rangle = \langle b^2 \rangle$. This allows the differential cross section to be split into two parts, representing coherent and incoherent scattering:

$$\left(\frac{d\sigma}{d\Omega}\right)_{coh} = \langle b\rangle^2 \sum_{i,j}^{N} \mathrm{e}^{-\mathrm{i}\boldsymbol{Q}(\boldsymbol{r}_j-\boldsymbol{r}_i)} = \frac{\sigma_{coh}}{4\pi}\sum_{i,j}^{N} \mathrm{e}^{-\mathrm{i}\boldsymbol{Q}(\boldsymbol{r}_j-\boldsymbol{r}_i)} \qquad \text{Equation 2.12}$$

$$\left(\frac{d\sigma}{d\Omega}\right)_{inc} = (\langle b^2\rangle - \langle b\rangle^2)N = \frac{\sigma_{inc}}{4\pi}N \qquad \text{Equation 2.13}$$

Where σ_{coh} is the coherent cross section and σ_{inc} is the incoherent cross section. Different isotopes scatter coherently and incoherently in differing proportions depending on their nuclear structure. Coherent scattering is caused by the neutrons interacting with all the nuclei in the sample as a collective, with the scattered neutrons from different nuclei interfering with each other. The elastic coherent scattering has $\boldsymbol{Q}$ dependence and contains information about the structure of the sample. Incoherent scattering is caused by the neutrons interacting independently with each individual nucleus in the sample with no interference between scattered neutrons from different nuclei. As $\boldsymbol{r}_i - \boldsymbol{r}_j = 0$ when $i = j$ the elastic incoherent scattering has no $\boldsymbol{Q}$ dependence and simply represents the total incoherent cross section of the sample.

In inelastic neutron scattering experiments ($\omega \neq 0$) the fraction of neutrons scattered into solid angle $d\Omega$ with final energy dE_f is measured, giving the doubly differential scattering cross section:[11]

$$\frac{d^2\sigma}{d\Omega dE_f} = \frac{1}{2\pi\hbar}\frac{k_f}{k_i}\int_{-\infty}^{\infty}\sum_{i,j} b_i b_j \langle e^{-\mathrm{i}\boldsymbol{Q}.\boldsymbol{r}_j(0)} e^{\mathrm{i}\boldsymbol{Q}.\boldsymbol{r}_i(t)}\rangle e^{-\mathrm{i}\omega t} dt \qquad \text{Equation 2.14}$$

As with the differential cross section, the doubly differential cross section can also be split into a coherent part and an incoherent part:

$$\left(\frac{d^2\sigma}{d\Omega dE_f}\right)_{coh} = \langle b\rangle^2 \frac{1}{2\pi\hbar}\frac{k_f}{k_i}\int_{-\infty}^{\infty}\sum_{i,j} \langle e^{-\mathrm{i}\boldsymbol{Q}.\boldsymbol{r}_j(0)} e^{\mathrm{i}\boldsymbol{Q}.\boldsymbol{r}_i(t)}\rangle e^{-\mathrm{i}\omega t} dt$$

Equation 2.15

$$= \frac{\sigma_{coh}}{8\pi^2\hbar}\frac{k_f}{k_i} S(\boldsymbol{Q},\omega)$$

$$\left(\frac{d^2\sigma}{d\Omega dE_f}\right)_{inc} = (\langle b^2\rangle - \langle b\rangle^2) \frac{1}{2\pi\hbar}\frac{k_f}{k_i}\int_{-\infty}^{\infty}\sum_{i} \langle e^{-\mathrm{i}\boldsymbol{Q}.\boldsymbol{r}_i(0)} e^{\mathrm{i}\boldsymbol{Q}.\boldsymbol{r}_i(t)}\rangle e^{-\mathrm{i}\omega t} dt$$

Equation 2.16

$$= \frac{\sigma_{inc}}{8\pi^2\hbar}\frac{k_f}{k_i} S(\boldsymbol{Q},\omega)_{self}$$

$S(\mathbf{Q},\omega)$ is known as the dynamic structure factor and contains all the information about the physics of the sample independent of instrumental parameters. It represents the probability of finding a particle at position $\mathbf{r}_t$ at time t given that there was _any_ particle at $\mathbf{r}_0$ at time t=0. The dynamic structure factor contains information about elastic scattering and therefore the structure of the material as well as inelastic scattering giving all of the dynamics of the system including collective motions such as phonons.

$S(\mathbf{Q},\omega)_{self}$ represents only the self-terms of the dynamic structure factor i.e. when $i = j$. It represents the probability of finding a particle at position $\mathbf{r}_t$ at time t given that _the same_ particle was at position $\mathbf{r}_0$ at time t=0. The gives information about only the individual atom dynamics such as long range diffusion and molecular vibrational modes. Because $S(\mathbf{Q},\omega)$ also contains the self-terms this means that these individual atom dynamics can be seen even in the case of purely coherently scattering nuclei.

When $S(\mathbf{Q},\omega)$ is plotted against ω different regions give information about different types of scattering and different types of dynamics. For quantised modes such as phonons or molecular vibrations the dynamics can be observed at fixed ω values, with higher frequency dynamics at a higher ω value than lower frequency dynamics. For diffusion dynamics the atomic displacements have zero restoring force and so evidence for these dynamics can take a range of ω values around the elastic line at $\omega = 0$. The different types of scattering and the type of information contained in them are shown in figure 2.4.

2.3.1.2. Quasielastic Neutron Scattering

Theoretically, the elastic peak in an inelastic neutron scattering experiment should be a delta function at $\omega = 0$; however, in reality each neutron scattering instrument has a finite resolution which broadens the elastic line into a Gaussian peak. This resolution can be related to the range of timescales of dynamics that can be probed by a particular instrument with higher resolutions corresponding to longer timescales and therefore slower dynamics.

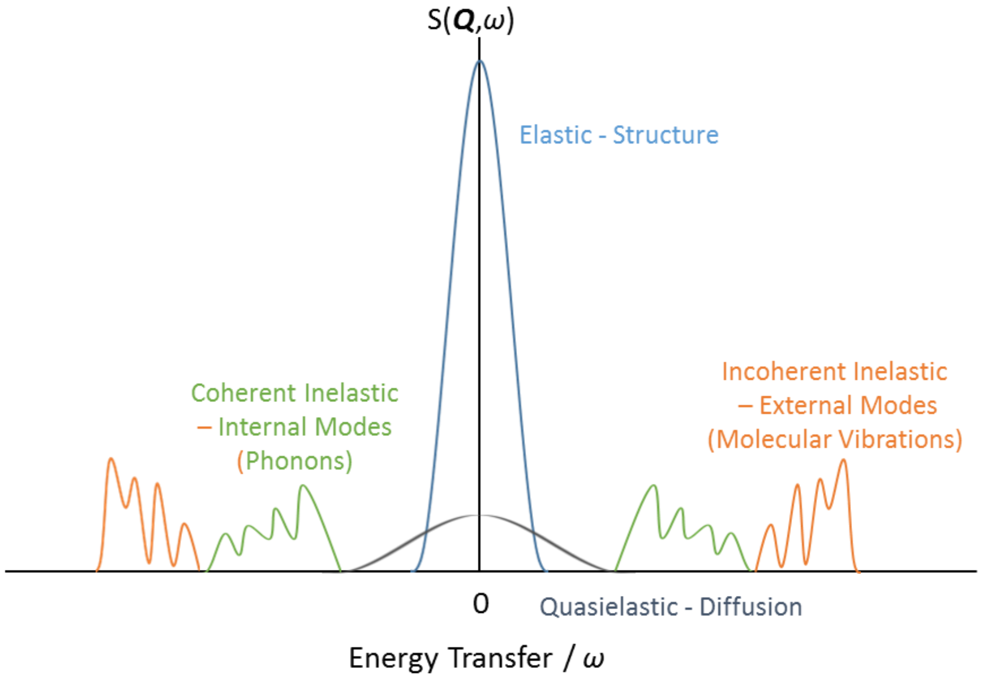

Figure 2.4: An example of a neutron scattering spectrum showing dynamic structure factor against energy transfer with the various types of scattering.

If diffusional dynamics occurring on a timescale approximately equivalent to those probed by the chosen neutron scattering instrument are present in a sample then evidence for them can be seen in a broad peak taking a Lorentzian form centred on the elastic line (figure 2.4). Because the energy transfer is very small in magnitude (relative to the instrumental resolution) this is referred to as quasielastic neutron scattering (QENS).

The finite resolution of neutron scattering instruments means that an elastic peak that is too broad may mask a QENS peak, making it impossible to measure dynamics that occur on these slow timescales. Because of this it is necessary to select an instrument with a resolution that matches the timescales of the dynamics that are to be probed in order to measure a QENS signal. Once a QENS peak is identified the variation of the linewidth can be used to determine details of the diffusional processes.

2.3.2. Neutron Production

Neutrons for use in scientific research are produced in one of two ways. The first is as a fission product in a nuclear reactor. The fission process begins with a neutron being absorbed by a nucleus of ^{235}U. This unstable ^{236}U nucleus then undergoes fission into two smaller nuclei (e.g. ^{141}Ba and ^{92}Kr) and releasing an average of 2.35 neutrons per fission event. These released neutrons can then be absorbed by other ^{235}U nuclei causing further fission events in a self-sustaining chain reaction causing a very large number of neutrons to be released. The neutron scattering experiments reported in this thesis were performed at the Institut Laue-Langevin (ILL) which has a reactor source that provides a continuous flux of 1.5 × 10^{15} neutrons s^{-1} cm^{-2}.

The second method of neutron production is known as spallation. This begins with the ionisation of H_2 and subsequent acceleration of H^- ions. These ions are then stripped of electrons using a thin foil of for example Al. The resulting protons are then further accelerated up to energies of 800 MeV then focused on a target made of a heavy metal such as tungsten or mercury. The protons interact with the target nuclei transferring part of their energy and causing an intra-nuclear cascade that leads to the expulsion of a large number of high energy neutrons (as well as other products such as protons and mesons).

2.3.2.1. Neutron Moderation

The neutrons produced by these methods have energies much too high (≈ 0.1 – 1 MeV for fast neutrons) and therefore wavelengths much too low ($2.8 \times 10^{-4} – 9 \times 10^{-4}$ Å) to interact with matter on atomic length scales (0.5 – 2.5 Å). To remedy this the neutrons have their energies reduced by elastic collision between the neutrons and the nuclei of atoms that make up a moderator medium. These collisions occur repeatedly with the neutrons losing energy until they are in thermal equilibrium with the moderator. In order for this to proceed efficiently the moderator must contain nuclei that are close in mass to a neutron and also have a low chance of absorbing. For this reason common moderators are: ^1H (as part of water); ^2D (either as D_2 or as part of heavy water); or carbon (usually in the form of graphite). The final energy distribution of the neutrons is dependent on the temperature of the medium, with a 300 K medium giving an average neutron energy of ≈ 25 meV and wavelength of 1.8 Å. Neutrons at this temperature are known as thermal neutrons, produced at the ILL using a D_2O moderator, and are well suited for a range of neutron diffraction and scattering experiments. However, in some experimental scenarios neutrons with higher (hot neutrons, $\lambda < 0.8$ Å) or lower energies (cold neutrons, $\lambda > 3$ Å) are required. Cold neutrons, with their larger wavelengths, give high resolutions at low $\boldsymbol{Q}$ and ω values. This allows materials with larger *d*-spacings (such as in macromolecular structures like proteins) and slower dynamics to be studied than possible with thermal neutrons. On the other hand hot neutrons provide access to large ω values allowing for the study of high frequency dynamics such as molecular vibrations. At the ILL secondary moderators are responsible for the production of hot and cold neutrons. These take the form of liquid D_2 at 25 K for cold neutrons, and solid graphite at 2000 K for hot neutrons.

2.3.3. Instrumentation

For this work two ILL instruments were used for neutron scattering experiments, IN6 and IN16b. Both of these instruments operate on a cold neutron source, useful for study of slow dynamics due to higher energy resolutions. A general overview of each of these instruments is given below with specific experimental parameters given in the relevant results chapters. All analysis was performed using the LAMP software.[12]

2.3.3.1. IN6

IN6 is a time-focusing time-of-flight neutron spectrometer operating from a cold neutron source with wavelengths between 4 and 6 Å, a maximum energy transfer range of $-200 < \omega < 3$ meV and a maximum $\boldsymbol{Q}$ of 2.6 Å. IN6 has an energy transfer resolution of between 170 µeV at the lowest wavelength and 50 µeV at the highest wavelength (governed by the duration of the neutron pulses used, see below) allowing dynamics on the order of 10s of picoseconds to be observed. The set-up of IN6 can be seen in figure 2.5.

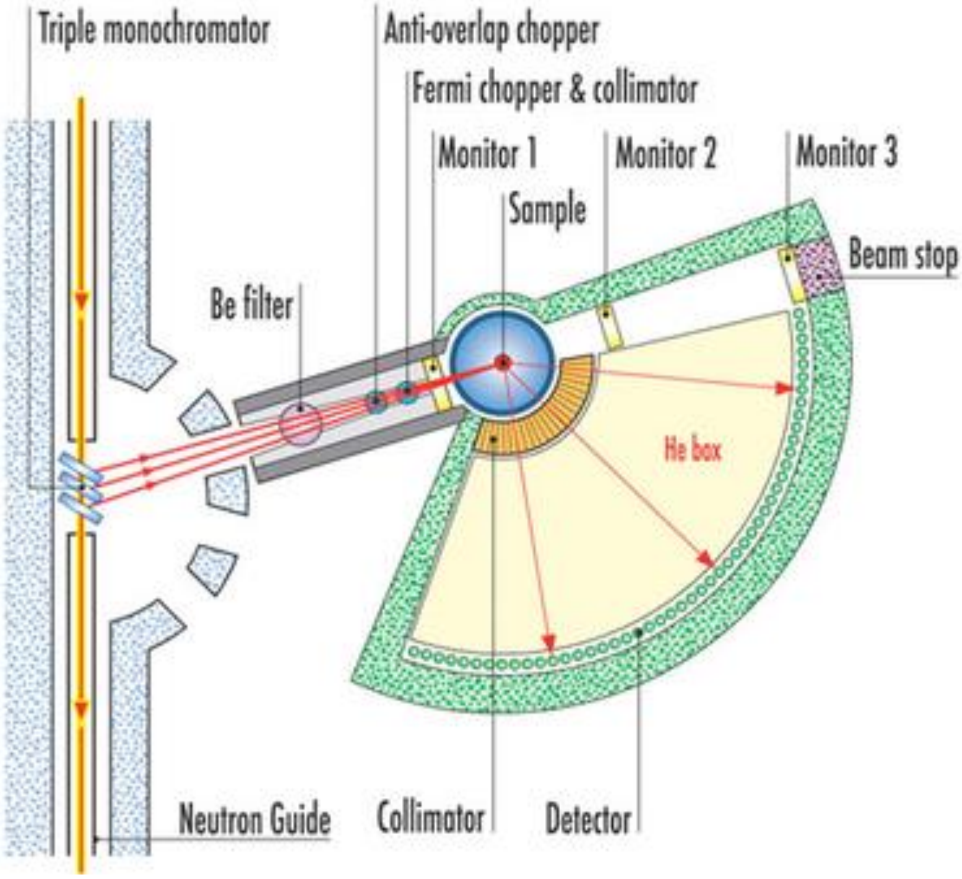

Figure 2.5: Layout of the ILL instrument IN6.[13]

Time-of-flight spectroscopy is a method of determining the energy transfer between the scattered neutrons and the sample. This requires neutrons with a known initial energy which is achieved in IN6 through the use of a graphite monochromator that extracts neutrons of the desired wavelength from the main beamline. The beam from the monochromator also contains higher order (lower wavelength) reflections which are removed using a beryllium filter leaving a beam of neutrons with a single wavelength. This continuous beam is divided into pulses by a Fermi chopper which then goes on to interact with the sample at a known time. After interacting with the sample the neutrons pass through an oscillating collimator. This only allows neutrons that are coming from the direction of the sample through thereby reducing background from neutrons reflected by other parts of the instrument. The speed of the scattered neutrons, and therefore their energy, is then determined by the time-of-flight of the neutron between the sample and the detector and the known distance between them. In order to prevent overlap between the fastest scattered neutrons from one pulse and the slowest from the previous pulse a frame overlap chopper is placed before the Fermi chopper that can rotate more slowly so as to only let every *n*th pulse through. After detection, as both the initial and final energies are known, the energy transfer to the sample can be calculated. The momentum transfer $\boldsymbol{Q}$ can then also be calculated based on the angle at which the neutron was scattered. Because the Fermi chopper has slits of a finite size, the neutron pulses have a finite duration. This means that the initial interaction times have an uncertainty which is propagated to the time-of-flight. It is this that governs the instrument resolution.

IN6 increases the neutron flux at the sample by using the time-focusing technique. Three neutron beams of distinct energy are extracted using three different monochromators, and pass through the instrument as described above. The Fermi chopper allows the pulse of the slowest neutrons through first and the fastest neutrons last with the speed of the chopper set so that all three beams arrive at the detectors at the same time giving an overall intensity triple that of only a single monochromator.

2.3.3.2. IN16b

IN16b is backscattering spectrometer offering very high energy transfer resolutions of up to ≈ 0.75 µeV allowing very slow dynamics on timescales of several nanoseconds to be measured. The instrument operates with 6.271 Å neutrons from an ILL cold source with a maximum energy transfer range of ± 31 µeV and momentum transfer range $0.1 < \boldsymbol{Q} < 1.8$. The experiments reported in this thesis used IN16b in high flux mode. The setup of IN16b in this mode can be seen in figure 2.6.

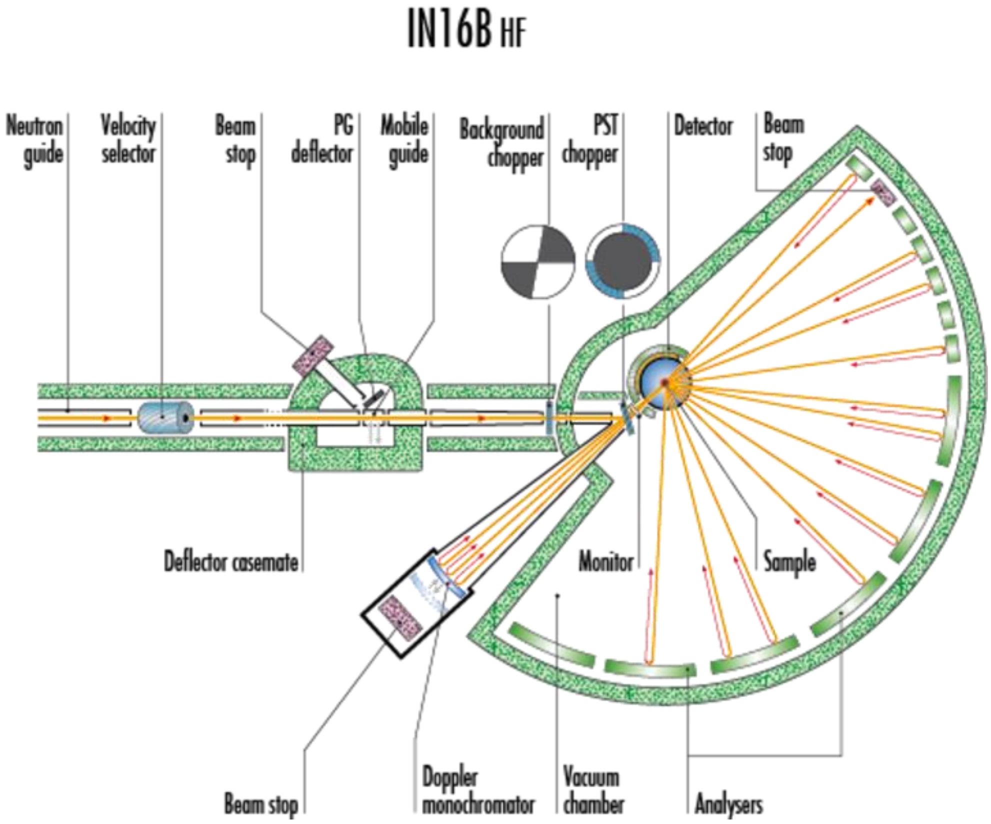

Figure 2.6: Layout of the ILL instrument IN16b.[14]

The high energy transfer resolution of IN16b is achieved using an instrumental technique called neutron backscattering.[15] In IN16b the energy transfer during neutron scattering is precisely determined through control of both the initial neutron energy (through the use of monochromator crystals) and the final neutron energy (by using analyser crystals). Both the monochromator and analyser crystals operate under the same principle: only those incident neutrons that fulfil the Bragg condition, $\lambda = 2d\sin\theta$, where d is the spacing of the lattice planes parallel to the crystal surface, are reflected and so in theory a monochromatic outgoing beam with a known wavelength is produced. However, as the beam incident on the crystal cannot be perfectly collimated the incident angle has some variation $\Delta\theta$. In addition, the monochromator crystal will not be perfect having a variation of Δd in its lattice spacing. These two factors leads to a non-monochromatic outgoing beam with a $\Delta\lambda$ given by the differential of the Bragg equation (equation 2.17):

$$\frac{\Delta\lambda}{\lambda} = \Delta\theta \cot\theta + \frac{\Delta d}{d} \qquad \text{Equation 2.17}$$

From this it can be seen that, to a first order approximation, setting the angle θ to 90° gives a $\Delta\lambda$ that only depends on Δd. Fulfilling this θ = 90° condition is known as backscattering. In

IN16b the backscattering condition is fulfilled in both the monochromator and the analyser crystals, allowing precise control of both the initial and final neutron energies. To further increase the resolution, IN16b uses Si(111) monochromator and analyser crystals that have a small $\Delta d/d$ = 1.86×10^{-5}. This allows the very narrow energy resolutions of up to 0.75 µeV to be obtained. The use of these crystals requires the instrument to operate with a neutron wavelength of 6.271 Å in order to fulfil the backscattering condition.

In high flux mode (figure 2.6) the initial neutron energies are first selected by a velocity selector, this consists of rotating blades that spin at such a frequency as to only allow neutrons with wavelengths ≈ 6 Å through. In the low background mode of IN16b this first wavelength selection occurs at the PG (pyrolytic graphite) deflector. This reduces the background by deflecting the neutrons out of the path of the main beamline but also reduces the overall flux at the sample. The neutron beam is then pulsed using a background chopper. The pulses are deflected towards the monochromator crystal using a phase space transformation (PST) chopper. This consists of a moving PG mosaic crystal that shifts the pulses from a highly collimated beam with a wide wavelength band to a broader beam with a narrower band around the desired 6.271 Å wavelength, so increasing the flux at that wavelength.

As described above, the monochromator is a Si(111) crystal that is aligned to fulfil the backscattering condition. This is mounted on a Doppler drive that can move the crystal back and forth perpendicular to the lattice plane. Due to the Doppler Effect, the velocity of the monochromator crystal changes the *d*-spacing that the neutron beam sees. This allows the initial energy of the neutron pulse to be varied by changing the velocity of the Doppler drive, while retaining the high resolution provided by the backscattering geometry. The neutrons, with a range of energies defined by the Doppler drive velocity profile, travel back through the PST chopper to the sample and are scattered. The analyser crystals reflect back those neutrons with wavelength 6.271 Å back to the detectors. As all the detected neutrons have the same energy the time in which they arrive must depend only on their initial energies allowing ω to be calculated. The angle at which the neutrons are scattered at then allows $\boldsymbol{Q}$ to be determined.

2.3.4. Analysis

2.3.4.1. *Analysis of Inelastic Neutron Scattering Data*

On the picosecond timescales probed by IN6 phonon modes can be observed. As the population of these modes increases with temperature the inelastic intensity also increases. This increase must be taken into account in order for a potential QENS signal to be clearly identified. To do this the inelastic neutron scattering spectra are corrected by dividing $S(Q,\omega)$ by the Bose population factor n_B. For a state with energy ω at temperature T the Bose population factor is given by equation 2.18:

$$n_\mathrm{B} = \frac{1}{\mathrm{e}^{\frac{\hbar\omega}{k_\mathrm{b}T}} - 1} \qquad \text{Equation 2.18}$$

Where, $\hbar$ is the reduced Plank constant and k_b is the Boltzmann constant. By applying this correction any variation in the spectra with temperature due to phonon modes is taken to into account.

As well as probing picosecond timescales for long range oxygen diffusion dynamics, IN6 data have also been used to plot the density of states, $G(Q,\omega)$. $G(Q,\omega)$ can be calculated from $S(Q,\omega)$ using equation 2.19:

$$G(Q,\omega) = \frac{S(Q,\omega)\omega}{Q^2 n_\mathrm{B}} \qquad \text{Equation 2.19}$$

2.3.4.2. *Analysis of Quasielastic Neutron Scattering Data*

QENS signals measured is this thesis have been fitted using the Chudley-Elliott model (equation 1.8, given in Chapter 1, Section 1.4.2).[16] This allows the residence times τ and the jumps distances l to be found by plotting the Q dependence of the QENS linewidth Γ and fitting with this model. Additionally, assuming the Chudley-Elliott model, the linewidth Γ is proportional to the diffusion coefficient D and so follows an Arrhenius relationship with temperature allowing the activation energy of the observed dynamics to be calculated from the gradient of a plot of $\ln(\Gamma)$ against T^{-1}.

2.4. Solid State NMR

2.4.1. Theory

The fundamental principle of nuclear magnetic resonance (NMR) is the interaction of nuclear spins with a magnetic field. Nuclei that contain an even number of both protons and neutrons have a spin (S) of zero. All other nuclei have a non-zero spins (either integer or half integer) and so will have a non-zero magnetic moment (μ). As this is a quantum phenomenon the direction of the spin is also quantised. The projection of the spin in a direction commonly referred to as the z direction is given by the quantum number m, which can take values from $+S$ to $-S$ in half integer steps giving a total of $2S + 1$ states. The z component of the magnetic moment is given by $\mu_z = m\gamma\hbar$, where γ is the gyromagnetic ratio and $\hbar$ is Planck's constant.

When a nucleus is placed in a magnetic field, its magnetic moment interacts with the field and the states lose their degeneracy, gaining or losing energy depending on their alignment with the field. In NMR the field is defined to be aligned with the z direction and the states have energy:

$$E = -\mu_z B = -m\gamma\hbar B \qquad \text{Equation 2.20}$$

Where B is the magnetic field strength. At equilibrium there are more nuclei in the lower energy state producing an overall magnetization vector, M_0, in the z direction. The energy differences between the states means that transition of the spins from the lower energy state to the higher state is possible by absorption of photons of matching frequency. This is referred to as resonant absorption and it is this that is the basis of NMR measurements. The excitation takes the form of a pulse produced by a second applied magnetic field, B_{xy}, in the x-y plane. Usually a 90° pulse is used, so called because the excitation moves the samples overall magnetisation vector, M, from its equilibrium direction, $M = M_z = M_0$, into the x-y plane, $M = M_{xy}$. The vector processes around the direction of B, at a frequency equal to the resonant frequency and this oscillating magnetic field is picked up by an induction coil producing a signal. The different magnetisation vectors involved in an NMR experiment are shown in figure 2.7.

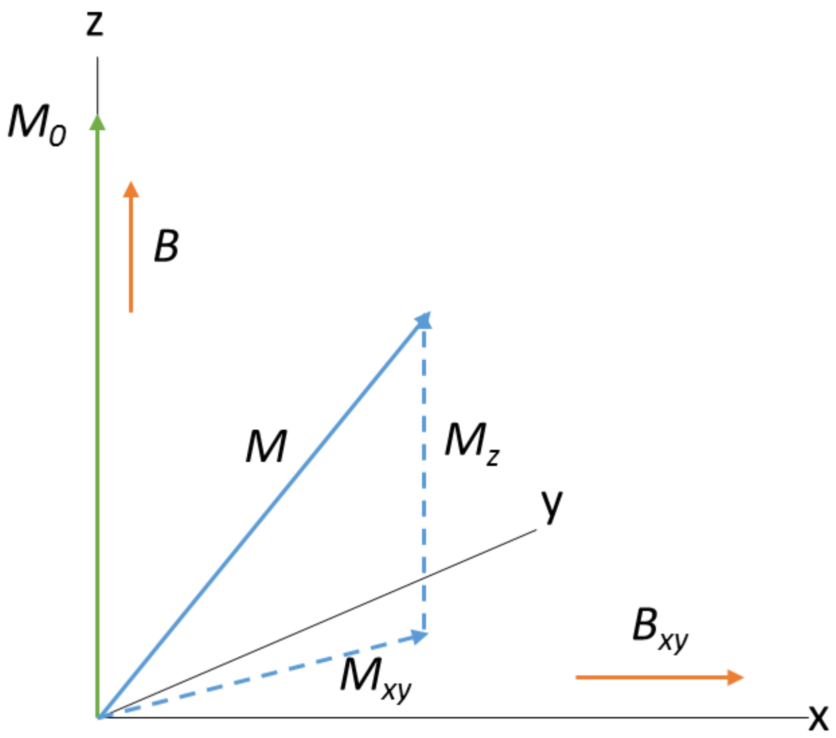

Figure 2.7: The magnetisation vectors associated with NMR experiments. The orange arrows are applied magnetic fields, the green arrow is the equilibrium magnetisation vector, the solid blue arrow is *M*, the overall magnetisation vector after excitation and the dotted blue arrows are the components of *M*.

A greater absorption, and therefore more intense signal, will be observed when the absolute difference in population between the lower energy and higher energy states is higher. Three factors affect this; the total population of nuclei under investigation, which is dependent on the relative abundance of the nucleus compared to other isotopes; the temperature, with higher temperatures populating higher energy states, evening out the populations; and the energy difference between states. Looking at equation 2.20 and bearing in mind the fact that the selection rule for transition between the states is $\Delta m = \pm 1$ it is clear that the energy difference will be higher for higher absolute values of B and γ. As γ is fixed by the isotope under investigation then for greater NMR signal higher magnetic fields are needed.

2.4.1.1. NMR Relaxation

The signal observed in an NMR measurement undergoes two forms of relaxation, spin-lattice relaxation and spin-spin relaxation. Spin-lattice relaxation, given time constant T_1, is the process by which the z component of the magnetization vector, M_z, returns to the equilibrium state, $M_z = M = M_0$. For example, following a 90° pulse the system begins to undergo relaxation governed by equation 2.21:

$$M_z = M_0\left(1 - \mathrm{e}^{t/T_1}\right) \qquad \text{Equation 2.21}$$

Where t is the time since the pulse. Spin-lattice relaxation is caused by the nuclei excited by the pulse losing energy to the surrounding lattice and decaying back to the lower energy state. The rate at which this occurs can be increased due to lattice motions, such as vibrations or diffusion. These motions cause fluctuating magnetic fields in the sample that can induce decay provided the frequency of motion resonates with the transition frequency. Due to the changes in frequencies of motion with temperature, T_1 will also vary.

Spin-spin relaxation, given time constant T_2, is the process by which the x-y component of a samples magnetisation vector M_{xy} decays due to the nuclear spins losing coherence. After excitation out of equilibrium by a 90° pulse, the nuclear spins in a sample will be in phase with overall magnetisation vector M_{xy0}. Due to different nuclei feeling slightly different magnetic fields due to interactions with other spins, each will precess at a different frequency causing the spins to become out of phase. This relaxation is governed by equation 2.22:

$$M_{xy} = M_{xy0}\mathrm{e}^{-t/T_2} \qquad \text{Equation 2.22}$$

2.4.1.2. *Chemical Shifts*

If the magnetic moment of the nucleus and the applied field were the only factors affecting the energy then finding information about the chemical structure would be impossible as all nuclei of the same isotope would resonate at the same frequency. However, the magnetic field at the nucleus is also affected by the presence of electrons around the nucleus which, as moving charges, produce their own induced magnetic field. This field opposes the applied field and so the nucleus “feels” a lower overall magnetic field B_0. This is called shielding of the nucleus. The amount of shielding caused by the electrons highly depends on the local chemical environment and so the same isotope in a different site will experience a different B_O and so resonate at a different frequency than a theoretical isolated nucleus. This is known as the chemical shift of the nucleus. It is the chemical shifts from which information about structure of compounds can be deduced using NMR.

The frequencies of the chemical shifts are dependent on the applied magnetic field and are also very small in comparison to the absorption frequency, v_0. In order to account for these factors the frequency, v, is converted into parts per million (ppm) using equation 2.23:

$$ppm = \frac{v - v_{ref}}{v_0} \times 10^6 \qquad \text{Equation 2.23}$$

Where v_{ref} is the frequency of a reference nuclei which defines 0 ppm and against which all other nuclei are measured. The use of a reference and *ppm* allows absolute values of chemical shift to be reported rather than simply differences and means that reported values should be the same for all spectrometers regardless of their magnetic field strengths.

Because a sample will normally contain the target nucleus in a variety of chemical environments a single frequency of incident photons will not be able to detect all the chemical shifts. To account for this, a pulse of radiation is used which is made up of a range of frequencies with a bandwidth that is inversely proportional to the duration. This allows nuclei of all chemical shifts to be excited simultaneously. The resulting signal contains contributions from the frequencies of all the nuclei that were excited and using a Fourier transform these frequencies and their intensity can be extracted producing the NMR spectrum.[17]

2.4.1.3. Magic Angle Spinning

There are several anisotropic interactions that a nucleus undergoes which leads to broad lines being observed in NMR spectra. These include chemical shift anisotropy, which is caused by the generally non-spherical distribution of electrons around the nucleus; dipolar coupling, which is caused by the interaction of the magnetic moment of one nucleus with another; and quadrapolar coupling, which is caused by the non-spherical charge distribution of nuclei with spins greater than ½. All of these interactions are dependent on the orientation of the nuclear spins with the applied magnetic field B. In the case of a liquid the nuclei are free to move which leads to a time averaging of these anisotropic effects to 0. However, in solid state NMR the nuclei have a fixed orientation relative to B. In a powder sample (as studied in this work) each crystallite is orientated randomly and this leads a large range of chemical shifts for each nuclear site and therefore very broad peaks.

The anisotropic effects all have the same angular dependence (shown in equation 2.24) and can be averaged out by using a technique called magic angle spinning (only partially in the case of quadrapolar couplings). In this technique the sample is spun at an angle $\theta \approx 54.7°$ relative to B, which is the solution to equation 2.24 when $A(\theta)$ is set to zero. This causes a narrowing of the NMR signals from each nuclei allowing information about the individual sites occupied by the nuclei to be derived.

$$A(\theta) = 3\cos^2\theta - 1 \qquad \text{Equation 2.24}$$

2.4.2. Instrumentation

In this thesis solid state ^{23}Na NMR spectra were recorded using a Bruker Avance III HD spectrometer and wideline (non-spinning) probe accommodating samples packed into 5 mm o.d. glass tubes. These spectra were obtained using a solid-echo (i.e., 90° – delay – 90° – acq) with a 0.5 s recycle delay, a 30 µs delay between pulses, and 90° pulses of 2 µs in duration. 512 transients were accumulated for each temperature point. Spectra were referenced to an external sample of aqueous 0.1 M NaCl. These measurements were carried out by David Apperley as part of the Durham University Solid State NMR Service.

Additionally T_1 measurements were carried out with the aid of Cory Widdifield and Paul Hodgkinson for temperatures ranging from 25 to 150 °C at 132.18 MHz using a Bruker Avance III HD spectrometer and a 4 mm (rotor o.d.) magic-angle spinning probe. The saturation-recovery method, using a train of 20 saturation pulses was used on a non-spinning sample. For these measurements a reference sample of solid NaCl was used.

2.5. Impedance Spectroscopy

2.5.1. Theory

Impedance spectroscopy is a technique used to find the electrical properties of materials. An alternating sinusoidal voltage (V) is applied across the sample at a constant angular frequency $\omega=2\pi v$. This produces a current (I) through the material that changes identically with the applied voltage except for a phase shift (φ) which varies with ω. The equations for the applied voltage and the resulting current are given below:[18]

$$V = V_0 \mathrm{e}^{\mathrm{i}\omega t} \qquad \text{Equation 2.25}$$

$$I = I_0 \mathrm{e}^{\mathrm{i}(\omega t+\varphi)} \qquad \text{Equation 2.26}$$

Where t is time and V_0 and I_0 are the maximum amplitudes of V and I. The phase difference between the current and the voltage means that Ohm's Law $V=IR$, where R is resistance, does not apply in the same way as in a direct circuit. Instead, for alternating circuits, a complex quantity called the impedance (Z) is used. Z is given by the following equation:

$$Z = \frac{V_t}{I_t} = \frac{V_0 \mathrm{e}^{\mathrm{i}\omega t}}{I_0 \mathrm{e}^{\mathrm{i}\omega t+\varphi}} = Z_0 \mathrm{e}^{-\mathrm{i}\varphi} = Z_o(\cos\varphi - i\sin\varphi) \qquad \text{Equation 2.27}$$

Where $Z_0 = V_0/I_0$. The impedance contains contributions from not only resistance but also reactive components. These reactive components are the capacitance, C, which is the ability of the sample to store charge and the inductance, *L*, which is the generation of a voltage by the sample in response to a changing current. The real component of the impedance, *Z′*, is related to the resistance of the sample and the imaginary part, *Z′′*, is related to the inductance and capacitance. It is clear from equation 2.27 that if $\varphi = 0$ then the imaginary part will disappear and that $Z' = R = Z_0$. As φ varies with ω, the resistance can be found by taking a series of measurements of the impedance at a range of frequencies. A Nyquist plot of *Z′* against *Z′′* is then made with each point representing a different ω. The plot forms a semicircle and the point at which the *Z′* is crossed gives a value for the resistance *R* of the sample.

In such a plot two or more semicircles are often seen each with its own value for *R*. These represent the responses of different regions of the sample. The capacitance of a material is inversely related to the thickness of the region with the bulk being the thickest and grain boundaries usually second thickest. Therefore by using the relationship $\omega_{max}RC = 1$, where ω_{max} is the frequency at the maximum value of *Z′′* for the semicircle, to calculate the capacitance, the region responsible for the each semicircle can be identified.

It is also common to observe a Warburg response which is seen as a 45° line in the graph at low frequencies. This represents the diffusion of the charge carriers into the sample and is indicative of ionic conduction. These features can be seen in figure 2.8.

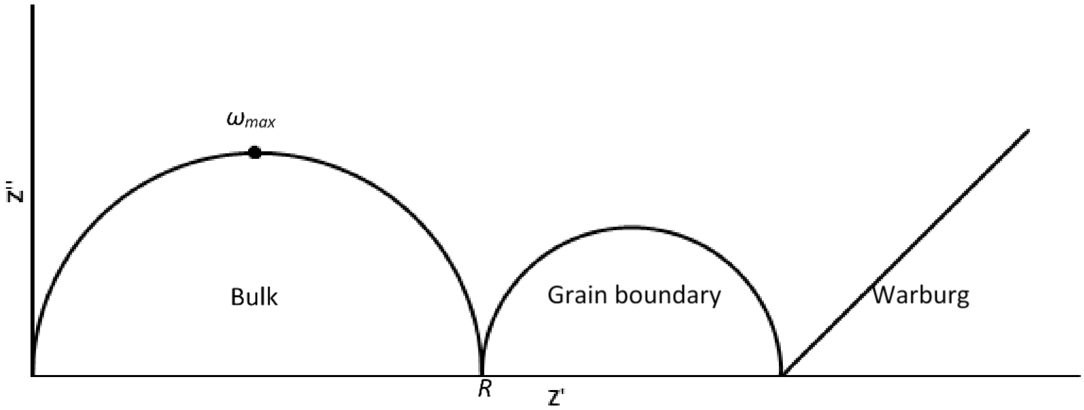

Figure 2.8: A typical Nyquist plot for a sample undergoing impedance spectroscopy showing the responses from different regions and the Warburg response to diffusion effects. R is the resistance of the bulk region and ω_{max} is the frequency at which the capacitance of the bulk region can be calculated.

The resistance of a sample depends on its dimensions and so the conductivity, σ, is calculated using equation 2.28 to allow comparison between samples:

$$\sigma = \frac{l}{RA} \qquad \text{Equation 2.28}$$

Where l is the thickness of the sample and A is its area. To find the activation energy, E_a, for conduction in the sample, the conductivity is recorded as a function of temperature T. The conductivity follows an Arrhenius relationship:

$$\sigma = \frac{\sigma_0}{T} \mathrm{e}^{-\frac{E_a}{RT}} \qquad \text{Equation 2.29}$$

Where σ_o is the pre-exponential factor and R is the gas constant. Therefore a plot of ln(σT) against 1000/T has a gradient of $-E_a/R$ allowing the activation energy to be determined.[19]

2.5.2. Instrumentation

Measurements of impedance were taken in air using a Solartron 1260A analyser over frequency range 0.1 Hz to 10 MHz with voltage amplitude of 100 mV. To observe the variation of impedance with temperature measurements were taken every 25 °C up to 800 °C, beginning from the temperature at which the sample conductivity was high enough to produce a reading. The sample temperature was recorded using an S type thermocouple.

2.5.3. Sample Preparation

Approximately 0.4 g of sample was first ground in a mortar and pestle and then pressed into pellet of diameter 10 mm, then fired at the synthesis temperature of that particular sample for 12 hours to increase density to at least 75 % of the expected density given by Rietveld refinement. The pellet was then weighed again and its thickness and diameter recorded with a Vernier calliper. The sample was coated with platinum paste on both sides and attached to platinum electrodes on a Probostat cell. To ensure firm attachment the cell with the sample was then fired at 800°C for 30 minutes.

2.6. Computational Methods

2.6.1. Theory

In order to model physical and chemical systems and calculate their properties such as ground state energy, equilibrium structure, and dynamics, two broad categories of computational techniques can be defined, classical and *ab initio*, based on their underlying theoretical basis.

2.6.1.1. Classical Methods

One method of simulating chemical systems involves the use of classical mechanics in determining the behaviour of atoms. In this approach each atom is modelled as a charged particle with its bonds described as spring-like oscillators whose strength is given by interatomic force fields. The force fields are made up of two potential energy contributions, bonding and nonbonding. The bonding contribution is the sum of bond energies, bond angle energies and torsion angle energies and contributes to atoms linked by covalent bonds. The nonbonding contribution models longer range electrostatics using a Coulomb potential and van der Waals forces using, for example, a Lennard Jones potential.

The interatomic potentials in classical modelling are approximations derived from either empirical data, such as bond lengths from XRD and force constants from vibrational spectroscopy, or *ab initio* calculations. Due to these approximations, while classical calculations are relatively fast compared to *ab initio* methods, they may also lose some accuracy especially when used to model a system that is very different to that used to derive the potentials. In addition, because the atomic bonds are defined at the start of the calculations, these methods cannot simulate bond breaking and formation. While classical calculation have been used extensively in literature and can provide some information about likely ionic conduction pathways by looking at the overlap of the regions visited by oxygens in different sites (Chapter 1, section 1.3.2), these methods were not used in this work as the ability of oxygen atoms to move between sites was desired. Instead, *ab initio* quantum mechanical methods were used in the form of density functional theory calculations allowing full observation and quantisation of oxygen movement through various pathways.

2.6.1.2. Ab Initio Methods

Ab initio (meaning ‘from first principles’) methods are calculations in which quantum mechanics and physical constants are used to calculate forces continuously during the simulations, rather than the empirically fitted force fields used in classical methods.[20]

In order to calculate atomic forces using quantum mechanics the Schrödinger equation for the system must be solved. However, for systems more complex than a hydrogen atom this cannot be solved analytically and so a series of approximations must be made. The first of these is the Born-Oppenheimer approximation which states that, due to the large mass differences between nuclei and electrons, the electrons in a system can be said to react instantaneously to a change in the positions of nuclei. This makes the two motions separable and so the total wavefunction of a system Ψ can be written as the product of the electronic ψ_e and nuclear ψ_n wavefunctions.

$$\Psi = \psi_e \times \psi_n \qquad \text{Equation 2.30}$$

This allows the electronic wavefunction to be calculated with all nuclei in fixed coordinates providing an external potential V_n. The electronic wavefunction can then be used to generate a potential which acts as a parameter in the calculation of the nuclear wavefunction. The total electronic ground state energy E_0 is given in equation 2.31:[21]

$$E_0 = \langle \psi_0 | T + V_n + E_c + E_{ex} | \psi_0 \rangle \qquad \text{Equation 2.31}$$

Where T is the kinetic energy term, E_c is the classical electron coulomb interaction and E_{ex} is a non-classical exchange-correlation energy.

Calculating the total electronic wavefunction by solving the Schrödinger equation is nevertheless a very computationally demanding task with each electron having its own wavefunction with four degrees of freedom. Hartree-Fock is one method that attempts to do this, but neglects any electron correlation effects except those required by the Pauli Exclusion Principle.[22] In addition to this simplification Hartree-Fock calculations are infeasible to carry out in a reasonable time for systems with large numbers of electrons such as those involving many transition metal atoms.

2.6.1.3. Density Functional Theory

Density functional theory (DFT) is an alternative method of calculating the ground state energy that does not involve calculating a many-body wavefunction. Instead DFT only requires that the ground state electron density $\rho(\boldsymbol{r})$ be used.[21] This gives the probability of finding an electron in a volume element d$\boldsymbol{r}$ and is a function of only three spatial variables no matter the number of electrons. The relationship between the ground state energy and the electron density is stated in two theorems proved by Hohenberg and Kohn.[23] The first theorem states that the total energy of a system is a unique functional of the electron density. The second theorem states that the electron density that minimises the total energy is the exact ground state density. These two theorems mean that the ground state energy (and therefore all ground state properties) of a many particle system is a uniquely defined functional of the ground state electron density and can be determined by minimisation of the energy functional with respect to the electron density (keeping the total number of electron in the system constant). This means that equation 2.31 can now be written as:

$$E_0(\rho) = T(\rho) + V_n(\rho) + E_c(\rho) + E_{ex}(\rho) \qquad \text{Equation 2.32}$$

E_0 can be approximated by using the Kohn-Sham method.[24] Kohn and Sham showed that the real density functionals in equation 2.32 can be written as functionals of a fictitious non-interacting system of electrons moving in an external potential and then solving a one particle Schrödinger equation for each electron. The electron density $\rho(\boldsymbol{r})$ is obtained by summing over the Kohn-Sham single-electron orbitals ϕ_i:

$$\rho(\boldsymbol{r}) = \sum_{i=1}^{n} |\phi_i|^2 \qquad \text{Equation 2.33}$$

The forms of the potential due to the nuclei ($V_n(\rho)$) and the coulomb interactions ($E_c(\rho)$) are known:[25]

$$V_n(\rho) = \int V_n(\boldsymbol{r})\rho(\boldsymbol{r})d\boldsymbol{r} \qquad \text{Equation 2.34}$$

$$E_c(\rho) = \iint \frac{\rho(\boldsymbol{r})\rho(\boldsymbol{r}')}{\boldsymbol{r} - \boldsymbol{r}'} d\boldsymbol{r}d\boldsymbol{r}' \qquad \text{Equation 2.35}$$

However, the forms that the kinetic energy term $T(\rho)$ and the exchange-correlation energy $E_{ex}(\rho)$ take are not known although $T(\rho)$ can be split into two parts, an interacting part and a non-interacting part, $T_s(\rho)$, which has the form:

$$T_s(\rho) = -\frac{1}{2}\sum_{i=1}^{n} \nabla_i^2 \phi_i \qquad \text{Equation 2.36}$$

The remaining interacting part is added to the $E_{ex}(\rho)$ and must be estimated using one of several approximations. One method of estimating is the Local Density Approximation (LDA) in which for a small region the energy is taken to be the same as that for a homogenous electron gas of the same density.[24] This approximation only accounts for the density at the coordinates where the functional is evaluated. An alternative approximation called the Generalised Gradient Approximation (GGA)[26] which takes into account the gradient of the density at those coordinates and is more accurate for systems in which the density is widely varying.

For all the calculations in this thesis the wavefunctions ϕ_i were calculated either through the VASP[27] or the CASTEP software[28], using projector augmented waves (PAW) pseudopotentials.[29] The pseudopotentials model the atoms as a combination of the nuclei and core electrons with a set of valence electrons. The core electrons are considered non-moving and with the nucleus form a single potential. This allows the calculation of only the valence electron pseudo-wavefunctions in a way that can be described with a smaller set of plane waves. The specific parameters of each calculation are given in the experimental sections of the relevant chapter.

2.6.2. Techniques

2.6.2.1. Geometry Optimisation

In geometry optimisation calculations the goal is to find the equilibrium structure of the simulated material by minimising the forces acting on each atom. This should also lead to a single point energy minimum. The way this is achieved for both classical and *ab initio* methods is by following an iterative algorithm such as the conjugant gradient method[30] used in VASP and the BFGS (Broyden–Fletcher–Goldfarb–Shanno) algorithm[31] used by CASTEP. The forces acting on each atom in the starting configuration are calculated. If these forces do not fall below some predefined tolerance then each atom is moved by a small increment in a way that is predicted to reduce these forces. Then the forces acting on this new configuration are calculated as well as the energy change between the two configurations and the process is repeated until the forces and the energy changes fall below their tolerances. The final atomic positions should therefore represent a minimum in the potential energy surface giving the equilibrium structure.

2.6.2.2. Molecular Dynamics

Molecular dynamics (MD) calculations simulate the movement of atoms step by step over a simulated period of time. They do this by applying Newton’s laws of motion to each atom starting from the initial positions and recalculating at every time step to give a continuous trajectory of each atom that can show long range diffusion as well as vibrations and rotations of atoms and molecules. This can be used to calculate diffusion pathways of oxygen atoms in oxide ion conductors. One important aspect to the use of molecular dynamics is the fulfilment of the ergodic hypothesis. This states that the time average of a variable (as would be calculated by molecular dynamics) is the same as the ensemble average (the average over all possible states at a single point in time, as would be seen in a macroscopic measurement). This means that in order to get experimentally relevant information from MD the simulated time must be long enough for the particles to pass through a statistically representative number of states.[32]

Unlike geometry optimisation in which the simulated temperature is effectively 0 K (i.e. atoms have no velocity). A dynamics calculation requires an initial temperature to be defined from which initial velocities of each atom are assigned randomly according to a Maxwell-Boltzmann distribution. By using the initial positions $\boldsymbol{r_0}$, velocities $\boldsymbol{v_0}$ and accelerations $\mathbf{a_0}$ ($\boldsymbol{F_0}$/atomic mass) of each atom, new positions and velocities after one time step of length *t* can be easily calculated (equations 2.37 and 2.38):

$$\boldsymbol{r_t} = \boldsymbol{r_0} + \boldsymbol{v_0}t + \frac{1}{2}\boldsymbol{a_0}t^2 \qquad \text{Equation 2.37}$$

$$\boldsymbol{v}_t = \boldsymbol{v_0} + \boldsymbol{a_0}t \qquad \text{Equation 2.38}$$

After each time step the forces on each atom are recalculated and the process is repeated for the next step.

The *ab initio* molecular dynamics (AIMD) simulations in this thesis were calculated using the VASP program.[27] An NVT ensemble was used meaning that the number of atoms, the volume of the simulation box and the average temperature of the simulation was kept constant. The temperature was kept constant by exchanging energy with a Nosé-Hoover thermostat.[33] The time steps are reported in the individual analysis chapters. PAW pseudopotentials[29] were used with the GGA PBE (Perdew-Burke-Ernzerhof) functionals.[26] Due to the large sizes of the unit cells used the calculations were sampled at the gamma point. Analysis was performed both in MDANSE[34] and with my own python codes. Cloud plots were produced in LAMP.[12]

A common method of analysis of the AIMD trajectories is the production of mean square displacement (MSD) curves. In MDANSE[34] (used in this thesis) the mean square displacement of one individual atom $\langle r^2 \rangle$ after a number of frames *m* is calculated using equation 2.39:

$$\langle r^2 \rangle = \frac{1}{N-m} \sum_{k=0}^{N-m-1} (r_{k+m} - r_k)^2 \qquad \text{Equation 2.39}$$

Where *N* is total number of frames in the trajectory. The total MSD is then the average MSD over all atoms of interest. It can be seen from equation 2.39 that $\langle r^2 \rangle$ is calculated by averaging over all pairs of frames r_{k+m} and r_k separated by the number of frames *m*. As the number of possible pairs (*N*-*m*) is smaller as *m* gets closer to *N* the MSD value is averaged over a smaller number of data points leading to poorer statistics towards the end of a simulation. This can lead to the MSD value fluctuating wildly in this region.

In addition to this the AIMD trajectories were also used to produce phonon density of states $G(\omega)$. In MDANSE this is calculated using equations 2.40 and 2.41:

$$G(\omega) = \frac{1}{2\pi}\sum_{0}^{t_{tot}} \mathrm{e}^{\mathrm{i}\omega t}\langle C_v(t)\rangle \qquad \text{Equation 2.40}$$

$$\langle C_v(t)\rangle = \langle \boldsymbol{v_i}(t_0).\boldsymbol{v_i}(t_0 + t)\rangle_{t_0,i} \qquad \text{Equation 2.41}$$

Where, $\boldsymbol{v}_i(t_0)$ is the velocity of atom i at initial time t_0, $\boldsymbol{v}_i(t_0 + t)$ is the velocity of atom i at time $t_0 + t$, and t_{tot} is the total time length of the simulation. $<C_v(t)>$, the velocity autocorrelation function, is averaged over all atoms i in the simulation and all possible initial times t_0.

2.6.2.3. Phonon Calculations

Computational simulations were also used to calculate phonon density of states.[35] The first step in this calculation is the production of a Hessian matrix, $\mathbf{D}(\boldsymbol{r})$ (a matrix whose elements are the force constants of the ions). This matrix is calculated assuming the harmonic approximation (all ions in the crystal act as harmonic oscillators), which is valid as long as the ions remain close to their equilibrium positions as is generally the case for phonons. The Fourier transform of this matrix, the dynamical matrix $\mathbf{D}(\boldsymbol{q})$, can give the values of the frequencies, ω, and eigenvectors, ξ, of the normal modes through its eigenvector equation 2.42:

$$\omega^2\xi = \mathbf{D}(\boldsymbol{q})\xi \qquad \text{Equation 2.42}$$

The knowledge of both the eigenvalues and eigenvectors allows the phonon dispersion relation, $\omega(\boldsymbol{q})$ to be derived. This is integrated over all $\boldsymbol{q}$ to give the phonon density of states which is the number of modes within a certain energy range.

In this thesis phonon calculations were carried out in CASTEP. To calculate the force constants for use in the Hessian matrix the finite displacement method was employed.[36] In this method an atom is moved by a small amount in the x direction and the resulting forces on all other atoms calculated. This is repeated in y and z (symmetry equivalent displacements need not be repeated). From the resulting forces and the known displacement a force constant may be calculated. This is repeated for all atoms in the cell.

2.6.2.4. *Electron Localisation Function*

Computational methods can also be used to determine the localisation of electrons in a system which can be used to describe electronic properties such as lone pairs. The electron localisation function (ELF), $\eta(\boldsymbol{r})$ is defined as follows:[37]

$$\eta(\boldsymbol{r}) = \frac{1}{1 + {X_{BE}}^{2}(\boldsymbol{r})} \qquad \text{Equation 2.43}$$

$$X_{BE}(r) = \frac{D(\boldsymbol{r})}{D_h(\boldsymbol{r})} \qquad \text{Equation 2.44}$$

Where $D(\boldsymbol{r})$ is the probability density of finding and electron with the same spin at distance $\boldsymbol{r}$ from another electron, and $D_h(\boldsymbol{r})$ is the equivalent for a uniform electron gas. An electron is said to be more localised if $D(\boldsymbol{r})$ is low, however $D_h(\boldsymbol{r})$ has been defined arbitrarily and therefore the ELF can only be said to be a relative measure of electron localisation, and from equation 2.43 can only take values between 0 and 1.

2.7. References

1. A. K. Cheetham and P. Day, *Solid State Chemistry Techniques*, Oxford University Press, New York, 1987.
2. A. R. West, *Solid State Chemistry and its Applications*, John Wiley & Sons Ltd., Chichester, 1984.
3. L. E. Smart and E. A. Moore, *Solid State Chemistry: An Introduction*, CRC Press, London, 2012.
4. F. Hippert, E. Geissler, J. L. Hodeau, E. Lelièvre-Berna and J.-R. Regnard, *Neutron and X-ray Spectroscopy*, Springer Science & Business Media, 2006.
5. C. Giacovazzo, *Fundamentals of Crystallography*, Oxford University Press, New York, 2002.
6. A. A. Coelho, J. S. O. Evans, I. R. Evans, A. Kern and S. Parsons, *Powder Diffraction*, 2012, **26**, S22-S25.
7. P. Thompson, D. E. Cox and J. M. Hastings, *Journal of Applied Crystallography*, 1987, **20**, 79-83.
8. G. S. Pawley, *Journal of Applied Crystallography*, 1981, **14**, 357-361.
9. H. M. Rietveld, *Journal of Applied Crystallography*, 1969, **2**, 65-71.
10. B. H. Toby, *Powder Diffraction*, 2012, **21**, 67-70.
11. G. L. Squires, *Introduction to the Theory of Thermal Neutron Scattering*, Cambridge University Press, New York, 2012.
12. D. Richard, M. Ferrand, G. and J. Kearley, *Journal of Neutron Research*, 1996, **4**, 33-39.
13. IN6 Instrument Layout, https://www.ill.eu/instruments-support/instruments-groups/instruments/in6/description/instrument-layout/, (accessed September, 2017).
14. IN16b Instrument Layout, https://www.ill.eu/instruments-support/instruments-groups/instruments/in16b/description/instrument-layout/, (accessed September, 2017).

15. B. Frick and M. Gonzalez, *Physica B: Condensed Matter*, 2001, **301**, 8-19.
16. C. T. Chudley and R. J. Elliott, *Proceedings of the Physical Society*, 1961, **77**, 353-361.
17. D. C. Apperley, R. K. Harris and P. Hodgkinson, *Solid-State NMR Basic Principles and Practice*, Momentum Press, New York, 2012.
18. D. C. Sinclair, *Bol Soc Esp Ceram V*, 1995, **34**, 55-65.
19. X. Kuang, M. A. Green, H. Niu, P. Zajdel, C. Dickinson, J. B. Claridge, L. Jantsky and M. J. Rosseinsky, *Nature Materials*, 2008, **7**, 498-504.
20. G. H. Grant and W. G. Richards, *Computational chemistry*, Oxford University Press, 1995.
21. T. D. Kühne, *Wiley Interdisciplinary Reviews: Computational Molecular Science*, 2014, **4**, 391-406.
22. R. M. Martin, *Electronic structure: basic theory and practical methods*, Cambridge university press, 2004.
23. P. Hohenberg and W. Kohn, *Physical Review*, 1964, **136**, B864-B871.
24. W. Kohn and L. J. Sham, *Physical Review*, 1965, **140**, A1133-A1138.
25. M. Freyss, *State-of-the-Art Report on Multi-scale Modelling of Nuclear Fuels*, 2015, 225.
26. J. P. Perdew, K. Burke and M. Ernzerhof, *Phys Rev Lett*, 1996, **77**, 3865-3868.
27. G. Kresse and J. Furthmüller, *Computational Materials Science*, 1996, **6**, 15-50.
28. S. J. Clark, M. D. Segall, C. J. Pickard, P. J. Hasnip, M. I. J. Probert, K. Refson and M. C. Payne, *Z Anorg Allg Chem*, 2005, **220**, 567-570.
29. G. Kresse and D. Joubert, *Physical Review B*, 1999, **59**, 1758-1775.
30. H. B. Schlegel, *Journal of Computational Chemistry*, 1982, **3**, 214-218.
31. B. G. Pfrommer, M. Côté, S. G. Louie and M. L. Cohen, *Journal of Computational Physics*, 1997, **131**, 233-240.
32. M. E. Tuckerman and G. J. Martyna, *The Journal of Physical Chemistry B*, 2000, **104**, 159-178.
33. W. G. Hoover, *Physical Review A*, 1985, **31**, 1695-1697.
34. G. Goret, B. Aoun and E. Pellegrini, *Journal of Chemical Information and Modeling*, 2017, **57**, 1-5.
35. A. Togo and I. Tanaka, *Scripta Materialia*, 2015, **108**, 1-5.
36. G. Kresse, J. Furthmüller and J. Hafner, *EPL (Europhysics Letters)*, 1995, **32**, 729.
37. A. D. Becke and K. E. Edgecombe, *The Journal of Chemical Physics*, 1990, **92**, 5397-5403.

Chapter 3. Investigations into Fast Ion Conduction in Doped $SrSiO_3$, $SrGeO_3$ and $BaZrSi_3O_9$

3.1. Abstract

In this chapter the results of a variable temperature solid state ^{23}Na NMR investigation into nominal $Sr_{0.6}Na_{0.4}SiO_{2.8}$ are reported. These results show conclusively that the charge carriers in the material are Na^+ ions rather than O^{2-}. The preparation, characterisation and conductivity properties of the series $Sr_{1-x}La_xSiO_{3+0.5x}$ and $Sr_{1-x}La_xGeO_{3+0.5x}$ are reported. Additionally, the attempted doping of $BaZrSi_3O_9$ with Y^{3+} and Ce^{3+} is also reported along with the resulting conductivity properties.

3.2. Introduction and Background

Due to the low cost and ready availability of SiO_2, the successful creation of a silicate based oxide ion conductor suitable for use in applications is a desirable goal. One example of such a material is strontium silicate ($SrSiO_3$) which, along with the germanate analogue ($SrGeO_3$), received considerable attention due to the very high conductivities reported for these materials on doping with K^+ and Na^+.[1-4] While these results later proved to be incorrect,[5-8] (see section 3.2.2) further investigation of $SrSiO_3$ as well as materials with similar structural features such as $BaZrSi_3O_9$, using dopant cations which are not likely to be the mobile species themselves, is warranted to allow potential development of a silicate oxide ion conductor viable for application.

3.2.1. Structure of $SrTO_3$ (T = Si/Ge)

The parent compounds $SrSiO_3$ and $SrGeO_3$ have been reported to have several different crystalline forms, including triclinic ($P\bar{1}$)[9] and hexagonal ($P\bar{6}2m$)[10] for $SrGeO_3$, and high pressure polymorphs with triclinic ($P\bar{1}$) and monoclinic ($P2_1/c$) space groups for $SrSiO_3$.[11] However, the structure of interest in terms of oxide ion conduction is a monoclinic phase with space group C2/c that exists at room temperature and pressure and has been reported for both materials.[12, 13] This monoclinic structure (shown in figure 3.1a) consists of layers of Sr^{2+} ions in the *ab* plane that are each coordinated above and below by four oxygen atoms. These oxygen atoms belong to layers of isolated T_3O_9 clusters made up of three corner-sharing TO_4 tetrahedra (figure 3.1c). These two types of layers alternate throughout the structure; however, as shown in figure 3.1b, the T_3O_9 clusters do not lie above one another in the stacking direction, instead eclipsing every seventh layer giving rise to a structure that could be said to be six-layered.

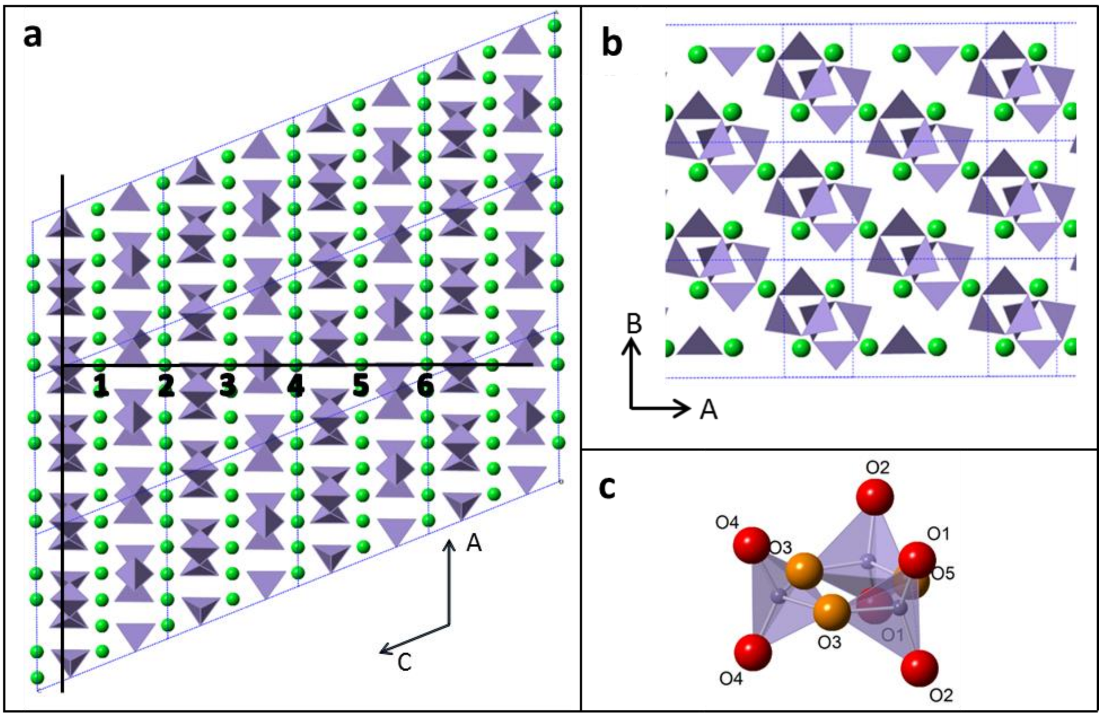

Figure 3.1: a) Monoclinic C2/c structure of $SrTO_3$ (T = Si, Ge) shown looking down the b axis, Sr^{2+} ions are shown in green and T_3O_9 clusters are shown in purple. The eclipsing of the layers is shown. b) A view of two layers in the monoclinic structure of $SrTO_3$ (T = Si, Ge) perpendicular to the ab plane. c) T_3O_9 cluster within the monoclinic $SrSiO_3$ structure made up of three corner sharing SiO_4 tetrahedra. Purple atoms represent Si/Ge atoms, orange represent bridging oxygen atoms and red are terminal oxygen atoms.

In addition, an alternative, more disordered structure has been proposed by Evans *et al.*[6] who observed discrepancies between experimentally measured X-ray diffraction patterns and the monoclinic model. They proposed a trigonal model for the $SrSiO_3$ structure with cell parameters: a = 4.12 Å, c = 10.12 Å, V = 148.88 $Å^3$ and space group $P\bar{3}1$ presumed to be formed due to kinetic effects. This structure can be seen in figure 3.2. The cell parameters are related to those of the monoclinic cell by the relations: $a_t = (1/3)a_m$, $b_t = (\surd 3/3)b_m = a_t$, $c_t = c_m$, and $V_t = (1/6)V_m$. The structure is closely related to the monoclinic structure with layers of Sr atoms and Si_3O_9 clusters forming perpendicular to the *ab* plane (figure 3.2a); however, each Si and bridging O site is split between three sites all one third occupied (figure 3.2b). Within a single layer it is necessary for the Si_3O_9 groups to be ordered as in the monoclinic model (figure 3.1b) in to prevent the overlap of atoms. This means that the trigonal structure arises due to the lack of long range interlayer ordering.

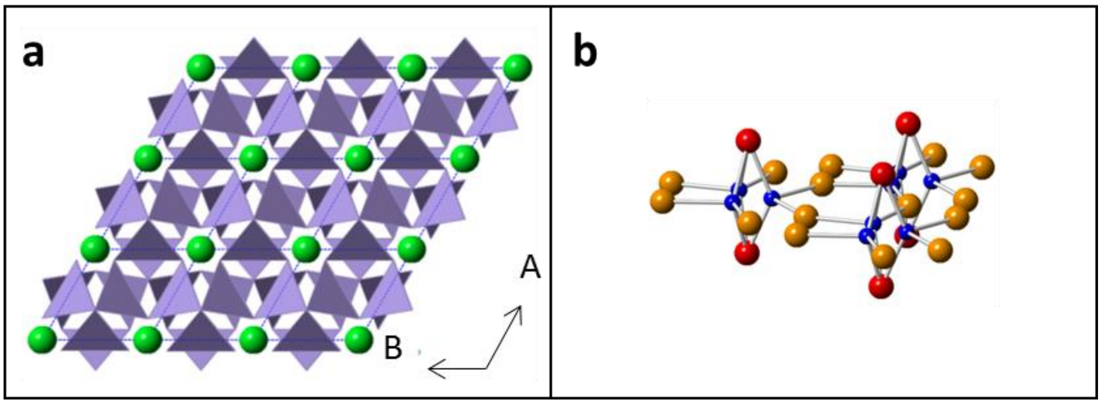

Figure 3.2: a) A view of two layers in the trigonal structure of $SrSiO_3$ proposed by Evans *et al.*[6] perpendicular to the *ab* plane. b) Disordered S_3O_9 ring in the trigonal structure of $SrSiO_3$ showing all 1/3 occupied sites. Green sphere represent Sr atoms, purple tetrahedra represent SiO_4 tetrahedra, blue spheres disordered Si atoms, red sphere represent terminal O atoms and orange spheres represent disordered bridging O atoms.

3.2.2. Reports of Oxide Ion Conductivity in $SrSiO_3$ and $SrGeO_3$ Based Materials

The first report that these materials could form the basis for a new class of oxide ions conductors was published in 2012 by Goodenough and Singh.[1] They argued that substituting Sr^{2+} with K^+ would lead to the formation of terminal oxygen vacancies in the T_3O_9 clusters (shown in red in figure 3.1b) that could not be eliminated by corner sharing with adjacent clusters due to steric hindrance from the Sr^{2+} and K^+ ions. This would lead to oxide ion conduction *via* vacancy hopping from cluster to cluster. However, neither evidence for the formation of terminal oxygen vacancies nor the precise nature of this vacancy hopping mechanism were given and as the distance between terminal O sites is ≈ 4 Å in $SrSiO_3$[13] it seems unlikely that such a mechanism is feasible. The highest conductivity reported in this paper was 1.04×10^{-2} S cm^{-1} for $Sr_{0.8}K_{0.2}Si_{0.5}Ge_{0.5}O_{2.9}$ at 625 ˚C, putting the material firmly over the threshold for a good oxide ion conductor.

In 2013 the authors published another paper[2] where they claimed to have synthesised a series of Na-doped $SrSiO_3$ materials. The $Sr_{1-x}Na_xSiO_{3-0.5x}$ series showed a linear increase in conductivity up to nominal $x = 0.45$ which was the highest doping level reported. These materials showed a much higher conductivity than most other oxide ion conductors with $\sigma > 10^{-2}$ S cm^{-1} being achieved at temperatures as low as 525 °C for the $x = 0.4$ sample. The formation of the $Sr_{1-x}Na_xSiO_{3-0.5x}$ series was confirmed through neutron diffraction experiments.[3] However although the occupancies of Sr/Na on each site were refined it is not clear whether the total occupancies were constrained to fit the nominal stoichiometry expected. The analysis showed that vacancies were formed and were distributed over all the oxygen sites. The number of vacancies increased as the sodium proportion increased from

20 % to 40 % as might be expected if more doping occurred. The conductivity of these materials was shown to remain stable over a 200 hour period in air and a reducing atmosphere of 5 % H_2-N_2 and also showed no change with varying partial pressure of oxygen from 10^{-30} atm to 1 atm.[4] This was claimed to show that the material is a pure oxide ion conductor and electrical insulator even though it does not preclude the possibility of other ionic charge carriers such as Na^+.[8] The material was also shown to be compatible with various anode and cathode materials[2] and have a low thermal expansion coefficient of 12.1×10^{-6} K^{-1}.[4] All these attributes appeared to make this material an excellent candidate for an IT-SOFC.

However, in 2014 a paper was published by Bayliss *et al.*[5] that called into question some of the claims made in regards to K^+ and Na^+ doping.[1, 2] They pointed out that alkali metals are usually avoided as dopants as the possibility of conduction *via* dopant ions is likely, and that Goodenough's papers show no evidence that O^{2-} is the primary charge carrier. Another problem is the apparent lack of dopant defect interactions in the materials instead showing a linear increase in conductivity up to 45 % Na^+. The authors carried out their own neutron powder diffraction (NPD) experiments on a sample of nominal composition $Sr_{0.8}K_{0.2}Si_{0.5}Ge_{0.5}O_{2.9}$ and found that that the conductivity of the sample was significantly lower than that reported by Goodenough. Additionally, better Rietveld refinement fits to their NPD data could be obtained using a $SrSiO_3$ structural model without including K^+. Oxygen tracer diffusion experiments led to the conclusion that the material shows no oxygen conductivity. These two observations suggest that conductivity could be caused by K^+ mobility in an amorphous phase which was further supported by TOF-SIMS chemical ion mapping which showed that two phases were present in the material, one high in K^+ and low in Sr^{2+} and one with the reverse.

A paper published by Evans *et al.*[6] showed similar problems with the nominally Na-doped materials. NPD Rietveld refinements on the $Sr_{1-x}Na_xSiO_{3-0.5x}$ (x = 0.1, 0.2, 0.3, 0.4) series showed much lower proportions of Na^+ than expected from the nominal stoichiometry (e.g. the nominally $Sr_{0.6}Na_{0.4}SiO_{2.8}$ sample gave an actual Na^+ level of 0.06(2)). As excellent fits could be obtained using a model of a single crystalline phase based on $SrSiO_3$ this indicates that most of the Na^+ must be present in an amorphous phase. This possible small level of doping means that a very low number of O^{2-} vacancies would be created, and therefore that the observed conduction was unlikely to be due to a Na-doped $SrSiO_3$ phase. The presence of two phases was confirmed with SEM EDX which showed a low Na^+ phase and a high Na^+ phase. ^{23}Si solid state NMR spectra of the nominally Na-containing materials showed in two peaks, a sharp peak from a crystalline phase and a much broader peak indicating an amorphous phase. The intensity of this amorphous peak relative to the crystalline peak was observed to increase with increasing nominal Na^+ doping level. Finally, the quantification of this amorphous content was carried out. XRD patterns were collected for the nominally Na-doped materials mixed with a known proportion of a crystalline Si standard. By dividing this known proportion of standard by the proportion given in Rietveld refinement the total proportion of crystalline material in the sample can be found with the remaining proportion being amorphous content. The weight percentage of the amorphous phase was shown to increase linearly with nominal Na^+ doping level and correlate with increased conductivity. All of these results indicated that little, if any, Na^+ doping occurs into $SrSiO_3$. Instead an amorphous phase is formed, that due to the weight percentages was concluded to be $Na_2Si_2O_5$, is responsible for the observed conductivity. Additional computational simulations using CASTEP and VASP performed at the Institut Laue-Langevin in Grenoble show that doping $SrSiO_3$ with Na is energetically unfavourable. Additionally, if it were to occur, then ab-initio molecular dynamics showed that diffusion of O^{2-} in the material was low compared to that of Na^+.[14]

These results were later confirmed in other papers. Tealdi *et al.*[7] mainly confirmed results of Evans *et al.*,[6] although they also showed that the Arrhenius plots for the conductivity of the nominally doped samples showed similar gradients to that of amorphous $Na_2Si_2O_5$ reported by Kaps[15] further supporting the likely identity of the amorphous phase. They confirmed this by slow cooling a sample of nominally 45 % Na-doped $SrSiO_3$, which caused the amorphous phase to crystallise, allowing it to be identified as α-$Na_2Si_2O_5$ *via* XRD. Bayliss *et al.*[8] reported results of density functional theory calculations that indicted that vacancy formation was energetically unfavourable, that vacancies were unlikely to move if they did indeed form and that doping would cause lattice expansion which goes against the observed expermental evidence.

3.2.3. Structure of $BaZrSi_3O_9$

Another material with potential to make a useful silicate based oxide ion conductor is bazirite ($BaZrSi_3O_9$) which was first documented in the 1970s[16] and is isostructural with benitoite ($BaTiSi_3O_9$)[17] the structure of which can be seen in figure 3.3.[18] The structure is similar to that of $SrSiO_3$ in that it contains alternating layers of Ba^{2+} and Ti^{4+} cations and isolated $Si_3O_9^{6-}$ clusters in the *ab* plane. However, it has the hexagonal space group $P\bar{6}c2$ rather than the monoclinic structure of $SrSiO_3$. The presence of these isolated Si_3O_9 clusters in a similarly layered structure as in $SrSiO_3$ (although eclipsing after two layers rather than six), that attracts interest in bazirite, due to the potential to prepare good silicate ionic conductors by suitable doping. Interest in $BaZrSi_3O_9$ has previously been focused on creating phosphors by doping with small amounts of trivalent rare earth metal cations including Bi,[19] Ce,[20] Eu, Sm, Dy, Tb and Pr[21, 22] on the Ba^{2+} site. Doping with larger amounts of trivalent atoms onto the Ba site therefore may create interstitial oxygen *via* charge balancing leading to oxide ion conductivity. Additionally, doping the Zr^{4+} site has also been successfully carried out with Cr^{3+},[23] indicating that the creation of vacancies may also be possible.

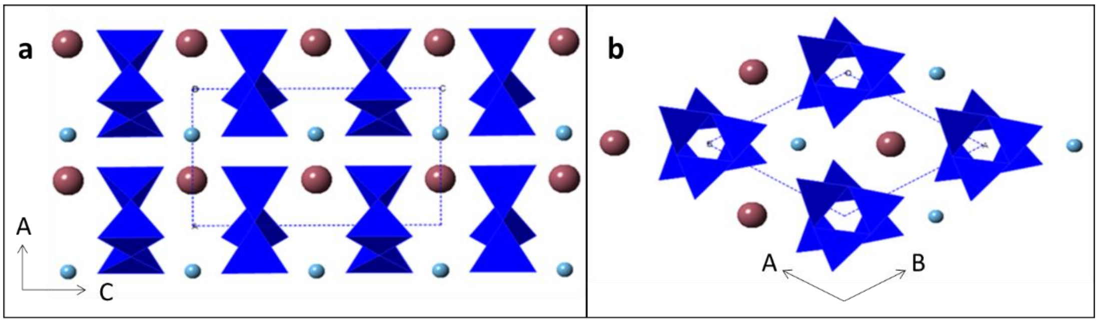

Figure 3.3: Structure of $BaTiSi_3O_9$ which is isostructural with $BaZrSi_3O_9$. Brown spheres represent Ba atoms, grey-blue spheres represent Ti/Zr atoms and blue tetrahedra represent Si_3O_9 clusters. a) The view down the *b*-direction showing the layered structure in the *ab* plane. b) The view down the *c*-direction showing the eclipsing of the Si_3O_9 clusters.

3.2.4. Objectives of This Work

In order to confirm the identity of the charge carriers in the nominally Na-doped $SrSiO_3$ materials a solid state ^{23}Na NMR study was undertaken in order to provide the first direct evidence of Na^+ mobility. Although it has been shown that K^+ and Na^+ doping of $SrSiO_3$ does not produce viable oxide ion conductors, these materials (and silicates in general) are still of interest in the development of oxide ion conductors due to the low cost and ready availability of SiO_2. The successful doping of $SrGeO_3$ with 5 % La^{3+} has been reported before,[24] and computational simulations show that doping with La^{3+} in order to form interstitial oxygen atoms is energetically favourable in both $SrSiO_3$ and $SrGeO_3$ and that these oxygen atoms are mobile which give rise to conduction.[14] Based on this, the synthesis of a series of materials with the form $Sr_{1-x}La_xSiO_{3+0.5x}$ was attempted for x=0 0.05, 0.10, 0.15 and 0.20 in order to determine whether they would make suitable oxide ion conductors. La-doped $SrGeO_3$ materials were also simulated, with similar promising results, so an analogous set of materials of the form $Sr_{1-x}La_xGeO_{3+0.5x}$ were synthesised.

As $BaZrSi_3O_9$ has similar structural features to $SrSiO_3$, in particular the isolated Si_3O_9 clusters, an investigation was undertaken in order to determine whether materials based on $BaZrSi_3O_9$ would make for oxide ion conductors viable for use in applications. Attempts were undertaken dope the parent compound with two dopants in attempts to create both vacancies and interstitial oxide ions. Y^{3+} was chosen to dope the Zr^{4+} site in order to create oxygen vacancies as they have similar ionic radii (Zr^{4+} = 0.72 Å, Y^{3+} = 0.9Å)[25] and is known to successfully dope onto Zr sites and lead to increased oxide ion conductivity in YSZ.[26] In order to create interstitial oxygen ions Ce^{3+} was chosen as a potential dopant on the Ba^{2+} site due to similar ionic radii (Ba^{2+} = 1.35 Å, Ce^{3+} = 1.01 Å).[25]

3.3. Experimental

3.3.1. Solid State ^{23}Na NMR Measurements on $Sr_{0.6}Na_{0.4}SiO_{2.8}$

Solid state ^{23}Na NMR (SSNMR) experiments were performed on a sample of nominal composition $Sr_{0.6}Na_{0.4}SiO_{2.8}$ previously synthesised by Abby Haworth. The experimental details of this synthesis and characterisation of the sample can be found in the supporting information of Evans *et al*., 2014.[6]

To determine whether measurements should be carried out using magic angle spinning or static samples, measurements were carried out using magic-angle spinning (MAS) at a rate of 12.2 kHz on a Varian 4 mm MAS probe. These measurements were carried out at ambient temperature. However as figure 3.2 shows, while the MAS spectrum is narrower than the static spectrum due to chemical shift and second order quadrapolar broadening being averaged out, there is still no Na^+ site resolution. Instead the peak remains broad, which is consistent with a range of sodium environments as would be found in a glass. As MAS was not providing site resolution, and could affect the observation of dynamics on a similar timescale, further experiments were conducted on non-spinning samples using a non-spinning probe capable of high-temperature operation.

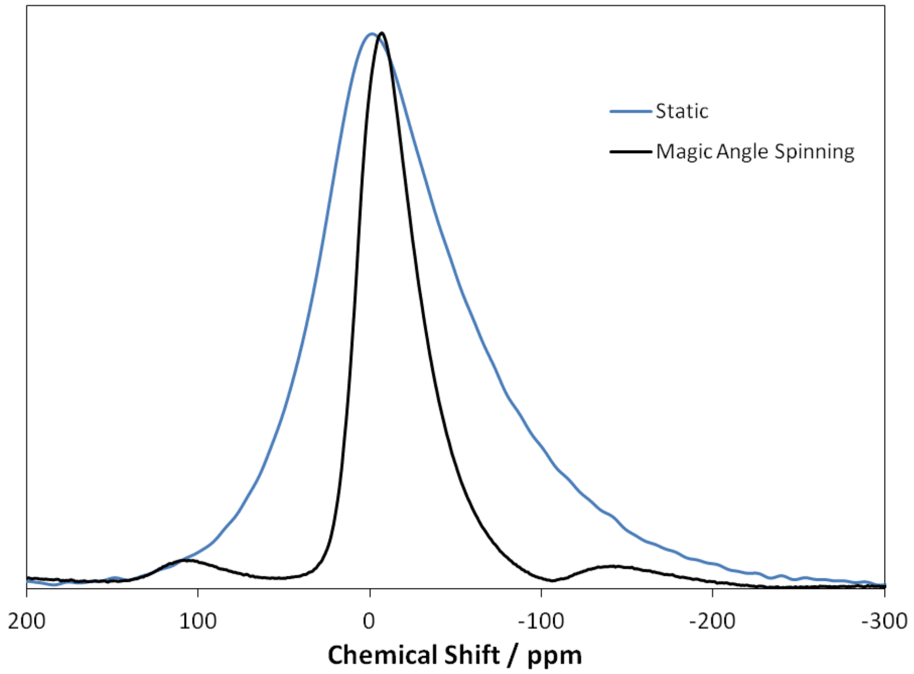

Figure 3.2: Overlap of static and MAS ^{23}Na SSNMR spectra for a sample with nominal composition $Sr_{0.6}Na_{0.4}SiO_{2.8}$. The spectra are normalised to the same maximum height.

The solid state ^{23}Na NMR spectra were recorded for a sample with nominal composition $Sr_{0.6}Na_{0.4}SiO_{2.8}$ at nine temperatures from 30 to 350 °C at 105.85 MHz using a Bruker Avance III HD spectrometer and wideline (non-spinning) probe accommodating samples packed into 5 mm o.d. glass tubes. These spectra were obtained using a solid-echo (i.e., 90° – delay – 90° – acq) with a 0.5 s recycle delay, a 30 µs delay between pulses, and 90° pulses of 2 µs in duration. 512 transients were accumulated for each temperature point. Spectra were referenced to an external sample of aqueous 0.1 M NaCl. These measurements were carried out by David Apperley as part of the Durham University Solid State NMR Service.

Additionally T_1 measurements were carried out in collaboration with Cory Widdifield and Paul Hodgkinson for temperatures ranging from 25 to 150 °C at 132.18 MHz using a Bruker Avance III HD spectrometer and a 4 mm (rotor o.d.) magic-angle spinning probe. The saturation-recovery method, using a train of 20 saturation pulses was used on a non-spinning sample. For these measurements a reference sample of solid NaCl was used.

3.3.2. Synthesis of the $Sr_{1-x}La_xSiO_{3+0.5x}$ Series

Two gram samples of the series $Sr_{1-x}La_xSiO_{3+0.5x}$ were prepared for $x = 0$, 0.025, 0.05, 0.10, 0.15 and 0.20 from stoichiometric amounts of $SrCO_3$, La_2O_3 and SiO_2. The masses used for each sample are given in table 3.1. La_2O_3 undergoes conversion to $La_2(CO_3)_3$ in air. Therefore before carrying out these syntheses a 2 g sample of La_2O_3 was heated to 1000 ˚C for 16 hours with a heating and cooling rate of 5 ˚C min^{-1} in order to convert any $La_2(CO_3)_3$ back to La_2O_3.

The required masses of each reactant were mixed and ground thoroughly. They were then placed in an alumina crucible and heated for 156 hours with intermediate grindings at a temperature of 1200 ˚C with a heating and cooling rate of 5 ˚C min^{-1}. Sample purity was confirmed by X-ray diffraction, using the Rietveld method implemented in TOPAS Academic as described in Chapter 2 section 2.2.4.2[27, 28]

Table 3.1: Reagent masses for synthesis of $Sr_{1-x}La_xSiO_{3+0.5x}$ series

Composition (*x*)	Mass of Reagent / g		
	$SrCO_3$	La_2O_3	SiO_2
0	1.8035	-	0.7340
0.025	1.7426	0.0493	0.7274
0.05	1.6828	0.0977	0.7210
0.10	1.5664	0.1920	0.7084
0.15	1.4540	0.2832	0.6962
0.20	1.3453	0.3712	0.6845

3.3.3. Synthesis of the $Sr_{1-x}La_xGeO_{3+0.5x}$ Series

Two gram samples of the $Sr_{1-x}La_xGeO_{3+0.5x}$ series ($x = 0$, 0.05, 0.10, 0.15 and 0.20) were prepared from stoichiometric amounts of $SrCO_3$, La_2O_3 and GeO_2. The masses used in the syntheses are given in table 3.2. Before carrying out these synthesis the La_2O_3 was heated at 1000 ˚C for 16 hours with a heating and cooling rate of 5 ˚C min^{-1} in order to convert any $La_2(CO_3)_3$ back to La_2O_3.

Table 3.2: Reagent masses for synthesis of $Sr_{1-x}La_xSiO_{3+0.5x}$ series

Composition (*x*)	Mass of Reagent / g		
	$SrCO_3$	La_2O_3	GeO_2
0	1.4177	-	1.0048
0.05	1.3279	0.0771	0.9907
0.10	1.2406	0.1521	0.9770
0.15	1.1557	0.2251	0.9637
0.20	1.0731	0.2960	0.9507

The required masses of each reactant were mixed and ground thoroughly. They were placed in an alumina crucible and heated for 96 hours with intermediate grindings at a temperature of 1200 ˚C with a heating and cooling rate of 5 ˚C min^{-1}. Sample purity was confirmed *via* X-ray diffraction as described in Chapter 2 section 2.2.4.2.

3.3.4. Synthesis of Y- and Ce-doped $BaZrSi_3O_9$

A 2 g sample of the parent compound $BaZrSi_3O_9$ was prepared from stoichiometric amounts of $BaCO_3$, ZrO_2 and SiO_2 powders. In addition to this, 2g samples of $BaZr_{0.95}Y_{0.05}Si_3O_{8.975}$ and $Ba_{0.95}Ce_{0.05}ZrSi_3O_{9.025}$ were also prepared using the same reactants with Y_2O_3 and CeO_2 added respectively. The masses of each powder were weighed out and thoroughly ground together. They were then placed in an alumina crucible and fired at various temperatures and durations depending on the sample with intermediate grindings. The masses used in each synthesis as well as the firing temperatures and times are given in table 3.3. Sample purity was confirmed *via* X-ray diffraction as described in Chapter 2 section 2.2.4.2.

Table 3.3: Reagent masses, heating times and temperatures for the syntheses of doped $BaZrSi_3O_9$ compounds. Heating and cooling rates were 5 ˚C min^{-1} for all firings.

Compound	Mass / g					Time / h	
	$BaCO_3$	ZrO_2	SiO_2	Y_2O_3	CeO_2	1300 ˚C	1350 ˚C
$BaZrSi_3O_9$	0.8640	0.5395	0.7892	-	-	-	144
$BaZr_{0.95}Y_{0.05}Si_3O_{8.975}$	0.8650	0.5131	0.7901	0.0247	-	192	48
$Ba_{0.95}Ce_{0.05}ZrSi_3O_{9.025}$	0.8198	0.5389	0.7883	-	0.0376	-	96

3.4. Solid State NMR Investigation of Na-doped $SrSiO_3$

3.4.1. Static NMR Spectra

Figure 3.3 shows the static ^{23}Na NMR spectra collected at nine temperatures over the range of 30 to 350 °C. At low temperatures, the figure shows a single very broad asymmetric peak. This is consistent with an overlap of many different resonances caused by a wide range of Na^+ environments present in an amorphous phase such as that identified in previous work.[6, 29, 30] As the temperature increases the peak shape narrows and becomes more symmetrical around the weighted mean chemical shift. This can be attributed to the exchange phenomena[31] and indicates that the Na^+ ions in the material are mobile. As the temperature increases the rate of exchange between sodium environments also increases causing the previously wide range of detected chemical shifts to average out resulting in the observed change in peak shape. The only alternative explanation for the peak shape change would be the material melting at 200-300 °C. As this does not occur[2, 6, 8] the change in peak represents the first direct experimental evidence of Na^+ mobility in nominal $Sr_{0.6}Na_{0.4}SiO_{2.8}$.

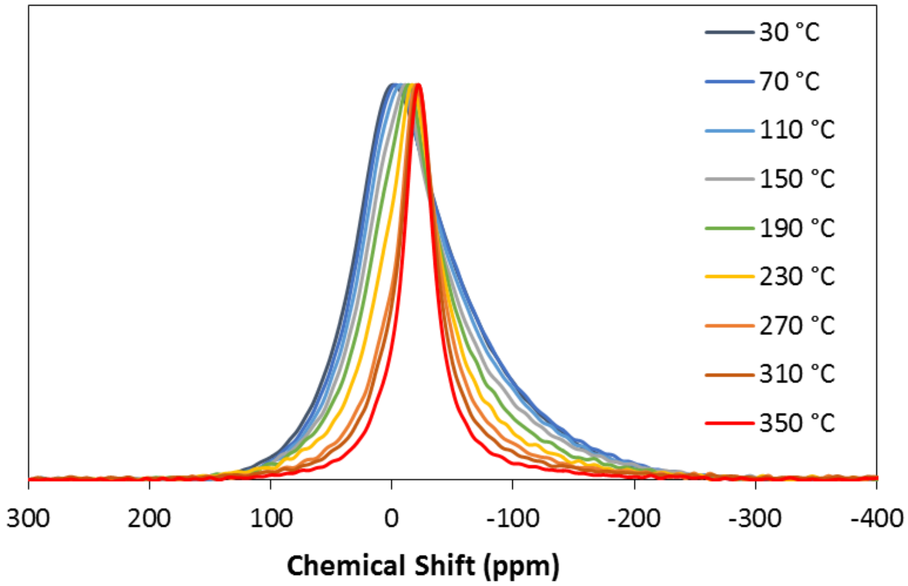

Figure 3.3: ^{23}Na SSNMR spectra for a sample of nominal composition $Sr_{0.6}Na_{0.4}SiO_{2.8}$ taken at temperatures from 30-350 °C in 40 °C increments.

A method for determining the activation energy for the mobility of the Na^+ ions is by using the linewidths, taken as the full width half maximum (FWHM), of the spectrum peaks. This requires that the temperature be high enough to reach the limit of fast exchange, in which all inhomogeneous broadening has been removed, and only the intrinsic lineshape remains around an average chemical shift value. This can be observed by a plateauing of FWHM values at high temperatures. Unfortunately, this limit was not reached in these experiments (as shown in figure 3.4) and, due to safety concerns, bringing the spectrometer to higher temperatures was not possible. It is also questionable as to whether this limit can be observed in this material, as it has been shown that the amorphous $Na_2Sr_2O_5$ phase undergoes a transition to a crystalline phase above 490 ˚C which leads to a reduction in conductivity.[32]

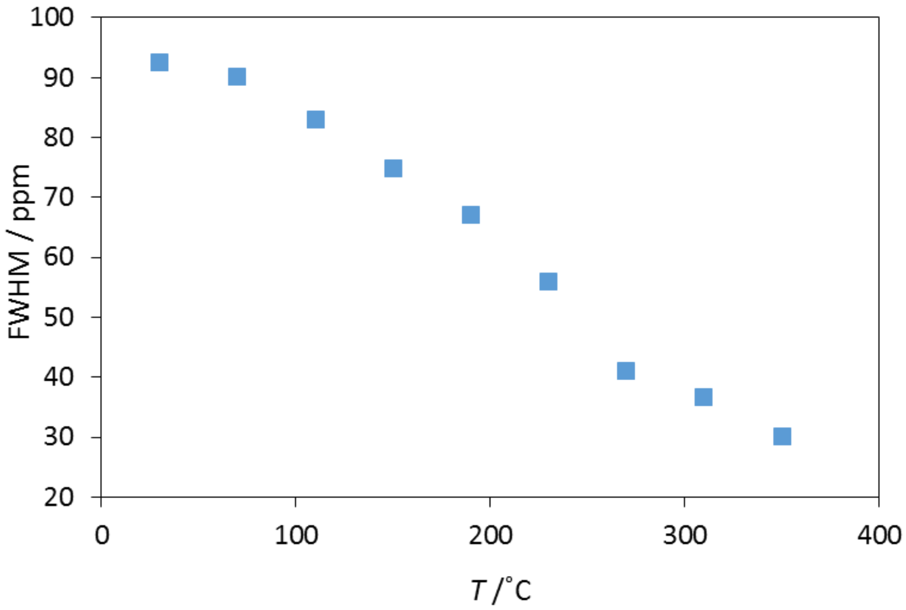

Figure 3.4: Plot of FWHM of ^{23}Na SSNMR spectra for a sample of nominal composition $Sr_{0.6}Na_{0.4}SiO_{2.8}$ against temperature. The uncertainties in the FWHM are of the order the size of the data points used. The FWHM values would plateau at high temperatures if the limit of fast exchange had been reached.

3.4.2. *T_1* Relaxation Time Analysis

As an alternative way to determine the activation energy for the dynamics of the Na^+ ions in the material, T_1 (spin-lattice) relaxation times were measured at a range of temperatures from 25 to 150°C. As the ionic jumps modulate local NMR interactions (such as quadrupolar couplings), driving relaxation, the T_1 relaxation times are proportional to the rate of motion and so obey an Arrhenius relationship with temperature.[31] These results are shown in figure 3.5.

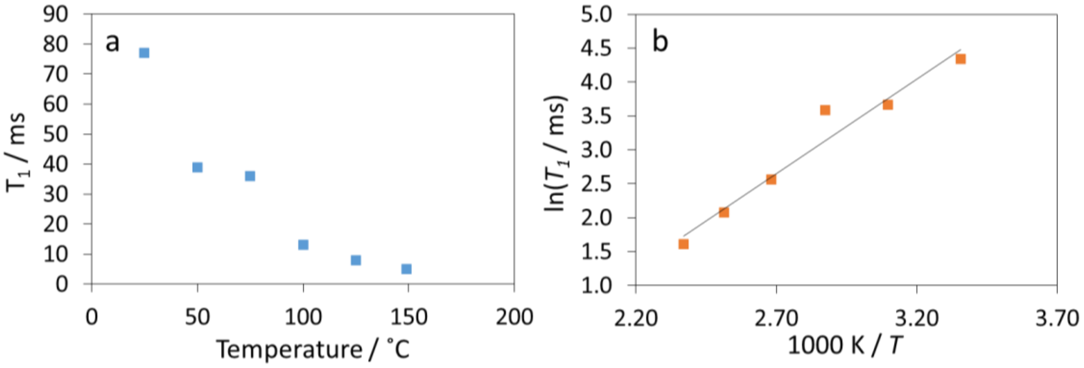

Figure 3.5: a) Plot showing T_1 relaxation times against temperature for a sample of nominal composition $Sr_{0.6}Na_{0.4}SiO_{2.8}$ taken at temperatures from 25-150 °C in steps of 25 °C. b) Arrhenius plot of the data.

The relaxation times decrease with increasing temperature, implying that the jump rate of the ions is increasing towards the ^{23}Na Larmour frequency (132 MHz). The Arrhenius plot shows a linear trend allowing an activation energy of 0.24(3) eV to be determined. This value for E_a is slightly lower than that measured using impedance spectroscopy, 0.324(9) eV,[4] however this difference is consistent with those differences found for ionic mobility in a variety of materials (including alkali metal, oxide and fluoride ion conductors) using the two techniques.[33] Selected examples of activation energies determined by impedance spectroscopy and solid state NMR for different types of Na^+ ion conductors are given in Table 3.4. It has been suggested that the lower activation energies observed using solid state NMR are due to the local motion of the sodium and the surrounding atoms, which contribute to the NMR relaxation in addition to the longer-range diffusional motion of the Na^+ ions.[34, 35] In other words, these differences are likely to reflect different averaging of the underlying distribution of dynamic processes in glassy materials by the different techniques.

Table 3.4: Activation energies for a range of sodium ion conductors reported in literature determined using impedance spectroscopy (IS) and NMR techniques. The error values given are those reported in the cited articles (if provided).

	E_a (IS) / eV	E_a (NMR) / eV	References
$NaAlSi_3O_8$	0.88	0.46(2)	[34, 36]
$Na_{0.8}In_{0.8}Sn_{0.2}S_2$	0.56	0.36	[37]
$Na_2B_{12}H_{12}$	0.21(1)	0.41(3)	[38, 39]
$Na_3Zr_2Si_2PO_{12}$	0.29	0.135	[35]
"$Sr_{0.6}Na_{0.4}SiO_{2.8}$"	0.32(1)	0.24(3)	[4], This work

The lower value for the activation energy determined from NMR T_1 also agrees well with an *ab initio* molecular dynamics (AIMD) simulation of the ionic mobility in amorphous and crystalline $Na_2Si_2O_5$, which also found an activation energy (0.17 eV) lower than that found through impedance.[40] The discrepancy between the NMR and AIMD values can be accounted for by a relatively low accuracy of the quantitative parameters obtained in the simulation due to a relatively short run time and size of the simulation box.

Since the publication of this work[41] several more studies on this material have been carried out, including further NMR studies confirming the findings reported here and finding a similar activation energy.[42, 43] In addition it has also been confirmed that the reported conductivity in K-doped strontium silicates is also not due to oxygen but rather K^+ conduction in $K_2Si_2O_5$.[44]

3.5. Characterisation of the $Sr_{1-x}La_xSiO_{3+0.5x}$ Series

3.5.1. Powder X-Ray Diffraction

Figure 3.6 shows a collected powder XRD pattern along with Rietveld fit for the parent $SrSiO_3$ compound. The fitting was carried out using two $SrSiO_3$ phases; the first was the monoclinic, C12/c1,[12] and the second was a more disordered trigonal $P\bar{3}1c$ phase that was proposed by the Evans group when discrepancies were discovered between observed patterns and those predicted by the monoclinic structure.[6] These two structures are discussed in detail in section 3.2.1. Two phases were chosen for the fitting as this gave a better fit than using either single phase. The refined parameters include background terms, zero point, scale factor, a single temperature factor for each phase and peak shape terms. The lattice parameters a, b, c and angle β for the monoclinic phase, and a and c for the trigonal phase were also refined.

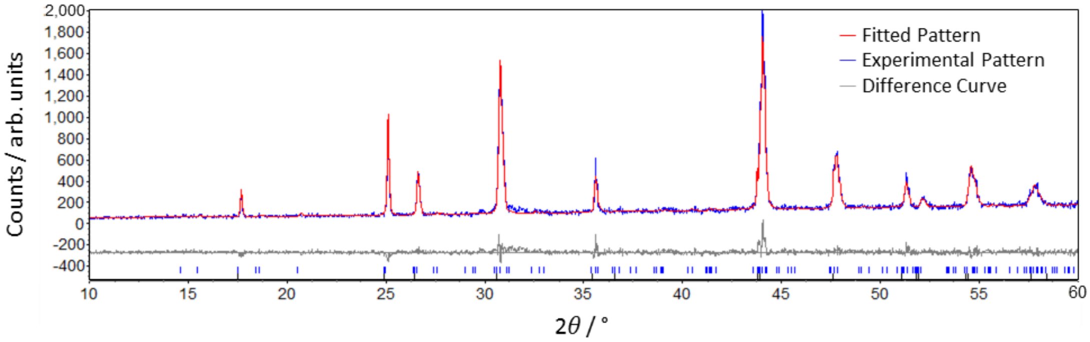

Figure 3.6: Powder XRD pattern collected for $SrSiO_3$ fitted with Rietveld refinement using monoclinic (represented by blue tick marks) and trigonal phases (represented by grey tick marks) of $SrSiO_3$. R_{wp} = 10.31 % The final Rietveld fit gave weight percentages of 52(1) % monoclinic and 48(1) % trigonal.

A stacked plot showing the XRD diffraction patterns collected for the nominally La-doped samples $Sr_{1-x}La_xSiO_{3+0.5x}$ is displayed in figure 3.7. The plots show that pure doped phases could not be formed. While the sample contains some amount of the parent phase indicated by the blue peaks there are also several peaks that represent impurities. These impurity peaks get more intense relative to the $SrSiO_3$ peaks as the nominal doping level increases. This suggests that the impurity phases contain most of the lanthanum rather than it being successfully doped into the structure. Additionally, the background level rises as 2θ increases and gets more intense as the nominal doping level increases. Due to the relationship between the background and the doping level it is likely that this is due to amorphous material containing a large amount of the lanthanum in the reactants.

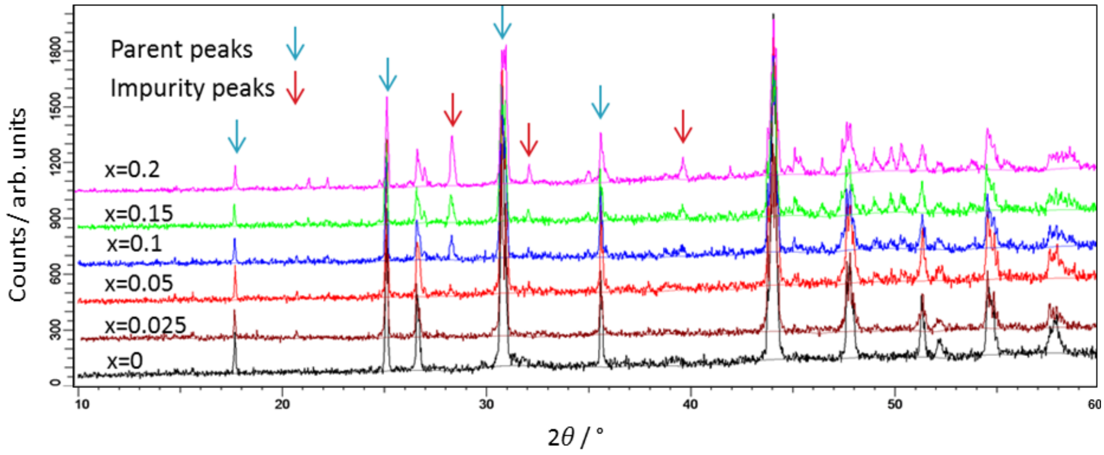

Figure 3.7: Powder XRD patterns collected for $Sr_{1-x}La_xSiO_{3+0.5x}$ samples matching the values of *x* given in the plots. The blue arrows indicate parent $SrSiO_3$ peaks and red arrows indicate impurity peaks.

A powder XRD pattern collected for the *x* = 0.2 sample with a Rietveld fit which includes two identified impurities is shown in figure 3.8. The fit shows that some impurity peaks could be tentatively identified. The solid black diamonds indicate impurity peaks that were fitted with a Sr-doped lanthanum silicate apatite phase with space group $P6_3/m$. The model used had formula $La_{8.65}Sr_{1.35}Si_6O_{26.32}$,[45] however, the exact doping level could be any based on the parent $La_{10}Si_6O_{27}$. The hollow ovals represent peaks that could not be matched, including a relatively intense peak at 27 °. It seems most likely that these peaks are caused by a different phase or phases containing lanthanum and silicon.

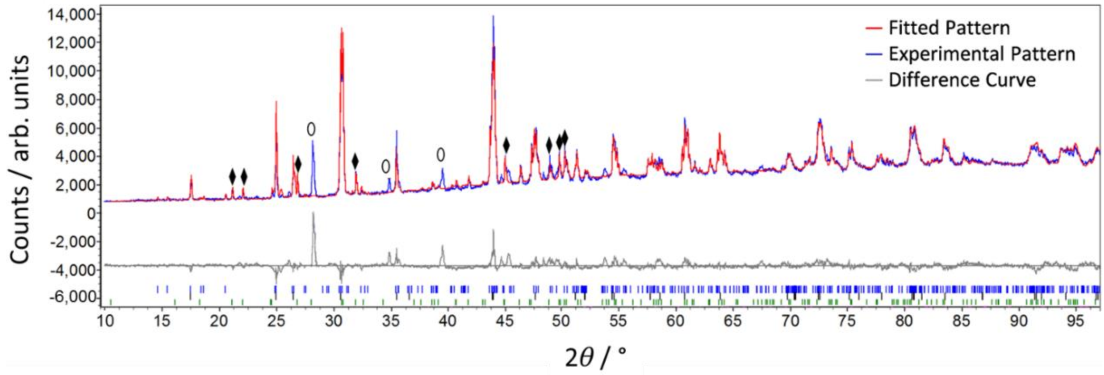

Figure 3.8: Powder XRD patterns collected for $Sr_{0.8}La_{0.2}SiO_{3.1}$ sample fitted using the Rietveld method modelled with monoclinic (blue tick marks) and trigonal (black tick marks) $SrSiO_3$ phases an lanthanum silicate apatite impurity phase[45] (green tick marks). R_{wp} = 11.77 %. The solid diamonds indicate peaks matching the impurity phase, hollow ovals indicate unfitted peaks.

Lanthanum silicate apatites are known to require high temperatures of around 1600-1700 °C to synthesise a pure sample.[46] Because of this attempts were made to synthesise the sample at lower temperature in the hope that a temperature could be found where formation of impurities was slow in comparison to formation of a doped phase; however, these were unsuccessful. It appears that the impurity phases form at lower temperatures and are more favourable than doping a $SrSiO_3$ phase.

While it is clear that for the most part doping has been unsuccessful the pattern recorded for the $x = 0.025$ sample differs very little from that of the parent material. This could either mean that the proportion of impurities is simply too low to be detected or that a small amount of doping is occurring. To investigate this, the variation of cell parameters for the monoclinic $SrSiO_3$ phase with dopant level was investigated. This was done by using a silicon standard. The samples were mixed with 25 % Si with a precisely known cell parameter. The Si peaks (space group: $Fd\overline{3}m$, cell parameter = 5.431195 Å) were fitted using the Pawley method while keeping the cell parameter fixed. This allows them to be used as a precise reference to allow accurate parameters for other phases in the fit to be calculated. Plots of unit cell parameters for the monoclinic $SrSiO_3$ phase against nominal doping level of La are given in figure 3.9 for a, b, c, the angle β and the cell volume V.

These plots show a significant change in all the cell parameters, except the unit cell volume between the undoped and the $x = 0.025$ samples. This change is negative for all parameters except for b, which shows a relatively large increase, and V. A decrease in cell parameters might be expected if doping did occur as the ionic radius of La^{3+} (1.16 Å) is smaller than that of Sr^{2+} (1.26 Å);[25] however, it is also possible that the additional oxygen interstitial atoms required to charge balance lead to an increase in b and V. For cell parameter c no further significant change is observed from $x = 0.025$ to $x = 0.20$. This would seem to indicate that no additional doping occurs despite the nominal amount of La increasing. However, all the other parameters behave in different ways. Cell parameter a appears to follow a reasonably linear increase, which might be evidence for continued doping if not for the fact that the changes are in the opposite direction to change between the undoped and $x = 0.025$ samples. For b and β there are very large changes between 0.025 and 0.05 and then no significant changes in behaviour following that. These changes also seem inconsistent with further doping occurring as they are in the opposite direction. It is possible that the systematic increase in impurities peaks visible in the patterns from 0.05 to 0.20 is causing less precise values to be calculated. This can partially be seen by the increase in the size of the error bars as x increases.

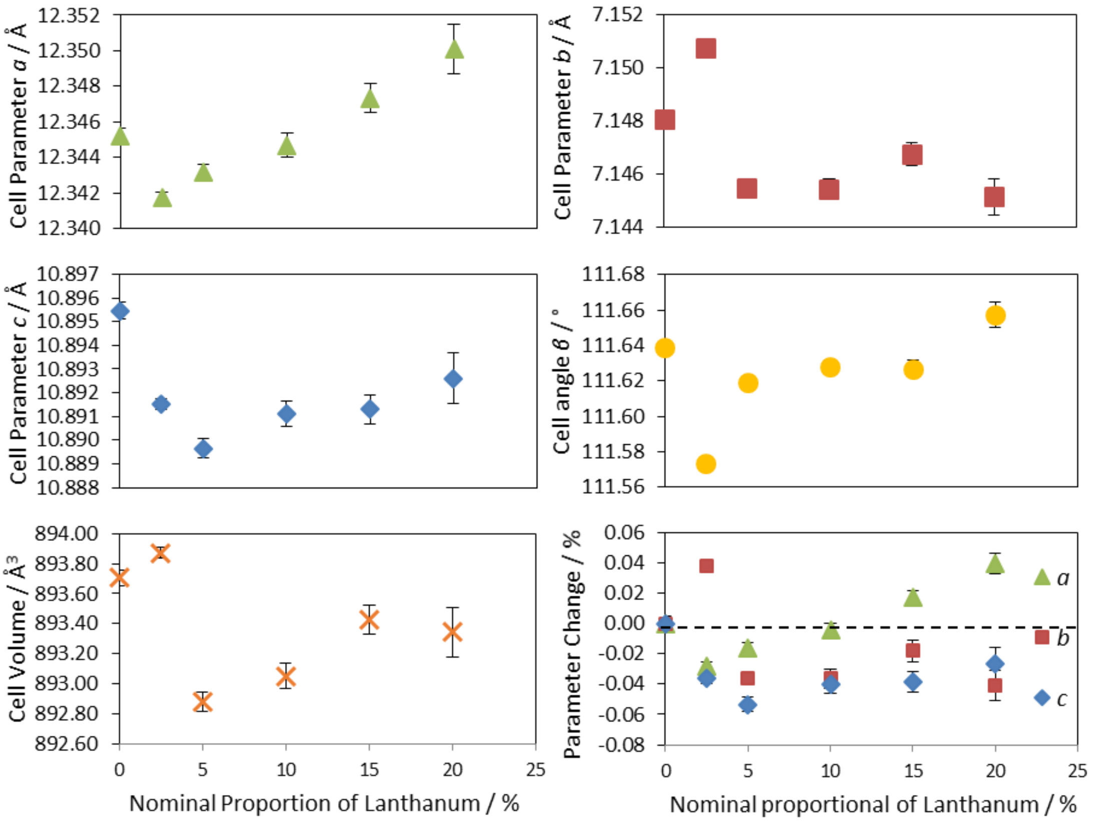

Figure 3.9: Plots showing the variation of cell parameters *a*, *b*, *c*, *β* and *V* with the nominal doping level *x* for the Sr$_{1-x}$La$_x$SiO$_{3+0.5x}$ materials. The percentage variation is also shown in the sixth plot.

Currently it seems that doping may occur in a small amount at up to the x = 0.025 level; and that this amount does not increase as x further increases due to the presence of impurity phases containing the La whose formation is favoured over further doping. Otherwise, it is possible that cell parameters results are too imprecise to definitely say whether any doping occurs at any level. It is worth noting that the cell parameters for the nominally Na-doped SrSiO$_3$ samples showed similar large jumps from x = 0 to x = 0.051 and it known that doping in that case occurs far below the nominal level.[47]

3.5.2. Impedance Spectroscopy

Although pure phases were not formed impedance measurements were carried out in order to test the conductivity of the samples. Figure 3.10 shows a Nyquist plot for the nominal composition Sr$_{0.9}$La$_{0.1}$SiO$_{3.05}$ sample at 772 ˚C.

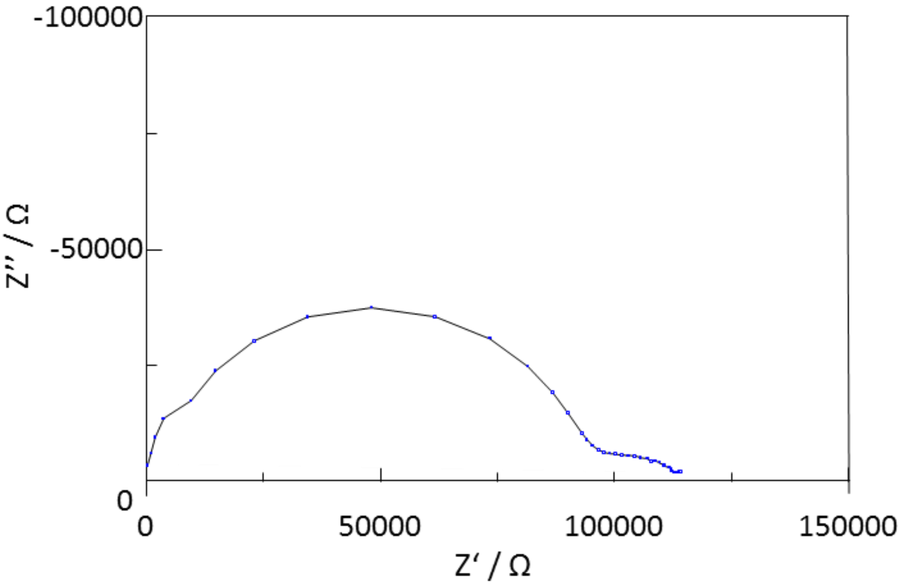

Figure 3.10: Nyquist plot showing how the real part *Z'* and imaginary part *Z''* of the complex impedance vary with frequency for a sample of nominal composition $Sr_{0.9}La_{0.1}SiO_{3.05}$ recorded at 772 °C.

The plot shows one semicircle and one shoulder. These features were fitted using an equivalent circuit consisting of a resistor and a capacitor in parallel for each feature as shown in figure 3.11.

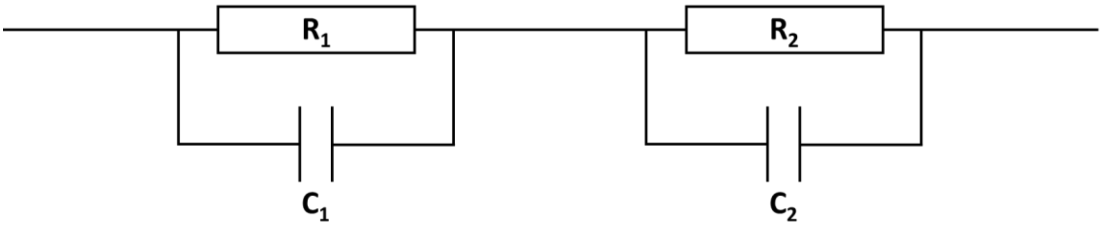

Figure 3.11: Equivalent circuit setup used for fitting the Nyquist plot shown in figure 3.10. R_1, R_2 represent resistors and C_1, C_2 represent capacitors for the large semicircle and small shoulder.

The semicircle gives a capacitance of 7.6(1) × 10^{-11} F and was assigned to the bulk response. The shoulder peak gives a capacitance value of 1.1(6) × 10^{-8} F and was assigned to the grain boundary. Contrary to what is expected in an oxide ion conductor, no Warburg element is observable in this plot and one does not appear at lower temperatures. In addition, the capacitance remains low at low frequencies reaching values of the order 10^{-8} F for a frequency of 0.1 Hz whereas for an oxide ion conductor this would be expected to be of the order of 10^{-6} F due to transfer of electrons to and from O^{2-} at the sample-electrode interface.[48, 49] These factors indicate that oxide ion conduction is not a dominant effect.

Figure 3.12 shows the Arrhenius plots for conductivity for the $Sr_{1-x}La_xSiO_{3+0.5x}$ series. The conductivities were measured up to temperatures of around 800 °C. It should be noted that the apatite impurity phase found during analysis of the XRD patterns is in itself an oxide ion conductor[50] so it may be that any conductivity seen in the nominally La-doped $Sr_{1-x}La_xSiO_{3+0.5x}$ materials is due to this impurity.

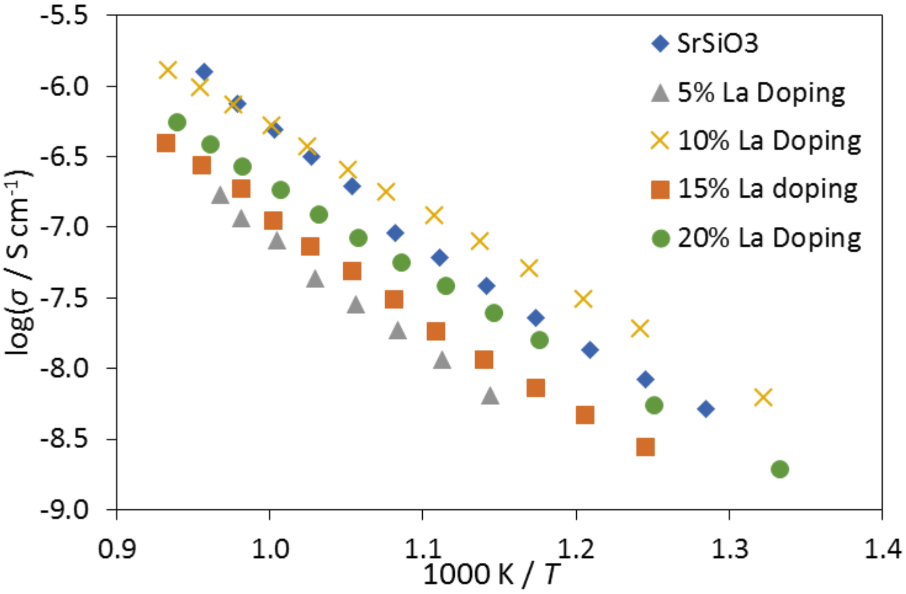

Figure 3.12: Arrhenius plots showing the variation of conductivity with temperature for the $Sr_{1-x}La_xSiO_{3+0.5x}$ series.

It is clear from the plots that the conductivity of this series of materials is poor. At high temperatures the highest conductivity shown is by the undoped sample which, with a conductivity of 1.31×10^{-6} S cm^{-1} at 776 °C, is 4 orders of magnitude below that needed to be considered as a worthy candidate for applications based on oxide ion conductivity. All of the doped samples have lower conductivities than the undoped sample, except for the nominally 10 % doped sample at low temperatures, and the maximum difference between the conductivities is one order of magnitude, relatively close compared to the difference from ideal oxide ion conductors. Given that it seems unlikely that much doping occurs in these materials it is perhaps not surprising that the La containing samples do not show much conductivity difference. The fact that they are in general lower could be the result of the impurity phases which can lead to a large number of grain boundaries reducing the conductivity and counteracting any conductivity due to the apatite impurity.

3.6. Characterisation of the $Sr_{1-x}La_xGeO_{3+0.5x}$ Series

3.6.1. Powder X-Ray Diffraction

Figure 3.13 shows a collected powder XRD pattern along with Rietveld fit for the parent $SrGeO_3$ compound. As with the $SrSiO_3$ two phases were used in this fit, the monoclinic C12/c1 phase,[12] and the disordered trigonal $P\overline{3}1c$ phase described in section 3.4.1 except with Ge atoms substituted for Si. The refined parameters include background terms, zero point, scale factor, a single temperature factor for each phase and peak shape terms. The lattice parameters a, b, c and angle β for the monoclinic phase and a and c for the trigonal phase were also refined.

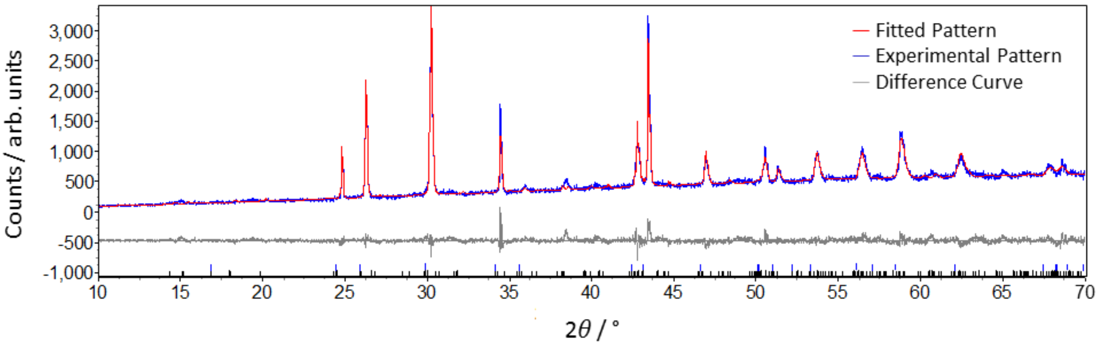

Figure 3.13: Powder XRD pattern collected for $SrGeO_3$ fitted with Rietveld refinement using monoclinic (represented by blue tick marks) and trigonal phases (represented by grey tick marks) of $SrGeO_3$. R_{wp} = 7.23 %. The final Rietveld fit gave phase proportions of 36(1) % monoclinic and 64(1) % trigonal.

A stacked plot showing the XRD diffraction patterns collected for the $Sr_{1-x}La_xGeO_{3+0.5x}$ series samples is displayed in figure 3.14. The plot shows that the attempted doping of $SrGeO_3$ with La^{3+} results in similar problems as with $SrSiO_3$. The peaks of the parent $SrGeO_3$ phase can be seen (marked with blue arrows), but several impurity peaks are also present (marked with red arrows). These are only visible above the $x = 0.05$ level indicating that doping up to this level may indeed by possible as suggested in literature.[24] The impurity peaks become more intense relative to the $SrGeO_3$ peaks as the nominal doping level increases suggesting that, as with the silicate materials, the impurity phases contain most of the lanthanum. It appears that doping may occur up to the 5 % level if it occurs at all.

As with the silicate patterns shown in figure 3.7 the patterns for the germanate materials show a high background that increases in intensity with the nominal doping level. This increase is more extreme than in the silicate synthesis and could indicate that a larger amount of amorphous material was formed in these syntheses. In contrast to the silicate patterns, impurity peak matching for these patterns was not successful. This may be due to many of the apatite lanthanum germanate peaks overlapping with the $SrGeO_3$ peaks, although the major impurity peak at 33° does not match any apatite peak.

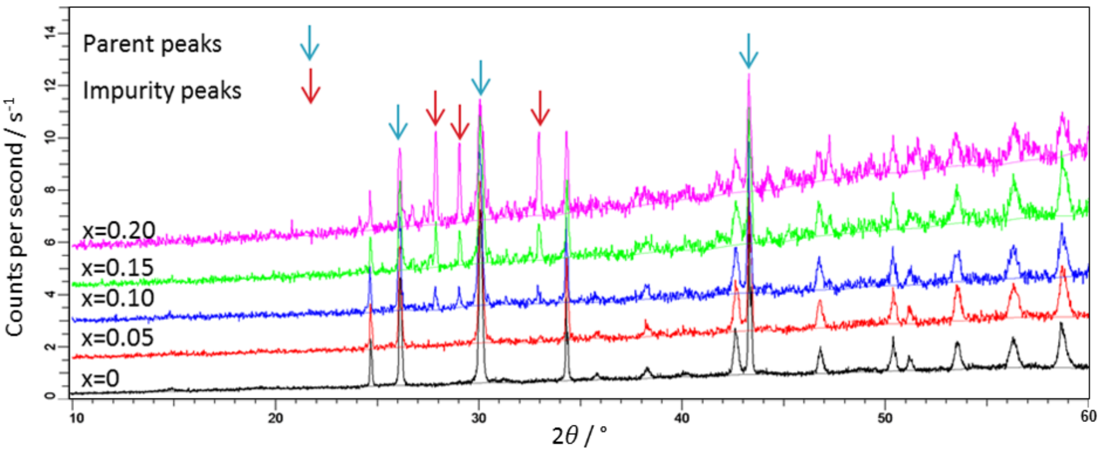

Figure 3.14: Powder XRD patterns collected for $Sr_{1-x}La_xGeO_{3+0.5x}$ samples matching the values of *x* given in the plots. The blue arrows indicate parent $SrSiO_3$ peaks and red arrows indicate impurity peaks.

The variation of cell parameters for the parent monoclinic $SrGeO_3$ phase with dopant level was investigated using a silicon standard. Plots of unit cell parameters against nominal doping level of La are given in figure 3.15 for *a*, *b*, *c*, the angle β and the cell volume *V*.

These plots show that most of the cell parameters changed very little between the undoped and the $x = 0.05$ samples which would indicate that no doping is taking place. However, cell parameters *c* and *V* show relatively large decreases. The small changes observed for the other cell parameters are also negative however given the size of the error bars it is difficult to claim that these are significant differences. These changes may indicate doping due to the lower ionic radius of La^{3+} (1.16 Å) compared to that of Sr^{2+} (1.26 Å)[25]. For cell parameter *c* further changes are relatively small indicating that no additional doping occurs despite the nominal amount of La increasing. For all the other cell parameters this is also true. It can be seen on the plot of relative change that changes in *a* and *b* are small in comparison to that of *c*. As with the silicates it is likely that the systematic increase in impurities in the sample is causing less precise values to be calculated.

Comparing to the plots shown in figure 3.9 for the silicates it appears that the change in cell parameters between the undoped and $x = 0.05$ samples broadly matches. From the data presented it seems that a small amount of doping occurs up to the $x = 0.05$ level; and that this amount does not increase as *x* further increases due to the presence of impurity phases containing the La whose formation is favoured over further doping. This would agree with the previous literature reports of doping up to this level.[24]

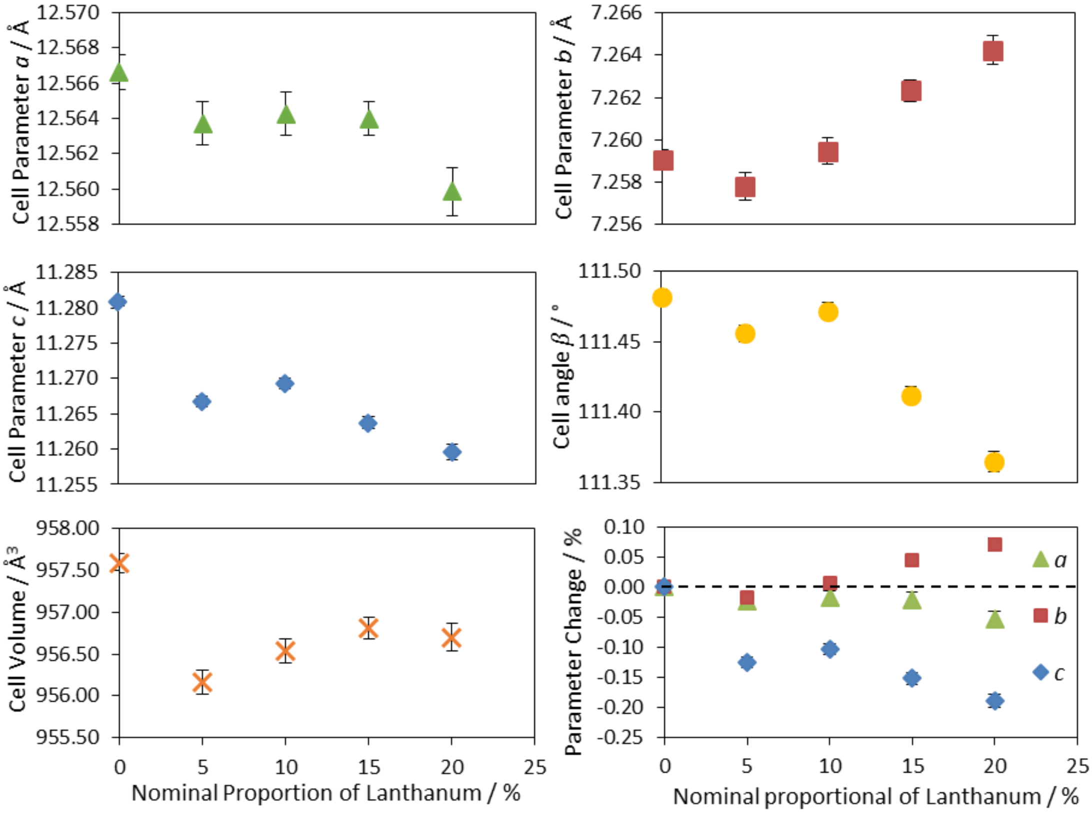

Figure 3.15: Plots showing the variation of cell parameters *a*, *b*, *c*, *β* and *V* with the nominal doping level *x* for the $Sr_{1-x}La_xGeO_{3+0.5x}$ materials. The percentage variation is also shown in the sixth plot.

3.6.2. Impedance Spectroscopy

Although pure phases were not formed impedance measurements were carried out in order to test the conductivity of the samples. Figure 3.16 shows a Nyquist plot for the nominal composition $Sr_{0.95}La_{0.05Ge}O_{3.025}$ sample at 798 ˚C. The plot shows two semicircle regions. The point at 7500 Ω has a Z'' value that is higher than expected, however this is likely due to an experimental artefact caused by the Solartron 1260A at a frequency of 1 Mhz. Fitting using the equivalent circuit shown in figure 3.11 gave a capacitance of 6.4(7) × 10^{-12} F and was assigned to the bulk response. The smaller semicircle gives a capacitance value of 4.0(3) × 10^{-8} F and was assigned to the grain boundary. No Warburg element is observable in this plot and one does not appear at lower temperatures. The capacitance reaches a value of the order of 10^{-7} F at 0.1 Hz which is just about at the level that might be expected for an oxide ion conductor,[49, 51] however overall the evidence for oxide ion conduction is inconclusive.

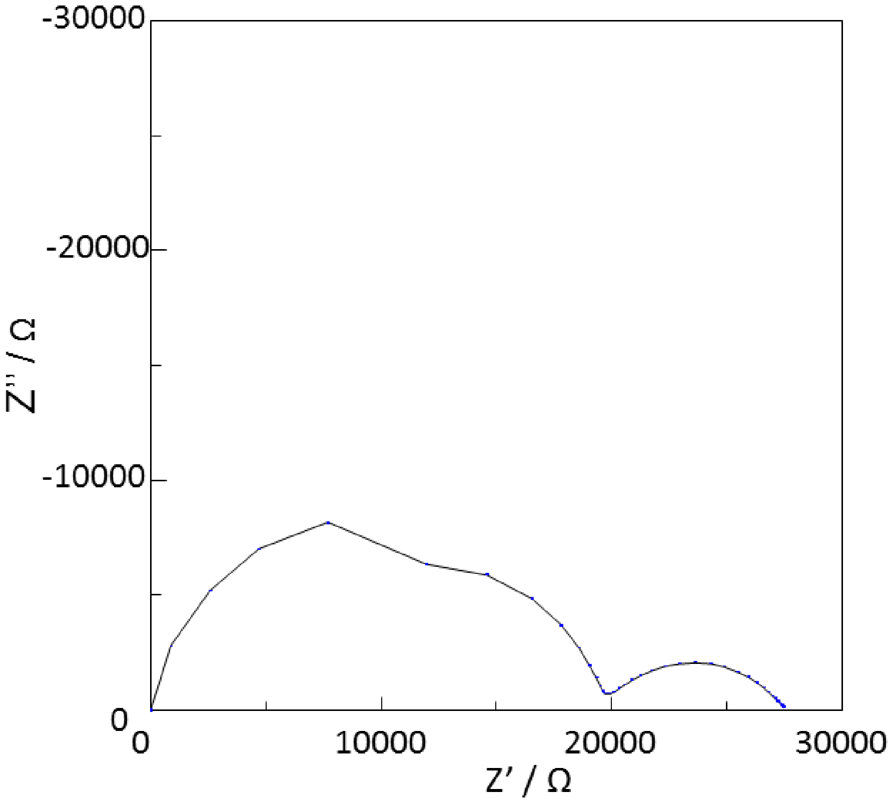

Figure 3.16: Nyquist plot showing how the real part Z' and imaginary part Z'' of the complex impedance vary with frequency for a sample of nominal composition $Sr_{0.95}La_{0.05}GeO_{3.025}$ recorded at 798 °C.

Figure 3.17 shows the Arrhenius plots for conductivity for the $Sr_{1-x}La_xGeO_{3+0.5x}$ series. The conductivities were measured up to temperatures of around 800 °C. While this plot shows that the $SrGeO_3$ materials have a generally higher conductivity than the $SrSiO_3$ materials the conductivities are still poor. The highest conductivity shown by these sample is 1.69×10^{-5} S cm^{-1} for the nominally 5 % doped sample at 798 °C which is 3 orders of magnitude below that needed to be considered as a worthy candidate for applications based on oxide ion conductivity. The nominally 10 % doped sample displays conductivity very close to the nominally 5 % doped sample. The other two doped samples display conductivity that although somewhat higher that the undoped sample at the temperatures studied is a full order of magnitude below that of the higher conductivity samples. This could be due to the increasing amount of impurities present including the possible amorphous phase which could have lower conductivity. The fact that both the nominally 5 % and 10 % La-doped samples are so close and clearly higher than the undoped sample indicates that there may be indeed a small amount of doping occurring that is increasing the conductivity.

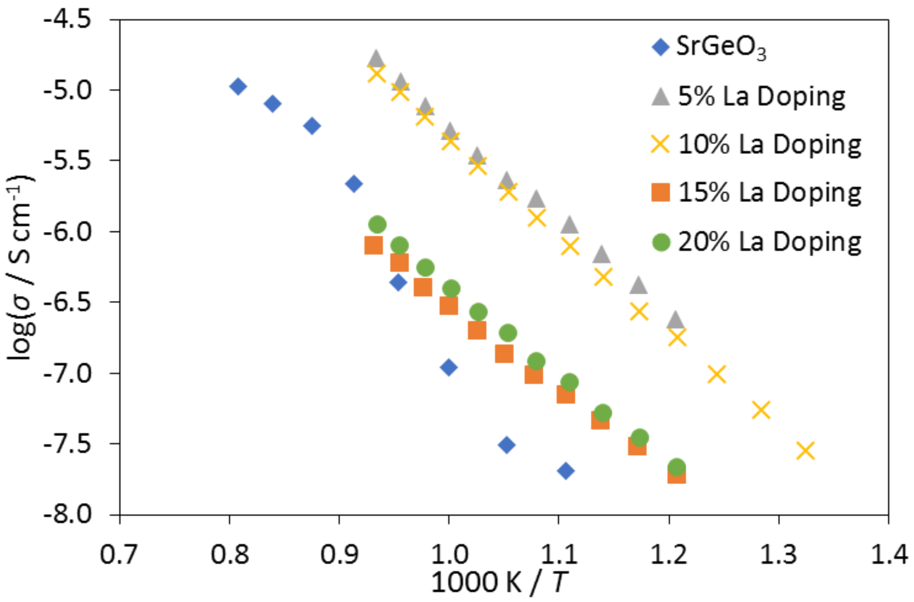

Figure 3.17: Arrhenius plots showing the variation of conductivity with temperature for the $Sr_{1-x}La_xGeO_{3+0.5x}$ series.

The undoped $SrGeO_3$ showed unusual behaviour compared to the other samples. The plot deviates substantially from linearity appearing to show a relatively rapid increase in conductivity between 650 and 850 °C. This could be evidence of some sort of gradual phase change between these two temperatures.

3.7. Characterisation of Y- and Ce-doped $BaZrSi_3O_9$

3.7.1. Powder X-Ray Diffraction

Figure 3.18 shows the collected powder XRD patterns for the three materials fitted *via* Rietveld refinement. The Rietveld refinements were carried out using a starting model based on the $BaTiSi_3O_9$ structural analogue[18] with the Ti atoms replaced with Zr atoms as well as a monoclinic ($P2_1/c$) ZrO_2[52] impurity phase. The refinement parameters include background terms and zero point; scale factors, peak shape terms, and a single temperature factor for each phase; and the lattice parameters a and c for $BaZrSi_3O_9$ and a, b, c and β for ZrO_2.

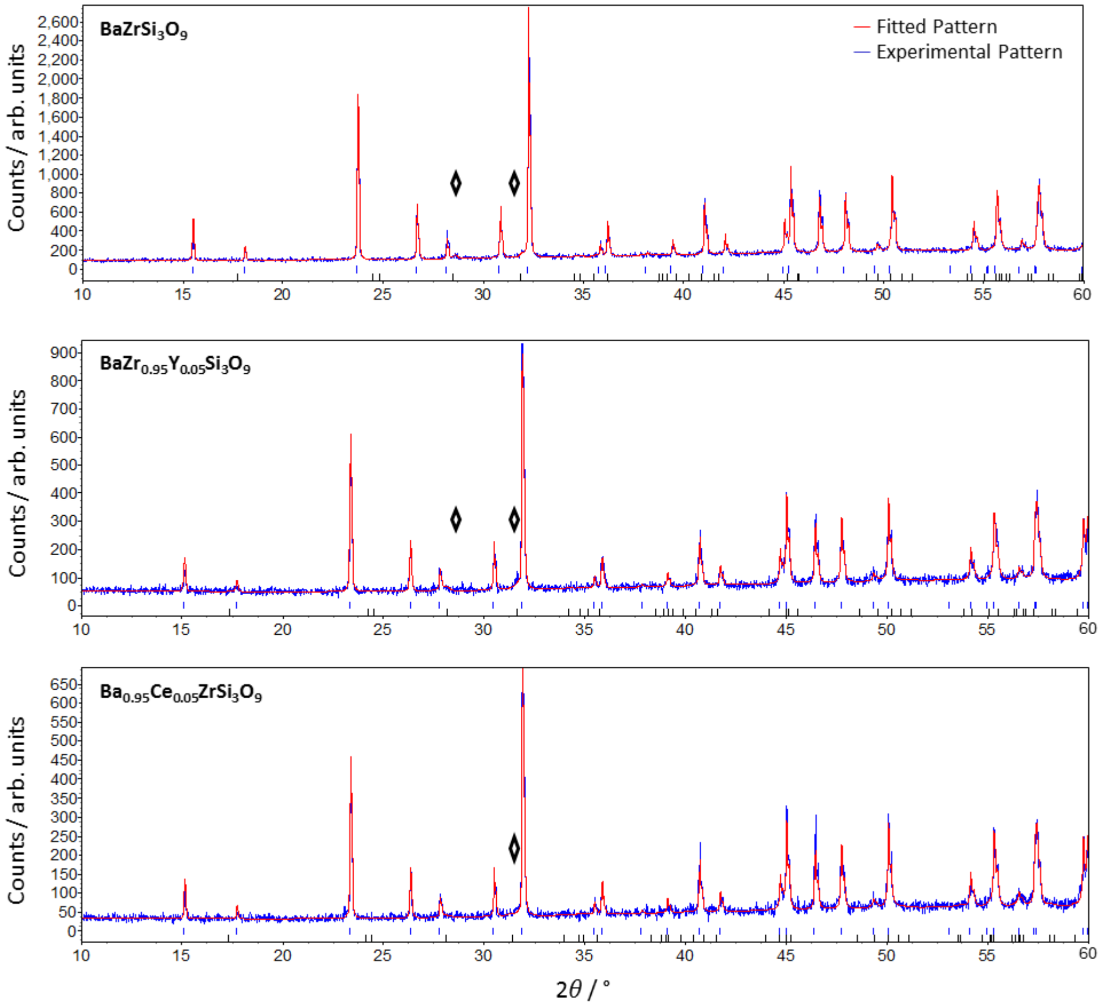

Figure 3.18: XRD patterns collected for the three synthesised materials fitted *via* Rietveld refinement with a $BaZrSi_3O_9$ phase (blue tick marks) and a ZrO_2 impurity phase (black tick marks). ZrO_2 impurity peaks are marked with diamonds. a) $BaZrSi_3O_9$: Lattice parameters *a* = 6.7783(2) Å and *c* = 10.0296(4) Å; R_{wp} = 9.63 % b) $BaZr_{0.95}Y_{0.05}Si_3O_{8.975}$: Lattice parameters *a* = 6.7723(3) Å and *c* = 10.0180(6) Å; R_{wp} = 12.79 %. c) $Ba_{0.95}Ce_{0.05}ZrSi_3O_9$: Lattice parameters *a* = 6.7735(2) Å and *c* = 10.0208(6) Å; R_{wp} = 14.49 %.

The refinements fit all the peaks observed in the collected patterns, those attributed to the ZrO_2 impurity phase are marked with a diamond. These peaks were not removed despite repeat firings. With Rietveld refinement using both phases the weight percentage of the ZrO_2 refined to 9(3) % for $BaZrSi_3O_9$, 13(4) % for $BaZr_{0.95}Y_{0.05}Si_3O_{8.975}$ and 10(4) % for $Ba_{0.95}Ce_{0.05}ZrSi_3O_9$ indicating that for all samples some unreacted material remains. Despite the presence of the ZrO_2 impurity peaks all the samples were deemed sufficiently pure to proceed with impedance measurements.

The cell parameters of the parent material, $BaZrSi_3O_9$, refined to *a* = 6.7783(2) Å and *c* = 10.0296(4) Å, and are larger than those of $BaTiSi_3O_9$ (*a* = 6.6387(3) Å and *c* = 9.7554(4) Å). This is to be expected as Zr^{4+} has larger ionic radius than Ti^{4+}.[25] The cell parameters refined for $BaZr_{0.95}Y_{0.05}Si_3O_{8.975}$ (*a* = 6.7723(3) Å and *c* = 10.0180(6) Å) and $Ba_{0.95}Ce_{0.05}ZrSi_3O_9$ (*a* = 6.7735(2) Å and *c* = 10.0208(6) Å) are both about 0.1 % smaller than those calculated for the parent compound. For $Ba_{0.95}Ce_{0.05}ZrSi_3O_9$ this increase is expected as Ce^{3+} has a smaller ionic radius and higher charge than that of Ba^{2+}, both factors that would bring the atoms closer together. On the other hand, for $BaZr_{0.95}Y_{0.05}Si_3O_{8.975}$ it might be expected that cell parameters would get larger on doping, as Y^{3+} has a larger ionic radius and lower charge than Zr^{4+}, however the creation of oxygen vacancies could be responsible for counteracting this, leading to an overall slightly smaller cell. Given these two competing factors and the low difference in cell parameters it is difficult to say whether the Y^{3+} doping was successful, however no other impurity peaks are seen in the XRD patterns.

3.7.2. Impedance Spectroscopy Measurements

Figure 3.19 shows a Nyquist plot for the $BaZrSi_3O_9$ sample at 800 ˚C, the highest measured conductivity for all the samples. The plot shows one large semicircle. Fitting this semicircle with an equivalent circuit of a resistor and capacitor in parallel gave a capacitance of 8.0(5) × 10^{-12} F indicating a bulk response.[48]

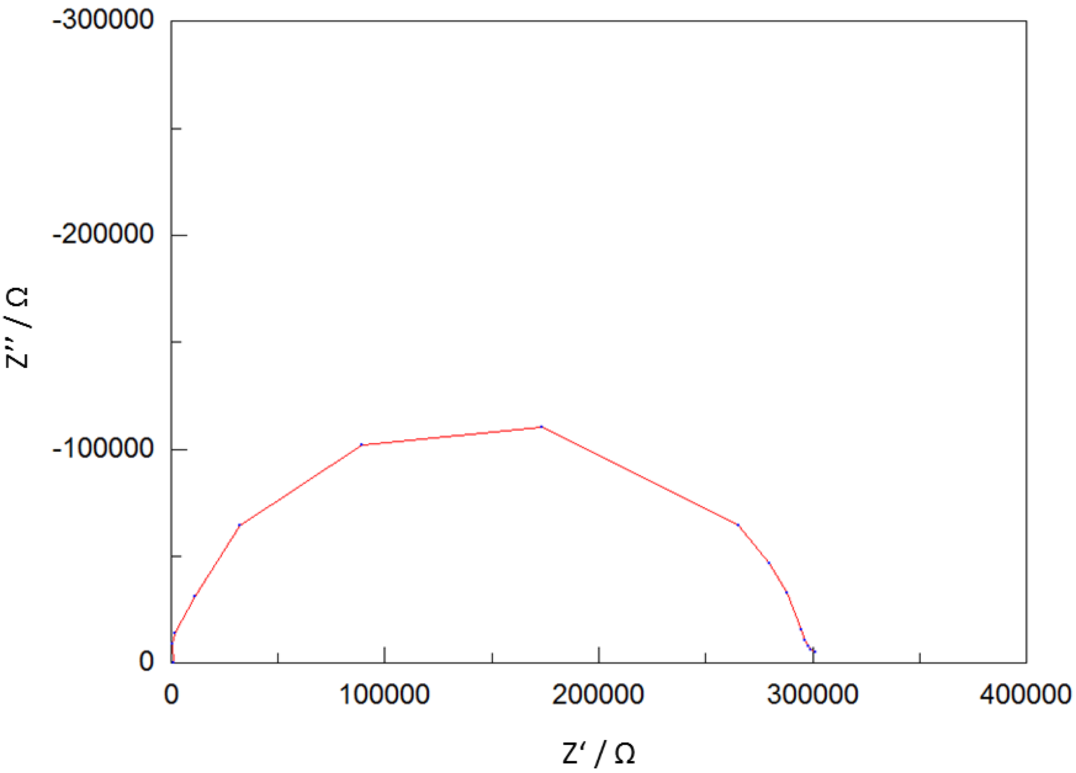

Figure 3.19: Nyquist plot showing how the real part *Z'* and imaginary part *Z''* of the complex impedance vary with frequency for a sample of $BaZrSi_3O_9$ recorded at 800 °C.

No Warburg element is observable in this plot and one does not appear at lower temperatures; in addition the capacitance remains low at low frequencies reaching value on the order of 10^{-9} F for a frequency of 0.1 Hz. Both of these factors run counter to the expectation for an oxide ion conductor indicating that oxide conduction is not a dominant effect.[51]

Figure 3.20 shows the variation of conductivity with temperature for the three samples. The three plots all follow the expected linear trend and give similar activation energies of 0.475(3) eV for $BaZrSi_3O_9$, 0.55(4) eV for $BaZr_{0.95}Y_{0.05}Si_3O_{8.975}$ and 0.54(2) eV for $Ba_{0.95}Ce_{0.05}ZrSi_3O_9$. The parent material $BaZrSi_3O_9$ has the highest conductivity of the three materials reaching 8.8×10^{-7} S cm^{-1} at 800 °C. However, this is approximately five orders of magnitude lower than that required to be considered a suitable candidate for applications based on oxide ion conductivity.[53]

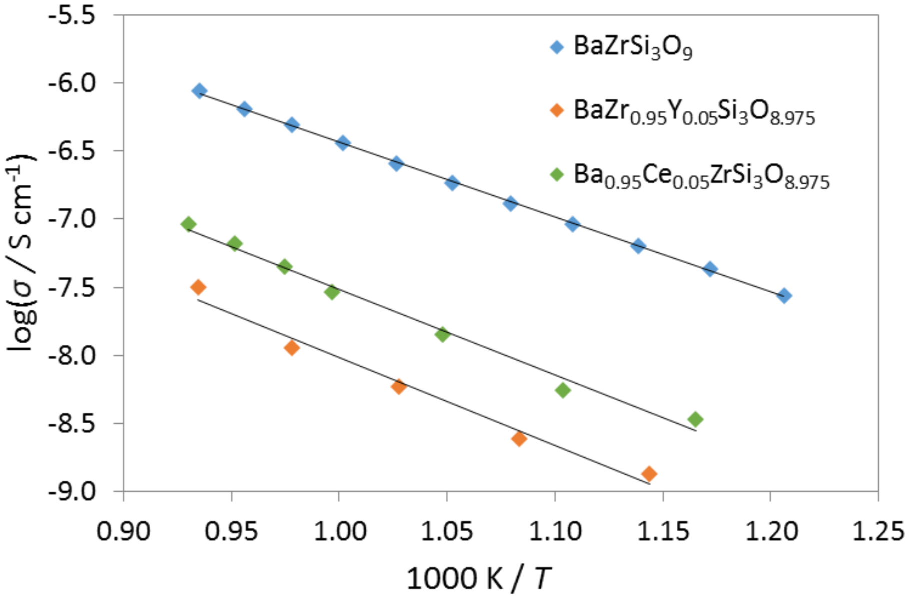

Figure 3.20: Arrhenius plots of the variation of conductivity with temperature for $BaZrSi_3O_9$, $BaZr_{0.95}Y_{0.05}Si_3O_{8.975}$ and $Ba_{0.95}$ $Ce_{0.05}ZrSi_3O_9$.

The conductivity value of $BaZr_{0.9}Y_{0.05}Si_3O_{8.975}$ is one and half orders of magnitude lower than the parent compound with a value of 3.2×10^{-8} S cm^{-1} at 800 °C. A possible explanation for this decrease is it that that doping the material with Y^{3+} was unsuccessful and that the Y_2O_3 either remained unreacted or formed an additional impurity phase that is either amorphous or too low in proportion to be seen in the XRD pattern. This impurity could then cause lower conductivity values to be measured by introducing additional grain boundary effects in the pellet or acting as an insulator and so be responsible for the lower conductivity.

$Ba_{0.95}Ce_{0.05}ZrSi_3O_9$ also has conductivity lower than the parent compound by approximately one order of magnitude with a value of 9.3×10^{-8} S cm^{-1} at 800 °C. Unlike for the nominally Y-doped material, the doping of $BaZrSi_3O_9$ with Ce^{3+} has previously been shown to be possible,[20] making the presence of an additional impurity phase an unlikely explanation for the reduction in conductivity. Another possible explanation is the greater charge on the Ce^{3+} cations when compared to the Ba^{2+}, this may make the movement of oxygens from regions around the Ce^{3+} more difficult leading to the lower conductivity values measured. Due to the lower conductivities measured in $BaZr_{0.9}Y_{0.05}Si_3O_{8.975}$ and $Ba_{0.95}Ce_{0.05}ZrSi_3O_9$ compared to the parent material, it was decided not to try doping with higher proportions of Y^{3+} and Ce^{3+}.

3.8. Conclusions

The narrowing of the broad signal in the ^{23}Na solid state NMR spectra of nominally $Sr_{0.6}Na_{0.4}SiO_{2.8}$ and the decrease of the corresponding T_1 times with temperature, in conjunction with the impedance measurements and other characterisation methods reported in the literature, indicate that the Na^+ ions in this material (and therefore other nominally Na-doped $SrSiO_3$ materials) are mobile, and that this mobility is a thermally activated process. The consistency in the activation energy values found for the thermally activated process responsible for the averaging of the Na^+ ion environments by solid state NMR and the conduction process probed by impedance is strong evidence that the dominant charge carriers in the nominally Na-doped $SrSiO_3$ materials are in fact sodium ions in an amorphous $Na_2Si_2O_5$ phase. This conclusion is also consistent with previous findings based on high-resolution powder neutron diffraction and tracer diffusion measurements,[5, 6] which show that although a very low level of oxygen vacancy creation in $SrSiO_3$ cannot be ruled out, the oxide ions are not responsible for the high conductivity measured in these samples. This is the first definitive and direct experimental evidence that the conductivity observed in this material is due to fast Na^+ conduction rather than oxide ion mobility.

Doping of $SrSiO_3$ with lanthanum has proven to not be possible, except for potentially in very small amounts. Similarly, doping $SrGeO_3$ with La^{3+} was also unsuccessful above a potential 5 % doping level. It appears that the lanthanum is instead being used in a competing phase, or phases, that preferentially form rather than doping into the parent material. The conductivity of the samples was low and did not show characteristic signs of oxide ion conductivity. Because of these factors it does not seem worthwhile to continue investigation into La^{3+} doping of these materials.

The doping of $BaZrSi_3O_9$ with 5 % Y^{3+} and Ce^{3+} appears to have been successful with no crystalline impurities containing the dopant ions observed in the XRD patterns of either of the doped materials. Small ZrO_2 peaks are visible however, consistent with the parent compound. The trends in cell parameters are inconclusive as the differences between doped and parent materials are very small and the expected combined effect of dopant cation size, charge and creation of oxygens vacancies/interstitials on cell parameters is not clear. All three materials performed very poorly as oxide ion conductors, with their conductivities being many orders of magnitude lower than that required to be considered a suitable candidate for applications based on oxide ion conductivity. The doped materials had lower conductivities than the parent and so it was decided not to carry out further doping attempts.

3.9. References

1. P. Singh and J. B. Goodenough, *Energy & Environmental Science*, 2012, **5**, 9626-9631.
2. P. Singh and J. B. Goodenough, *Journal of the American Chemistry Society*, 2013, **135**, 10149-10154.
3. R. Martinez-Coronado, P. Singh, J. Alonso-Alonso and J. B. Goodenough, *Journal of Materials Chemistry A*, 2014, **2**, 4355-4360.
4. T. Wei, P. Singh, Y. Gong, J. B. Goodenough, Y. Huang and K. Huang, *Energy & Environmental Science*, 2014, **7**, 1680-1684.
5. R. D. Bayliss, S. N. Cook, S. Fearn, J. A. Kilner, C. Greaves and S. J. Skinner, *Energy & Environmental Science*, 2014, **7**, 2999-3005.
6. I. R. Evans, J. S. O. Evans, H. G. Davies, A. R. Haworth and M. L. Tate, *Chemistry of Materials*, 2014, **26**, 5187-5189.
7. C. Tealdi, L. Malavasi, I. Uda, C. Ferrara, V. Berbenni and P. Mustarelli, *Chemical Communications*, 2014, **50**, 14732-14735.
8. R. D. Bayliss, S. N. Cook, D. O. Scanlon, S. Fearn, J. Cabana, C. Greaves, J. A. Kilner and S. J. Skinner, *Journal of Materials Chemistry A*, 2014, **2**, 17919-17924.
9. T. N. Nadezhina, E. A. Pobedimskaya, V. V. Ilyukhin, N. N. Nikishina and N. V. Belov, *Doklady Akademii Nauk SSSR*, 1977, **233**, 1086-1089.
10. W. Hilmer, *Soviet Phys. Cryst.(English Transl.)*, 1963, **7**, 573-576.
11. K. I. Machida, G. Y. Adachi, J. Shiokawa, M. Shimada and M. Koizumi, *Acta Crystallographica B*, 1982, **38**, 386-389.
12. F. Nishi, *Acta Crystallographica C*, 1997, **53**, 399-401.
13. F. Nishi, *Acta Crystallographica C*, 1997, **53**, 534-536.
14. J. Hack, Summer Project Report, Durham University and Institut Laue-Langevin, 2014.
15. C. Kaps, *Journal of Non-Crystalline Solids*, 1984, **65**, 189-192.
16. B. R. Young, *Mineral Mag*, 1978, **42**, 35-40.
17. Y. Takahashi, H. Masai, T. Fujiwara, K. Kitamura and S. Inoue, *Journal of the Ceramic Society of Japan*, 2008, **116**, 357-360.
18. C. Hejny, R. Miletich, A. Jasser, P. Schouwink, W. Crichton and V. Kahlenberg, *American Mineralogist*, 2012, **97**, 1749-1763.
19. Z. Tang, D. Wang, Y. Wang, W. U. Khan and S. Du, *Materials Research Bulletin*, 2016, **83**, 336-339.
20. S. Liu, Y. Liang, Y. Zhu, X. Wu, R. Xu, M. Tong and K. Li, *Optics & Laser Technology*, 2016, **84**, 1-8.
21. Y. Jin, Y. Hu, L. Chen and X. Wang, *Optical Materials*, 2014, **36**, 1814-1818.

22. H. Guo, Y. Wang, G. Li, J. Liu, P. Feng and D. Liu, *Journal of Materials Chemistry C*, 2017, **5**, 2844-2851.
23. X. Wu, D. Xu, W. Li, T. Wang, L. Cao and J. Meng, *Luminescence*, 2017, **32**, 1554-1560.
24. H. Mizoguchi, T. Kamiya, S. Matsuishi and H. Hosono, *Nature Communications*, 2011, **2**, 470.
25. R. D. Shannon, *Acta Crystallographica A*, 1976, **32**, 751-767.
26. K. Nomura, *Solid State Ionics*, 2000, **132**, 235-239.
27. A. A. Coelho, J. S. O. Evans, I. R. Evans, A. Kern and S. Parsons, *Powder Diffraction*, 2012, **26**, S22-S25.
28. H. M. Rietveld, *Journal of Applied Crystallography*, 1969, **2**, 65-71.
29. X. Xue and J. F. Stebbins, *Physics and Chemistry of Minerals*, 1993, **20**, 297-307.
30. X. Y. Xue, J. F. Stebbins, M. Kanzaki, P. F. McMillan and B. Poe, *American Mineralogist*, 1991, **76**, 8-26.
31. D. C. Apperley, R. K. Harris and P. Hodgkinson, *Solid-State NMR Basic Principles and Practice*, Momentum Press, New York, 2012.
32. Y. Jee, X. Zhao and K. Huang, *Chemical Communications*, 2015, **51**, 9640-9642.
33. P. Heitjans and S. Indris, *Journal of Physics: Condensed Matter*, 2003, **15**, R1257-R1289.
34. A. George and J. Stebbins, *Physics and Chemistry of Minerals*, 1996, **23**, 526-534.
35. N. Nakamura, *Zeitschrift Fur Naturforschung Section A*, 1994, **49**, 337-344.
36. R. Maury and J. Iiyama, *Bollettino Svizzero Di Mineralogia E Petrografia* 1967, **47**, 3-11.
37. P. Colombet, M. Danot and J. Rouxel, *Materials Research Bulletin*, 1979, **14**, 813-820.
38. T. J. Udovic, M. Matsuo, A. Unemoto, N. Verdal, V. Stavila, A. V. Skripov, J. J. Rush, H. Takamura and S.-i. Orimo, *Chemical Communications*, 2014, **50**, 3750-3752.
39. A. V. Skripov, O. A. Babanova, A. V. Soloninin, V. Stavila, N. Verdal, T. J. Udovic and J. J. Rush, *The Journal of Physical Chemistry C*, 2013, **117**, 25961-25968.
40. X. Lei, Y. Jee and K. Huang, *Journal of Materials Chemistry A*, 2015, **3**, 19920-19927.
41. J. R. Peet, C. M. Widdifield, D. C. Apperley, P. Hodgkinson, M. R. Johnson and I. R. Evans, *Chemical Communications*, 2015, **51**, 17163-17165.
42. K. K. Inglis, J. P. Corley, P. Florian, J. Cabana, R. D. Bayliss and F. Blanc, *Chemistry of Materials*, 2016, **28**, 3850-3861.
43. P.-H. Chien, Y. Jee, C. Huang, R. Dervişoğlu, I. Hung, Z. Gan, K. Huang and Y.-Y. Hu, *Chem. Sci.*, 2016, **7**, 3667-3675.
44. J. Xu, S. Liu, Q. Wang, J. Xiaofeng, X. Li and X. Kuang, *Journal of Materials Chemistry A*, 2016, **4**, 6313-6318.
45. L. León-Reina, J. M. Porras-Vázquez, E. R. Losilla and M. A. G. Aranda, *Solid State Ionics*, 2006, **177**, 1307-1315.
46. E. Kendrick, M. S. Islam and P. R. Slater, *Journal of Materials Chemistry*, 2007, **17**, 3104-3111.
47. H. G. Davies, Master of Chemistry MChem Research Project Report, Durham University, 2014.
48. D. C. Sinclair, *Bol Soc Esp Ceram V*, 1995, **34**, 55-65.
49. J. T. S. Irvine, D. C. Sinclair and A. R. West, *Advanced Materials*, 1990, **2**, 132-138.
50. J. Sansom, *Solid State Ionics*, 2001, **139**, 205-210.
51. X. Kuang, M. A. Green, H. Niu, P. Zajdel, C. Dickinson, J. B. Claridge, L. Jantsky and M. J. Rosseinsky, *Nature Materials*, 2008, **7**, 498-504.
52. D. K. Smith and W. Newkirk, *Acta Crystallographica*, 1965, **18**, 983-991.
53. J. B. Goodenough, *Annual Review of Materials Research*, 2003, **33**, 91-128.

Chapter 4. Oxide Ion Dynamics and Conduction Mechanisms in $La_2Mo_2O_9$

4.1. Abstract

In this chapter the first quasielastic neutron scattering (QENS) study of oxide ion dynamics on a nanosecond timescale is presented, investigating diffusion processes in $La_2Mo_2O_9$. The findings from an in depth *ab initio* molecular dynamics (AIMD) investigation into $La_2Mo_2O_9$, with a larger simulation box and significantly longer simulation time than that previously reported, are also presented. From this combination of experimental and computational approaches, new atomic-level insight into the conduction processes occurring in this material is provided.

4.2. Introduction and Background

4.2.1. Structure of $La_2Mo_2O_9$

The oxide ion conducting properties of lanthanum molybdate were first reported by Lacorre *et al.*[1] The conductivity reaches 6×10^{-2} S cm^{-1} at 800 °C after an abrupt increase of two orders of magnitude at 560 °C, accompanying a phase transition from the low temperature α-form to the high temperature β-form. The average structure of the high temperature β-$La_2Mo_2O_9$ is cubic, with space group $P2_13$ and a cell parameter $a = 7.20$ Å.[2] It contains a single unique Mo site and three unique O sites.[3] The room temperature α-$La_2Mo_2O_9$ structure was found to be a complex superstructure with unit cell dimensions of $\approx 2a \times 3a \times 4a$ relative to β-$La_2Mo_2O_9$ and a very small monoclinic distortion.[4] The oxygen atoms in this phase are distributed over 216 unique sites making up 4-, 5- and 6-coordinate MoO_x polyhedra (figure 4.1a).

The β-structure represents a time and space average of the α-form, and the α-to-β structural phase transition corresponds to an order-disorder transition which results in the increased mobility of the oxide ions in the material (figure 4.1b);[4] this relationship was subsequently confirmed by a neutron total scattering study.[5] The relationship between the two forms of $La_2Mo_2O_9$ suggests that the oxide ions from all unique crystallographic sites participate in the conduction process in the highly conducting high-temperature form.[4] This has also been implied by low frequency internal friction measurements,[6] in which the time delay of a sample's strain response to an applied stress is determined. These measurements showed two internal friction peaks, representing energy loss due to internal relaxation processes, which were assigned to oxygen diffusion between different pairs of oxygen sites O1↔O2 and O1↔O3.

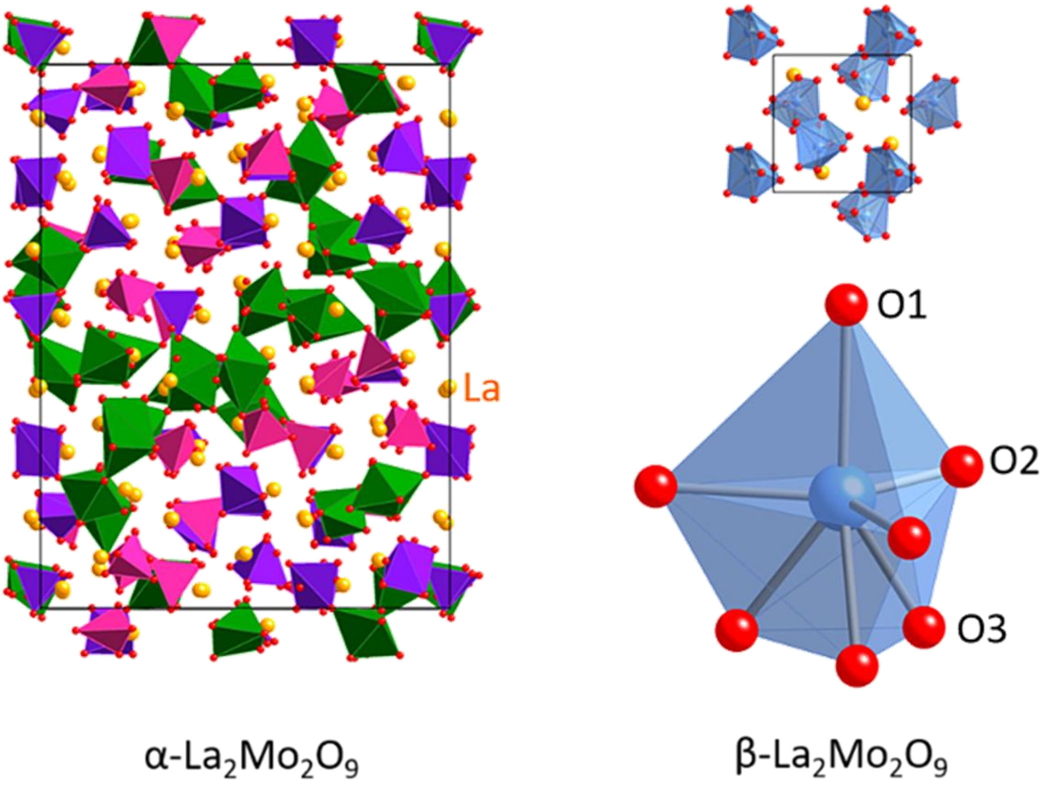

Figure 4.1: a) the room temperature structure of α-$La_2Mo_2O_9$ emphasising different MoO_x coordination polyhedra; b) the structure of β-$La_2Mo_2O_9$ and disordered coordination environment around each Mo.

4.2.2. Mechanisms of Oxide Ion Conduction in $La_2Mo_2O_9$

Research into $La_2Mo_2O_9$ and related materials has largely been focused on trying to eliminate the abrupt structural phase transition and stabilise the highly conducting β-form at lower temperatures. This has been attempted by doping with a large number of different cations including alkali metals,[7-9] alkali earths,[9, 10] rare earths,[3, 11-16] Bi[17-19] and Pb[20] on the La site and transition metals[9, 10, 13, 16, 21, 22] and S[9] on the Mo site. In many cases this has been successful, leading to higher conductivity below 580 °C than in the parent material. In addition, the phase transition has been shown to be suppressed in $La_2Mo_2O_9$ nanowires which also show extremely high conductivity.[23] Despite these successes the utility of these materials in SOFCs is limited by their reducibility under an H_2 atmosphere which leads to structural changes and electronic conductivity.[24-27] Attempts to remedy this with W^{6+} doping on the Mo site has met with some success, with a $La_2Mo_{0.6}W_{1.4}O_9$ electrolyte showing good stability in the 550-650 °C temperature range, but requiring further investigation to find compatible electrode materials.[28, 29] The mixed electronic and ionic conductivity has led to the studies of reduced $La_2Mo_2O_9$ ($La_2Mo_2O_{7-\gamma}$) as an anode material in SOFCs which have shown good results up to 700 °C.[30, 31]

Investigation into the precise mechanisms of conduction in $La_2Mo_2O_9$, on the other hand, has been relatively sparse. Initially it was assumed that the partially occupied O2 and O3 sites were the cause of conductivity, with the O1 sites remaining static.[9] It was also observed that doped compounds that maintain the β-phase at low temperature exhibit a change from Arrhenius to Vogel-Fulcher-Tammann (VFT) behaviour at higher temperatures.[3] The difference between these behaviours is described in Chapter 1, section 1.2.1. In an attempt to explain this, Lacorre *et al.*[32] proposed that tilting of $O1La_3Mo$ tetrahedral units as temperature increased allowed greater volume for O2 and O3 oxygens to diffuse. They performed a series of classical molecular dynamics simulations at 1227 °C with these units titled at various angles and found that a 5° rotation led to an order of magnitude increase in diffusion coefficient (calculated from mean square displacements of the O2 and O3 ions), although they did not show that such rotations occur in the real material.

A later neutron diffraction study by the same group[33] found that, instead of this tilting, the structural changing accompanying the increase in conductivity was expansion of the faces of the oxygen-centred $O1La_3Mo$ tetrahedral units, allowing the O1 atoms, previously thought to be static, to leave their site and diffuse to partially occupied sites on adjacent Mo atoms. This extra conduction path was therefore proposed to be the origin of the VFT behaviour. However, this study was carried out on a Bi-doped sample, $La_{1.7}Bi_{0.3}Mo_2O_9$, rather than the parent compound.

An *ab initio* molecular dynamics (AIMD) study of $La_2Mo_2O_9$ by Hou *et al.*, performed every 100 °C from 627 to 1227 °C,[34] also found that O1 atoms were involved in oxygen diffusion, being a part of one of the two diffusion paths found. The first pathway they proposed involves an O2 ion jumping to an unoccupied O3 site in a neighbouring MoO_x polyhedron. This is accompanied by the movement of an existing O3 ion in that polyhedron to a vacant O2 site on the same polyhedron. This new O2 atom can then repeat the first step to another polyhedron giving overall long range diffusion that is aided by the variable coordination number of the Mo atoms. The second pathway involves similar exchange of oxygen atoms between tetrahedra but instead the oxygen atom in O1 site is displaced to an O2 site by an O3 atom from an adjacent tetrahedron. The second pathway was found to have much higher activation energy than the first (1.24 eV versus 0.5 eV), but despite this their study did not investigate explicitly how the mechanisms changed with temperature. They also only used a small simulation box consisting of a single β-unit cell which could lead to a poor sampling of diffusion events.

The two process proposition was supported in a study by Kezionis *et al.*[35] who carried out an analysis based on a distribution of relaxation times using broadband impedance spectroscopy. They observed two relaxation processes in $La_2Mo_2O_9$; one process which is present in both low- and high- temperature phases (referred to as the α-process), although reaching a maximum around the phase transition, and a different process which dominates in the β-phase (the β-process). They proposed that the reason for the continued presence of the α-process in the high temperature phase could be because it remains as part of the overall conductivity mechanism, in effect being a part of the β-process.

4.2.3. Objectives of This Work

The objective of the work presented in this chapter was to investigate the mechanisms of oxide ion conduction in $La_2Mo_2O_9$. Neutron scattering experiments were carried out on both IN6 and IN16b at the ILL in order to probe dynamics on picosecond and nanosecond timescales respectively. *Ab initio* molecular dynamics simulations were carried out at 500, 800, 900 and 1000 °C in order to identify diffusion mechanisms present and to allow quantitative analysis of how increasing temperatures affects these processes.

4.3. Experimental

4.3.1. Synthesis of $La_2Mo_2O_9$ samples for IN16b and IN6 experiments

10g samples of $La_2Mo_2O_9$ were prepared from stoichiometric amounts of La_2O_3 and MoO_3. The La_2O_3 was weighed out separately and heated at 1000 °C for 12 hours to remove any traces of $La_2(CO_3)_3$. The reactants were thoroughly mixed and ground together then placed in an alumina crucible and fired at 900 ˚C for 72 hours with intermediate grinding and heating and cooling rates of 5 ˚C min^{-1}. Sample purity was confirmed by laboratory powder X-ray diffraction (XRD) as described in chapter 2.2.

4.3.2. X-ray Diffraction

Variable temperature XRD data was also collected to investigate the evolution of the unit cell parameters of $La_2Mo_2O_9$ over the temperature range from room temperature to 800°C. Patterns were recorded over a 2θ range of 10-120° on heating and cooling with a temperature increment of 10 °C and with a collection time of 15 minutes at each temperature. A small amount of Al_2O_3 was used as an internal standard. The experiments were carried out on a Bruker AXS D8 Advance diffractometer with a Vantec detector, Cu $K_{\alpha1}$ radiation, and an Anton Paar HTK1200 high-temperature attachment and a Vantec detector. Collected patterns were fitted by Reitveld refinement[36] using TOPAS Academic.[37] The data in the entire temperature range were fitted using the monoclinic α-phase structural model, by varying the unit cell parameters and three isotropic temperature factors (one each for La, Mo and O).

4.3.3. Quasielastic and Inelastic Neutron Scattering

Neutron scattering data probing picosecond timescales were collected on time-of-flight spectrometer IN6 at the Institut Laue-Langevin (ILL) with an incident neutron wavelength of 5.92 Å. Data were collected at 200 °C and from 500-900 °C in steps of 100 °C. At each temperature data were collected for 8 hours. Data were also collected on a vanadium sample at 20 °C for 6 hours to provide the instrument resolution function.

Neutron scattering data probing nanosecond timescales were collected on the backscattering spectrometer IN16b at the ILL. A 10 g powdered sample was placed in a cylindrical Nb sample holder and exposed to neutrons with an incident wavelength of 6.27 Å. Initially measurements of elastic intensity were made from 450-900 °C with a heating rate of 1/110 °C s^{-1}. Data points were counted every 60 seconds. After confirming the onset of dynamics occurring at 560 °C, QENS measurements were performed at eight temperatures between 550 °C and 750 °C with an energy transfer window of ±10 μeV. Data were collected for 3 hours at each temperature except at 570 °C, just after the onset of dynamics, for which a total of 6 hours of data were collected. For the analysis of QENS data, a resolution function was determined from low temperature data from the sample and a standard vanadium sample – the resolution full-width at half-maximum was 0.73 μeV. The data from both the IN6 and IN16b neutron scattering experiments were analysed using the LAMP software.[38]

4.3.4. Computational

Ab initio molecular dynamics (AIMD) calculations were carried out using DFT method implemented in the VASP code.[39] The simulations were performed on a 2 × 2 × 2 supercell of the cubic high temperature $P2_13$ structure[2] giving a simulation box containing 32 La, 32 Mo and 144 O atoms. The O2 and O3 locations were chosen using a random number generator from the partially occupied sites in the high temperature structure in order to match the required stoichiometry and site occupancies. PAW pseudopotentials[40] were used with GGA-PBE functionals.[41] The electronic structure was sampled only at the gamma point. The AIMD calculations were performed at 500 °C, 800 °C, 900 °C and 1000 °C in the NVT ensemble. For the 500 °C and 1000 °C simulations 3.25×10^5 steps of 2 fs were calculated giving a total of 650 ps of simulation time. For the 800 °C and 900 °C temperatures 50,000 steps were calculated giving 100 ps of simulation time. It should be noted that while the lowest temperature simulated was 500 °C, this cannot be directly compared to experimental temperatures and so it cannot be said to be simulating the low temperature α-phase, despite being nominally below the phase transition. Instead all simulations should be thought of as based on β-$La_2Mo_2O_9$ but with atoms given higher or lower kinetic energy based on nominal temperature. Mean square displacements and density of states were produced using the MDANSE code[42] and cloud plots for trajectory visualisation were produced using LAMP.[38] A phonon density of states (DOS) was also determined from gamma-point phonons calculated using DFT with the finite displacement method. This calculation was performed on a slightly smaller 2 × 2 × 1 supercell, produced in the same way as the 2 × 2 × 2 supercell described above, but for which the calculation time was approximately ten times shorter.

4.4. Results and Discussion

4.4.1. Sample Purity Confirmation

Figure 4.2 shows the collected powder XRD pattern for the synthesised $La_2Mo_2O_9$. Rietveld refinement[36] was carried using a starting model based on the room temperature α-phase as described by Evans *et al.*[2] The refinement parameters include background terms, zero point, scale factor, a single temperature factor, peak shape terms and the cell parameters *a*, *b, c* and the cell β angle.

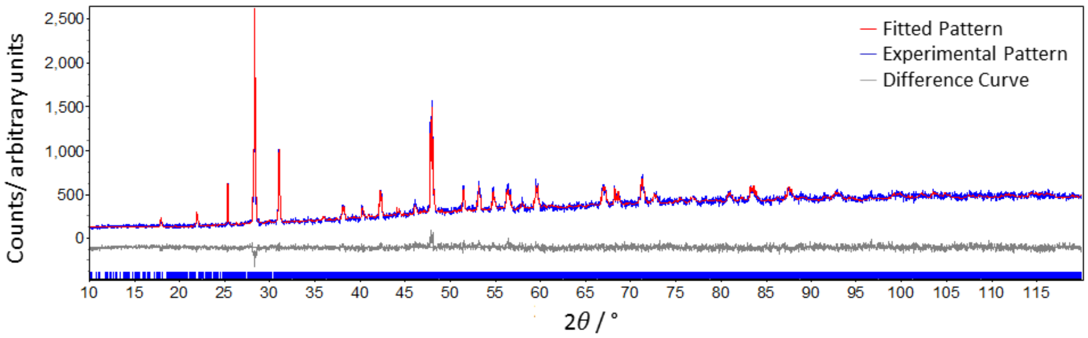

Figure 4.2: XRD pattern collected for synthesised $La_2Mo_2O_9$ fitted via Rietveld refinement. The cell parameters found were a = 14.3463(4) Å, b = 21.4932(5) Å, c = 28.6136(7) Å and β = 90.462(2)°. R_{wp} = 6.07 %.

All peaks observed in the experimental pattern have been fitted with no impurities observed. The cell parameters match those found by Evans *et al.* very closely. Given these factors and the low value for R_{wp} it was decided that this sample is pure and suitable for QENS studies.

4.4.2. Probing Dynamics on the Picosecond Timescale

4.4.2.1. The Variation of Scattering Function with Temperature

Figure 4.3a, shows the inelastic neutron scattering data collected on IN6. The variation of the angle-integrated scattering function, $S(\omega)$, with temperature shows inelastic contributions that increase in amplitude with increasing temperature. However, this increase can be accounted for at all temperatures by the phonon Bose population factor (Chapter 2, section 2.3.4.1). The $S(\omega)$ spectra after applying the correction $S(\omega)/n_B$ can be seen in figure 4.3b. As the spectra match very closely it is clear that the difference in intensity in figure 4.3a is due to increases in phonon intensity with temperature and therefore there is no quasielastic signal present. The oxygen diffusion dynamics in $La_2Mo_2O_9$ are therefore slower than the picosecond timescales probed by IN6 and previously observed in $Bi_{26}Mo_{10}O_{69}$[43] and $Sr_2Fe_2O_5$.[44]

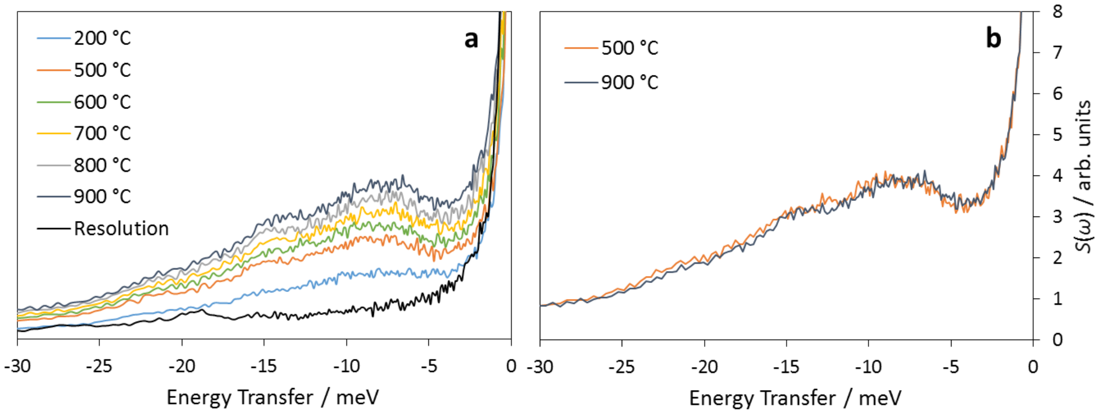

Figure 4.3: a) The Q-integrated scattering function, $S(\omega)$, against neutron energy transfer at various temperatures for a sample of $La_2Mo_2O_9$ measured on IN6. A resolution function from a vanadium sample has been provided for comparison. b) $S(\omega)$ after correction for the Bose population factor. Only two temperatures are shown here for clarity.

4.4.2.2. Comparison of Phonon Density of States from Different Techniques

Figure 4.4a shows the density of states (DOS) measured on IN6 at 900 °C compared with the density of states calculated from complementary AIMD simulations at 1000 °C and DFT phonon calculations. All three curves match closely, with the two main peaks located at 20 and 40 meV clearly present in all three cases. The lower intensity of the 40 meV peak in the experimental DOS may be due to a broadening of the feature which can also be seen as relatively high intensity compared to the calculated curves in the 50-80 meV region. This may be due to high oxygen mobility increasing the range of oxygen environments and could indicate that the AIMD calculations, despite being nominally performed at 1000 °C, underestimate the overall conductivity seen in experiments in this temperature range. The phonon calculation is based on a static (0 K) structure and so the features are even narrower than the AIMD curve. The two calculated DOS curves both have a third peak at 100 meV, whereas the experimental DOS is not so clear at high energies since the high energy phonons are weakly populated at the temperature of the measurement and the Bose population factor is applied to a weak signal.

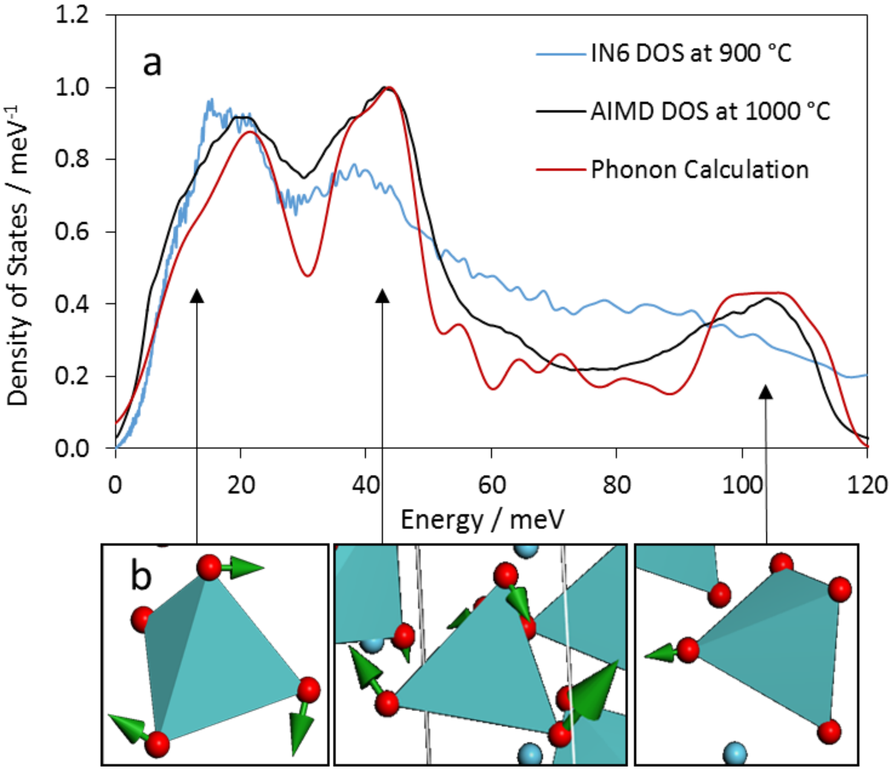

Figure 4.4: a) Phonon DOS calculated from AIMD and DFT phonon calculations compared with experimental results from IN6 neutron scattering. The calculated curves have been weighted according to neutron scattering power of La, Mo and O and all three curves have been scaled to reach a maximum value of 1. b) Types of modes associated with the three main peaks in the DOS. The green arrows represent simultaneous atom movement with the size scaled to the distance moved. Red atoms are O and blue atoms and polyhedra are Mo.

The agreement between the three methods of determining the DOS supports the validity of the AIMD simulations and provides evidence that conclusions drawn from them are reliable. The locations of the peaks are consistent with those found in similar oxide ion conducting materials such as $Bi_{26}Mo_{10}O_{69}$.[43] The phonon calculations allow the identification of the types of modes that make up each part of the DOS. The lowest energy modes found in the first peak are librations of the Mo-O polyhedra; the second peak is made up of bending modes involving distortions of the polyhedra. These give way to stretching modes found in the high energy band. Representative examples of these motions can be seen in figure 4.4b.

4.4.3. Probing Dynamics on the Nanosecond Timescale

4.4.3.1. The Variation of Elastic Intensity with Temperature

A plot of elastic intensity against temperature for $La_2Mo_2O_9$ is shown in figure 4.5. There is a large decrease of around 30 % in the elastic intensity around 560 °C, deviating from the gradual decrease in intensity due to Debye-Waller effects (the loss of elastic intensity to inelastic background noise due to thermal motions) observed elsewhere in the temperature range. This coincides with the α-to-β phase transition described in 5.1.1. The phase transition leads to higher conductivity and indicates the onset of oxygen dynamics on the nanosecond timescales probed by IN16b. These data represent the first direct observation of oxygen dynamics via neutron scattering on these timescales which are the longest reported to date.

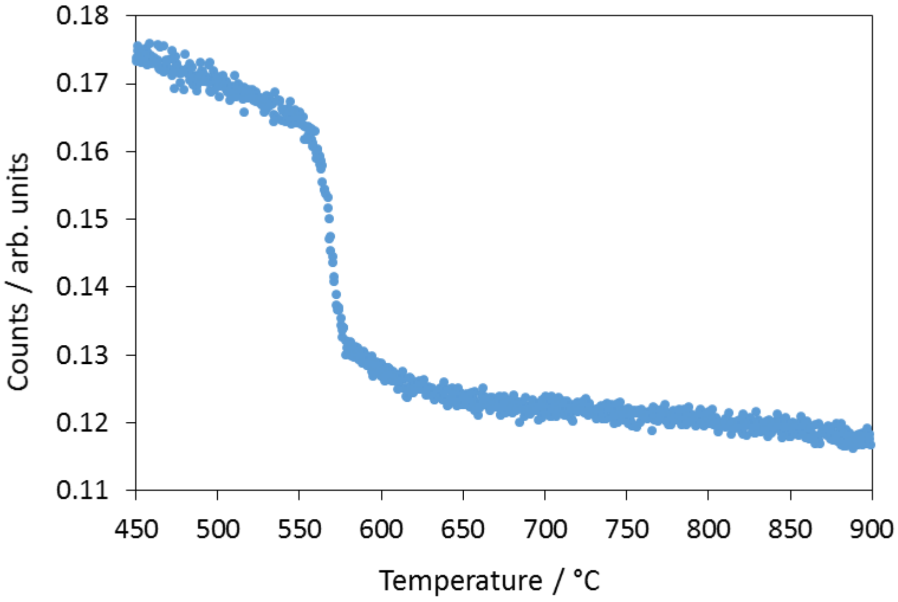

Figure 4.5: A plot of the elastic intensity against temperature for a neutron scattering experiment on $La_2Mo_2O_9$ carried out with IN16b. Each temperature point was collected for 60 seconds.

An abrupt decrease of Bragg intensity (beyond that due to the Debye-Waller factor) can also be observed in the plot of the variation of the $La_2Mo_2O_9$ scale factor from Rietveld refinements against the variable temperature XRD data (figure 4.6a) demonstrating the potential use of laboratory XRD data as a preliminary screening method for neutron scattering experiments. The scale factor shown is normalised relative to that of an Al_2O_3 internal standard (in which no phase transition occurs, figure 4.6b). The observed decrease in the cooling data is around 16 %, lower in magnitude than that seen in the neutron elastic data, mainly due to the relative scattering power of oxygen to La and Mo being much lower for X-rays than neutrons.

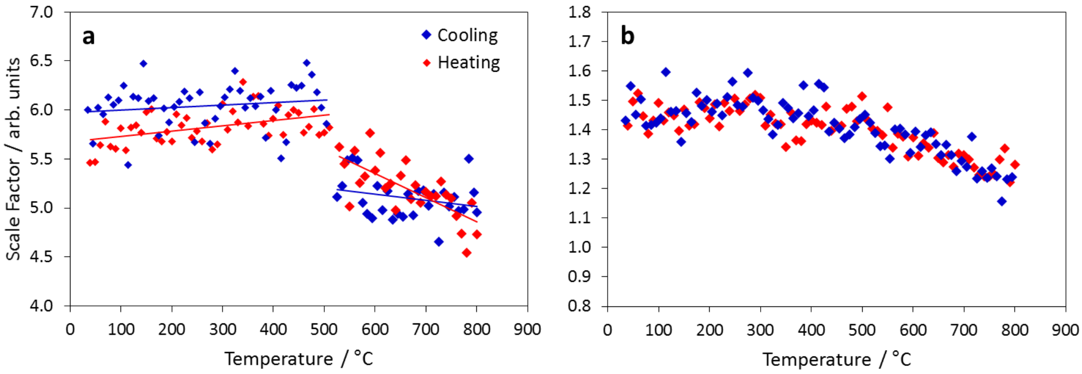

Figure 4.6: a) The scale factors found during Rietveld refinement of variable temperature XRD data against temperature for a sample of $La_2Mo_2O_9$ normalised with an Al_2O_3 internal standard. Best fit lines are shown for pre and post phase transition data to guide the eye. b) The scale factors for the alumina standard shown for comparison. Data points recorded while heating are shown in red while data points while cooling are shown in blue.

4.4.3.2. The Variation of Scattering Function with Temperature

Plots of $S(\omega)$ against energy transfer, figure 4.7a, for a selection of the measured temperatures show an elastic peak as well as a clear quasielastic signal above 550 °C that evolves with temperature. No QENS signal is observed in the 550 °C data set, which is similar to the resolution function in terms of linewidth. At 570 °C and above the QENS signal is very clear, with broadening becoming visually apparent at 610 °C. This broadening becomes very large at high temperatures with the amplitude of the QENS peak therefore becoming very low at 750 °C. This broadening is due to the continued increase in the rate of motion as temperature increases, and the evolution of the spectral linewidth of this Lorentzian peak (Γ) can be used to determine an activation energy for the dynamic process. To do this, the QENS features at each temperature except 750 °C were fitted with a delta function representing the elastic peak and a Lorentzian for the quasielastic peak, both convoluted with the resolution function as shown in figure 4.7b. A flat background was used in the fitting. The resulting values of Γ are plotted against temperature in figure 4.8a. The points at 550 and 750 °C clearly do not fit the trend. For 550 °C this is due to the aforementioned lack of QENS signal. The very large broadening at 750 °C makes a reliable fit impossible due to the Lorentzian linewidth being larger than the measured energy transfer window.

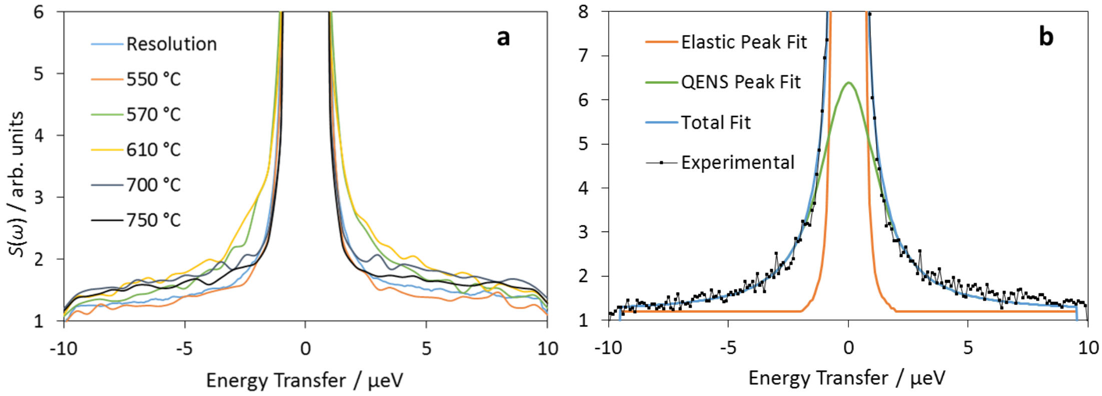

Figure 4.7: a) $S(\omega)$ spectra for inelastic neutron scattering measurements on $La_2Mo_2O_9$ at various temperatures with a maximum energy transfer of ±10 μeV. The data has been summed over all Q. A resolution function is also shown. b) Fitting of the 570 °C dataset.

Assuming a Chudley-Elliott jump diffusion model, as has been shown for other ionic conductors, the linewidths Γ obtained from these fits are proportional to the diffusion coefficients and so can be expected to follow an Arrhenius relationship with temperature.[45] A plot of ln(Γ) against 1000/T (figure 4.8b) yields an activation energy of 0.61(5) eV. This is in very good agreement with the value of 0.66(9) eV found by Liu *et al.*[46] for oxide ion diffusion in β-$La_2Mo_2O_9$ using ^{18}O tracer experiments above 570 °C.

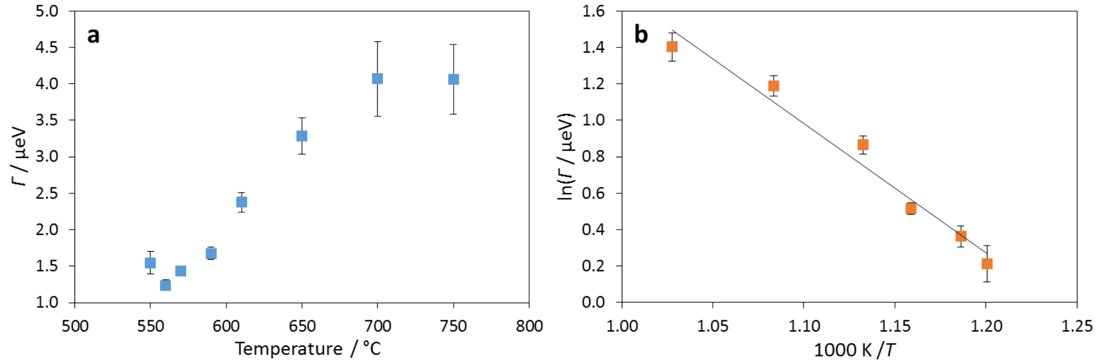

Figure 4.8. a) A plot of the QENS spectral linewidth Γ against temperature for $La_2Mo_2O_9$ over a 550-750 °C temperature range. The linewidths were determined by least squares fitting and the error bars represent the uncertainties from these fits. b) An Arrhenius plot showing the variation of the spectral linewidth with inverse temperature. Points for 550 °C and 750 °C have been omitted (see text).

Both these activation energies are lower than the value of 1.2 eV found for β-$La_2Mo_2O_9$ by Lacorre *et al.*[1] using impedance spectroscopy. Differences between activation energies determined from macroscopic measurements such as impedance spectroscopy and microscopic measurements such as neutron scattering or NMR have previously been reported for oxide ion conductors[47, 48], Na^+ conductors[49-51] and Li^+ conductors.[52, 53] In the present case it was also found that the microscopic measurements give significantly lower activation energies. This is presumably related to grain boundary or pellet density effects in impedance measurements leading to higher values, whereas the direct observation of dynamics using neutron scattering techniques have no (or minimal) dependence on sample morphology or form.

4.4.3.3. Fitting of the Q Dependence of the Scattering Function

Data collection at 570 °C was carried out for twice the duration as at other temperature in an attempt to gain good enough statistics to show the variation of the scattering function with ***Q***. The scattering functions at each ***Q*** value at 570 °C have been fitted with a Lorentzian (QENS peak) and a delta function (elastic peak) convoluted with the resolution as described in the previous section. The linewidth Γ of the Lorentzian is expected to follow the Chudley-Elliott model (equation 1.8, given in Chapter 1, Section 1.4.2).[45] The fit of this model to the Γ values at 570 °C is shown in figure 4.9. ***Q*** values close to Bragg peaks, (***Q*** = 0.82 0.95, 1.72, 1.90 Å^{-1}), have been removed as the large increase in elastic intensity at these values distorts the fits.

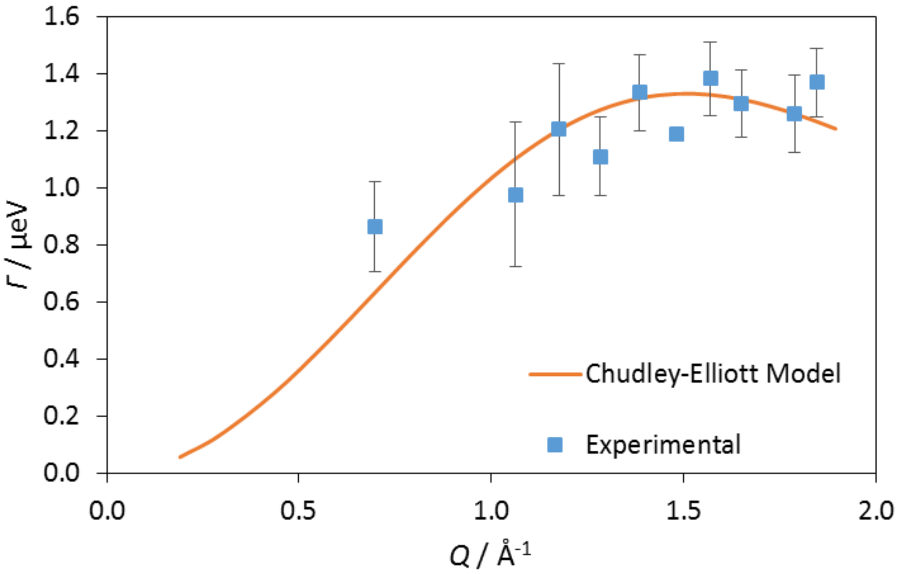

Figure 4.9: Values of QENS spectral linewidth Γ against *Q* for a sample of $La_2Mo_2O_9$ at 570 °C fitted with the Chudley-Elliott model. *Q* values corresponding to Bragg peaks have been removed.

The values for the jump distance, l, and lifetime, τ, obtained from this fit are 3.0(1) Å and 1.8(2) ns, respectively. The lifetime found is in good agreement with the approximately nanosecond relaxation times found by Kezionis *et al.*[35] for the process occurring at higher temperatures (which they refer to as the β-process, equivalent to the process involving O1 atoms found using AIMD, *vide infra*). The lifetime also matches well with the timescales probed by IN16b potentially indicating that the β-process is the one being probed by this instrument.

4.4.4. Conduction Mechanisms Investigated by *Ab Initio* Molecular Dynamics

4.4.4.1. Investigation of Oxygen Diffusion as a Function of Temperature

The high–temperature β-$La_2Mo_2O_9$ contains three crystallographically unique oxygen sites: one fully occupied site on the three-fold axis (O1) and two partially occupied sites with fractional occupancies 0.78 (O2) and 0.38 (O3), disordered around the three-fold axis of the cubic unit cell (figure 4.1). Figure 4.10 shows the mean square displacement (MSD) of the oxygen atoms at each temperature for the first 100 ps calculated. As expected, the MSDs grow larger as temperature increases indicating increased oxide ion mobility. There is no evidence of the MSD saturating at any of the temperatures indicating that the motion is not confined to a fixed volume.

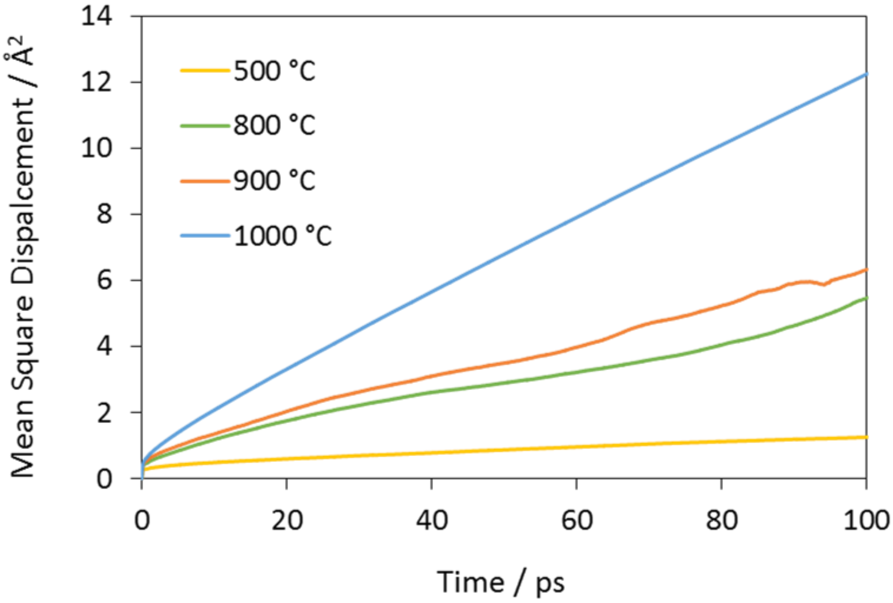

Figure 4.10: Mean square displacements for oxygen atoms calculated from trajectories of 100 ps from AIMD simulations at several temperatures.

This is in contrast to the MSDs reported by Hou *et al.*[34], who found saturation at temperatures up to 927 °C, possibly due to a small simulation box used, providing poor sampling of diffusion events at intermediate temperature. In our simulations, apart from at the lowest temperature simulated, the average displacement is above 2.2 Å, i.e. longer than the shortest distance between different oxygen sites on the disordered MoO_x polyhedra (figure 4.1), indicating that substantial oxide ion migration between different Mo sites is occurring. Figure 4.11 shows the MSDs at 500 °C and 1000 °C over the full length of the simulations carried out at these temperatures. The 500 °C MSD gives a final average displacement over 500 ps of ≈ 1.9 Å, larger than the shortest distance between the O sites on the same MoO_x polyhedron, but smaller than the shortest O-O distance between two adjacent MoO_x polyhedra. This means that some jumping between sites is occurring, albeit at a significantly lower rate than at the higher temperature. The 1000 °C MSD continues to grow with time without saturation reaching an average displacement of ≈ 7.1 Å, almost equivalent to the length of a β-$La_2Mo_2O_9$ unit cell edge, indicating significant long-range oxide ion diffusion.

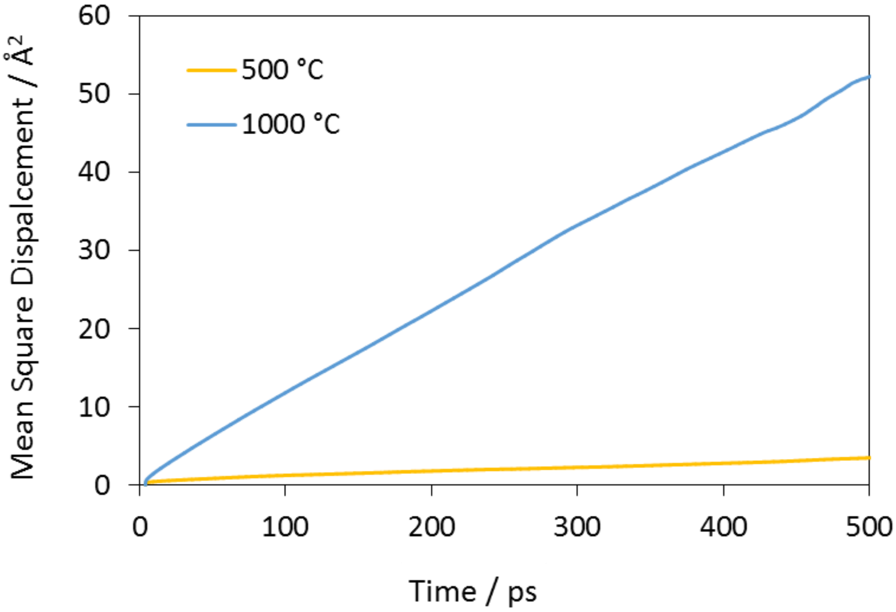

Figure 4.11: Mean square displacements for oxygen atoms calculated from the full trajectories of AIMD simulations at 500 and 1000 °C.

In order to compare the number of diffusion events occurring at 500 °C and 1000 °C, the oxide ion jumps that occurred during each trajectory were counted. For this purpose, a jump was defined as an oxide ion moving a distance of at least 1.5 Å (the smallest distance between crystallographic sites shown in figure 4.1) within 500 simulations steps, and it was noted whether the closest Mo atom was the same or different before and after the jump. On this basis, each jump was classified as an intra-MoO_x or an inter-MoO_x jump. Table 4.1 shows the numbers of jumps recorded at each temperature.

At both temperatures approximately 60 % of the events were intra-MoO_x jumps, with the rest being inter-MoO_x jumps. This indicates that the overall oxide ion migration mechanisms in $La_2Mo_2O_9$ consists of two main processes: the movement of oxide ions from one site to a vacant site on the same Mo atom, which is a local motion, and jumping between different Mo atom sites, which accounts for the long-range motion. It is the ability of Mo^{6+} to support variable coordination environments that allows this long-range motion to occur. The average jump distance at both temperatures is 1.8(3) Å, which is slightly longer than the distance between nearest crystallographic sites.

Table 4.1: The number of intra-MoO_x and inter-MoO_x oxide ion jumps counted over the entire simulation at 500 °C and 1000 °C. Percentages of each type are also shown.

Jump Type	500 °C		1000 °C	
	Count	%	Count	%
Intra-MoO_x	143	62	1113	60
Inter-MoO_x	88	38	755	40
Total	231	100	1868	100

Plots of the evolution of the coordination number (defined here as the number of oxygen atoms within 2.5 Å, determined based on the pair distribution function obtained from the calculations) of each Mo atom throughout the simulations illustrate that Mo atoms change coordination number between 4, 5 and 6; this is demonstrated for three Mo atoms in figure 4.12.

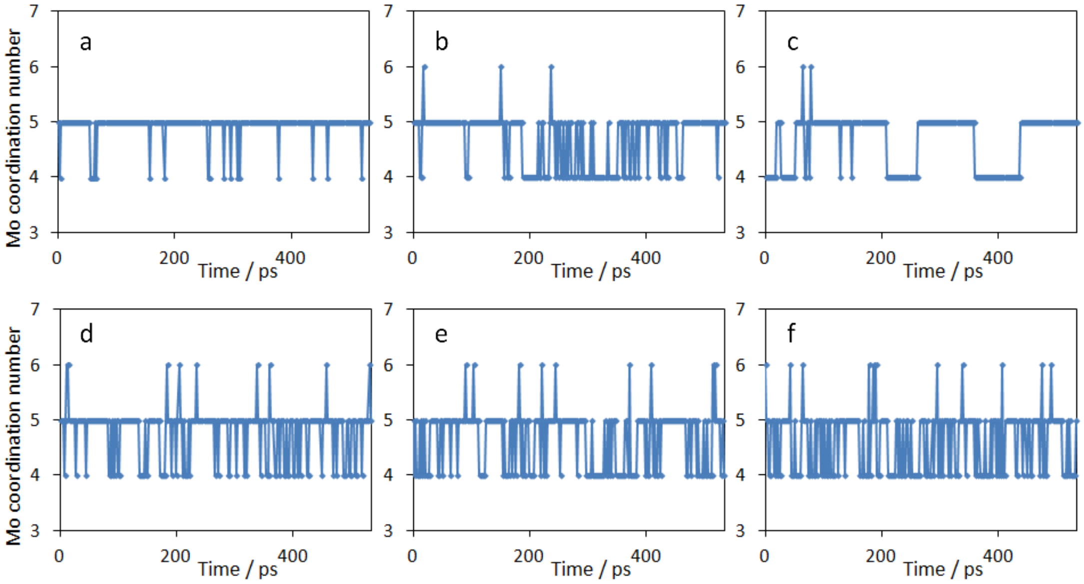

Figure 4.12: Variation of the coordination numbers of three Mo atoms over the course of the simulation. The top three are at 500 °C and the bottom three are at 1000 °C. The same three Mo atoms were chosen at each temperature represented by a/d; b/e; and c/f.

It should be noted that no Mo was observed becoming 3- or 7-coordinate, which indicates that an oxide ion can only jump from a 5- or 6-coordinate Mo to a 4- or 5-coordinate one.

The ratio of 4:5:6 coordinate Mo polyhedra in the room-temperature monoclinic structure is 15:15:18, and the fact that oxide ions cannot diffuse away from a 4-coordinate Mo, enhances the intra-site diffusion at elevated temperatures. The ≈ 40 % proportion of inter-MoO$_x$ jumps therefore represents significant long-range diffusion on a similar time-scale as intra-MoO$_x$ motions.

4.4.4.2. *Investigation of the Behaviour of Individual Oxygen Sites*

Figures 5.13a and 5.13b compare the MSDs of the oxide ions that are initially located on each oxygen site shown in figure 4.1. At 1000 °C (figure 4.13b), the O1, O2 and O3 site oxide ions all undergo significant displacement, which indicates that all sites are involved in the long-range conduction process at high temperature. However, at 500 °C the MSD of the O atoms belonging initially to the O1 site saturates very quickly (figure 4.13a), with an average displacement of ≈ 1.4 Å, whereas the O2 and O3 show no sign of saturation. The distance of 1.4 Å is shorter than the distance between the O1 sites and O2/O3, indicating that the O1 ions at lower temperatures remain confined and do not take part in conductivity.

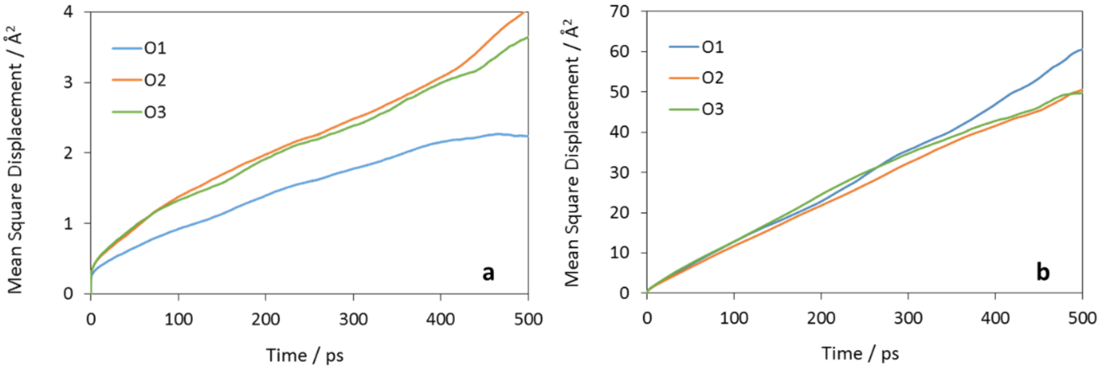

Figure 4.13: a) Mean square displacements for oxide ions initially located in each of the three oxygen sites during the simulation at 500 °C. The unusual behaviour of the MSDs at the end of the x-axis is due to statistical reasons (see Chapter 2, section 2.6.2.2). b) MSDs for oxide ions initially located in each of the three sites during the simulation at 1000 °C. Note that the y-axis scale is around 10× larger in b) than a).

The confinement of the O1 ions to their site is further confirmed by inspection of cloud plots showing the regions visited by oxygen atoms during the MD simulations. At 500 °C (figure 4.14a) the clouds for the O1 atoms are indeed confined to one site, and represent local thermal motion. In contrast, the O2 oxygen atoms move between the available vacant O2 and O3 sites surrounding a given Mo, i.e. undergo intra-MoO$_x$ motion (figure 4.14b). While relatively less frequent, the O2 and O3 oxide ions can also be seen to undergo inter-MoO$_x$ motion, i.e. exchange between different Mo atoms, as shown in figure 4.14c where an O2 from a 5-coordinate Mo moves to a vacant O3 site on an adjacent 4-coordinate Mo.

At 1000 °C the O1 atoms can leave their site and contribute to the overall conductivity (figure 4.14d). Corbel *et al.*[33], suggested that the O1 oxygens leave their site to jump directly to O2 and O3 sites on adjacent Mo atoms, a distance of approximately 2.8 Å. However, it was found that O1 ions move to an O2 site within the same Mo coordination sphere first, and from there follow the same intra-MoO_x and inter-MoO_x jump mechanisms as O2 and O3 atoms.

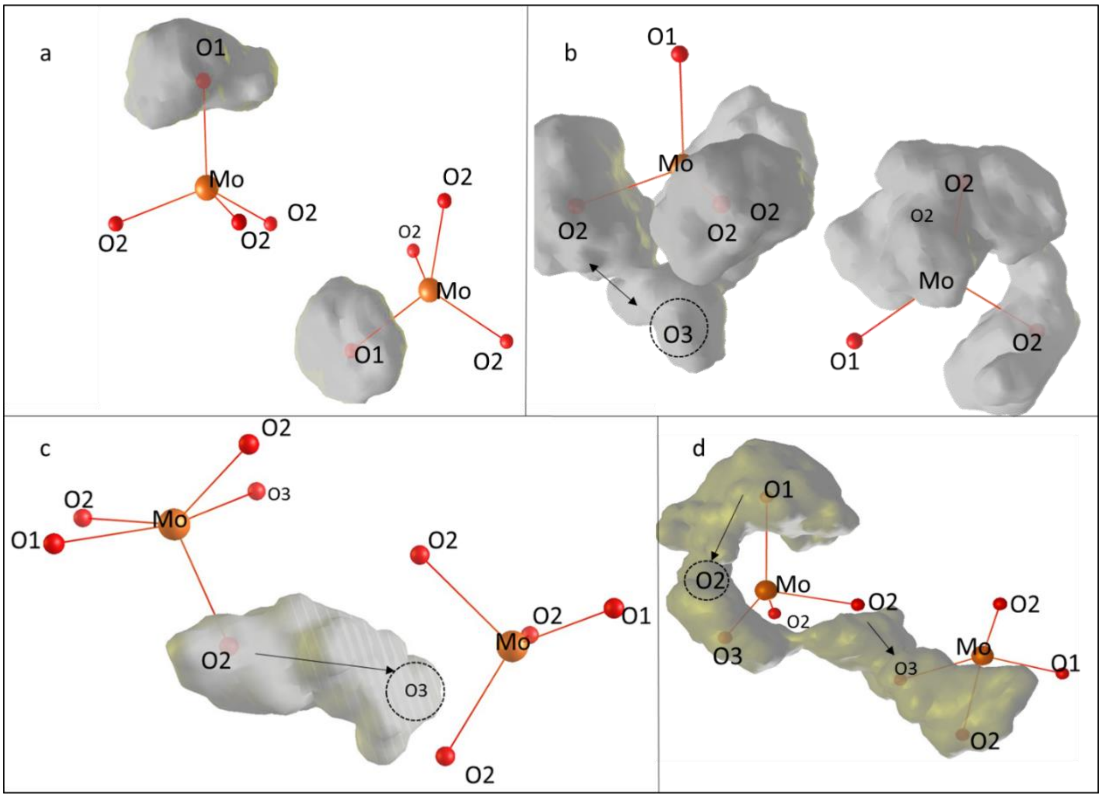

Figure 4.14: Representative cloud plots showing the space visited by oxide ions during the course of the AIMD simulations. a) O1 atoms undergoing localised thermal motion during simulation at 500 °C. b) O2 atoms undergoing intra-MoO_x motion to an O3 site during the same simulation. c) A cloud showing an inter-MoO_x jump between two adjacent Mo atoms at 500 °C. d) Long-range motion of an O1 ion during the course of the simulation at 1000 °C.

The mechanisms found are similar to those reported by Hou *et al.*[34] although the key difference is that they found two oxide ion migration processes occurring at all temperatures, one involving the O1 site and one without. The simulations reported here indicate that the O1 sites are activated at higher temperatures than O2 and O3, providing extra charge carriers and vacancies initially allowing for increased intra-MoO_x motion of oxide ions, which then translates into increased long-range inter-MoO_x diffusion.

This activation of O1 at higher temperatures agrees well with the recent experimental observations by Kezionis *et al.*[35] They find two processes leading to the bulk conductivity in

$La_2Mo_2O_9$, the α-process below the phase transition (and persisting above it), equivalent to our low temperature process involving O2 and O3, and the β-process which appears above the phase transition, equivalent to our high temperature process involving O1. Our findings also explain why the α-process could be observed even at higher temperatures, as this process still remains as a significant part of the overall conductivity mechanism. The nanosecond order relaxation times they report for the high temperature process coincide with the timescales observable by IN16b and agree well with our Chudley-Elliott fitting of the QENS data. The longer jump distance calculated from the Q dependence may be due to mainly the β-process being measured. In the simulations it was found that this high temperature process involves the O1 sites which require larger jump distances (2.5 Å from O1 site to O2 sites) than the other process involving O2 and O3 sites. This 2.5 Å distance compares much more favourably to the 3 Å jump distance found from IN16b and indicates that it is this process that is "seen" by IN16b.

4.5. Conclusions

In this work, quasielastic and inelastic neutron scattering measurements have been combined with AIMD simulations to directly observe and provide atomic-level understanding of the oxide ion dynamics on the nanosecond time-scale in the solid electrolyte $La_2Mo_2O_9$. This represents the first atomic-level understanding of the oxide ion dynamics in $La_2Mo_2O_9$ which is consistent with the experimental observations on this material.

The successful use of the relatively easily accessible laboratory based variable temperature XRD data has been demonstrated as a screening method for potential neutron scattering experiments. The QENS measurements suggest that oxide ion diffusion in $La_2Mo_2O_9$ occurs on nanosecond timescales. The activation energy determined from the QENS measurements, 0.61(5) eV, is consistent with the values obtained from other techniques. These results represent observation of oxygen dynamics by neutron scattering on the longest timescales reported to date. The fitting of the Q dependence of the QENS signal provides a conductivity timescale that agrees with macroscopic measurements, further reinforcing the link between the micro and macroscopic processes.

The AIMD simulations reveal that a combination of variable coordination number of Mo and the ease of movement of oxide ions within an MoO_x coordination sphere ultimately leads to the high long-range conduction observed in $La_2Mo_2O_9$. At low temperatures, the dominant process is the intra-MoO_x exchange between the O2 and O3 sites, although some inter-MoO_x

motion occurs; the O1 oxygens are confined to their sites and not involved in the conduction process. At higher temperatures the O1 sites become involved and the oxide ions become free to move from O1 to the partially occupied O2 and O3 sites to contribute to the overall conduction mechanism. Long-range diffusion then proceeds via the exchange of oxide ions in O2 and O3 sites in one Mo coordination sphere with O3 and O2 sites on adjacent Mo atoms, assisted by intra-MoO_x jumps within each coordination sphere. While intra- and inter-site jumps can be distinguished in the simulations, they occur on similar time- and length-scales of several nanoseconds and angstroms respectively, which is characteristic of a uniform diffusion process. The time and length scales obtained from AIMD simulations are consistent with those obtained from QENS experiments and provide an explanation for jump distances found from Chudley-Elliott fitting.

4.6. References

1. P. Lacorre, F. Goutenoire, O. Bohnke, R. Retoux and Y. Laligant, *Nature*, 2000, **404**, 856-858.
2. F. Goutenoire, O. Isnard and R. Retoux, *Chemistry of Materials*, 2000, **12**, 2575-2580.
3. S. Georges, *Solid State Ionics*, 2003, **161**, 231-241.
4. I. R. Evans, J. A. K. Howard and J. S. O. Evans, *Chemistry of Materials*, 2005, **17**, 4074-4077.
5. L. Malavasi, H. Kim, S. J. L. Billinge, T. Proffen, C. Tealdi and G. Flor, *Journal of the American Chemical Society*, 2007, **129**, 6903-6907.
6. Q. F. Fang, X. P. Wang, G. G. Zhang and Z. G. Yi, *Journal of Alloys and Compounds*, 2003, **355**, 177-182.
7. X. P. Wang, Z. J. Cheng and Q. F. Fang, *Solid State Ionics*, 2005, **176**, 761-765.
8. C. Tealdi, G. Chiodelli, L. Malavasi and G. Flor, *Journal of Materials Chemistry*, 2004, **14**, 3553-3557.
9. F. Goutenoire, O. Isnard, E. Suard, O. Bohnke, Y. Laligant, R. Retoux and P. Lacorre, *Journal of Materials Chemistry*, 2001, **11**, 119-124.
10. C. Tian, Q. Yin, J. Xie, J. Yang, H. Sun, B. Ji and W. Bao, *Journal of Rare Earths*, 2014, **32**, 423-428.
11. T. Paul and A. Ghosh, *Journal of Applied Physics*, 2015, **117**, 235101.
12. G. Corbel, P. Durand and P. Lacorre, *Journal of Solid State Chemistry*, 2009, **182**, 1009-1016.
13. D. Marrero-López, J. Canales-Vázquez, W. Zhou, J. T. S. Irvine and P. Núñez, *Journal of Solid State Chemistry*, 2006, **179**, 278-288.
14. T. Paul and A. Ghosh, *Journal of Applied Physics*, 2016, **119**, 065104.
15. G. Corbel, E. Chevereau, S. Kodjikian and P. Lacorre, *Inorganic chemistry*, 2007, **46**, 6395-6404.
16. T. Jin, M. Madhavarao, C. Cheng, D. Tsai and M. Hung, *Solid State Ionics*, 2007, **178**, 367-374.
17. X. Liu, H. Fan, J. Shi, G. Dong and Q. Li, *International Journal of Hydrogen Energy*, 2014, **39**, 17819-17827.
18. O. A. Alekseeva, I. A. Verin, N. I. Sorokina, A. E. Krasil'nikova and V. I. Voronkova, *Crystallography Reports*, 2010, **55**, 583-590.

19. X. P. Wang, Q. F. Fang, Z. S. Li, G. G. Zhang and Z. G. Yi, *Applied Physics Letters*, 2002, **81**, 3434-3436.
20. S. Takai, Y. Doi, S. Torii, J. Zhang, T. Y. S. P. Putra, P. Miao, T. Kamiyama and T. Esaka, *Solid State Ionics*, 2013, **238**, 36-43.
21. O. A. Alekseeva, A. M. Antipin, A. Gagor, A. Pietraszko, N. E. Novikova, N. I. Sorokina, E. P. Kharitonova and V. I. Voronkova, *Crystallography Reports*, 2013, **58**, 829-834.
22. S. Georges, O. Bohnke, F. Goutenoire, Y. Laligant, J. Fouletier and P. Lacorre, *Solid State Ionics*, 2006, **177**, 1715-1720.
23. W. Liu, W. Pan, J. Luo, A. Godfrey, G. Ou, H. Wu and W. Zhang, *Nature Communications*, 2015, **6**, 8354.
24. D. Marrero-López, J. Canales-Vázquez, J. C. Ruiz-Morales, J. T. S. Irvine and P. Núñez, *Electrochimica Acta*, 2005, **50**, 4385-4395.
25. S. Georges and M. Salaun, *Solid State Ionics*, 2008, **178**, 1898-1906.
26. S. Georges, F. Goutenoire, Y. Laligant and P. Lacorre, *Journal of Materials Chemistry*, 2003, **13**, 2317-2321.
27. G. Buvat, H. Sellemi, U. K. Ravella, M. Barre, S. Coste, G. Corbel and P. Lacorre, *Inorganic chemistry*, 2016, **55**, 2522-2533.
28. D. Marrero-López, J. Peña-Martínez, J. C. Ruiz-Morales, D. Pérez-Coll, M. C. Martín-Sedeño and P. Núñez, *Solid State Ionics*, 2007, **178**, 1366-1378.
29. C. Tealdi, G. Chiodelli, G. Flor and S. Leonardi, *Solid State Ionics*, 2010, **181**, 1456-1461.
30. G. Buvat, E. Quarez and O. Joubert, *Journal of Power Sources*, 2016, **302**, 107-113.
31. X. C. Lu and J. H. Zhu, *Journal of The Electrochemical Society*, 2008, **155**, B1053-B1057.
32. P. Lacorre, A. Selmi, G. Corbel and B. Boulard, *Inorganic chemistry*, 2006, **45**, 627-635.
33. G. l. Corbel, E. Suard and P. Lacorre, *Chemistry of Materials*, 2011, **23**, 1288-1298.
34. C. J. Hou, Y. D. Li, P. J. Wang, C. S. Liu, X. P. Wang, Q. F. Fang and D. Y. Sun, *Physical Review B*, 2007, **76**, 014104.
35. A. Kežionis, D. Petrulionis, E. Kazakevičius, S. Kazlauskas, A. Žalga and R. Juškėnas, *Electrochimica Acta*, 2016, **213**, 306-313.
36. H. M. Rietveld, *Journal of Applied Crystallography*, 1969, **2**, 65-71.
37. A. A. Coelho, J. S. O. Evans, I. R. Evans, A. Kern and S. Parsons, *Powder Diffraction*, 2012, **26**, S22-S25.
38. D. Richard, M. Ferrand, G. and J. Kearley, *Journal of Neutron Research*, 1996, **4**, 33-39.
39. G. Kresse and J. Furthmüller, *Computational Materials Science*, 1996, **6**, 15-50.
40. G. Kresse and D. Joubert, *Physical Review B*, 1999, **59**, 1758-1775.
41. J. P. Perdew, K. Burke and M. Ernzerhof, *Phys Rev Lett*, 1996, **77**, 3865-3868.
42. G. Goret, B. Aoun and E. Pellegrini, *Journal of Chemical Information and Modeling*, 2017, **57**, 1-5.
43. C. D. Ling, W. Miiller, M. R. Johnson, D. Richard, S. Rols, J. Madge and I. R. Evans, *Chemistry of Materials*, 2012, **24**, 4607-4614.
44. J. E. Auckett, A. J. Studer, E. Pellegrini, J. Ollivier, M. R. Johnson, H. Schober, W. Miiller and C. D. Ling, *Chemistry of Materials*, 2013, **25**, 3080-3087.
45. C. T. Chudley and R. J. Elliott, *Proceedings of the Physical Society*, 1961, **77**, 353-361.
46. J. Liu, R. J. Chater, B. Hagenhoff, R. J. H. Morris and S. J. Skinner, *Solid State Ionics*, 2010, **181**, 812-818.
47. N. Kim, C. Hsieh, H. Huang, F. Prinz and J. Stebbins, *Solid State Ionics*, 2007, **178**, 1499-1506.
48. K. Fuda, K. Kishio, S. Yamauchi, K. Fueki and Y. Onoda, *Journal of Physics and Chemistry of Solids*, 1984, **45**, 1253-1257.

49. J. R. Peet, C. M. Widdifield, D. C. Apperley, P. Hodgkinson, M. R. Johnson and I. R. Evans, *Chemical Communications*, 2015, **51**, 17163-17165.
50. K. Yamada, K. Kumano and T. Okuda, *Solid State Ionics*, 2005, **176**, 823-829.
51. T. J. Udovic, M. Matsuo, W. S. Tang, H. Wu, V. Stavila, A. V. Soloninin, R. V. Skoryunov, O. A. Babanova, A. V. Skripov, J. J. Rush, A. Unemoto, H. Takamura and S. Orimo, *Advanced Materials*, 2014, **26**, 7622-7626.
52. A. B. Santibáñez-Mendieta, C. Didier, K. K. Inglis, A. J. Corkett, M. J. Pitcher, M. Zanella, J. F. Shin, L. M. Daniels, A. Rakhmatullin, M. Li, M. S. Dyer, J. B. Claridge, F. Blanc and M. J. Rosseinsky, *Chemistry of Materials*, 2016, **28**, 7833-7851.
53. K. Arbi, M. G. Lazarraga, D. Ben Hassen Chehimi, M. Ayadi-Trabelsi, J. M. Rojo and J. Sanz, *Chemistry of Materials*, 2004, **16**, 255-262.

Chapter 5. Oxide Ion Dynamics and Conduction Mechanisms in $Bi_{0.913}V_{0.087}O_{1.587}$

5.1. Abstract

In this chapter the results of quasielastic neutron scattering (QENS) and inelastic neutron scattering (INS) studies into the oxide ion dynamics in $Bi_{0.913}V_{0.087}O_{1.587}$ are presented. The dynamic processes observed are the first directly observed on the nanosecond timescale in δ-Bi_2O_3 type materials. The findings from an in depth *ab initio* molecular dynamics (AIMD) investigation into $Bi_{0.913}V_{0.087}O_{1.587}$, with a significantly longer simulation time than that previously reported, are also presented. From this combination of experimental and computational approaches, new insight into the conduction processes occurring in this material is provided.

5.2. Introduction and Background

5.2.1. Structure of $Bi_{0.913}V_{0.087}O_{1.587}$

$Bi_{0.913}V_{0.087}O_{1.587}$ is an oxide ion conductor created by doping Bi_2O_3 in an attempt to stabilise its highly conductive high temperature δ-phase. Discussion of the literature regarding the use of Bi_2O_3 as an oxide ion conductor is given in Chapter 1, this introduction will focus on $Bi_{0.913}V_{0.087}O_{1.587}$ and other related doped materials. The $Bi_{0.913}V_{0.087}O_{1.587}$ material was reported in 2012 by Kuang *et al.*[1] who found that it has the highest reported oxide ion conductivity of any doped Bi_2O_3 phase, 3.9×10^{-2} Scm^{-1} at 500 °C. This exceeds the 1×10^{-2} Scm^{-1} threshold to be considered to be useful as an oxide ion conductor making this a very good candidate. The doping was found to successfully stabilise the δ-Bi_2O_3 structure from room temperature up to 500 °C after which partial decomposition to $Bi_{0.889}V_{0.111}O_{1.611}$ and V-doped γ-Bi_2O_3 occurs, accompanied by a drop in conductivity, before reformation of $Bi_{0.913}V_{0.087}O_{1.587}$ at 825 °C. The structure of the $Bi_{0.913}V_{0.087}O_{1.587}$ is shown in figure 5.1 and takes the form of a pseudo-cubic 3×3×3 supercell (figure 5.1a) of the fluorite structure (figure 5.1b). The structure can be thought of as being composed of two sublattices seen in figure 5.1a. The first of these is made up of isolated VO_4 tetrahedra, with V^{5+} centres separated from each other by around 6.7 Å; the V sites shown in the figure are partially occupied (22 %) by Bi atoms. Between these VO_4 groups the bulk of the material is made up of a network of corner and edge-sharing OBi_4 tetrahedra with intrinsic oxide vacancies (25 %) similar to δ-Bi_2O_3, a region of which can be seen in figure 5.1b. It is the presence of this extended Bi-O sublattice that is thought to be a significant factor in the high conductivity of the material. A similarly V-doped phase $Bi_{0.852}V_{0.148}O_{1.648}$ was found to have much lower conductivity,[2] attributed to the higher amount of VO_4 groups disrupting the 3-dimensional connectivity of the Bi-O sublattice.

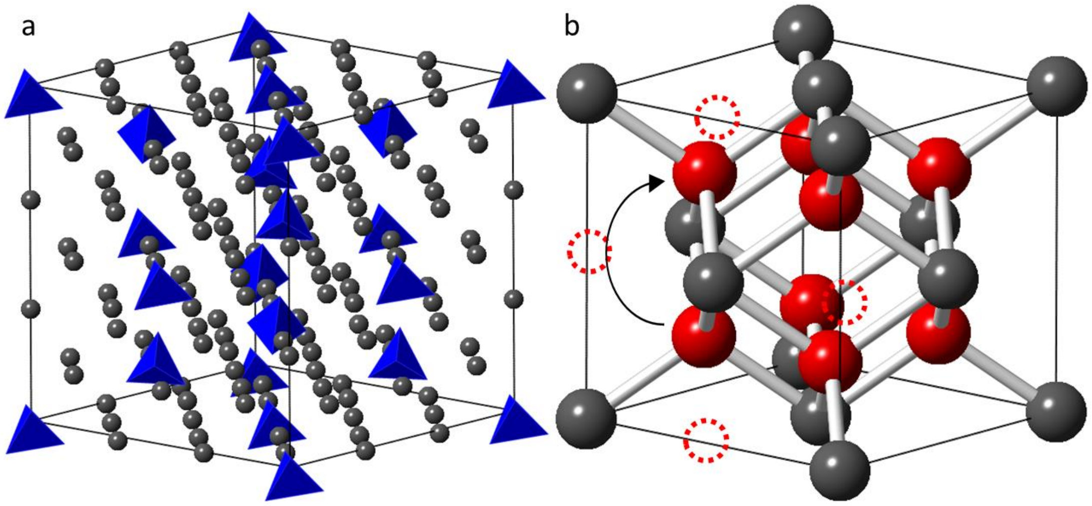

Figure 5.1: a) The pseudocubic structure of $Bi_{0.913}V_{0.087}O_{1.587}$ showing the sublattice of dopant VO_4 tetrahedra. The V sites shown here are ≈ 22 % occupied by Bi. b) The fluorite type structure of the Bi-O sublattice, the oxygen sites are 25 % vacant. Grey atoms represent Bi, blue atoms V, red atoms O. The dashed red circles show the locations of the octahedral holes and the arrow shows the commonly accepted pathway of a diffusing oxygen atom.

5.2.2. Mechanisms of Oxide Ion Conduction in $Bi_{0.913}V_{0.087}O_{1.587}$

The oxide ion conduction in the δ-Bi_2O_3 phase has been widely studied. It consists of a vacancy hopping mechanism in the <100> direction between two nearest neighbour oxygen sites. This takes place *via* one of the vacant octahedral holes in the fluorite structure which acts as a transition site.[3, 4] Some of these octahedral holes are shown as red circles in figure 5.1b with an arrow indicating the conduction pathway. In their paper reporting the synthesis and properties of $Bi_{0.913}V_{0.087}O_{1.587}$, Kuang *et al*.[1] also reported the results of *ab initio* molecular dynamics (AIMD) simulations carried out at 200, 400 and 600 °C for 20 ps of simulation time. These simulations showed that oxide ion mobility through the Bi-O sublattice in $Bi_{0.913}V_{0.087}O_{1.587}$ proceeds *via* the same mechanism as that present in δ-Bi_2O_3, although this mechanism was only observed above 200 °C. Oxide ion exchange between the Bi-O sublattice and the V-O sublattice was also observed, with oxide ions moving from the VO_x groups into adjacent OBi_4 site vacancies (the sites of the red atoms in figure 5.1b) and *vice versa*. This exchange was shown to be facilitated by the relative freedom with which the oxide ion could move within the VO_4 groups. The movement of oxide ions from the Bi-O sublattice to the VO_4 groups was observed to cause an increase in the average V coordination number from 4 to 4.33, implying the creation of additional vacancies within the Bi-O sublattice. These additional vacancies further promote conductivity in the Bi-O sublattice *via* the vacancy hopping mechanism. Overall the very high conductivity seen in $Bi_{0.913}V_{0.087}O_{1.587}$ was attributed to three factors; the extended δ-Bi_2O_3-like Bi-O sublattice, the ability of V^{5+} to support variable coordination number, and the freedom of the oxide ions to undergo localised motions within the VO_x groups.[1]

Similar sets of mechanisms involving interaction between variable coordinate dopant cations and the Bi-O sublattice have been observed in AIMD studies of other doped Bi_2O_3 materials, although in all cases much higher simulations temperatures were used. $Bi_{0.852}V_{0.148}O_{1.648}$,[2] as described above, has similar mechanisms; however, the oxide ion transfer between the V-O and Bi-O sublattices was found to be more predominant, likely due to the larger amount of V in the material. $Bi_{0.722}Mo_{0.278}O_{1.917}$ ($Bi_{26}Mo_{10}O_{69}$),[5] due to the high proportion of Mo, has quite a different structure with a monoclinic P2/c space group, made up columns of δ-Bi_2O_3 like regions surrounded by connected MoO_x groups. The mechanism found in AIMD simulations at 900 °C was found to have much larger contribution from the MoO_x groups with a "zig-zag" mechanism between the edges Bi_2O_3 columns *via* MoO_5 polyhedra being seen. $Bi_{0.933}Re_{0.066}O_{1.633}$ ($Bi_{28}Re_2O_{49}$)[6] has a structure made up of a sublattice of isolated ReO_4 tetrahedra with a δ-Bi_2O_3 like Bi-O sublattice in between. AIMD simulations on this material at 1100 °C showed similar conduction pathways as those described for $Bi_{0.913}V_{0.087}O_{1.587}$. The case of $Bi_{0.9375}Nb_{0.0625}O_{1.5625}$[7] is somewhat different as the Nb atoms are statistically distributed across the Bi sites rather than forming a separate sublattice. This means that the mechanism observed during AIMD calculations carried out at 900 °C was vacancy hopping through the δ-Bi_2O_3 like structure with no additional processes observed.

In addition to *ab initio* molecular dynamics studies, there have been several inelastic neutron scattering (INS) studies reported that probe oxide ion dynamics in these materials: two on δ-Bi_2O_3 itself,[8, 9] and one on $Bi_{0.722}Mo_{0.278}O_{1.917}$ ($Bi_{26}Mo_{10}O_{69}$).[5] The first study on δ-Bi_2O_3 was carried out by Mamontov probing timescales of 100s of picoseconds[8] and saw evidence for long range oxide ion diffusion in the form of a quasielastic neutron scattering (QENS) signal. Fitting their data with a Chudley-Elliott (C-E) model[10] gave jump distances of 2.64-2.84 Å for various temperatures showing excellent agreement with the 2.83 Å distance between nearest neighbour oxide ion sites in the <100> direction in δ-Bi_2O_3, therefore matching the believed conductivity pathway. They did however, discount their collected data with *Q* values above 1.7 Å^{-1}, the inclusion of which gave a higher value of 3.19-3.24 Å for the jump distances, claimed to be due to the appearance of Bragg peaks above 1.9 Å^{-1} negatively affecting the data. The second INS probing timescales of 10s of picoseconds reported by Wind *et al.*[9] also saw a QENS signal caused by long range oxide ion diffusion. Using a modified C-E model, created in an attempt to take into account the coherent scattering nature of oxygen (see chapter 1), to fit their data, a value of 3.33 Å was found for the jump distance. This value is larger than the 2.83 Å distance between nearest neighbour oxygen sites and significantly further away than the values reported by Mamontov using the standard C-E model. To explain this Wind *et al.* proposed that this jumps could occur in other direction with longer distances including the <110> and <111> directions (i.e. between any two oxygen sites in figure 1b). The 3.33 Å distance found represents the weighted average over all these possible jumps. While this gives a better fit to the data using their modified C-E model, no direct evidence of these longer distance jumps was provided and disagrees with the mechanism established in literature for δ-Bi_2O_3.[3, 4] The INS study on $Bi_{0.722}Mo_{0.278}O_{1.917}$ ($Bi_{26}Mo_{10}O_{69}$), reported by Ling *et al.*,[5] probed picosecond timescales and also showed a QENS signal. Due to the strongly localised *Q* dependence of the QENS signal intensity, resembling that found for rotation of C_{60}[11] and Zn tetrahedra in Zn_6Sc,[12] this signal was attributed to the localised motions of oxide ions within MoO_x polyhedra rather than long range diffusional motion.

5.2.3. Objectives of This Work

The objective of the work presented in this chapter was to investigate the various mechanisms of oxide ion conduction in $Bi_{0.913}V_{0.087}O_{1.587}$. Neutron scattering experiments were carried out on the ILL spectrometer IN6 in order to potentially observe the oxide ion dynamics on picosecond timescales, potentially observing localised motions as seen in $Bi_{0.722}Mo_{0.278}O_{1.917}$ ($Bi_{26}Mo_{10}O_{69}$).[5] Additional neutron scattering measurements were carried out on IN16b to probe longer nanosecond timescales with the goal of observing slower longer range mobility. *Ab initio* molecular dynamics calculations were carried out on $Bi_{0.913}V_{0.087}O_{1.587}$ at 200, 400, and 600 °C for much longer simulations times than previously reported[1] to identify the conduction mechanisms present in the material and allow some quantitative analysis of the mechanisms relative contribution to the overall conductivity.

5.3. Experimental

5.3.1. Synthesis of $Bi_{0.913}V_{0.087}O_{1.587}$ for Neutron Scattering Experiments

A 10 g sample of $Bi_{0.913}V_{0.087}O_{1.587}$ was synthesised from 7.7131 g of Bi_2O_3 and 0.2869 g of V_2O_5. The required masses were weighed out and thoroughly mixed and ground together in a mortar and pestle. The precursor powder was placed in an alumina crucible and fired sequentially at 700, 750, 800 and 850 ˚C with heating and cooling rates of 5 ˚C min^{-1}. The sample was heated for 12 hours at each temperature with cooling and grinding in between. Sample purity was confirmed by X-ray diffraction, using the Rietveld method implemented in TOPAS Academic as described in Chapter 2, section 2.2.4.2[13, 14]

5.3.2. Quasielastic and Inelastic Neutron Scattering

Neutron scattering data were collected on time-of-flight spectrometer IN6 at the Institut Laue Langevin (ILL) with an incident neutron wavelength of 5.1 Å. The 10 g sample was placed in a cylindrical Nb sample holder and data were collected at 200, 300, 400 and 500 °C with a collection time of 6.5 hours. Data were also collected on a vanadium sample at 20 °C for 6 hours for use in normalisation and to provide a resolution function.

Neutron scattering data probing nanosecond timescales were collected on the backscattering spectrometer IN16b at the ILL with an incident neutron wavelength of 6.27 Å. The 10 g powdered sample was placed in a cylindrical Nb sample holder. Measurements of elastic intensity, (ω = 0 μeV), and inelastic intensity at 2 μeV, were made from 100-500 °C with a heating rate of 0.04 °C s^{-1}. Data points were collected in pairs with elastic intensity measured for 30 seconds then immediately followed by an inelastic intensity measurement lasting 2 minutes. QENS measurements were then performed at 10 temperatures (40, 200, 250, 300, 333, 366, 400, 450, 475, and 500 °C). Data were collected for 6 hours at each temperature with an energy transfer window of ±10 μeV. In order to gain better statistics, and allow the $\boldsymbol{Q}$ dependence of the scattering function to be determined, additional data were collected at 400 °C and 450 °C giving a total of 18 hours at these temperatures. For the analysis of QENS data, a resolution function from a standard vanadium sample that was also used in normalisation – the resolution full-width at half-maximum was 0.73 μeV. The data from both the IN6 and IN16b neutron scattering experiments were analysed using the LAMP software.[15]

5.3.3. Computational

Ab initio molecular dynamics (AIMD) calculations were carried out using DFT method implemented in the VASP code.[16] The simulations were performed on a pseudo-cubic 3 × 3 × 3 fluorite supercell of the $Bi_{0.913}V_{0.087}O_{1.587}$ structure. This cell contains 96 Bi and 12 Bi/V sites. To ensure all sites were fully occupied by a single atom, 9 of these shared sites were chosen using a random number generator to be occupied by V and the remaining 3 by Bi. Oxygen sites were then assigned randomly to make each V atom four coordinate and provide a total of 171 oxygens in the supercell. This gives a final formula of $Bi_{99}V_9O_{171}$ which is the closest whole number formula possible to $Bi_{0.913}V_{0.087}O_{1.587}$ for this size supercell. For all calculations PAW pseudopotentials[17] were used with GGA-PBE functionals[18] and before all other calculations geometry optimisation was carried out on the structure. The electronic structure was sampled only at the gamma point. A phonon density of states (DOS) was also determined from gamma-point phonons calculated using DFT with the finite displacement method. The AIMD calculations were performed at 200 °C, 400 °C, and 600 °C in the NVT ensemble. 120000 steps of 2 fs were calculated giving a total of 240 ps of simulation time. Mean square displacements and density of states were produced using the MDANSE code[19] and cloud plots for trajectory visualisation were produced using LAMP.[15]

5.4. Results and Discussion

5.4.1. Sample Purity Confirmation

Figure 5.2 shows the collected powder XRD pattern for the synthesised $Bi_{0.913}V_{0.087}O_{1.587}$. Rietveld fitting was carried out using a pseudo-cubic 3 × 3 × 3 fluorite superstructure with P1 symmetry. The refinement parameters include background terms, zero point, scale factor, a single isotropic temperature factor, peak shape terms and the cell parameters.

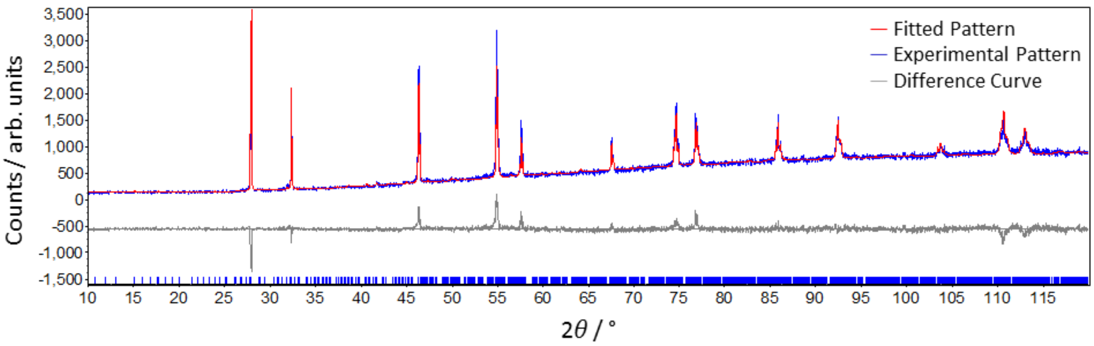

Figure 5.2: XRD pattern collected for synthesised $Bi_{0.913}V_{0.087}O_{1.587}$ fitted *via* Rietveld refinement. The cell parameters found were $a = 16.64(1)$, $b = 16.64(1)$, $c = 16.65(1)$, $\alpha = 89.88(9)$, $\beta = 89.88(4)$ and $\gamma = 89.88(8)$. $R_{wp} = 6.94$ %

All peaks observed in the experimental pattern have been fitted with no extra peaks observed and so it was decided that this sample is pure and suitable for QENS studies.

5.4.2. Probing Dynamics on the Picosecond Timescale

5.4.2.1. The Variation of Scattering Function with Temperature

The inelastic neutron scattering data collected on IN6 for $Bi_{0.913}V_{0.087}O_{1.587}$ are shown in figure 5.3a. The variation of the angle-integrated scattering function, $S(\omega)$, with temperature shows inelastic contributions that increase in intensity as the temperature increases. The spectra after applying the correction for the Bose population (Chapter 2, section 2.3.4.1) can be seen in figure 5.3b. The spectra match very closely and therefore the apparent differences seen in figure 5.3a can be entirely accounted for by the higher temperatures giving higher population to the phonon modes, with no evidence of a quasielastic signal. This likely means that the oxide ion diffusion dynamics in $Bi_{0.913}V_{0.087}O_{1.587}$ occur on a slower timescale than the picosecond timescales probed by IN6 and previously observed in other oxide ion conductors reported in literature such as in $Bi_{0.722}Mo_{0.278}O_{1.917}$ ($Bi_{26}Mo_{10}O_{69}$)[5] and $Sr_2Fe_2O_5$.[20] The QENS signal in $Bi_{0.722}Mo_{0.278}O_{1.917}$ was ascribed to movement of oxygen atoms within the MoO_x coordination spheres, and while similar behaviour of oxygens in the vanadium coordination spheres of $Bi_{0.913}V_{0.087}O_{1.587}$ is thought to occur[1] the large differences in structure likely makes the dynamics of oxide ion diffusion different enough to account for the difference in QENS signals. This could be due to the much lower proportion of V in $Bi_{0.913}V_{0.087}O_{1.587}$ compared to Mo in in $Bi_{0.722}Mo_{0.278}O_{1.917}$ making a QENS signal too weak to detect, or simply because the different cations lead to dynamics on different timescales.

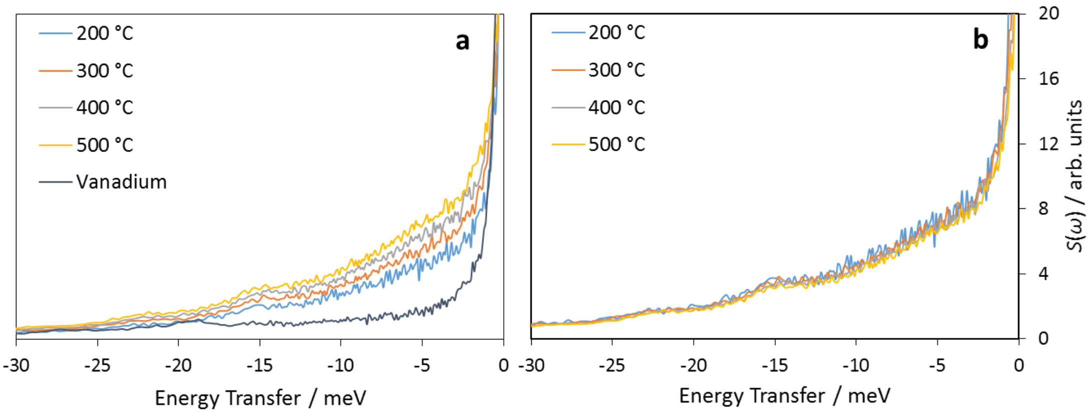

Figure 5.3: a) The *Q*-integrated scattering function, *S*(*ω*), against neutron energy transfer at various temperatures for a sample of $Bi_{0.913}V_{0.087}O_{1.587}$ measured on IN6. A resolution function from a vanadium sample has been provided for comparison. b) *S*(*ω*) after correction for the Bose population factor.

5.4.2.2. Comparison of Phonon Density of States from Different Techniques

Figure 5.4a shows the density of states measured on IN6 at 400 °C compared with the density of states calculated from complementary AIMD simulations at 400 °C and DFT phonon calculations. Several discrepancies between the curves are evident. Despite several attempts to improve these, including performing phonon calculations and AIMD on different starting structures and calculating the AIMD DOS for only later portions of the simulations to try to better account for disorder by only looking at the structure after a period of mobility, the discrepancies remained. The two calculated DOS curves are reasonably similar at low and high energies; however, the peak at 40 meV in the AIMD curve appears to be split into two for the phonon calculation. This could be due the disorder and mobility of the oxygen atoms in the molecular dynamics calculation compared to the static 0 K nature of the phonon calculation causing the two peaks to merge in the former. The experimental curve has similar peak locations at low energies with the features at 10 meV, 15-19 meV and 20-25 meV being present in all cases; however, the intensities are very different and above 25 meV the experimental curve becomes very broad. The partial DOS curves from AIMD simulations (figure 5.4b) show that the low energy features are accounted for by mainly the Bi atoms with higher energies being entirely oxygen atom contributions. This suggests the possibility that the calculated curves both underestimate the disorder in the oxygens, caused by their mobility, which is high enough at the temperatures of the experiment that all features broaden due to the wide range of oxygen environments. This could indicate that the AIMD simulation temperatures do not accurately match with experimental temperatures, a fact also noted in the simulations of oxide ion mobility in apatite materials (chapter 6).

The broadness of the experimental curve is consistent with that found in INS measurements on δ-Bi_2O_3[9] indicating that similar “liquid-like” diffusion occurs in both cases, albeit measured at lower temperatures here (400 °C) than in the study of the undoped material (730 °C).

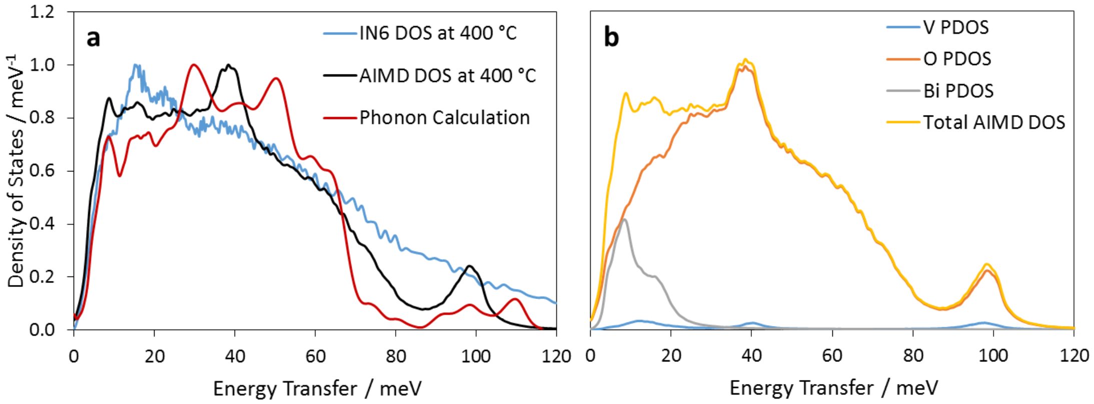

Figure 5.4: a) Phonon DOS calculated from AIMD and DFT phonon calculations compared with experimental results from IN6 neutron scattering. The calculated curves have been weighted according to neutron scattering power of Bi, V and O and all three curves have been scaled to reach a maximum value of 1. b) Partial density of states for each element calculated from AIMD simulations. Each element has been weighted according its neutron scattering power.

5.4.3. Probing Dynamics on the Nanosecond Timescale

5.4.3.1. The Variation of Elastic Intensity with Temperature

Plots of elastic and inelastic intensity (at 2 μeV) against temperature are shown in figure 5.5. The decrease in elastic intensity (figure 5.5a) begins with a fairly shallow gradient between 100 and 300 °C which corresponds to no increase in the inelastic intensity (figure 5.5b). This indicates that the loss in intensity cannot being explained by the formation of a quasielastic peak and instead may simply be a loss to the background caused by Debye-Waller effects (i.e. elastic intensity is lost to inelastic background noise due to thermal motions of the scattering atoms). However, above 300 °C the gradient of the elastic intensity *vs. T* plot becomes much steeper which corresponds to a large increase in inelastic intensity of ≈ 66 %. This indicates that at 300 °C there is an onset of oxide ion dynamics in the nanosecond timescale window of IN16b causing the appearance of a QENS peak. The subsequent (≈ 425 °C) decreases in elastic intensity gradient and inelastic intensity indicates that the QENS peak has reached maximum intensity and is now broadening as the rate of oxide ion mobility increases with temperature.

This onset of dynamics at 300 °C corresponds to a change in gradient in the impedance measurements performed by Kuang *et al.* with the oxide ion conductivity changing activation energy from 1.1 eV to 0.68 eV at 300-350 °C.[1] This correspondence means that the dynamics observed in these microscopic neutron scattering measurements are likely to be the same as those observed with macroscopic impedance measurements.

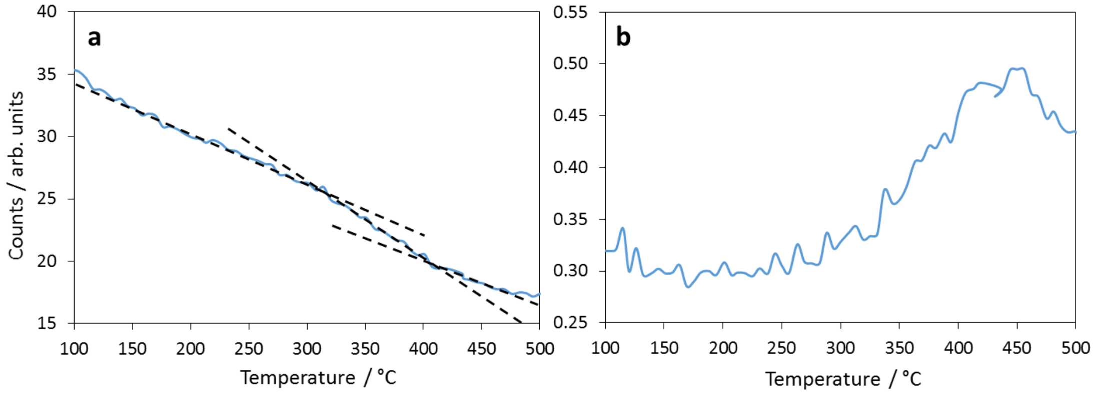

Figure 5.5: a) Plots of the elastic intensity against temperature for neutron scattering experiments on $Bi_{0.913}V_{0.087}O_{1.587}$ carried out with IN16b. Each temperature point was collected for 30 seconds. Also shown are best fit lines to indicate the changes in gradient at 300 and 425 °C b) Plots of the inelastic intensity measured at 2 μeV against temperature. Each temperature point was collected for 120 seconds.

5.4.3.2. The Variation of Scattering Function with Temperature

Plots of $S(\omega)$ against energy transfer for the 10 studied temperatures are shown in figure 5.6, along with a vanadium resolution function. Below 300 °C all spectra are similar to the resolution function with no clear temperature-dependent QENS peak visible; however, at 300 °C and above a very clear QENS signal appears in addition to the elastic peak. As expected from the plot of inelastic intensity this QENS peak increases in amplitude at 2 μeV while broadening until 450 °C, at which temperature the broadening causes a decrease in amplitude.

The increasing intensity and broadening of the QENS signal indicates that the rate of motion is increasing as temperature increases, and so the evolution of the QENS linewidth (Γ) was plotted against temperature to allow an activation energy to be calculated. The $S(\omega)$ data were fitted with a delta function representing the elastic peak and a Lorentzian for the quasielastic peak, both convoluted with the resolution function, as shown for $La_2Mo_2O_9$ in figure 4.7b. A flat background was used in the fitting. The resulting values of Γ are plotted against temperature in figure 5.7a. Temperatures 300 °C and below have been omitted due to the low intensity of the QENS peak making it very difficult to get a reliable fit.

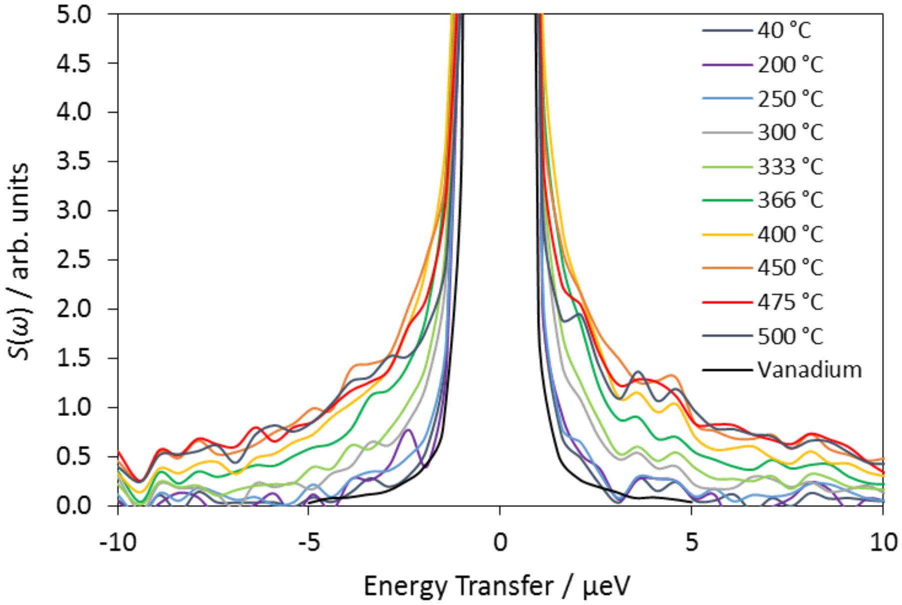

Figure 5.6: $S(\omega)$ spectra for inelastic neutron scattering measurements on $Bi_{0.913}V_{0.087}O_{1.587}$ at various temperatures with a maximum energy transfer of ±10 µeV. The data has been summed over all Q. A vanadium resolution function is also shown.

Assuming a Chudley-Elliott diffusion model, the linewidths, Γ, follow an Arrhenius relationship with temperature (T) with a gradient proportional to the activation energy.[10] A plot of $\ln(\Gamma)$ against $1000/T$ is shown in figure 5.7b and gives an activation energy of 0.32(2) eV. This is lower than the value of 0.68 eV found by Kuang *et al.* from impedance measurements in this temperature range.[1]

This difference between the activation energies determined from the macroscopic impedance measurements and the microscopic measurements is consistent with those found for nominally Na-doped $SrSiO_3$ (chapter 3) and $La_2Mo_2O_9$ (chapter 5), as well previous literature reports on oxide ion conductors,[21, 22] Na^+ conductors,[23-25] and Li^+ conductors[26, 27] (see table 3.3). These effects are likely due to grain boundaries and pellet density in impedance measurements leading to higher values of activation energy than the direct observation of dynamics, independent of sample morphology, by neutron scattering and other microscopic techniques.

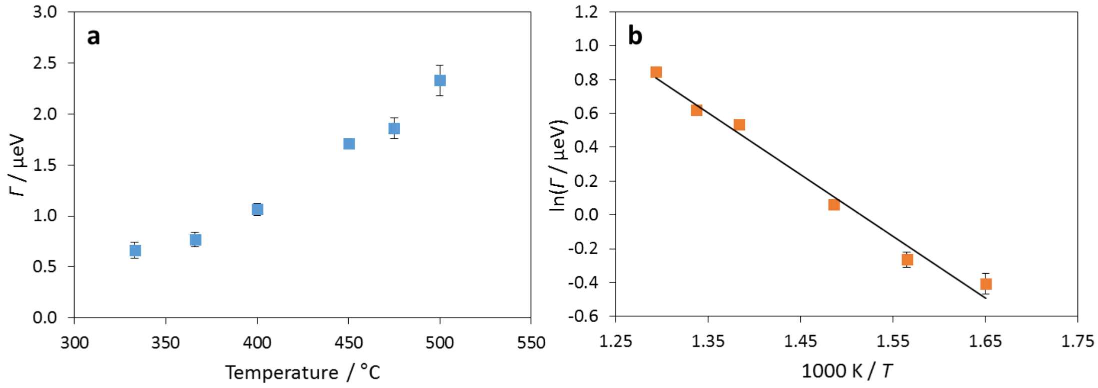

Figure 5.7: a) A plot of the QENS spectral linewidth *Γ* against temperature for $Bi_{0.913}V_{0.087}O_{1.587}$ over a 333-500 °C temperature range. The linewidths were determined by least squares fitting. b) An Arrhenius plot showing the variation of the spectral linewidth with inverse temperature.

5.4.3.3. Fitting of the Q Dependence of the Scattering Function

Due to being at positions of maximum inelastic intensity additional data collection were performed at 400 °C and 450 °C for a total of 18 hours in an attempt to achieve sufficiently good statistics to allow the variation of the scattering function with ***Q*** to be investigated. The scattering functions at each ***Q*** value were separately fitted with a Lorentzian (QENS peak) and a delta function (elastic peak) convoluted with the resolution function. The linewidth *Γ* of the Lorentzian is expected to follow the Chudley-Elliott model[10] (equation 1.8, given in Chapter 1, section 1.4.2). The fits of this model to the *Γ* values at 400 °C and 450 °C are shown in figure 5.8a and b respectively. ***Q*** values at which Bragg peaks are present (***Q*** = 1.06, 1.38, 1.79 Å^{-2}) have been removed as the large increase in elastic intensity at these values distorts the fits.

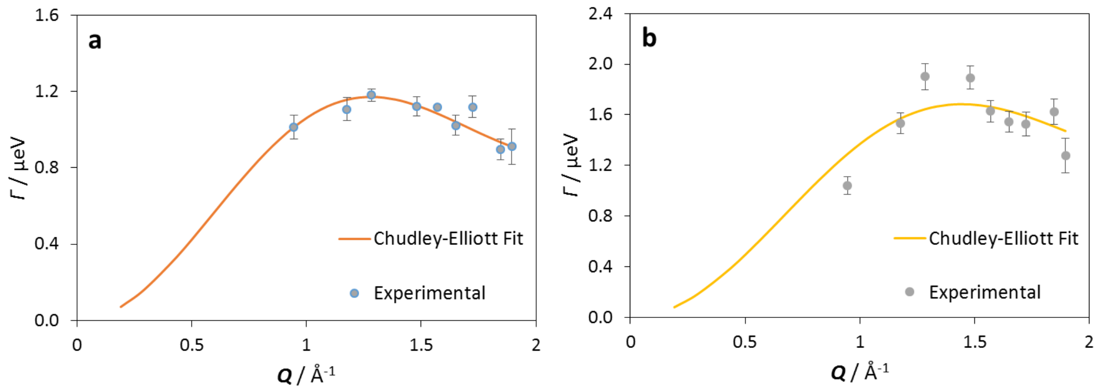

Figure 5.8: Values of QENS spectral linewidth *Γ* against *Q* for a sample of $Bi_{0.913}V_{0.087}O_{1.587}$ at a) 400 °C and b) 450 °C fitted with the Chudley-Elliott model. *Q* values corresponding to Bragg peaks have been removed.

The fitted value calculated for the lifetime and jump distance, respectively, were 2.1(1) ns and 3.5(2) Å at 400 °C and 1.4(5) ns and 3.1(1) Å at 450 °C. The lifetime values match well with the timescales probed by IN16b and also follow the expected trend that higher temperature leads to faster dynamics. The jump distances exceeds the ≈ 2.83 Å distance between nearest neighbour oxygen sites, this may be due to contributions from oxygen jumps to more distant sites as discussed by Wind *et al*. in their neutron scattering study of δ-Bi_2O_3 which found a jump value of 3.3 Å.[9] However, it could be due to the presence of Bragg peaks in the data which, while being discounted from the fit, may still have a negative influence on the data. This problem was described by Mamontov who saw similar high jump distance values when including *Q* ranges above the first Bragg peak, and so excluded all *Q* values above 1.7 $Å^{-1}$ from their fits.[8] Unfortunately, the first Bragg peak in this data occurs at 1.06 Å and doing likewise would not leave enough data to fit. To remedy this much higher *Q* resolution at low *Q* would be required.

An attempt was also made to fit the $Bi_{0.913}V_{0.087}O_{1.587}$ data presented here with the coherent Chudley-Elliott model (C-E) (equation 1.9) proposed by Wind *et al.*,[9] which attempts to take into account the effects of oxygen being an almost purely coherent neutron scatterer. This model presents difficulties as the absolute values of $S(Q)$ must be determined. Following the same assumption that Wind *et al*. used for their δ-Bi_2O_3 data, that $S(Q) = 1$ at the highest *Q* value measured, gave much worse fits to the $Bi_{0.913}V_{0.087}O_{1.587}$ data than the standard C-E model. This could be due to the presence of Bragg peaks in these data but may also simply be due to the *Q* range measured not being large enough. As well as these difficulties, which mean the model is not applicable to the $Bi_{0.913}V_{0.087}O_{1.587}$ data, the necessity of taking into account such coherent scattering effects is uncertain. It has been shown that using the standard C-E model gives reasonable fits to δ-Bi_2O_3 QENS data,[8] possibly meaning that the standard C-E model is sufficient for QENS measurements of oxide ion dynamics. This could be due to coherency effects being too small to have a noticeable impact on such measurements. However, as the dynamics that cause the QENS signals are purely incoherent, at least in the case where the timescales studied are long enough that it can be said to represent long range diffusion, then the QENS peak may represent only the self-terms in $S(Q,\omega)$, and so coherent scattering effects would not be present.

5.4.4. Conduction Mechanisms Investigated by *Ab Initio* Molecular Dynamics

Figure 5.9a shows the mean square displacement (MSD) of the oxygen atoms at each temperature over the course of the simulation. As expected, the MSDs grow larger as temperature increases indicating increased oxide ion mobility. There is no evidence of the MSD saturating at any of the temperatures indicating that the motion is not confined to a fixed volume. The average distance moved at the highest simulated temperature (600 °C) is ≈ 2.6 Å, which is less than the distances between nearest neighbour O sites (≈ 2.8 Å). Given that this represents the average displacement of the 172 oxygen atoms and that some of them will not move very much (or jump back and forth between sites thus having zero displacement), over the course of the simulation this indicates that some of the oxygen atoms are undergoing significant diffusion.

The division of oxygen atoms into those that begin bonded to vanadium and those that are initially part of the Bi-O sublattice reveals additional information. As shown in figure 5.9b, the MSDs for the O that begin in the Bi-O sublattice the MSDs do not appear to saturate and increase with temperature. However, they are lower than the V-O MSDs at equivalent temperatures, with the 600 °C MSD reaching an equivalent average displacement only after 200 ps of simulation time. The 200 °C Bi-O MSD is very flat indicating that very little movement within the Bi-O sublattice is occurring at this temperature.

In contrast the V-O MSDs, which appear less smooth than the Bi-O MSDs due to the relatively small number of oxygen atoms being averaged over (36 being in V coordination spheres vs 135 in the Bi-O sublattice), increase at a much faster rate before plateauing at roughly 5 Å^2. While the plateauing is not observed at the lowest temperature, it can be assumed that this is due to the simulation not being long enough to reach the 5 Å^2 value. This is evidence that those oxygen atoms that are initially bonded to a V^{5+} find it unfavourable to leave the VO_x group, likely due to restrictions on the coordination of V^{5+} meaning that an oxygen cannot diffuse away from a VO_4 group to leave it VO_3 (see figure 5.11 and associated text). It does appear to be possible though as the MSDs are not a true plateau and do continue to increase by a small amount once the 5 Å^2 is reached indicating that some of the oxygen atoms move to the Bi-O sublattice and contribute to the long range diffusion. The plateauing was not described by Kuang *et al.* in their simulations[1] which is due to their simulations only extending to 20 ps and so this behaviour not being seen. This shows the potential importance of long simulation times to fully understanding the behaviour of oxide ion conductors. The difference in behaviours of the two sets of oxygen atoms indicates that there may be two processes occurring in this material on different timescales, a process which make up the long range diffusion through the Bi-O sublattice and a faster process involving oxide ion mobility within individual VO_x groups.

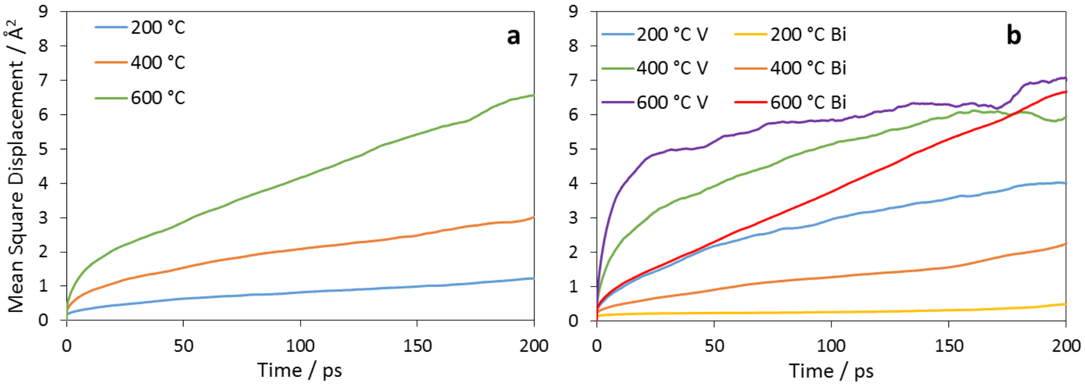

Figure 5.9: a) Mean square displacements for all oxygen atoms in the simulation box calculated from AIMD simulations at several temperatures. b) Mean square displacements for oxygen atoms starting bonded to vanadium (V) or part of the Bi-O sublattice (Bi).

Diffusion coefficients, *D*, were calculated at each temperature by determining the gradients of the MSDs. Making an Arrhenius plot of these values should yield a straight line with a gradient proportional to the activation energy. For the MSDs for all the oxygen atoms (figure 5.10a) the activation energy calculated was 0.17(1) eV. This is very small in comparison to both the 0.32(2) eV value found using QENS and the impedance measurements value found by Kuang *et al.*, 0.68 eV. This value is likely largely affected by contributions from the oxygen atoms bonded to V which appear to be involved in a separate process. A plot of the *D* values calculated only using the Bi-O sublattice oxygen atoms against 1000/*T* is shown in figure 5.10b. The activation energy calculated from this plot is 0.38(1) eV, which is in excellent agreement with the QENS measurements, indicating that the dynamics observed in the QENS measurements are mainly the long range diffusion through the Bi-O sublattice. A better agreement between AIMD and microscopic measurements such as QENS rather than macroscopic impedance measurements is expected as individual atomic motions are being probed. Given this level of agreement between computational and neutron scattering techniques despite the differences and approximations made in DFT it is possible to be confident in the reliability of the simulations and the oxide ion dynamics processes found.

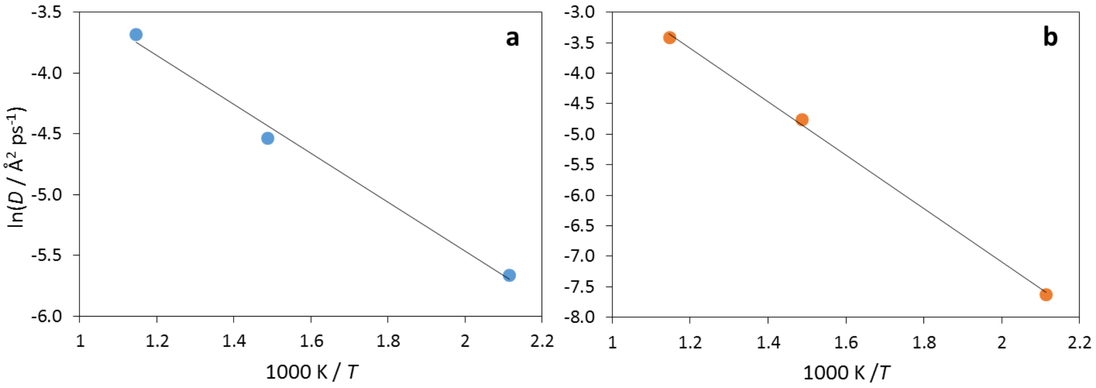

Figure 5.10 a) Arrhenius plot of diffusion coefficients calculated from the gradients of the MSDs for all oxygen atoms shown in figure 5.9a. b) Arrhenius plot of diffusion coefficients calculated from the gradients of the MSDs for oxygen atoms beginning as part of the Bi-O sublattice shown in figure 5.9b. The error bars are of the order of the size of the data points used.

In order to investigate the two different processes that are occurring over the course of the simulations, the number of diffusion events occurring at each temperature were counted. For this purpose, a jump was defined as an oxide ion moving a distance of at least 1.5 Å (smaller than the distance between oxygen sites so as not to miss any jumps) within 500 simulations steps. The jumps were grouped into several categories based on the closest cations before and after the jump. Intra-V are jumps between two O sites within a single vanadium coordination sphere; this is equivalent to the fast process discussed above. Bi-Bi is a jump within the Bi-O sublattice, either between two different Bi atoms or from one site to another in the same Bi coordination sphere. These were grouped together as the connected nature of the Bi-O sublattice means that each oxygen atom is bonded to four bismuths and so the specific closest Bi is not as meaningful. This is the equivalent of the slow process described above. Finally V-Bi and Bi-V represent jumps from the VO_4 tetrahedra to the Bi-O sublattice and *vice versa*.

As expected from the MSDs the number of total jumps as well as jumps of each type increases substantially as temperature increases, with the largest increase being between the 200 and 400 °C simulations. This may be related to the 300 °C activation of dynamics observed in the QENS data and the change in gradient observed in impedance measurements, and while simulation temperatures and experimental temperatures are not always equivalent this may indicate that in this case some direct comparison can be drawn. The number of intra-V jumps dominates at all temperatures representing 68.0 % of the oxide ion jumps at 200 °C, but decreasing to 55.8 % of jumps at 600 °C as the other processes become more prominent. The proportion of jumps attributed to movement within the Bi-O sublattice (long range diffusional motion) appears to make a significant portion of the total jumps. However, it is important to note that at any one time significantly fewer oxygen atoms are within the V coordination spheres compared to those in the Bi-O sublattice (initially 36 and 135 oxygen atoms respectively although this varies slightly throughout the simulation, figure 5.11). This means the intra-V jumps are all attributable to only ≈ 27 % of the oxygen atoms and that per atom less than one Bi-Bi jump occurs at 200 °C compared to ≈ 9 intra-V jumps. This lends credence to the proposal that the intra-V process occurs much faster than the Bi-O sublattice process.

Table 5.1. The number of each type of oxide ion jumps described in the text counted over the entire AIMD simulations at each of the three temperatures. Percentages of each type are also shown.

Jump Type	200 °C		400 °C		600 °C	
	Count	%	Count	%	Count	%
Intra-V	339	68.0	863	59.3	1062	55.8
V-Bi	19	3.8	70	4.8	106	5.6
Bi-V	20	4.0	73	5.0	108	5.7
Bi-Bi	111	24.2	450	30.9	628	32.9
Total	499		1456		1904	

The number of jumps between the Bi-O sublattice and the VO_4 coordination spheres and *vice versa* are quite low at all temperatures in comparison to the two main mechanisms although the proportion does increase slightly with temperature. However, they demonstrate that dynamic interactions between the two sublattices occur, as observed by Kuang *et al.*,[1] and that atoms initially in one may contribute to either process. To investigate this further, plots of the average coordination number (defined here as the number of oxygen atoms within 2.6 Å, determined based on the pair distribution function obtained from the calculations) of the vanadium atoms at each temperature were created. These are shown in figure 5.11.

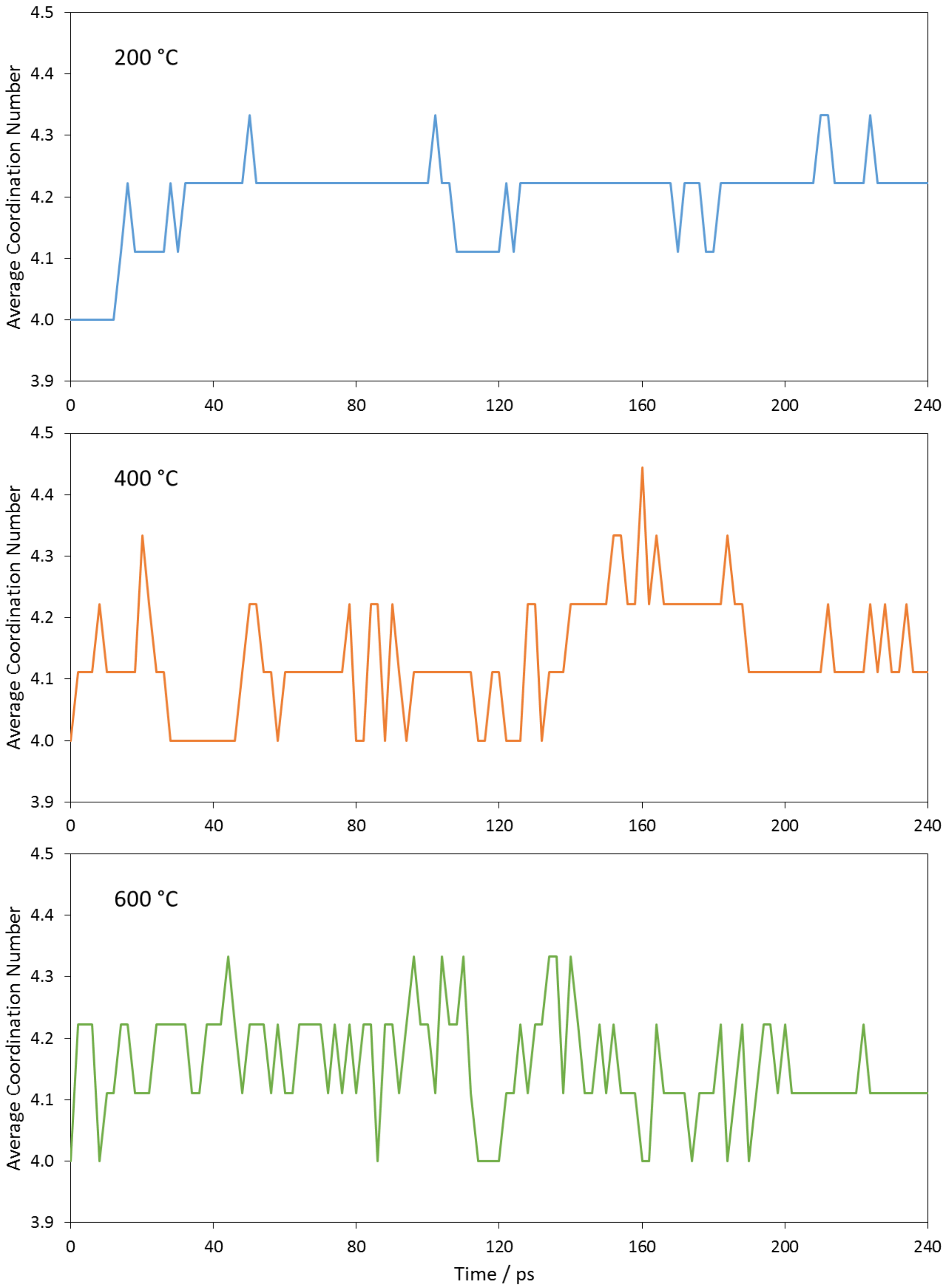

Figure 5.11: Variation of the average coordination numbers of the V atoms over the course of the simulations at each temperature.

The average coordination number of the vanadium atoms varies over the course of each of the simulations between a minimum of 4 (all 9 V atoms 4 coordinate, the initial state) and a maximum of 4.44 (4 V atoms 5 coordinate, 5 V atoms 4 coordinate, only seen at 400 °C). This means that oxygen atoms are moving between the Bi-O and V-O sublattices, causing VO_4

groups to become VO_5 groups and *vice versa*. It can be seen that the average coordination number changes more rapidly as temperature increases, agreeing with the numbers for Bi-V and V-Bi jumps in table 5.1 and showing that transfer between sublattices occurs more often as temperature increases. It should be noted that no V atoms ever became 3 or 6 coordinate, which means that exchange of oxygen atoms between the sublattices is restricted somewhat by the current coordination number of the V atoms (i.e. VO_5 groups cannot accept an additional oxygen atom from the Bi-O sublattice and VO_4 groups cannot donate one to it) accounting for the relatively low proportions Bi-V and V-Bi jumps seen in table 5.1. This also helps account for the plateauing seen in the V-O MSDs in figure 5.9b as they remain confined to the VO_4 group unless an oxygen is donated to it making it VO_5 and potentially allowing another oxygen to move away. The faster speed of the internal VO_x process likely facilitates these exchanges by providing a swift redistribution of oxygen atoms within the VO_x group and allowing more opportunities for vacancies and oxygen atoms to come close enough together to jump. That the VO_4 groups can accept an additional O from the Bi-O sublattice to become VO_5 is significant as this allows the creation of additional vacancies within the sublattice, providing more sites for other oxygen atoms to diffuse to thus increasing mobility.

These results indicate that oxide conduction in $Bi_{0.913}V_{0.087}O_{1.587}$ proceeds by two main mechanisms, each within one of the two sublattices in the structure. The first is a slower process through the Bi-O sublattice. This mechanism is responsible for the long range conduction in the material and involves oxide ion jumps from one site in the Bi-O sublattice to an adjacent vacant site. This can be seen in figure 5.12 for 200 °C and 600 °C. At the lower temperature no movement of oxygen atoms are seen in the region shown here, as expected from the low MSDs and jump counts. At the higher temperature there is significant diffusion of oxide ions between sites. This movement involves only jumps in the <100> direction to the nearest neighbour oxygen sites *via* octahedral holes in the structure (as shown in figure 5.1b). This is most clearly seen in figure 5.12b at the location where the octahedral hole is marked with a circle. This pathway matches with the well-known conduction mechanism in δ-Bi_2O_3[3, 4] as well as other doped B_2O_3 materials such as $Bi_{28}Re_2O_{49}$,[6] $Bi_{0.9375}Nb_{0.0625}O_{1.5625}$[7] and $Bi_{46}V_8O_{89}$.[2] Contrary to the claims by Wind *et al.*[9] diffusion between other sites such as those in the <110> and <111> directions (the face and body diagonals of the cube in figure 5.1b) were not seen to occur, although they studied the parent material rather than a doped one.

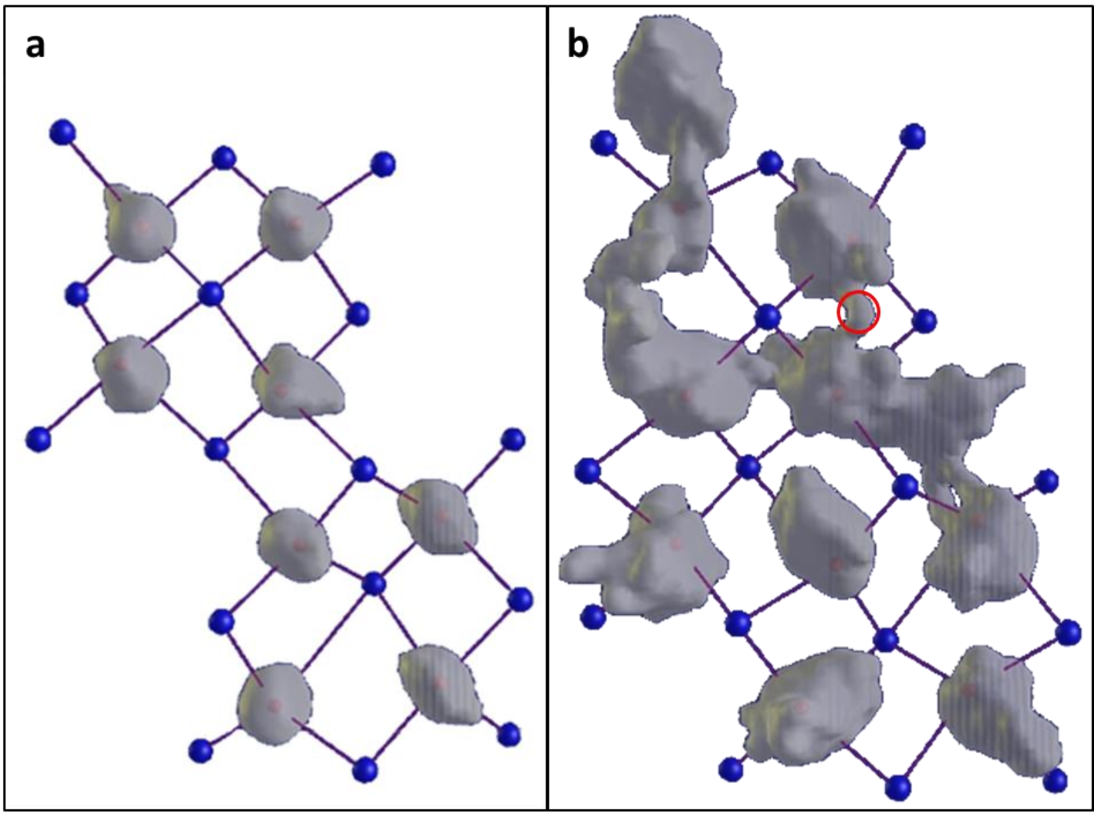

Figure 5.12: Cloud plots showing the same portion of the Bi-O sublattice at a) 200 °C and b) 600 °C. The blue spheres are Bi atoms and the grey cloud shows the volume visited by the 8 oxygen atoms at the centre of each group of 4 Bi atoms. The red circle indicates the location of an octahedral hole in the structure.

The second process is the rapid movement of oxygen atoms within a VO_x group. This process can be seen in the cloud plots in figure 5.13. At the low temperature the clouds are focused around the oxygen sites in the static structure although they have some overlap, showing that movement between these sites is possible even at this low temperature. At the higher temperature the cloud is effectively spherical indicating that the locations of the individual oxygen atoms have become less restricted and that the atoms are free to move within the V coordination sphere (although they will of course still be restricted by the positions of other O atoms in the same VO_x group).

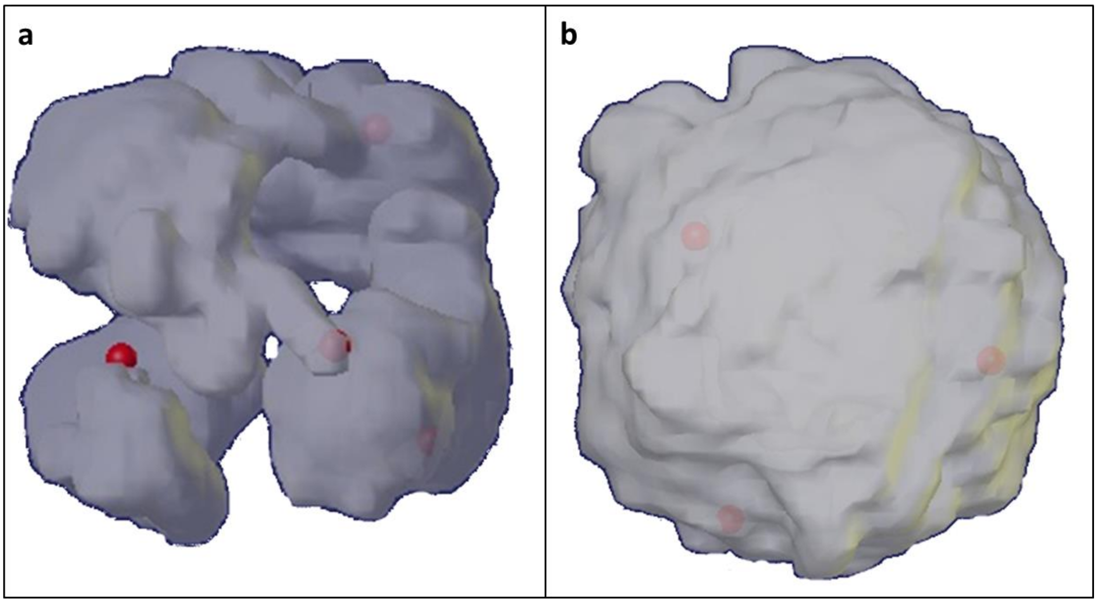

Figure 5.13: Cloud plots showing the same VO_4 group at a) 200 °C and b) 600 °C. The red spheres are O atoms and the grey cloud shows the volume visited by the 4 oxygen atoms initially in the sphere.

While this mechanism is solely local motions within a single VO_x group and so does not contribute directly to the long range dynamics in the material, due to the flexible coordination number of V it provides a way to indirectly aid conductivity through the transfer mechanism of oxide ions from the V-O sublattice to the Bi-O sublattice and *vice versa*. The internal movement facilitates this transfer *via* the rapid redistribution of oxide ions, making space for an additional oxide ion to enter the coordination sphere or filling the vacancy left behind when one leaves. This provides a method of creating additional vacancies by the donation of an oxide ion to form a VO_5 polyhedron so increasing oxide ion mobility in the network. This role of the variable coordination cations in doped δ-Bi_2O_3 has been observed before in $Bi_{28}Re_2O_{49}$[6], $Bi_{0.9375}Nb_{0.0625}O_{1.5625}$[7], $Bi_{26}Mo_{10}O_{69}$ and $Bi_{46}V_8O_{89}$[2], although in the case of Nb^{5+} doping it was found to have a more subtle role as the Nb atoms do not form a specific sublattice as is the case in the other materials, instead being distributed statistically across all Bi sites.

Both of these mechanisms as well as the transfer mechanism were seen previously in the simulations by Kuang *et al.*[1] However, the longer simulation times and quantitative analysis of the mechanisms carried out here reveal additional information. The plateauing of the VO_4 oxygen MSDs (figure 5.9b), indicating that the oxygens beginning in the VO_4 coordination sphere find it difficult to move away from it. This along with the relatively low number of Bi-V and V-O jumps counted as shown in table 5.1, show that transfer between the two sublattices is infrequent and does not contribute directly to the long range diffusion which is almost purely due to oxide ion movement through only the Bi-O sublattice by a similar mechanism as seen in the parent δ-Bi_2O_3.[3, 4] Instead the creation of vacancies in the Bi-O sublattice caused by this transfer mechanism, itself facilitated by the intra-VO_x mechanism, further enhances this main long range diffusion mechanism.

5.5. Conclusions

In this chapter, extensive quasielastic and inelastic neutron scattering measurements have been used to directly observe oxide ion dynamics on the nanosecond time-scale in the oxide ion conductor $Bi_{0.913}V_{0.087}O_{1.587}$. This is the longest timescale neutron scattering study of any δ-Bi_2O_3 material and shows, together with previous studies,[5, 8, 9] that long range dynamics in these materials can occur on a wide range of timescales. In addition, it represents only the second case of oxide ion dynamics observed on a nanosecond timescale by quasielastic neutron scattering (after $La_2Mo_2O_9$ chapter 5) further demonstrating the usefulness of this technique in the study of oxide ion conductors.

Studies on IN6 have shown that oxide ion dynamics are too slow to be observable on the picosecond timescale of that instrument. Instead, dynamics have been confirmed to occur on nanosecond timescales through the use of IN16b. Plots of elastic and inelastic intensity versus temperature reveal an activation of dynamics at 300 °C, consistent with impedance measurements on this material, showing that the same process of long range conduction is observed by both techniques.[1] The activation energy determined from the QENS measurements, 0.32(2) eV, is lower than the activation energy found in those impedance measurements. However, this difference is consistent with that found for $La_2Mo_2O_9$ (and other ionic conductors) and is indicative of the differences between macroscopic techniques such as impedance measurements that may depend on sample morphology and form, and microscopic techniques such as neutron scattering for which there are no such effects. The fitting of the Q dependence of the QENS signal at two temperatures provides values of residence times that agree with IN16b and follow the expected trend of faster dynamics at higher temperatures. The jump distances are higher than the distances between nearest neighbour oxygen sites in $Bi_{0.913}V_{0.087}O_{1.587}$, potentially due to the presence of Bragg peaks in the Q range fitted; however, higher quality Q-dependant data, especially at low Q values would provide better fits and would be required in order to say this with certainty.

The AIMD simulations reveal two mechanisms that contribute to the oxide ion dynamics in the material. One of these, the movement of oxide ions through the Bi-O sublattice, is a slower process only seen occurring significantly at 400 °C and above. This is the cause of long range conduction in this material and is consistent with the mechanisms of conduction found in δ-Bi_2O_3[3, 4] as well as other doped δ-Bi_2O_3 materials.[2, 6, 7] Calculating an activation energy for this process gives a value of 0.38(2) eV, which is in excellent agreement with the QENS measurements, indicating that these simulations are reliable and that IN16b is indeed probing this long range conduction process. The second process is motion of oxygen atoms purely within the VO_x groups in the material. This process is faster than the first process, but does not directly contribute to the long range conduction. Instead it facilitates the movement of oxygen atoms into and out of the VO_x groups and in combination with the variable coordination number of V^{5+} allows the VO_4 groups to accept additional oxygens atoms from the Bi-O sublattice forming VO_5 groups. This creates additional vacancies in the Bi-O sublattice leading to an increase in mobility *via* the first process. These findings are consistent with those of Kuang *et al.*[1] but provide additional insight into specific points such as the role of the internal VO_x process in the overall conduction mechanism.

5.6. References

1. X. Kuang, J. L. Payne, M. R. Johnson and I. R. Evans, *Angew Chem Int Ed Engl*, 2012, **51**, 690-694.
2. X. Kuang, J. L. Payne, J. D. Farrell, M. R. Johnson and I. R. Evans, *Chemistry of Materials*, 2012, **24**, 2162-2167.
3. J. B. Goodenough, *Annual Review of Materials Research*, 2003, **33**, 91-128.
4. S. Boyapati, *Solid State Ionics*, 2001, **138**, 293-304.
5. C. D. Ling, W. Miiller, M. R. Johnson, D. Richard, S. Rols, J. Madge and I. R. Evans, *Chemistry of Materials*, 2012, **24**, 4607-4614.
6. J. L. Payne, J. D. Farrell, A. M. Linsell, M. R. Johnson and I. R. Evans, *Solid State Ionics*, 2013, **244**, 35-39.
7. M. L. Tate, J. Hack, X. Kuang, G. J. McIntyre, R. L. Withers, M. R. Johnson and I. R. Evans, *Journal of Solid State Chemistry*, 2015, **225**, 383-390.
8. E. Mamontov, *Solid State Ionics*, 2016, **296**, 158-162.
9. J. Wind, R. A. Mole, D. Yu and C. D. Ling, *Chemistry of Materials*, 2017, **29**, 7408-7415.
10. C. T. Chudley and R. J. Elliott, *Proceedings of the Physical Society*, 1961, **77**, 353-361.
11. D. A. Neumann, J. R. Copley, R. L. Cappelletti, W. A. Kamitakahara, R. M. Lindstrom, K. M. Creegan, D. M. Cox, W. J. Romanow, N. Coustel, J. P. McCauley, Jr., N. C. Maliszewskyj, J. E. Fischer and A. B. Smith, 3rd, *Phys Rev Lett*, 1991, **67**, 3808-3811.
12. B. Holger Euchner and Tsunetomo Yamada and Helmut Schober and Stephane Rols and Marek Mihalkovič and Ryuji Tamura and Tsutomu Ishimasa and Marc de, *Journal of Physics: Condensed Matter*, 2012, **24**, 415403.
13. A. A. Coelho, J. S. O. Evans, I. R. Evans, A. Kern and S. Parsons, *Powder Diffraction*, 2012, **26**, S22-S25.
14. H. M. Rietveld, *Journal of Applied Crystallography*, 1969, **2**, 65-71.

15. D. Richard, M. Ferrand, G. and J. Kearley, *Journal of Neutron Research*, 1996, **4**, 33-39.
16. G. Kresse and J. Furthmüller, *Computational Materials Science*, 1996, **6**, 15-50.
17. G. Kresse and D. Joubert, *Physical Review B*, 1999, **59**, 1758-1775.
18. J. P. Perdew, K. Burke and M. Ernzerhof, *Phys Rev Lett*, 1996, **77**, 3865-3868.
19. G. Goret, B. Aoun and E. Pellegrini, *Journal of Chemical Information and Modeling*, 2017, **57**, 1-5.
20. J. E. Auckett, A. J. Studer, E. Pellegrini, J. Ollivier, M. R. Johnson, H. Schober, W. Miiller and C. D. Ling, *Chemistry of Materials*, 2013, **25**, 3080-3087.
21. N. Kim, C. Hsieh, H. Huang, F. Prinz and J. Stebbins, *Solid State Ionics*, 2007, **178**, 1499-1506.
22. K. Fuda, K. Kishio, S. Yamauchi, K. Fueki and Y. Onoda, *Journal of Physics and Chemistry of Solids*, 1984, **45**, 1253-1257.
23. J. R. Peet, C. M. Widdifield, D. C. Apperley, P. Hodgkinson, M. R. Johnson and I. R. Evans, *Chemical Communications*, 2015, **51**, 17163-17165.
24. K. Yamada, K. Kumano and T. Okuda, *Solid State Ionics*, 2005, **176**, 823-829.
25. T. J. Udovic, M. Matsuo, W. S. Tang, H. Wu, V. Stavila, A. V. Soloninin, R. V. Skoryunov, O. A. Babanova, A. V. Skripov, J. J. Rush, A. Unemoto, H. Takamura and S. Orimo, *Advanced Materials*, 2014, **26**, 7622-7626.
26. A. B. Santibáñez-Mendieta, C. Didier, K. K. Inglis, A. J. Corkett, M. J. Pitcher, M. Zanella, J. F. Shin, L. M. Daniels, A. Rakhmatullin, M. Li, M. S. Dyer, J. B. Claridge, F. Blanc and M. J. Rosseinsky, *Chemistry of Materials*, 2016, **28**, 7833-7851.
27. K. Arbi, M. G. Lazarraga, D. Ben Hassen Chehimi, M. Ayadi-Trabelsi, J. M. Rojo and J. Sanz, *Chemistry of Materials*, 2004, **16**, 255-262.

Chapter 6. Lone Pair Effects and Oxide Ion Conduction Mechanisms in Bi-Doped $La_{10}Ge_6O_{27}$

6.1. Abstract

In this chapter the results of an extensive investigation into the oxide diffusion dynamics in the series $La_{10-x}Bi_xGe_6O_{27}$ (x=0, 2, 4) are presented. This investigation includes the first neutron scattering experiments on apatite type oxide ion conductors on the picosecond and nanosecond timescales. Also presented are the findings of *ab initio* molecular dynamics simulations (AIMD) carried out to probe the conduction mechanisms in these materials and explore the effects that Bi^{3+} doping has on individual oxide conduction mechanisms and overall conductivity. This represents the first computational investigation into the mechanisms of conduction in lone pair cation doped apatite oxide ion conductors.

The AIMD simulations are supported by the first explicit electronic calculations of the lone pair locations and orientations in apatite materials, calculated *via* the use of the electron localisation function (ELF).[1] To investigate the effects of different channel ions on the lone pair locations, ELFs were also calculated for cases in which the anion channel X sites were vacant ($Pb_6Bi_4Ge_6O_{24}$) and occupied by Cl^- ions ($Pb_{10}V_6O_{24}Cl_2$, $Pb_{10}As_6O_{24}Cl_2$) as well as $Bi_2La_8Ge_6O_{27}$.

6.2. Introduction and Background

6.2.1. Introduction to Apatite Type Materials

Apatite-type materials have been the subject of extensive study for a wide range of applications including purification of water,[2-5] luminescence,[6, 7] bone replacement,[8] Na^+ or K^+ ion conduction,[9-11] and in electrodes for mercury detection.[12, 13] Lanthanum silicate and germanate apatites are of particular interest due to their high oxide ion conductivities.[14-19] Conductivities have been reported reaching up to 0.06 S cm^{-1} at 800 °C for the mixed silicate-germanate $La_{9.33}Si_2Ge_4O_{26}$ composition,[20] with high conductivities also being reported at temperatures suitable for IT-SOFC applications (e.g. 3×10^{-3} S cm^{-1} at 500 °C for $La_{9.67}Si_{5.5}Mg_{0.5}O_{26}$).[21]

Apatites are a chemically flexible set of materials with the general formula $A_{10}(TO_4)_6X_{2\pm\delta}$, (A = 2+ or 3+ cation; T = Si^{4+}, Ge^{4+}, V^{5+}, P^{5+}; X = O^{2-}, halide, OH^-), that generally adopt a hexagonal $P6_3/m$ structure[22] although lower symmetries are possible, with some triclinic apatites reported[23-25]. The $P6_3/m$ structure comprises two crystallographically distinct A sites (referred to as A1 and A2), a tetrahedrally coordinated site T and four unique anion sites (referred to as O1-O3 and X), as shown in figure 1. The polyhedral connectivity is such that the $A_4(TO_4)_6$ framework (involving the A1, T and O1-O3 sites) forms channels in the *c*-crystallographic direction, and these channels are occupied by the A_6X_2 units (involving the A2 and X sites). The X sites can be occupied by anions including O^{2-}, F^-, Cl^- and OH^-. However, when the A2 sites are occupied by Pb^{2+}, it also possible for the X sites to be vacant, believed to be due to the lone pairs on the Pb^{2+} cations pointing towards the vacant X sites thus providing stabilisation of the channel without an anion.[26-28] This allows the so called "lacunar" apatites to support substitution by monovalent cations, which selectively occurs on the A1 sites,[27] while maintaining charge balance and the overall apatite structure.

In the case of oxide ion conducting lanthanum silicate and germanate apatites the channel X sites are filled with oxygen atoms (called O4), and to preserve charge balance the occupancy of the A sites varies between two extremes, $La_{10-x}T_6O_{27-1.5x}$ ($0 \leq x \leq 0.67$).[23] In addition to this, for $x < 0.67$, the structure contains an additional interstitial oxygen atom (O5), the location of which has been the subject of much debate and may vary depending on exact composition.[25, 29-35] Lanthanum germanate apatites have been shown to undergo a slight triclinic distortion for compositions where $x > 0.33$.[23, 24] This distortion is caused by expansion of the $(La1)_4(GeO_4)_6$ framework relative to the $(La2)_6(O4)_2$ channels leading to rotation of the GeO_4 tetrahedra,[36] and splitting the La1, La2 and Ge sites into 2, 3 and 3 distinct sites respectively.

Recently, a combination of high-resolution neutron powder diffraction and aberration-corrected scanning transmission electron microscopy confirmed the presence of interstitial O atoms (O5 sites) between the GeO_4 tetrahedra (red circles in figure 6.1, effectively forming GeO_5 groups), as well as the presence of Bi on the A2 crystallographic sites in $La_8Bi_2(GeO_4)_6O_3$, a triclinically distorted apatite-type oxide ion conductor.[25] The ionic conductivity of $La_8Bi_2(GeO_4)_6O_3$ is about half an order of magnitude higher than that of $La_{10}(GeO_4)_6O_3$ (1.3×10^{-2} S cm^{-1} and 7.8×10^{-3} S cm^{-1} at 775°C, respectively).[37] Similarly, other related pairs of pure-La and Bi-containing germanates exhibit the same trend. For example, the ionic conductivities of $La_8Ba_2(GeO_4)_6O_2$ and $La_6Bi_2Ba_2(GeO_4)_6O_2$ at 800°C were reported as 5.5×10^{-5} S cm^{-1} and 1×10^{-3} S cm^{-1}, respectively, and 5.3×10^{-5} S cm^{-1} and 3×10^{-3} S cm^{-1} for $La_8Sr_2(GeO_4)_6O_2$ and $La_6Bi_2Sr_2(GeO_4)_6O_2$.[38, 39]

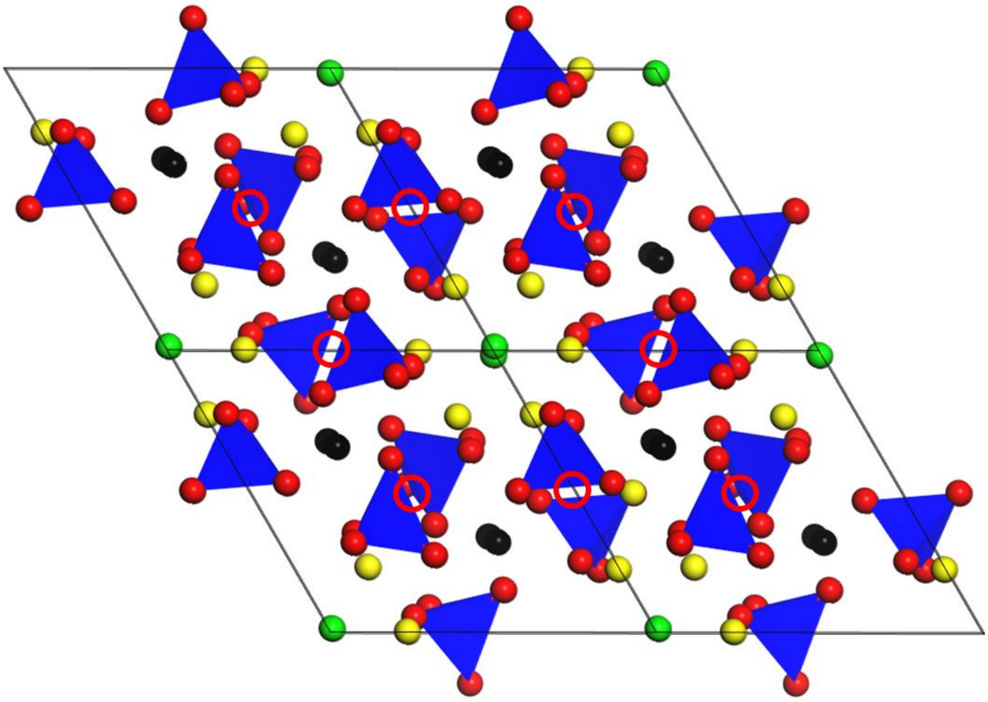

Figure 6.1*:* Structure of a hexagonal apatite material with general formula $A_{10}(TO_4)_6X_2$. Black spheres represent A1 sites as part of an $A_4(TO_4)_6$ framework, with blue tetrahedra representing the TO_4 groups, and red spheres the O1, O2 and O3 sites. Yellow spheres represent A2 sites that make up A_6X_2 units that lie within channels formed by this framework. Green spheres represent the X sites which may be O4, halide or vacant, depending on composition. Red circles indicate the locations of the interstitial oxygen atoms (O5) in hexagonal $La_8Bi_2(GeO_4)_6O_3$.[25]

6.2.2. Mechanisms of Oxide Ion Conduction in Apatite Materials

Oxide ion transport in apatites has been found experimentally to be highly anisotropic, with the *c*-direction conductivity observed in single crystals being several orders of magnitude higher than that in *a* and *b* directions.[16, 40, 41] The precise mechanism of oxide ion conductivity in apatite materials, however, has been highly debated in the literature, and appears largely dependent on the identity of the T atom as either Si or Ge. Different oxide ion migration pathways have been proposed. One occurs down the hexagonal channels, *via* an interstitialcy mechanism involving O4 atoms and interstitial oxygens residing in the channel, whose positions were determined using neutron powder diffraction.[42] This has been shown to be the case for $La_{9.33}Si_6O_{26}$ studied using both classical defect energy calculations[31] and density functional theory (DFT)-based nudged elastic band methods.[32] The latter method has also shown the same mechanism for $La_{10}Si_6O_{27}$.[43] An alternative proposed for $La_{9.33}Si_6O_{26}$ is an interstitial mechanism with a complex sinusoidal motion through the hexagonal channel representing the lowest energy pathway through classically calculated potential energy surface.[44, 45] For the germanate materials, interstitial O atoms have been found (computationally or experimentally) on the O5 sites between pairs of GeO_4 polyhedra.[25, 34] Diffusion can then occur in the *c*-direction, either directly between these O5 sites, as found by Kendrick *et al*. for $La_{9.33}Ge_6O_{26}$ using classical molecular dynamics and potential energy surfaces,[46] or between the O5 sites and an oxygen site on a GeO_4 polyhedron, as found by Imaizumi *et al*. in their *ab initio* molecular dynamics (AIMD) study on $La_{10}Ge_6O_{27}$.[33] The movement of oxide ions from the O4 sites to the GeO_4 framework and *vice versa*, has also been observed, acting as a 'feeder' for *c*-direction diffusion through the framework.[33, 46] Finally, conduction pathways between channels, approximately in the *ab* plane, have been also proposed in both lanthanum silicates[43, 44] and germanates.[33]

Based on the existing body of literature, it seems likely that multiple mechanisms should occur within the material, with the relative contribution and importance of the different pathways varying depending on composition and temperature. This is supported by classical molecular dynamics simulations carried out on $La_8Y_2Ge_6O_{27}$ by Panchmatia *et al.* which showed that all the oxide ions in this material are mobile, with multiple mechanisms occurring in both the *c*-direction and *ab* plane.[47] The AIMD calculations carried out on $La_{10}Ge_6O_{27}$ by Imaizumi *et al.* at 1750 and 2000 K also showed contributions from three mechanisms, although a cooperative *c*-direction mechanism through the GeO_4 framework dominated significantly.[33] This work was followed up with a first principles study using the nudged elastic band method which showed that this cooperative mechanism has the lowest activation energy and is more favoured than a purely interstitial mechanism. In addition kinetic Monte Carlo simulations at 500, 1000 and 1500 K showed that while the *c*-direction mechanism occurred an order of magnitude more frequently than *ab* plane conduction at 500 K, at 1500 K the relative occurrence rates became almost equal.[48]

6.2.3. Effects of Lone Pair Cations on Oxide Ion Conduction in Apatites

The effects that the inclusion of lone pair cations into apatites with occupied X sites have on the crystal structure and properties have been studied to a relatively limited extent, compared to lacunar phases. With regards to the structure, there appears to be a consensus that the lone pair cations prefer the A2 sites in the case of both Pb^{2+} and Bi^{3+} doping, attributed to the desire for a less sterically hindered or more stereochemically flexible environment.[3, 6, 7, 25, 49] The effect on oxide ion conductivity appears to be less clear-cut. Kendrick *et al*. describe three order of magnitude decreases of ionic conductivity of lanthanum silicate apatite oxide ion conductors on Bi^{3+} doping.[44] However, as described in section 6.2.1, lanthanum germanates follow the opposite trend. Based on the geometry of the structure, the adverse effect of Bi^{3+} doping on conductivity observed in lanthanum silicate materials has been attributed to the lone pairs presumably pointing towards the centre of the anion channel and, as a lone pair has similar size to an O^{2-} ion,[50, 51] thus blocking the O^{2-} diffusion within the channel.[44, 46] This has also been offered as an explanation for reductions in conductivity on Bi^{3+} doping observed in $La_2Mo_2O_9$;[52, 53] however, no computational investigations to confirm this effect have been performed in either case. The assumed lone pair location in oxide ion conducting apatites is based on an analogy with lacunar phases, without considering the fact the O^{2-} anions on the channel X sites lie in the same *ab* plane as the A2 (mixed La/Bi) sites (at $z \approx 0.25$, figure 6.7f), leaving little space for a lone pair.[26, 28] In an investigation into Pb^{2+} apatites containing monovalent channel anions, the locations of lattice voids determined using cavity calculations were used as an analogy for lone pair locations and also showed an orientation towards the channel centre.[54] However, in contrast to the O4 sites, the locations of the monovalent channel anions in the apatites used for these calculations are located at $z \approx 0$ between cations (figure 6.7e), giving more space for the lone pairs.[54, 55]

6.2.4. Objectives of this Work

The objective of the work presented in this chapter was to investigate in detail the mechanisms of oxide ion conduction in Bi-doped $La_{10}Ge_6O_{27}$ and to explain the conductivity increase seen upon doping. Neutron scattering experiments were carried out on the ILL spectrometers IN6 and IN16b in attempts to observe the oxide ion dynamics on picosecond and nanosecond timescales respectively. Electron localisation function calculations, which have previously been successfully applied to investigations of lone pairs in a number of functional oxides,[56-58] were carried out to identify the locations of the Bi^{3+} lone pairs in the material and compared with other apatite materials to examine the effects of different channel anions on the location. *Ab initio* molecular dynamics simulations were carried out on the series $Bi_xLa_{10-x}Ge_6O_{27}$ ($x = 0, 2, 4$) to identify the conduction mechanisms present in the materials and compare their relative abundances at the different doping levels in order to determine the effects of Bi^{3+} on the individual mechanisms and therefore overall conductivity.

6.3. Experimental

6.3.1. Synthesis of $La_{10}Ge_6O_{27}$ and $Bi_2La_8Ge_6O_{27}$

10 g samples of $La_{10}Ge_6O_{27}$ and $Bi_2La_8Ge_6O_{27}$ were prepared from stoichiometric amounts of La_2O_3 (Acros Organics, 99.9%), Bi_2O_3 (Acros Organics, 99.9%) and GeO_2 (Acros Organics, 99.999%). The reactants were thoroughly mixed and ground together, placed in an alumina crucible and fired at 1100 ˚C for 30 hours with intermediate grinding and heating and cooling rates of 5 ˚C min^{-1}. Sample purity was confirmed by X-ray diffraction, using the Rietveld method implemented in TOPAS Academic as described in Chapter 2, section 2.2.4.2[59, 60] The syntheses and phase purity confirmation experiments were carried out by Matthew Chambers at Durham University. Synthesis of $Bi_4La_6Ge_6O_{27}$ was also attempted; however, a pure sample could not be obtained.

6.3.2. Neutron Scattering

To investigate oxide ion dynamics on the picosecond timescale, neutron scattering data were collected on time-of-flight spectrometer IN6 at the Institut Laue Langevin (ILL) with an incident neutron wavelength of 5.1 Å. The $Bi_2La_8Ge_6O_{27}$ sample was placed in a cylindrical Nb sample holder and data were collected at 500 °C and 800 °C with a collection time of 6.5 hours. Data were also collected on a vanadium sample at 20 °C for 6 hours for use in normalisation and to provide a resolution function.

Neutron scattering data probing nanosecond timescales were collected on the backscattering spectrometer IN16b at the ILL with an incident wavelength of 6.27 Å. Data were collected for 10 g powdered samples of $La_{10}Ge_6O_{27}$ and $Bi_2La_8Ge_6O_{27}$ placed in cylindrical Nb sample holders. Measurements of elastic intensity, (ω = 0 μeV), and inelastic intensity at 2 μeV, were made from 100-900 °C with a heating rate of 0.04 °C s^{-1}. Data points were collected in pairs with elastic intensity measured for 30 seconds then immediately followed by an inelastic intensity measurement lasting 2 minutes. QENS measurements were then performed at two temperatures for each sample with an energy transfer window of ±10 μeV. Data were collected for 2.5 hours at 650 and 850 °C. For the analysis of QENS data, a resolution function from a standard vanadium sample that was also used in normalisation – the resolution full-width at half-maximum was 0.73 μeV. The data from both the IN6 and IN16b neutron scattering experiments were analysed using the LAMP software.[61]

6.3.3. Computational

Electron localisation function calculations were performed using density functional theory (DFT) carried out using the CASTEP[62] module integrated into the Materials Studio software. Ultrasoft pseudopotentials were used with GGA-PBE functionals.[63] The plane-wave energy cutoff (340 eV) and 3×3×2 k-point mesh were sufficient for convergence. Calculations were performed on 1×1×2 supercells of $Pb_6Bi_4Ge_6O_{24}$,[64] $Pb_{10}V_6O_{24}Cl_2$,[65] $Pb_{10}As_6O_{24}Cl_2$,[65] and $Bi_2La_8Ge_6O_{27}$.[25] Due to the requirement for fully occupied atom sites in these calculations, a random number generator was used to select which partially occupied sites to fill, as well as assign locations of dopant atoms from the available sites to match the required stoichiometry. In the case of $Bi_2La_8Ge_6O_{27}$, calculations were performed on three configurations with Bi atoms occupying different A2 sites to confirm that this did not affect the lone pair orientations obtained.

Ab initio molecular dynamics (AIMD) calculations were carried out using DFT method implemented in the VASP code[66]. PAW pseudopotentials[67] were used with GGA-PBE functionals.[63] The electronic structure was sampled only at the gamma point. Calculations were performed on 1×1×2 supercells of $La_{10}Ge_6O_{27}$, $Bi_2La_8Ge_6O_{27}$, and $Bi_4La_6Ge_6O_{27}$ based on triclinic $Bi_2La_8Ge_6O_{27}$ model described by Tate *et al.*[25] For the calculations, the interstitial oxygen atom positions were chosen at random from the available O5 sites to ensure the correct stoichiometry and the full site occupancy. The locations of the Bi atoms were also chosen randomly from the available La2 sites to match the required stoichiometry. AIMD calculations were performed at 1000 K, 1500 K, 1750 K and 2000 K in the NVT ensemble. These temperatures were chosen for direct comparison with the work of Imaizumi *et al.*,[33] and due to the relatively small number of atoms being probed. For each simulation 60,000 steps of 3 fs were calculated, giving a total of 180 ps of simulation time. Mean square displacements (MSD) and density of states (DOS) were calculated using the MDANSE code,[68] and cloud plots for trajectory visualisation were produced using LAMP.[61] Before any other calculations occurred all structures underwent geometry optimisation in order to minimise the forces on the atoms.

6.4. Results and Discussion

6.4.1. Sample Purity Confirmation

Figure 6.2 shows the collected powder XRD pattern for the synthesised $Bi_2La_8Ge_6O_{27}$. This pattern was collected by Matthew Chambers at Durham University. Rietveld refinement[60] was carried out using a starting model based on the structure described by Tate *et al.*[25] The refinement parameters included background terms, zero point, scale factor, a single temperature factor, peak shape terms and the cell parameters.

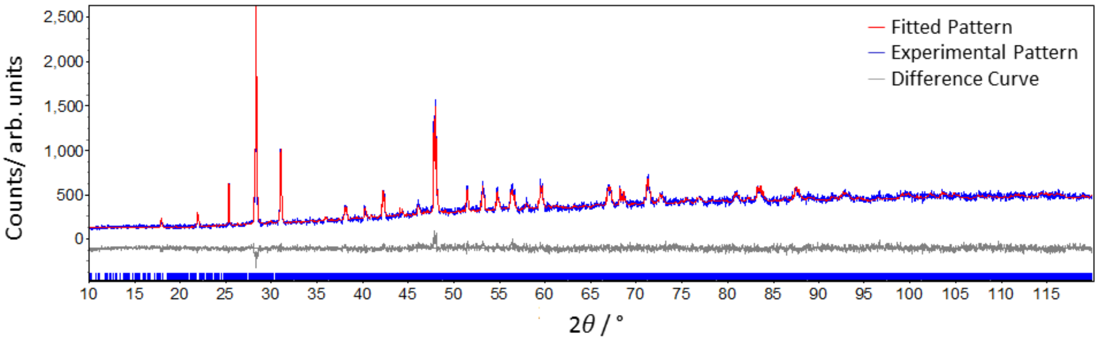

Figure 6.2: XRD pattern collected for synthesised $Bi_2La_8Ge_6O_{27}$ fitted *via* Rietveld refinement. The cell parameters found were a = 9.9076(4) Å, b = 9.9000(4) Å, c = 7.3488(2) Å and α = 90.523(4)°, β = 89.157(3)°, γ = 120.186(2)°. R_{wp} = 3.35 %.

All peaks observed in the experimental pattern have been fitted with no impurities observed. The cell parameters match those found by Tate *et al.* very closely. Given these factors and the low value for R_{wp} it was decided that this sample was of sufficiently good quality to undergo QENS studies.

6.4.2. Probing Dynamics on the Picosecond Timescale

6.4.2.1. The Variation of Scattering Function with Temperature

The inelastic neutron scattering data collected on IN6 for $Bi_2La_8Ge_6O_{27}$ is shown in figure 6.3a. The variation of the angle-integrated scattering function, $S(\omega)$, with temperature shows inelastic contributions, with those for the 800 °C measurement having a greater amplitude than those at 500 °C. However, this increase can be accounted for by the Bose population factor (Chapter 2, section 2.3.4.1). The spectra after applying the correction $S(\omega)/n_B$ (where n_B is given by equation 2.18) can be seen in figure 6.3b. The spectra match very closely and therefore the apparent differences seen in figure 6.3a are entirely due to the raised temperature increasing the population of phonon modes rather than a quasielastic signal. This means that the oxide ion diffusion dynamics in $Bi_2La_8Ge_6O_{27}$ occur on a slower timescale than the picosecond timescales probed by IN6 and previously observed in $Bi_{26}Mo_{10}O_{69}$[69] and $Sr_2Fe_2O_5$.[70]

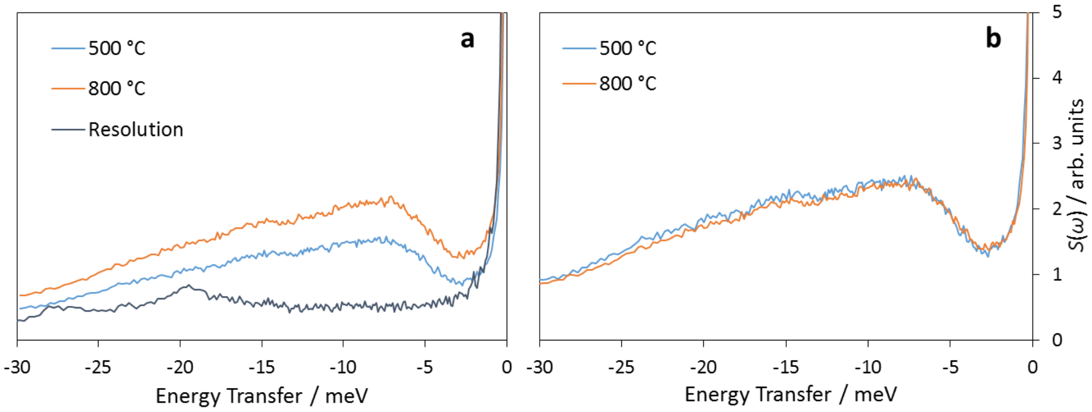

Figure 6.3: a) The *Q*-integrated scattering function, $S(\omega)$, against neutron energy transfer at various temperatures for a sample of $Bi_2La_8Ge_6O_{27}$ measured on IN6. A resolution function from a vanadium sample has been provided for comparison. b) $S(\omega)$ after correction for the Bose population factor.

6.4.2.2. Comparison of Phonon Density of States from Differing Techniques

Figure 6.4 shows the density of states for $Bi_2La_8Ge_6O_{27}$ measured on IN6 at 800 °C (where appreciable conductivity was observed experimentally) compared with the density of states calculated from AIMD simulations at 1500 K (the lowest simulated temperature where appreciable oxide ion dynamics were observed, see figure 6.8).

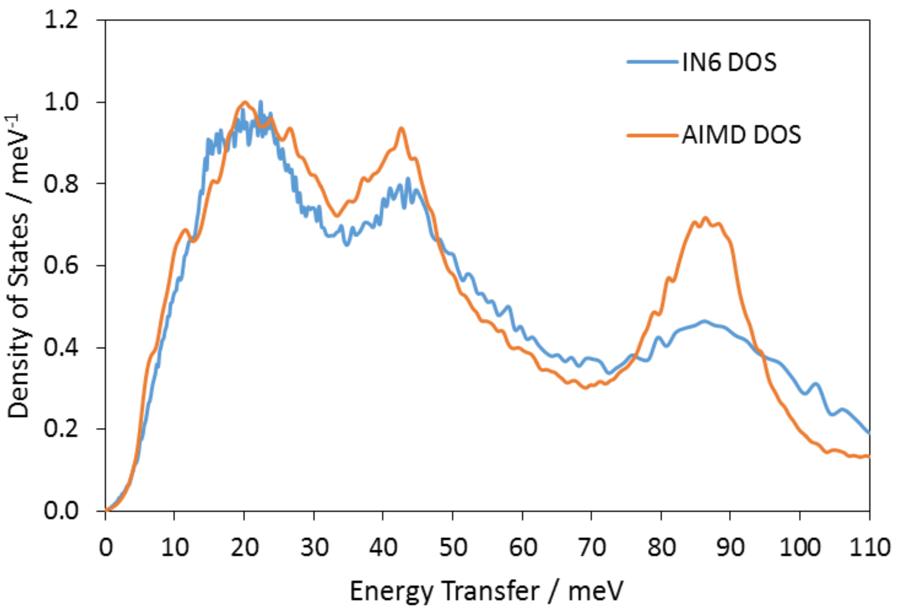

Figure 6.4: a) Phonon DOS calculated from AIMD and DFT phonon calculations compared with experimental results from IN6 neutron scattering. The calculated curve has been weighted according to neutron scattering power of Bi, La, Ge and O and all the curves have been scaled to reach a maximum value of 1.

The two curves shown in the figure match closely, with the peaks located at 20, 40 and 80 meV clearly present in both cases. The relative intensity of the high energy feature is lower in the experimental DOS, consistent with previous studies on oxide ion conductors[69] and $La_2Mo_2O_9$. This is likely due to low population of high-energy phonons at the measured temperature and applying the Bose population factor to a weak signal. The agreement between the two methods of determining the DOS supports the validity of the AIMD simulations and provides evidence that conclusions drawn from them are reliable. The locations of the peaks are consistent with those found in similar oxide ion conducting materials such as $Bi_{26}Mo_{10}O_{69}$[69] and $La_2Mo_2O_9$ (Chapter 4, section 4.4.2).

6.4.3. Probing Dynamics on the Nanosecond Timescale

6.4.3.1. The Variation of Elastic and Inelastic Intensity with Temperature

Plots of elastic and inelastic intensities (at 2 μeV) against temperature are shown in figure 6.5 for both $La_{10}Ge_6O_{27}$ and $Bi_2La_8Ge_6O_{27}$. The decrease in elastic intensity (figure 6.5a) for $Bi_2La_8Ge_6O_{27}$ is small (≈ 15 %) and is linear over the entire temperature range which is indicative of a decrease that is purely due to the Debye-Waller factor (i.e. elastic intensity is lost to inelastic background noise due to thermal motions of the scattering atoms). This indicates that no quasielastic signal is observable on these nanosecond timescales.

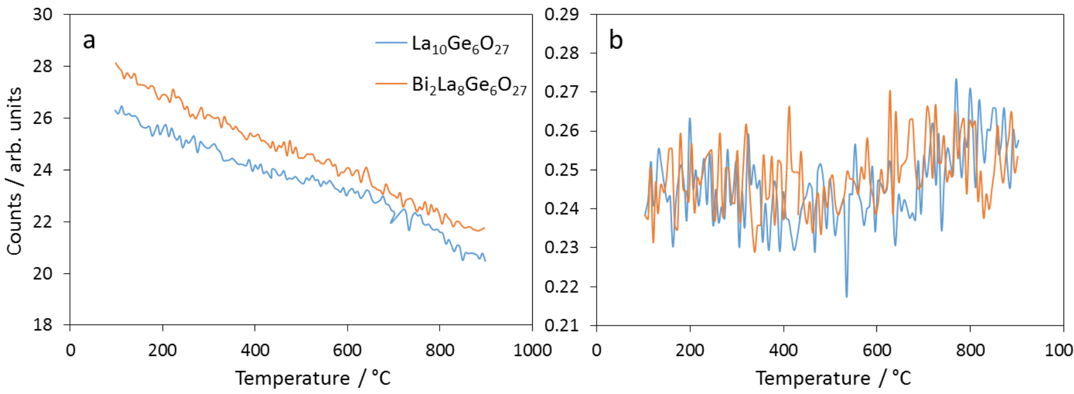

Figure 6.5: a) Plots of the elastic intensity against temperature for neutron scattering experiments on $La_{10}Ge_6O_{27}$ and $Bi_2La_8Ge_6O_{27}$ carried out with IN16b. Each temperature point was collected for 30 seconds. b) Plots of the inelastic intensity measured at 2 μeV against temperature. Each temperature point was collected for 120 seconds.

For $La_{10}Ge_6O_{27}$ the overall decrease is slightly higher (≈ 20 %) and a change in gradient is visible at around 600 °C potential indicating that dynamics begin to enter the nanosecond timescale window of IN16b. In figure 6.5b, the plots of inelastic intensity show very little change over the temperature range. At 600 °C it appears that the intensity may increase slightly in both materials, potentially indicating dynamics, although this change is small compared to the noise in the measurements.

6.4.3.2. The Variation of Scattering Function with Temperature

Figure 6.6 shows plots of *S*(*ω*) against energy transfer for both materials at 650 °C and 850 °C as well as a vanadium resolution function. The $La_{10}Ge_6O_{27}$, 650 °C spectrum matches the resolution function closely indicating a clear lack of a QENS signal. The remaining spectra appear to be slightly more intense than the resolution function at $\omega \neq 0$ and may be evidence of a weak QENS signal; however, due to the poor statistics in the data, attempts to fit a QENS peak to any of these spectra were not successful. This and the lack of any visible temperature dependence in the $Bi_2La_8Ge_6O_{27}$ spectra mean that it is difficult to be sure whether this is truly evidence of a QENS signal.

The scattering function plots agree with the elastic and inelastic intensity plots and indicate that dynamics in these apatite materials are potentially able to be seen on the nanosecond timescales probed by IN16b. However, the very weak signal observed in three of the datasets means that although dynamics could possibly be seen, they would require much longer data collection times to produce a useful signal.

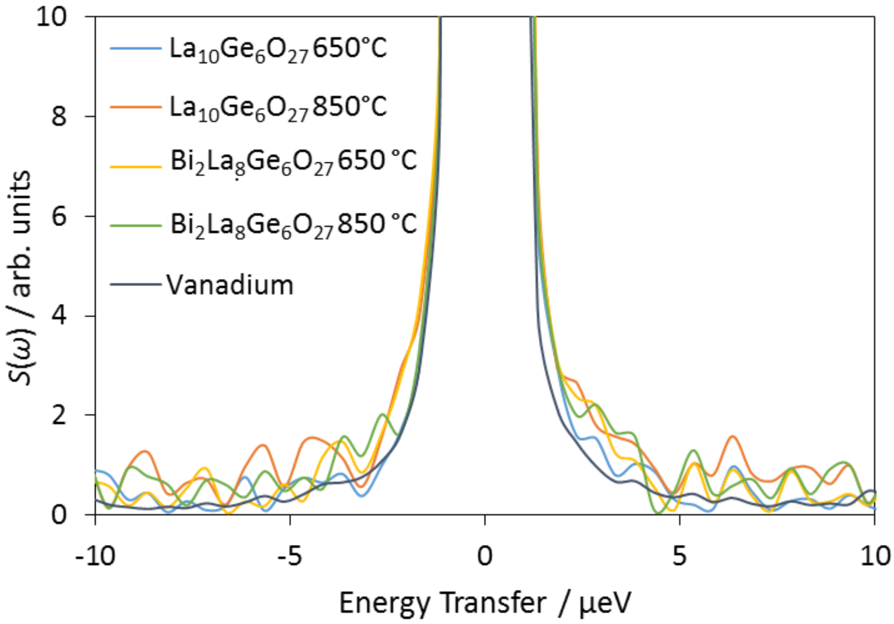

Figure 6.6 *S*(*ω*) spectra for inelastic neutron scattering measurements on IN16b for $La_{10}Ge_6O_{27}$ and $Bi_2La_8Ge_6O_{27}$ with a maximum energy transfer of ±10 μeV. A vanadium resolution function is also shown.

6.4.4. Locating Lone Pairs in Apatites Using the Electron Localisation Function

Electron localisation function (ELF) calculations were carried out to determine the orientations of the Bi^{3+} lone pairs in $Bi_2La_8Ge_6O_{27}$ so that potential interaction with any conduction mechanisms found by AIMD could be identified. As described in section 6.2.3, in the literature it has been assumed that the lone pairs point towards the anion channel centre without considering the effect that the identity and charge of the channel anion itself might have. Because of this ELFs were also calculated for $Pb_6Bi_4Ge_6O_{24}$, in which the channel X sites are vacant, and $Pb_{10}V_6O_{24}Cl_2$ and $Pb_{10}As_6O_{24}Cl_2$, which have Cl^- X anions. This series of vacant sites, monovalent Cl^- anions, and the divalent O^{2-} anions in $Bi_2La_8Ge_6O_{27}$ allows the effect that differently charged channel anions have on the location to be examined.

The ELFs calculated for $Pb_6Bi_4Ge_6O_{24}$, $Pb_{10}V_6O_{24}Cl_2$ and $Bi_2La_8Ge_6O_{27}$ can be seen in figure 6.7 where they are shown as purple regions. It can clearly be seen that the orientation of the lone pair differs greatly depending on the presence and identity of the channel anion. In the case of $Pb_6Bi_4Ge_6O_{24}$ the channel site X is unoccupied, and the lone pairs are orientated towards the middle of the channel, although at a 30° angle, pointing along the edges of a triangle made by the three Pb^{2+} in the same *ab* plane, rather than directly towards the channel centre (figure 6.7a). This can be understood in terms of the repulsion between the three lone pairs in the *ab* plane, and partially confirms the locations previously predicted for lacunar apatites.[26, 71] What was not predicted however is the fact that the lone pairs do not lie in the plane of the three A2 cations, instead pointing at a 30° angle out of it, also due to mutual repulsion of the lone pairs (figure 6.7d).

The structures containing the singly-charged Cl^- channel ions, $Pb_{10}V_6O_{24}Cl_2$ and $Pb_{10}As_6O_{24}Cl_2$, both exhibited very similar behaviour, indicating that the identity of the T site atoms has little effect on the lone pair locations. In both materials the lone pairs are orientated at a 45° angle from the channel centre, indicating additional repulsion caused by the Cl^- ions compared to the lacunar apatites (figure 6.7b). The locations found here differ significantly from the void spaces calculated by Baikie *et al*,[54] who found that the largest cavities around the Pb2 atoms were orientated significantly out of the plane of the cations towards the Cl^-. In this work, it was found that the lone pairs in these systems are oriented entirely within that plane, due to the Cl^- atoms repelling the lone pairs symmetrically from either side (figure 6.7e). This indicates that there can be a significant difference between the physical space in a structure and the electronic "space" that a lone pair can occupy.

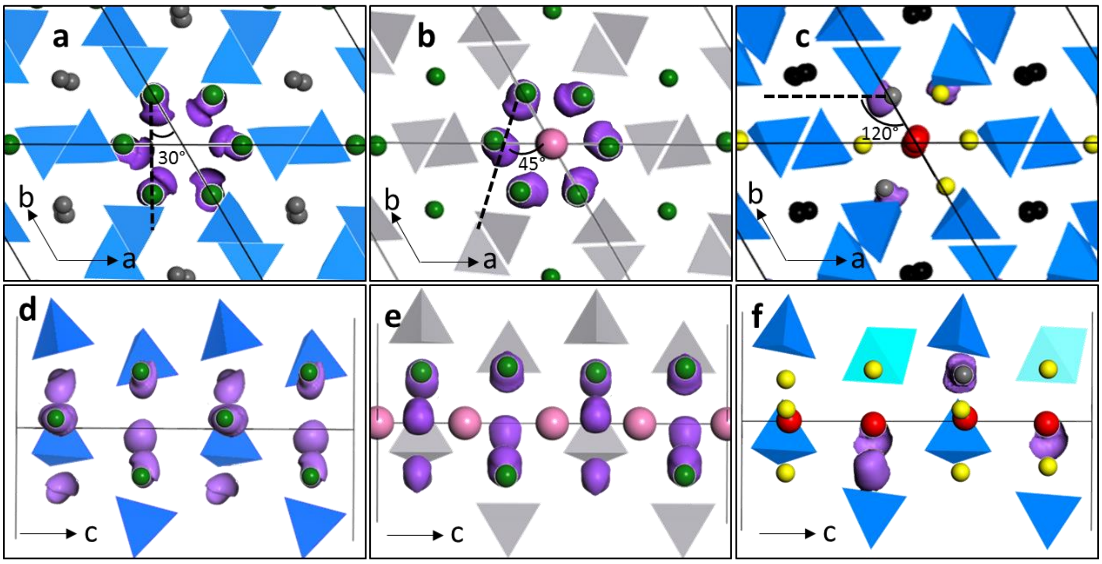

Figure 6.7: Locations and orientations of the lone pairs in a,d) $Pb_6Bi_4Ge_6O_{24}$, b,e) $Pb_{10}V_6O_{24}Cl_2$ and c,f) $Bi_2La_8Ge_6O_{27}$, looking directly down the *c*-axis in the (*ab*) plane (left) and along the c-axis (right) . Blue tetrahedra are GeO_4, light blue are GeO_5 groups, grey tetrahedra are VO_4, atoms are coloured light red - O4, pink - Cl, yellow - La2, black - La1, dark green - Pb, grey - Bi. The purple regions are the locations of lone pairs.

In the case of the oxide ion conductor, $Bi_2La_8Ge_6O_{27}$, the electrostatic effects are even more pronounced. The O^{2-} channel anions not only have twice the charge, but also lie in the same plane as the A2 cations (figure 6.7f), rather than offset in the *c*-direction as is the case for the Cl^- ion containing apatites previously discussed. The result of these factors is clearly visible in that the lone pairs are oriented away from the channels at a 120° angle (figure 6.7c). They remain within the *ab* plane of the cations, however, due to their relative position to the GeO_4 and GeO_5 groups located either side, and the fact that Bi^{3+} occupies only one third of the A2 sites, so there are fewer lone pairs present and their mutual repulsion is not as significant as in $Pb_6Bi_4Ge_6O_{24}$, where all A2 are occupied by lone pair containing cations. These lone pair locations differ significantly from the positions previously assumed for apatite-type oxides based on lacunar apatites.[25, 44, 46] Given that the lone pair cations are not orientated into the channel, physical and electronic blocking of an anion channel conduction mechanism caused by Bi^{3+} doping cannot be the cause of the reduced conductivity reported in lanthanum silicate apatite materials.[44, 46] The orientation towards the GeO_4 framework may in fact imply that some blocking of a conduction mechanism through this framework could occur. However, as it is known that such as mechanism is dominant in these materials,[33, 48] and that doping with Bi^{3+} actually increases the conductivity of the germanate apatites, the effects of the introduction of the lone pair must be more complex. These effects were further investigated by AIMD (section 6.4.5).

6.4.5. Conduction Mechanisms Investigated by *Ab Initio* Molecular Dynamics

In agreement with the behaviour found by Imaizumi *et al*,[33] the simulations at 1000 K showed no diffusion events, with all oxygen atoms remaining in their initial sites. This could be due to a simulation cell that is too small and a timescale too short to observe oxygen diffusion events at this temperature. By contrast, figure 6.8 shows the mean squared displacement (MSD) of oxygen atoms in the three simulated compositions at each of the higher temperatures that show long range diffusion. The MSDs shows no sign of plateauing, indicating that the motion is diffusional rather than being due to the local thermal vibrations of the O atoms. The maximum O^{2-} displacements increase progressively with increasing simulation temperatures, from about 2.3 Å at 1500 K to about 3.5 Å at 1750 K and to about 5 Å at 2000 K. The distance of 2.3 Å is slightly larger than the distance from the O sites in the GeO_4 tetrahedra to the adjacent O5 sites (≈ 2.2 Å), whereas 3.5 Å is significantly larger than that between the O sites in the GeO_4 tetrahedra (2.7-2.8 Å). This indicates significant long range diffusion of oxygen atoms in the material. The plots in figure 6.8 also show that the MSDs decrease with increased Bi content for 1500 K; however, at higher temperatures the opposite trend occurs with the MSDs increasing with Bi content. The simulations at the two higher temperatures are therefore consistent with the experimental findings in the temperature range with appreciable conductivity.[37]

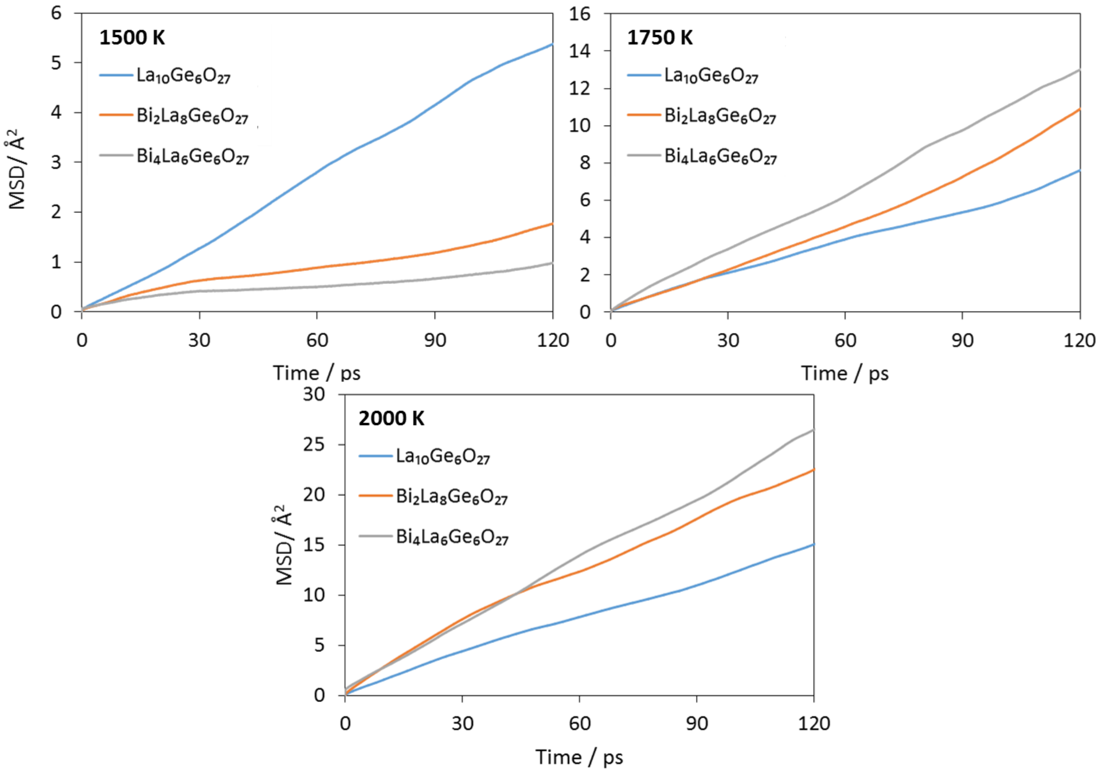

Figure 6.8: Mean square displacement curves calculated for $La_{10}Ge_6O_{27}$, $Bi_2La_8Ge_6O_{27}$, and $Bi_4La_6Ge_6O_{27}$ over the course of 120 ps of simulation time at 1500 K, 1750 K and 2000 K.

In the course of our AIMD simulations four clearly distinct oxide ion exchange mechanisms were observed for all compositions. Taken together they involve all the unique oxygen sites in the structure indicating that they all have the potential to move. These mechanisms are shown in figure 6.9 for $La_{10}Ge_6O_{27}$. The simulations at 1500 K show only two of the mechanisms, one involving the movement of oxide ions through the GeO_4 framework *via* the O5 sites (mechanism 1, figure 6.9a), and the other involving oxide ions moving from the GeO_4 framework into and out of the hexagonal column containing the O4 sites (mechanism 2, figure 6.9a, b and c). Additionally, in the higher temperature simulations, two further mechanisms were observed. One involves the oxide ion exchanges, in the *ab* plane, between the columns formed by the GeO_4 tetrahedra running down the *c*-axis (mechanism 3, figure 6.9b and c). The final mechanism involves the oxide ion transport in the *c*-direction *via* the O4 site-containing hexagonal column (mechanism 4, figure 6.9b). Mechanisms 1, 2 and 3 were observed by Imaizumi *et al*. and referred to as the "cooperative *c* axis", "cooperative O4", and "cooperative *ab* plane" mechanisms; mechanism 4 was not observed in their work.[48]

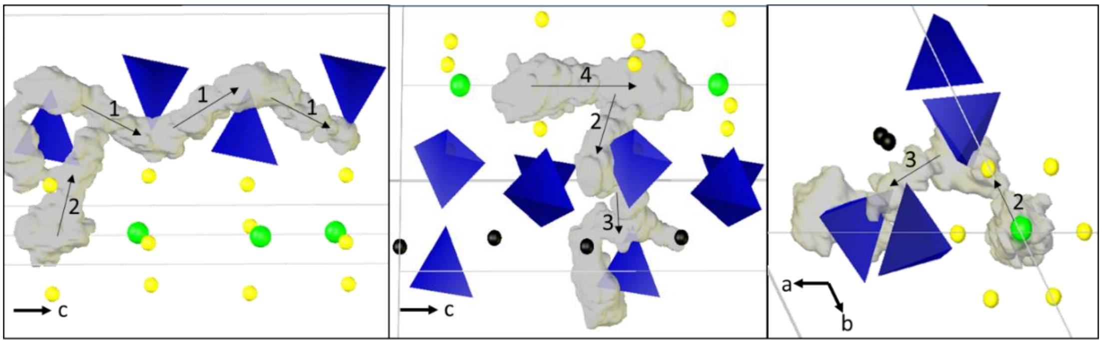

Figure 6.9: Cloud plots illustrating the four mechanisms of oxide ion conduction observed over the course of a 180 ps AIMD simulation on $La_{10}Ge_6O_{27}$ at 2000 K. Blue tetrahedra are GeO_4, green atoms are O4, yellow atoms are La2 and black atoms are La1. The grey clouds are regions visited by an oxygen atom over the course of the simulation.

Table 6.1 shows the number of times each exchange mechanism was observed over the course of each of the simulations, grouped by temperature and composition. For mechanisms 1 and 3, one instance was counted as when an O atom moved from the coordination sphere of one Ge centre to that of another; in other words, O atom jumps within a GeO_4 tetrahedron or jumps to a vacant O5 site associated with the same Ge centre were not counted. One instance of mechanism 2 was counted as a movement between and O4 site and the GeO_4 framework or *vice versa*. An instance of mechanism 4 was counted when an O moved from one O4 site to another.

Table 6.1: Number of instances of each oxide ion conduction mechanism observed in a 180 ps AIMD simulation at 1500 K, 1750 K and 2000 K for each of the three studied materials.

Mechanism	Number of Jumps								
	1500 K			1750 K			2000 K		
	0	2	4	0	2	4	0	2	4
1	21	11	3	24	31	44	40	46	50
2	7	5	4	8	16	26	29	33	40
3	0	0	0	2	8	17	10	24	35
4	0	0	0	1	0	1	8	8	12
Total	28	16	7	35	55	88	87	111	137

In agreement with the MSD curves shown in figure 6.8, the total number of oxide ion diffusion events decreases significantly with increasing doping level in the 1500 K simulations and increases with increasing Bi content at the higher temperatures. The reduced oxide ion mobility with increasing Bi-content observed in the 1500 K simulations may be due to the steric hindrance caused by the Bi lone pair pointing towards the GeO_4 framework (figure 6.7c and f) and therefore adversely affecting mechanism 1, dominant at this lower temperature.

In agreement with literature[33, 34] diffusion *via* the GeO_4 framework (mechanism 1) is the prevalent conduction mechanism at all temperatures. The relative number of instances of mechanisms 2 and 3 increase with temperature, whereas mechanism 4 seems to only be activated significantly at the highest temperature simulated. The number of instances of all activated oxide ion diffusion mechanisms increase with Bi content at the two highest temperatures. However, the relative proportion of the total diffusion events attributed to mechanism 1 decreases with Bi content, from 69 % to 50 % at 1750 K, and 46 % to 36 % at 2000 K. This may indicate that although a small steric hindrance on mechanism 1 caused by the lone pair remains at these temperatures, this mechanism no longer dominates as the contribution of the other three becomes more prominent. This increase in the relative contributions of the two *ab*-plane conduction mechanisms (2 and 3), indicate that the oxide ion conductivity of Bi-doped apatites could be more isotropic than the parent compounds, which could be significant in certain applications.

The fact that at 1500 K we observe only mechanisms 1 and 2, with 3 being seen only at higher temperatures, agrees with the behaviour reported by Imaizumi *et al.*[33] It is also consistent with the relative activation energies found in that work, with an activation energy of 1.17 eV found for mechanism 3, versus 0.64 eV and 0.76 eV for mechanisms 1 and 2, respectively.

Mechanism 4 was not observed by Imaizumi *et al.* in their simulations, and while it was only rarely seen in our AIMD simulations at higher temperatures, our results may indicate that some conduction directly down the O4-containing hexagonal channel in this way is possible in apatite-type germanates. While oxide ion transport directly down the O4 channel has been previously suggested in silicate apatites, many of these examples involve interstitial O sites within the channel itself.[31, 32, 43, 44] By contrast, our simulations show a vacancy mechanism *via* only O4 sites with vacancies created by mechanism 2, as has been proposed for the apatite-type silicate $La_{9.69}(Si_{5.70}Mg_{0.30})O_{26.24}$.[72]

One factor promoting diffusion on the introduction of Bi could be the change in coordination environment of the atoms in A2 sites due to the presence of the lone pair. Figure 6.10 shows, as a typical example, the differences in environment of a La atom in $La_{10}Ge_6O_{27}$ and a corresponding Bi atom in the same position in $Bi_2La_8Ge_6O_{27}$ after geometry optimisation.

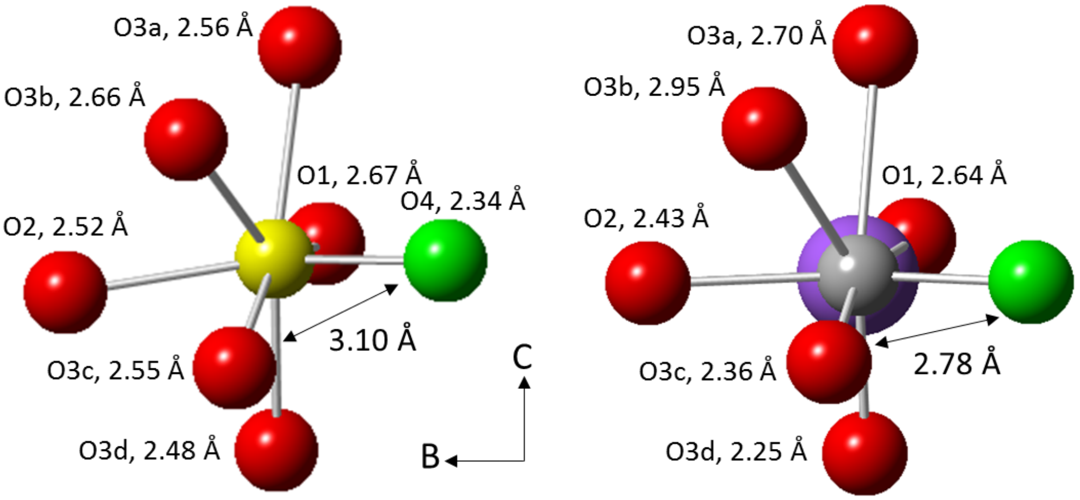

Figure 6.10: Comparison of the local environments around an A2 site in $La_{10}Ge_6O_{27}$ (left) and a Bi site in $Bi_1La_9Ge_6O_{27}$ (right). The yellow atom is La, grey is Bi, green is O4 and red are other O. The orange atoms are oxygens the have shorter bonds to Bi than the equivalent for La, and dark red have longer bonds. The mint green O4 indicates that the Bi-O4 bond is shorter than the La-O4. The purple region indicates the lone pair.

It can be seen that four of the Bi-O bonds, including the Bi-O4, get shorter in comparison to the equivalent La-O bonds, while two get longer. The shortening of the bonds to O4, O3c and O3d has the effect of bringing key oxygen sites involved in mechanism 2 closer together, which would make the O^{2-} jumps between these sites easier. The reduction of the distance between sites is especially notable in the case of the O4 atom and its nearest neighbour O3c, for which the distance changes from approximately 3.1 Å to around 2.8 Å, but is also significant for the next nearest neighbour O3d, for which the distance changes from 3.6 to

3.2 Å, a distance that makes movement between these sites much more feasible. Similar changes in the bonding pattern, typical for the introduction of a lone pair cation, are seen for all four La/Bi pairs of corresponding sites (see figure 6.11 for the full distribution of bond lengths), and are likely responsible for the large increase in instances of mechanism 2 upon Bi^{3+} doping at higher temperatures.

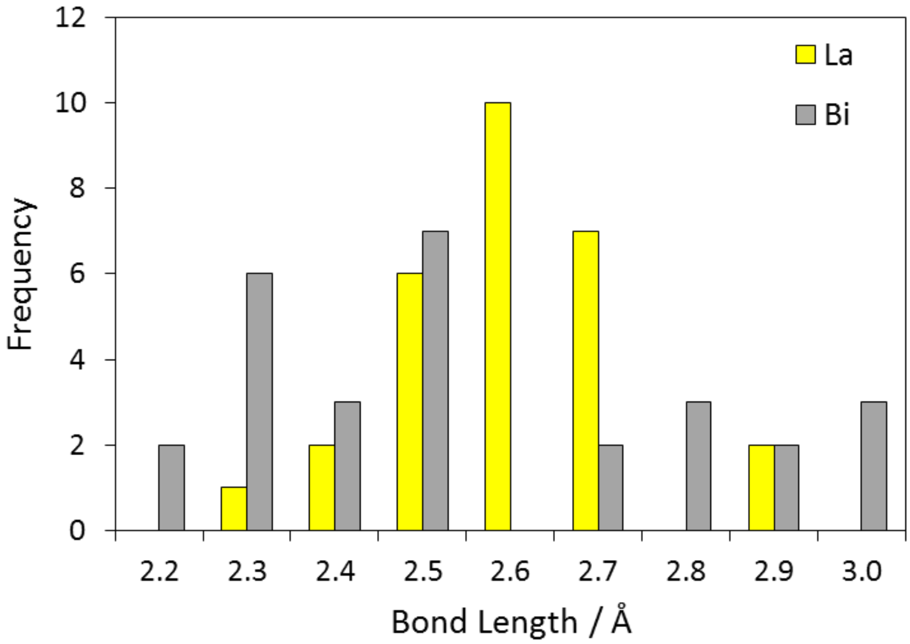

Figure 6.11: Distribution of bond lengths to oxygen for the Bi atom in $Bi_2La_8Ge_6O_{27}$ and the La atoms on the equivalent sites in $La_{10}Ge_6O_{27}$. On doping with Bi the coordination environment becomes less symmetric, with some of the bonds to oxygens becoming shorter than those in the parent material and some longer.

Another factor is the relative apparent weakness of some Bi-O bonds compared to the equivalent La-O bonds. Figure 6.12 shows the distribution of Mulliken bond populations[73-75] for the La-O and Bi-O bonds in equivalent A2 sites in $La_{10}Ge_6O_{27}$ and $Bi_2La_8Ge_6O_{27}$ calculated during DFT geometry optimisation. The Mulliken bond population represents the overlap of electronic orbitals between the atoms, where a value of 1 indicates maximum overlap while a value of 0 indicates non-bonding interaction and a negative value an antibonding state.[76] The degree of orbital overlap can be thought of as an indicator of bond strength[76] and a low value has been shown to correlate with the ease of defect formation and oxide ion mobility in pyrocholore[77] and Aurivillius[78, 79] fast ion conductors. It can be seen from figure 6.12 that the distribution of Mulliken populations is shifted to lower values for the Bi-O bonds in comparison to the La-O bonds. This indicates that the bonds around the Bi sites are apparently weaker and thus oxide ion mobility is facilitated in the doped materials. As can be seen in table 6.2, this decrease in orbital overlap is especially pronounced for the bonds to the O1 and O3a atoms, which are those on the same side of the Bi atom as the lone pair, with changes for the O3b and O3c atoms that are opposite it being much smaller. This suggests that it is repulsion caused by the lone pair introduced on Bi^{3+} doping that is reducing orbital overlap and therefore increasing oxide ion mobility.

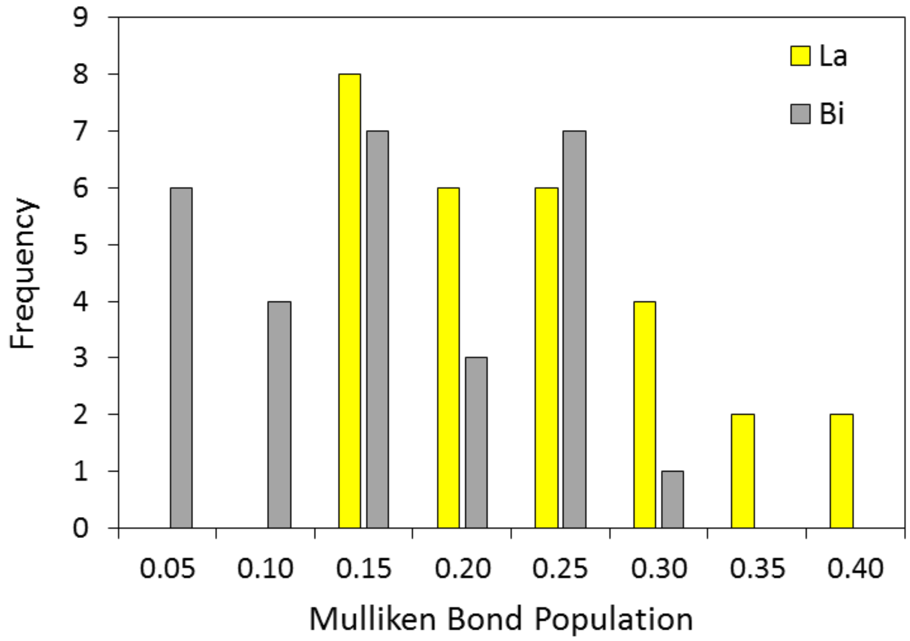

Figure 6.12: Distribution of Mulliken bond populations of the Bi-O bonds in $Bi_2La_8Ge_6O_{27}$ and the equivalent La-O bonds in $La_{10}Ge_6O_{27}$.

Table 6.2: The Mulliken bond populations of the bonds to oxygen from an A2 site containing La in $La_{10}Ge_6O_{27}$ and Bi in $Bi_2La_8Ge_6O_{27}$

Bonded Oxygen	Bi Site 1		Bi Site 2		Bi Site 3		Bi Site 4	
	La-O	Bi-O	La-O	Bi-O	La-O	Bi-O	La-O	Bi-O
O1	0.14	0.02	0.13	0.01	0.12	0.03	0.16	0.03
O2	0.17	0.11	0.14	0.04	0.15	0.05	0.19	0.11
O3a	0.15	0.07	0.22	0.09	0.23	0.06	0.15	0.08
O3b	0.15	0.14	0.21	0.19	0.2	0.16	0.21	0.14
O3c	0.19	0.22	0.3	0.23	0.29	0.28	0.19	0.21
O3d	0.27	0.13	0.21	0.13	0.22	0.17	0.26	0.14
O4	0.33	0.24	0.36	0.24	0.33	0.24	0.38	0.22

6.5. Conclusions

In this work an extensive computational investigation into lone pair containing apatites has been carried out with emphasis on how the presence of Bi^{3+} affects the oxide ion conduction mechanisms of the $Bi_xLa_{10-x}Ge_6O_{27}$ (x = 0, 2, 4) series. These results represent the first computational insights into the effects of lone pairs on oxide ion conducting apatite type materials.

The electron localisation function (ELF) calculations have been used to provide the first computational location of the cation lone pairs in a number of apatite materials. The identity and positions of the channel anions (or lack thereof) is responsible for the orientations of the lone pairs in these materials. It has been shown that the repulsion of the lone pair by the channel anions causes a shift in the orientation of the lone pairs from a 30° angle away from the channel centre in lacunar apatites, to 45° for monovalent Cl^- anions and 120° for O^{2-} anions. The last case is particularly interesting as the lone pair orientation is towards the GeO_4 / GeO_5 framework, rather than into the channel, which has significant implications for the ionic conduction mechanisms in these materials.

Ab initio molecular dynamics calculations have been used to investigate the effects of doping $La_{10}Ge_6O_{27}$ with lone pair containing Bi^{3+} on the individual oxide ion diffusion mechanisms that contribute to the overall conductivity. The simulations successfully reproduce a DOS found using neutron scattering giving an indication of their reliability. The simulations show that for the simulations at 1500 K doping with the lone pair cation decreases the overall mobility of oxygen which may be due to the lone pairs that are oriented towards the GeO_4 framework impeding the mechanism through this framework that is dominant at this temperature. At higher temperatures oxide ion mobility increases with Bi content, corroborating experimental results. Four oxide ion exchange mechanisms have been observed, and it has been shown that the dominant one is that involving oxide ion transport in the *c*-direction *via* the GeO_4 framework; however, Bi^{3+} doping increases the relative proportion of two mechanisms that transport oxide ions in the *ab* plane. This indicates that doping with lone pair cations could aid in promoting isotropic oxide ion mobility in apatites, a useful feature for application design. Also identified is the presence of a fourth conduction mechanism at high temperatures, previously not identified in lanthanum germanate apatites involving conduction down the anion channel in the *c*-direction.

The increased conductivity observed in Bi-doped $La_{10}Ge_6O_{27}$–based materials appears to be a combination of several factors. The first is the change in coordination environment around the A2 cations sites caused by the introduction of the lone pair. The shortening of some bonds and lengthening of others reduces the distance between the channel O4 atoms and its nearest neighbours in the GeO_4 framework, significantly easing transport between the channel and the framework. The transport is further facilitated by the reduced orbital overlap of the Bi-O bonds compared to the La-O as measured by the Mulliken bond population which can be thought of as indicative of apparently weaker bonds.

The neutron scattering results showed no quasielastic signal at the picosecond timescales probed by the IN6 spectrometer. At the nanosecond timescales probed by the IN16b spectrometer a potentially very weak QENS signal is seen but this is inconclusive. This could indicate that dynamics are slower, possibly requiring tens of nanoseconds timescales to be observed. This is backed up by the high simulation temperatures required to observe any diffusion events as the 180 ps simulation times may be much too short to see them at experimentally achievable temperatures.

6.6. References

1. A. Savin, R. Nesper, S. Wengert and T. F. Fässler, *Angew Chem Int Ed Engl*, 1997, **36**, 1808-1832.
2. N. C. da Rocha, R. C. de Campos, A. M. Rossi, E. L. Moreira, F. Barbosa Ado and G. T. Moure, *Environ Sci Technol*, 2002, **36**, 1630-1635.
3. E. Mavropoulos, A. M. Rossi, A. M. Costa, C. A. Perez, J. C. Moreira and M. Saldanha, *Environ Sci Technol*, 2002, **36**, 1625-1629.
4. S. Gao, J. Cui and Z. Wei, *Journal of Fluorine Chemistry*, 2009, **130**, 1035-1041.
5. L. Chen, K.-S. Zhang, J.-Y. He, W.-H. Xu, X.-J. Huang and J.-H. Liu, *Chemical Engineering Journal*, 2016, **285**, 616-624.
6. N. Lakshminarasimhan and U. V. Varadaraju, *Journal of Solid State Chemistry*, 2004, **177**, 3536-3544.
7. N. Lakshminarasimhan and U. V. Varadaraju, *Materials Research Bulletin*, 2014, **60**, 238-241.
8. J. T. B. Ratnayake, M. Mucalo and G. J. Dias, *J Biomed Mater Res B Appl Biomater*, 2017, **105**, 1285-1299.
9. T. Naddari, *Solid State Ionics*, 2003, **158**, 157-166.
10. B. Hamdi, H. Elfeki, A. Bensalah, P. Salles, P. Baules and J. Savariault, *Solid State Ionics*, 2006, **177**, 1413-1420.
11. A. Laghzizil, P. Barboux and A. Bouhaouss, *Solid State Ionics*, 2000, **128**, 177-181.
12. S. Lahrich, B. Manoun and M. A. E. Mhammedi, *Materials Research Bulletin*, 2014, **59**, 349-357.
13. S. Lahrich, B. Manoun and M. A. El Mhammedi, *Talanta*, 2016, **149**, 158-167.
14. M. S. Islam, J. R. Tolchard and P. R. Slater, *Chemical Communications*, 2003, DOI: 10.1039/b301179h, 1486-1487.
15. H. Arikawa, *Solid State Ionics*, 2000, **136-137**, 31-37.
16. S. Nakayama, M. Sakamoto, M. Higuchi, K. Kodaira, M. Sato, S. Kakita, T. Suzuki and K. Itoh, *Journal of the European Ceramic Society*, 1999, **19**, 507-510.
17. P. R. Slater, J. E. Sansom and J. R. Tolchard, *Chem Rec*, 2004, **4**, 373-384.

18. J. Xiang, Z.-G. Liu, J.-H. Ouyang and F.-Y. Yan, *Journal of Power Sources*, 2014, **251**, 305-310.
19. H. Li, T. Baikie, S. S. Pramana, J. F. Shin, P. J. Keenan, P. R. Slater, F. Brink, J. Hester, T. An and T. J. White, *Inorganic chemistry*, 2014, **53**, 4803-4812.
20. J. Sansom, *Solid State Ionics*, 2004, **167**, 23-27.
21. E. Kendrick, J. E. H. Sansom, J. R. Tolchard, M. S. Islam and P. R. Slater, *Faraday Discussions*, 2007, **134**, 181-194.
22. T. J. White and D. ZhiLi, *Acta Crystallographica B*, 2003, **59**, 1-16.
23. L. León-Reina, M. C. Martín-Sedeño, E. R. Losilla, A. Cabeza, M. Martínez-Lara, S. Bruque, F. M. B. Marques, D. V. Sheptyakov and M. A. G. Aranda, *Chemistry of Materials*, 2003, **15**, 2099-2108.
24. E. Abram, C. Kirk, D. Sinclair and A. West, *Solid State Ionics*, 2005, **176**, 1941-1947.
25. M. L. Tate, D. A. Blom, M. Avdeev, H. E. A. Brand, G. J. McIntyre, T. Vogt and I. R. Evans, *Advanced Functional Materials*, 2017, **27**, 1605625.
26. M. Mathew, W. E. Brown, M. Austin and T. Negas, *Journal of Solid State Chemistry*, 1980, **35**, 69-76.
27. M. El Koumiri, S. Oishi, S. Sato, L. El Ammari and B. Elouadi, *Materials Research Bulletin*, 2000, **35**, 503-513.
28. E. I. Get'man, S. N. Loboda, A. V. Ignatov, V. V. Prisedsky, M. A. Abdul Jabar and L. I. Ardanova, *Inorganic chemistry*, 2016, **55**, 2165-2173.
29. A. Jones, P. R. Slater and M. S. Islam, *Chemistry of Materials*, 2008, **20**, 5055-5060.
30. S. S. Pramana, W. T. Klooster and T. J. White, *Acta Crystallographica B*, 2007, **63**, 597-602.
31. E. Béchade, O. Masson, T. Iwata, I. Julien, K. Fukuda, P. Thomas and E. Champion, *Chemistry of Materials*, 2009, **21**, 2508-2517.
32. K. Matsunaga and K. Toyoura, *Journal of Materials Chemistry*, 2012, **22**, 7265-7273.
33. K. Imaizumi, K. Toyoura, A. Nakamura and K. Matsunaga, *Solid State Ionics*, 2014, **262**, 512-516.
34. E. Kendrick, A. Orera and P. R. Slater, *Journal of Materials Chemistry*, 2009, **19**, 7955-7958.
35. L. León-Reina, J. M. Porras-Vázquez, E. R. Losilla and M. A. G. Aranda, *Solid State Ionics*, 2006, **177**, 1307-1315.
36. T. Baikie, P. H. Mercier, M. M. Elcombe, J. Y. Kim, Y. Le Page, L. D. Mitchell, T. J. White and P. S. Whitfield, *Acta Crystallographica B*, 2007, **63**, 251-256.
37. M. L. Tate, C. A. Fuller, M. Avdeev, H. E. A. Brand, G. J. McIntyre and I. R. Evans, *Dalton Trans*, 2017, **46**, 12494-12499.
38. J. R. Tolchard, J. E. H. Sansom, P. R. Slater and M. S. Islam, *J Solid State Electrochem*, 2004, **8**, 668-673.
39. L. León-Reina, E. R. Losilla, M. Martínez-Lara, S. Bruque, A. Llobet, D. V. Sheptyakov and M. A. G. Aranda, *Journal of Materials Chemistry*, 2005, **15**, 2489-2498.
40. K. Fukuda, T. Asaka, M. Okino, A. Berghout, E. Béchade, O. Masson, I. Julien and P. Thomas, *Solid State Ionics*, 2012, **217**, 40-45.
41. Y. Kim, D.-K. Shin, E.-C. Shin, H.-H. Seo and J.-S. Lee, *Journal of Materials Chemistry*, 2011, **21**, 2940-2949.
42. L. León-Reina, E. R. Losilla, M. Martínez-Lara, S. Bruque and M. A. G. Aranda, *Journal of Materials Chemistry*, 2004, **14**, 1142-1149.
43. K. Imaizumi, K. Toyoura, A. Nakamura and K. Matsunaga, *Journal of Physics: Condensed Matter*, 2015, **27**, 365601.
44. E. Kendrick, M. S. Islam and P. R. Slater, *Journal of Materials Chemistry*, 2007, **17**, 3104-3111.
45. J. R. Tolchard, M. S. Islam and P. R. Slater, *Journal of Materials Chemistry*, 2003, **13**, 1956-1961.

46. E. Kendrick, M. S. Islam and P. R. Slater, *Chemical Communications*, 2008, DOI: 10.1039/b716814d, 715-717.
47. P. M. Panchmatia, A. Orera, G. J. Rees, M. E. Smith, J. V. Hanna, P. R. Slater and M. S. Islam, *Angew Chem Int Ed Engl*, 2011, **50**, 9328-9333.
48. K. Imaizumi, K. Toyoura, A. Nakamura and K. Matsunaga, *Journal of the Ceramic Society of Japan*, 2017, **125**, 105-111.
49. A. Bigi, A. Ripamonti, S. Brückner, M. Gazzano, N. Roveri and S. A. Thomas, *Acta Crystallographica B*, 1989, **45**, 247-251.
50. X. P. Wang, Q. F. Fang, Z. S. Li, G. G. Zhang and Z. G. Yi, *Applied Physics Letters*, 2002, **81**, 3434-3436.
51. P. Moore and J. Shen, *American Mineralogist*, 1984, **69**, 1173-1179.
52. F. Goutenoire, O. Isnard, E. Suard, O. Bohnke, Y. Laligant, R. Retoux and P. Lacorre, *Journal of Materials Chemistry*, 2001, **11**, 119-124.
53. P. Lacorre, F. Goutenoire, O. Bohnke, R. Retoux and Y. Laligant, *Nature*, 2000, **404**, 856-858.
54. T. Baikie, M. Schreyer, F. Wei, J. S. Herrin, C. Ferraris, F. Brink, J. Topolska, R. O. Piltz, J. Price and T. J. White, *Mineral Mag*, 2014, **78**, 325-345.
55. B. Badraoui, A. Aissa, A. Bigi, M. Debbabi and M. Gazzano, *Journal of Solid State Chemistry*, 2006, **179**, 3065-3072.
56. R. Seshadri and N. A. Hill, *Chemistry of Materials*, 2001, **13**, 2892-2899.
57. J.-M. Raulot, G. Baldinozzi, R. Seshadri and P. Cortona, *Solid State Sciences*, 2002, **4**, 467-474.
58. H. Y. Chang, S. H. Kim, P. S. Halasyamani and K. M. Ok, *Journal of the American Chemistry Society*, 2009, **131**, 2426-2427.
59. A. A. Coelho, J. S. O. Evans, I. R. Evans, A. Kern and S. Parsons, *Powder Diffraction*, 2012, **26**, S22-S25.
60. H. M. Rietveld, *Journal of Applied Crystallography*, 1969, **2**, 65-71.
61. D. Richard, M. Ferrand, G. and J. Kearley, *Journal of Neutron Research*, 1996, **4**, 33-39.
62. S. J. Clark, M. D. Segall, C. J. Pickard, P. J. Hasnip, M. I. J. Probert, K. Refson and M. C. Payne, *Z Anorg Allg Chem*, 2005, **220**, 567-570.
63. J. P. Perdew, K. Burke and M. Ernzerhof, *Phys Rev Lett*, 1996, **77**, 3865-3868.
64. H. H. Otto, *Crystal Research and Technology*, 2015, **50**, 922-928.
65. H. Okudera, *American Mineralogist*, 2013, **98**, 1573-1579.
66. G. Kresse and J. Furthmüller, *Computational Materials Science*, 1996, **6**, 15-50.
67. G. Kresse and D. Joubert, *Physical Review B*, 1999, **59**, 1758-1775.
68. G. Goret, B. Aoun and E. Pellegrini, *Journal of Chemical Information and Modeling*, 2017, **57**, 1-5.
69. C. D. Ling, W. Miiller, M. R. Johnson, D. Richard, S. Rols, J. Madge and I. R. Evans, *Chemistry of Materials*, 2012, **24**, 4607-4614.
70. J. E. Auckett, A. J. Studer, E. Pellegrini, J. Ollivier, M. R. Johnson, H. Schober, W. Miiller and C. D. Ling, *Chemistry of Materials*, 2013, **25**, 3080-3087.
71. S. V. Krivovichev, T. Armbruster and W. Depmeier, *Materials Research Bulletin*, 2004, **39**, 1717-1722.
72. R. Ali, M. Yashima, Y. Matsushita, H. Yoshioka, K. Ohoyama and F. Izumi, *Chemistry of Materials*, 2008, **20**, 5203-5208.
73. R. S. Mulliken, *The Journal of Chemical Physics*, 1955, **23**, 1833-1840.
74. R. S. Mulliken, *The Journal of Chemical Physics*, 1955, **23**, 1841-1846.
75. R. S. Mulliken, *The Journal of Chemical Physics*, 1955, **23**, 2338-2342.
76. M. D. Segall, R. Shah, C. J. Pickard and M. C. Payne, *Physical Review B*, 1996, **54**, 16317-16320.
77. K. Nakamura, M. Mori, T. Itoh and T. Ohnuma, *AIP Advances*, 2016, **6**, 115003.

78. V. M. Zainullina and V. P. Zhukov, *Physics of the Solid State*, 2001, **43**, 1686-1699.
79. Y. V. Emel’yanova, R. R. Shafigina, E. S. Buyanova, V. M. Zhukovskii, V. M. Zainullina and S. A. Petrova, *Russian Journal of Physical Chemistry*, 2006, **80**, 1725-1730.

Chapter 7. Overall Conclusions and Further Work

The exploratory syntheses carried out in the early stages of this PhD project, namely the attempted doping of the $SrSiO_3$, $SrGeO_3$ and $BaZrSi_3O_9$ were not a success. While in the case of $BaZrSi_3O_9$ no crystalline impurities were observed, indicating that doping may have been successful, the conductivity in the materials remained low. This is evidence that the T_3O_9 (T = Si/Ge) structural features do not facilitate oxygen mobility. This may be due to the distance between these clusters (≈ 4 Å between the closest oxygen sites) being too far for any vacancy hopping mechanism to occur. Additionally, it is likely to be more favourable for any interstitial oxygens created to reside within a T_3O_9 cluster, possibly forming a second bridging oxygen between two of the T atoms. This would lead to any possible movement occurring locally within the cluster rather than *via* a long range mechanism between clusters.

The work carried on the samples $La_2Mo_2O_9$, $Bi_{0.913}V_{0.087}O_{1.587}$ and Bi-doped $La_{10}Ge_6O_{27}$ in the latter stages of the thesis have met with considerably more success. Significant results have been gained through the use of both neutron scattering and computational techniques, showing the applicability of these techniques to oxide ion conducting materials and providing new insight into the links between the structure of such materials and the oxide ion diffusion mechanisms that result.

The neutron scattering work reported in this thesis has extended the range of timescales for which oxide ion dynamics have been observed to nanoseconds. In the future this could be pushed even further as tests on IN16b with GaAs(200) analyser and monochromator crystals are currently ongoing which have led to energy resolutions ≈ 75 neV so far (equivalent to timescales of ≈ 50 ns).[1] The calculated activation energies of the dynamics are consistently somewhat lower than those determined using impedance measurements as would be expected from microscopic and macroscopic techniques, and also evidenced in the existing literature. The fitting of the QENS data with the Chudley-Elliott model has given feasible timescales; however, the jump distances found have been slightly larger than the distances between oxygen sites for both $La_2Mo_2O_9$ and $Bi_{0.913}V_{0.087}O_{1.587}$. This may be due to the presence of Bragg peaks in the data making calculating values for the QENS linewidth difficult. It is likely also due to the low *Q* resolution and range available making fitting difficult. Remedying these problems is difficult as the presence of Bragg peaks is sample-dependent and the *Q* range and resolution are restricted by the neutron scattering instrument, which would also need to reach the nanosecond timescales required. Despite this, the match between the activation energy calculated from AIMD and QENS for $Bi_{0.913}V_{0.087}O_{1.587}$ shows that neutron scattering can provide direct evidence for oxygen conduction mechanisms. Additionally, if the AIMD simulations carried out in this thesis were extended to the nanosecond times required to calculate an $S(Q,\omega)$ spectrum at IN16b's energy resolution, direct comparison between the two could be made. Currently, this would require significant time investment but will be more feasible in the future as calculations become more efficient and computers become more powerful.

Due to the matching activation energies between the long range Bi-O sublattice process seen in AIMD simulations of $Bi_{0.913}V_{0.087}O_{1.587}$ and the dynamics probed by IN16b it appears that the QENS measurements are probing only this long range diffusion process. This means that it should be possible to perform neutron scattering experiments to observe the faster V-O sublattice process, similar to the local motions within MoO_x polyhedra seen in $Bi_{26}Mo_{10}O_{69}$.[2] Evidence for this process cannot be seen in the measurements on IN6, indicating that the picosecond timescales observed by this instrument are likely too short. An investigation on an instrument that can observe timescales intermediate between IN16b and IN6 is worth performing; however, due to the much lower number of oxygen atoms involved in this process (≈ 21 % of the total) it will require a proportionally higher count rate/time.

The fact that separate processes occur on different timescales may also be a factor in the weak signal seen in the IN16b measurements on the Bi-doped $La_{10}Ge_6O_{27}$ materials. The AIMD simulations reported in this thesis show that oxide ion conduction in this material proceeds through multiple mechanisms occurring with varying likelihood. This may mean that only one of these processes can be observed on the nanosecond timescales probed by IN16b which would lead to a weaker signal if only a small proportion of the oxide ions undergo this process. To investigate this further it would be necessary to collect additional data on IN16b for a long enough time to collect sufficient statistics for a QENS signal to be conclusively observed and analysed.

In the literature, neutron scattering experiments have been performed on proton exchange membrane fuel cells.[3] This investigation allowed confirmation that the protons in the *in situ* cell under an electric field exhibit the same behaviour as those in *ex situ* membranes proving that data gathered on the *ex situ* material can be used as realistic input for fuel cell modelling. In addition to the work already suggested, similar studies could be carried out on *in situ* solid oxide fuel cells to confirm that the dynamical processes match those found for *ex situ* materials.

It is clear from the AIMD simulations of all the materials studied in this thesis, $La_2Mo_2O_9$, $Bi_{0.913}V_{0.087}O_{1.587}$, $La_{10}Ge_6O_{27}$ that the variable coordination number of the Mo^{6+}, V^{5+} and Ge^{4+} atoms as well as the flexibility of the coordination environment itself are important factors in the overall conductivity in these materials. In $La_2Mo_2O_9$, the MoO_x polyhedra are close (≈ 2.2 Å between the closest oxygen sites on adjacent polyhedra) allowing the overall conduction mechanism to involve oxygen transfer within and between the MoO_x polyhedra with the Mo atoms varying between 4, 5 and 6 coordinate as necessary. In $Bi_{0.913}V_{0.087}O_{1.587}$, the VO_x polyhedra are separated by ≈ 6.7 Å and the (initially VO_4) polyhedra act to remove oxygen atoms from the Bi-O sublattice with the V atoms changing from 4 to 5 coordinate. This creates additional vacancies in the Bi-O sublattice increasing the long range conductivity by the vacancy hopping mechanism through this lattice. For the $La_{10}Ge_6O_{27}$ and doped materials, the ability of the germanium atoms to quickly vary between 4 coordinate (as GeO_4 tetrahedra) and 5 coordinate (as Ge_2O_9 with bridging interstitial oxygen) is crucial to three of the four conduction mechanisms identified in the simulations.

The effects of Bi-doping on the oxygen transport mechanisms in the $La_{10}Ge_6O_{27}$ AIMD simulations reveal that despite the lone pair orientation towards the GeO_4 framework, any blocking of the oxygen transport mechanism through this framework is minor and in fact doping increases the number of instances of all conduction mechanisms at higher temperatures, consistent with experimental data.[4] To further explore the influence of lone pairs on conductivity in apatite materials a similar investigation could be carried out on the silicate analogue $La_{10}Si_6O_{27}$, which has previously been reported to experience a drop in conductivity upon Bi^{3+} doping.[5] The reason for this was previously theorised to be due to blocking of a *c*-direction mechanism down the O4 channel (mechanism 4 in Chapter 6, figure 6.9) believed to the major conductivity mechanism in the silicate materials;[6-8] however, as the electron localisation function calculations reported here show, the lone pair is not orientated towards the channel. Such an investigation could provide an explanation for these differences in behaviour as well as provide quantitative analysis of conduction mechanisms in the undoped material.

The $La_2Mo_2O_9$ and $Bi_{0.913}V_{0.087}O_{1.587}$ simulations show oxide mobility when performed in the temperature range of experimental measurements, whereas the Bi-doped $La_{10}Ge_6O_{27}$ simulations require temperatures up to 1000 °C higher to see any diffusion events. The higher simulation temperatures required in the latter case may be due to the lower number of oxide interstitials (1/27 of the oxygens) compared to the vacancies in $La_2Mo_2O_9$ (18 oxygen atoms in the β-$La_2Mo_2O_9$ unit cell distributed over 24 sites giving 25 % vacancies) and $Bi_{0.913}V_{0.087}O_{1.587}$ (25 % vacancies in the Bi-O sublattice). This would mean that a diffusion event is relatively rare. Performing simulations on a larger cell at lower temperatures could lead to diffusion events being seen at these low temperatures as the larger number of atoms presents more opportunity for such a diffusion event to occur.

7.1. References

1. K. Kuhlmann, M. Appel, B. Frick and A. Mager, A Record in Backscattering Energy Resolution — First Tests on IN16B with GaAs 200, https://www.ill.eu/projet-refonte/instruments-support/instruments-groups/instruments/in16b/news/, (accessed February, 2017).
2. C. D. Ling, W. Miiller, M. R. Johnson, D. Richard, S. Rols, J. Madge and I. R. Evans, *Chemistry of Materials*, 2012, **24**, 4607-4614.
3. N. Martinez, A. Morin, Q. Berrod, B. Frick, J. Ollivier, L. Porcar, G. Gebel and S. Lyonnard, *The Journal of Physical Chemistry C*, 2018, **122**, 1103-1108.
4. M. L. Tate, C. A. Fuller, M. Avdeev, H. E. A. Brand, G. J. McIntyre and I. R. Evans, *Dalton Trans*, 2017, **46**, 12494-12499.
5. E. Kendrick, M. S. Islam and P. R. Slater, *Journal of Materials Chemistry*, 2007, **17**, 3104-3111.
6. K. Imaizumi, K. Toyoura, A. Nakamura and K. Matsunaga, *Journal of Physics: Condensed Matter*, 2015, **27**, 365601.
7. E. Béchade, O. Masson, T. Iwata, I. Julien, K. Fukuda, P. Thomas and E. Champion, *Chemistry of Materials*, 2009, **21**, 2508-2517.
8. K. Matsunaga and K. Toyoura, *Journal of Materials Chemistry*, 2012, **22**, 7265-7273.

Appendix I. Publications Arising from this PhD Project

Na^+ Mobility in Sodium Strontium Silicate Fast Ion Conductors

J. R. Peet, C. M. Widdifield, D. C. Apperley, P. Hodgkinson, M. R. Johnson and I. R. Evans, *Chemical Communications*, 2015, **51**, 17163-17165

Solid State NMR measurements were carried out by David Apperley as part of the Durham University Solid State NMR Service. T_1 measurements were carried in out the laboratory of Paul Hodgkinson with the aid of Cory Widdifield. Data analysis was carried out with the guidance of Paul Hodgkinson, David Apperley, and Cory Widdifield.

Direct Observation of Oxide Ion Dynamics in $La_2Mo_2O_9$ on the Nanosecond Timescale

J. R. Peet, C. A. Fuller, B. Frick, M. Zbiri, A. Piovano, M. R. Johnson and I. R. Evans, *Chemistry of Materials*, 2017, **29**, 3020-3028

Aid with neutron scattering experiments and resulting data analysis was given by Mohamed Zbiri for the spectrometer IN6 and Bernhard Frick for the spectrometer IN16b, both at the Institut Laue-Langevin. Data analysis of *ab initio* molecular dynamics simulations was aided by Chloe Fuller.

Location and Orientation of Lone Pairs in Apatite-Type Materials: A Computational Study

J. R. Peet, A. Piovano, M. R. Johnson and I. R. Evans, *Dalton Transactions*, 2017, **46**, 15996-15999

Dynamics in Bi(III)-containing Apatite-Type Oxide Ion Conductors: A Computational Study

J. R. Peet, M. S. Chambers, A. Piovano, M. R. Johnson and I. R. Evans, *Journal of Materials Chemistry A*, 2018,**6**, 5129-5135

Samples used in neutron scattering experiments were prepared and characterised by Matthew Chambers.